STUDIES ON FUNDAMENTAL PROBLEMS IN SEISMIC DESIGN ANALYSES OF CRITICAL STRUCTURES AND FACILITIES

by

Ikuo Katayama

May 19, 1990

STUDIES ON FUNDAMENTAL PROBLEMS IN SEISMIC DESIGN ANALYSES OF CRITICAL STRUCTURES AND FACILITIES

by

Ikuo Katayama

May 19, 1990

TABLE OF CONTENTS

Page

Abstract. vii

Acknowledgements. x

List of Figures xii

List of Tables. xxiv

CHAPTER 1. INTRODUCTION 1

1.1 OBJECTIVES AND SCOPE 1

1.2 DESCRITION OF PRESENT APPRAOCH TO SOLVE PROBLEMS 3

CHAPTER 2. IMPORTANCE OF THREE-DIMENSIONAL ANALYSIS IN SOIL-STRUCTURE INTERACTION ANALYSIS 6

2.1 OBJECTIVES AND SCOPE 6

2.2 ANALYTICAL REPRODUCTION OF THREE-DIMENSIONAL BEHAVIOR OF AN ARCH DAM 8

2.2.1 INTRODUCTION 8

2.2.2 PROFILE OF NAGAWADO DAM AND GEOLOGY OF THE SITE . . . 8

2.2.3 SEISMIC MOTION INSTRUMENTATION. 9

2.2.3.1 Location of accelerographs 9

2.2.3.2 Overall response characteristics of accelerographs. 10

2.2.4 OUTLINE OF THE RECORDED MOTIONS 10

2.2.4.1 Processing and correction of records 10

2.2.4.2 Characteristics of the recorded motions . . . 11

2.2.5 ANALYSES OF THE RECORDED MOTIONS 12

2.2.5.1 Fourier analysis 12

2.2.5.2 Characteristics of the dam and the foundation response 12

2.2.6 NUMERICAL MODELING OF THE DAM AND FOUNDATION 14

2.2.6.1 Formulation of equation of motion 14

2.2.6.2 Definition of input ground motions 17

2.2.6.3 Material properties 18

2.2.7 SIMULATION OF THE DAM RESPONSE 18

2.2.7.1 Application of equations 18

2.2.7.2 Results 20

2.2.8 IMPORTANT ASSUMPTIONS IN SIMULATION ANALYSIS 21

2.2.8.1 Spatial variation of input motion 21

2.2.8.2 Fixed boundary or far-field boundary 22

2.2.8.3 Reservoir water 22

2.2.8.4 Free-field motion 23

2.2.9 CONCLUSIONS 24

2.2.10 REFERENCES 24

2.3 ANALYTICAL REPRODUCTION OF THREE-DIMENSIONAL BEHAVIOR OF A NUCLEAR REACTOR BUILDING MODEL 52

2.3.1 INTRODUCTION 52

2.3.2 VALIDATION STUDY OF HASSI-4 AND HASSI-7 52

2.3.2.1 Outline of HASSI-4 53

2.3.2.2 Site investigations and soil properties . . . 57

2.3.2.3 Simulation of forced vibration test 58

2.3.2.4 Simulation of earthquake response motion of model 2C 60

2.3.2.5 The importance of three-dimensional approach to SSI analysis 64

2.3.3 CONCLUSIONS 67

2.3.4 REFERENCES 69

2.4 CONCLUSIONS 93

CHAPTER 3. PROBLEMS IN ESTIMATING PEAK GROUND MOTIONS FOR USE IN SEISMIC DESIGN ANALYSIS 96

3.1 OBJECTIVES AND SCOPE 96

3.2 REVIEW OF EMPIRICAL FORMULAS FOR ESTIMATING PEAK GROUND MOTIONS 97

3.2.1 INTRODUCTION 97

3.2.2 CLASSIFICATION OF EMPIRICAL FORMULAS 97

3.2.3 REVIEW OF EACH FORMULA 98

3.2.3.1 Type I curves - $A=a\cdot\exp(bM)(R+c)^{-n}$ 98

3.2.3.2 Type II curves - $A=a\cdot\exp(bM)R^{-n}\cdot\exp(-dR)$ . . . 100

3.2.3.3 Type III curves - $A=a\cdot\exp(bM)[R+c_1\cdot\exp(c_2M)]^{-n}$ 103
3.2.3.4 Type IV curves - $A=a\cdot\exp(bM)R^{-n}\cdot\exp[-d_1\cdot\exp(d_2M)\cdot R]$ 105

3.2.4 ANALYSIS OF REPRESENTATIVE FORMULAS 106

3.2.4.1 Strong motion data base 106

3.2.4.2 Fit in original form to the Japanese strong motion data 108

3.2.5 CONCLUSIONS 111

3.2.6 REFERENCES 111

3.3 NEW EMPIRICAL FORMULA 133

3.3.1 NEED FOR NEW EMPIRICAL FORMULA 133

3.3.2 PRELIMINARY REGRESSION ANALYSIS 135

3.3.3 NEW EMPIRICAL FORMULAS 136

3.3.3.1 Formulas for structures on the ground surface 136

3.3.3.2 Formulas for structures underground 137

3.3.3.3 On the application of formulas 137

3.3.4 REFERENCES 138

3.4 SEISMIC RISK MAP OF THE KANTO AREA 153

3.4.1 INTRODUCTION 153

3.4.2 CONSTRUCTION OF SOURCE MODEL FOR SEISMIC HAZARD ANALYSIS 154

3.4.2.1 Characteristics of seismic activity of the Kanto area 154

3.4.2.2 Contour map of upper surface of seismically active zones 155

3.4.2.3 Seismically active fields 156

3.4.2.4 Seismically active source regions 157

3.4.2.5 Seismicity parameters 158

3.4.3 ATTENUATION CURVES FOR ESTIMATING PGA AND PGV 159

3.4.4 SEISMIC HAZARD OF THE KANTO AREA 160

3.4.4.1 Seismic hazard maps for the Kanto area 160

3.4.4.2 Annual probability of exceedance 161

3.4.5 REFERENCES 162

3.5 CONCLUSIONS 186

CHAPTER 4. DEVELOPMENT OF SIMPLIFIED DYNAMIC ANALYSIS METHOD FOR BURIED STRUCTURES. 188

4.1 OBJECTIVES AND SCOPE 188

4.2 THEORETICAL BACKGROUND OF THE PROPOSED METHOD 190

4.3 APPLICATION TO A SIMPLE DUCT AND ITS VALIDATION 195

4.3.1 Introduction 195

4.3.2 Model duct and the surrounding soil 195

4.3.3 Input ground motion 195

4.3.4 Numerical models 196

4.3.5 Analyses 196

4.3.6 Results 197

4.3.7 Validation of GRAMBS in comparison with experimental result 199

4.3.8 References 200

4.4 APPLICATION TO ANA UNDERGROUND POWER TRANSMISSION SHAFT IN LAYERED SOIL 215

4.4.1 Observed response and analytical results 215

4.4.2 Simulation by GRAMBS 216

4.4.3 References 217

4.5 APPLICATION TO LARGE SCALE UNDERGROUND CAVITY 227

4.5.1 Model cavern assembly and analytical model 227

4.5.2 Dynamic analysis by FLUSH 227

4.5.3 Quasi-static analysis by GRAMBS 228

4.5.4 Comparison of the results by FLUSH and GRAMBS 228

4.5.5 References 229

4.6 CONCLUSIONS 236

CHAPTER 5. SUMMARY AND CONCLUSIONS. 238

ABSTRACT

Motivated by increasing demands for more rational and reliable methods for the seismic safety design of special structures and facilities such as dams, nuclear power plants and lifeline systems, some of the fundamental problems included in the seismic design and analyses of representative structures are studied based on observational facts.

The first item examined is the seismic soil-structure interaction (SSI) effects significant for the seismic analyses and design of critical facilities such as heavy structures like dams, nuclear reactor buildings and some lifeline structures.

The author clarified the significance of the radiation damping effects in the foundation impedance problem through a comparison of the recorded response motions and the predicted response motions of an arch dam by using a three-dimensional finite element code based on frequency domain analysis scheme and consisting of the three-dimensional finite dam elements attached with far-field impedances of infinite strips along the abutment and with the reservoir water elements upstream with transmitting boundaries defined by impedance ratios at the water-water boundary and the water-gorge and bottom boundary. Through the analysis that could successfully reproduce the recorded response motion of the dam, the significance of the far-field boundary effect, the characteristics of the reservoir water upstream to suppress the dam response of upstream-down stream direction and the spatial variation of the input motion to the dam were clarified.

Under the same item, the significance of three-dimensional SSI analysis for truly three-dimensional structures is reaffirmed through a comparison of the recorded motions obtained for a small scale model during the forced vibration test and two earthquakes of different ground motion intensities with the numerical simulation of these records by the linear three-dimensional analysis code HASSI-4, non-linear analysis code HASSI-7, the linear two-dimensional code HASSI-2D and non-linear analysis code FLUSH-VB. In the two-dimensional analyses, the frequency shift was not so significant but the over damping is very serious resulting into a serious underestimate of the response of the structure because of its incapability to make the generated wave at the soil-structure interface decay rapidly to the far-field. The strain levels of the free-field soil and the soil near the foundation structure are remarkably different and the soil strongly affected by the soil-structure interaction was limited

to a fairly small region, the radius of which was less than two times the radius of the structure. This confirms that only a three-dimensional analysis can reproduce the rapid decaying nature of the wave generated at the soil-structure interface of truly three-dimensional structures.

The second item that was studied extensively is the empirical formulas upon which practicing engineers have been relying for predicting and determining the design peak ground motions. By preparing a new strong motion record sets and considering the response nature of buried ducts, two sets of new empirical formulas for estimating both the maximum acceleration and velocity were derived as suitable formulas to predict the peak ground motions for structures on the ground and underground under seismic environment of our country, where high seismicity at very shallow to intermediate depths can continue to be expected.

As an application of these formulas and to provide a design data base for power transmission systems which include various types of structures constructed on ground and underground, the above two sets of new attenuation curves were combined with a three-dimensional source model of the Kanto area to assess its seismic hazard. Assuming a Poisson process of occurrence of earthquakes, the seismic hazard of the Kanto area was presented in forms of contour maps of the expected peak ground acceleration and velocity for representative exposure times which can be used for predicting the peak ground motions meaningful for both structures on the ground surface and buried in shallow depths.

The last item discussed is to provide the practicing engineering community with a more rational and reliable design analysis tool for buried structures. This involves the development and validation of the quasi-static two-dimensional analysis method GRAMBS.

The author proposed his simplified analysis method GRAMBS(Ground Response Acceleration Method for Buried Structures) for the cross-sectional design of structures such as buried ducts and tunnels in layered soils. Assuming a plane strain dynamic system consisting of buried structures surrounded by a layered soil, it was shown theoretically that the proposed GRAMBS is a quasi-static method which approximately predicts the maximum response of buried structures surrounded by soil which otherwise would require a two-dimensional dynamic finite element analysis.

By introducing the acceleration distribution at the time when the portion of the soil in contact with the structure reaches the maximum strain energy state as the conserved body force acting on the system and

using the converged strain-dependent soil properties, both given by the response analysis of the free-field soil surrounding the structure, the GRAMBS solves the system idealized by a two-dimensional finite element model as a static problem.

The results obtained by GRAMBS of the maximum cross-sectional forces of a single story duct surrounded by a uniform soil as a parametric study for varying conditions of embedment depth, soil properties and thickness of the soil layer were very close to those obtained by the more rigorous dynamic analysis code FLUSH-VB.

Based on the fact that the FLUSH could successfully reproduce the cross-sectional bending moment of a single story duct model embedded in a dry sand layer obtained from an experiment performed and reported by Tohma and others(1985) of CRIEPI, the validity of GRAMBS was confirmed for application to a single story duct surrounded by a uniform soil.

The data and the results of the study on the comparison between the observed maximum response of re-bar stress and contact soil pressure of a multi-storiy shaft in a multi-layered soil and those responses numerically reproduced by FLUSH-VB(Kaizu and others, 1989(a), (b),1989) were also obtained by GRAMBS. The agreement between the observed maximum response of the stress and pressure and those obtained by GRAMBS was very good. With this and the above result, the validity of GRAMBS was finally confirmed. Another example of its application to a large scale cavern assembly was also shown and compared with the corresponding results by FLUSH-VB.

ACKNOWLEDGEMENTS

Foremost, I wish to thank Professor Yoshikazu Yamada of Kyoto University for encouraging me to continue this work with various kind of advice and critical review of manuscript, without which the objective of this work would not be in form. Thanks are due to Professor Kenzo Toki of Disaster Prevention Research Institute of Kyoto University and Assistant Professor Hirokazu Iemura of Kyoto University for their critical reading and encouraging criticism.

I wish to thank Dr. Yoshiji Niwa, the professor Emeritus, Kyoto University, who first kindly suggested me to submit the dissertation in the near future at that time, almost ten years ago.

I benefited greatly from innumerable discussions with Dr. Joseph Penzien, Professor Emeritus, University of California at Berkeley on all aspects of soil-structure interaction problems and also with Professor Alfredo H.-S. Ang, University of California at Irvine on the probabilistic hazard analysis.

I want to thank my colleague Mr. Tomio Tsuzuki on his work to amend the three-dimensional finite element code used in reproducing the observed response of the arch dam. On this item, I am grateful to Dr. Toshio Fujii, and Mr. Kenichiro Egawa of Tokyo Electric Power Company Inc., for giving me the chance to analyze and simulate the unprecedentedly precious response records of the arch dam and allowed me to submit the results outside.

I wish to thank my colleagues, Dr. Akira Niwa, Messors Yoshiya Kubo, Hitoshi Nakase, and the people who extensively contributed to our in-house field experiment and earthquake response observation at the small scale reactor building model at Kazusaminato. On this item, Messors Y. Nozawa and Y. Teramura, the former trainees in my department from Tokyo Electric Power Company Inc., are also acknowledged very much for their contribution to the site work and part of the analyses.

I am grateful to Messors Masanobu Adachi, T. Tsuzuki, Y. Seshimo, K. Ozeki, my colleagues and Mr. M. Shimada, a liaison engineer with us from Shimizu corporation for two years, for their efforts in running computers for the parametric study of the single-storied duct in the course of developing the GRAMBS.

I wish to thank Mr. Buichi Sakurai, the chairman of the Engineering

Research Institute of Tokyo Electric Power Company Inc., for allowing me to include the observed data and the results of simulation obtained at the underground power transmission shaft. Mr. M. Kaizu of the Institute is also greatly acknowledged for providing me the relevant original drawings he prepared for his papers submitted to some academic societies.

I also benefited from critical review by Mr. T. Annaka, my colleague and co-worker in engineering seismology, on the three-dimensional modeling of the seismicity of the Kanto area.

Other people having been around me and supportive to me during the course of my work, many of whom I can not include here, are also greatly acknowledged.

Finally, I thank my parents for giving me genuine motivation and for their patient support in completion of this dissertation, before the face of whom now I can not report the work done. I thank my friend, Dr. ken-ichi Hasegawa, Ikuo Hama, and Hazel and C. K. Lewe in Texas, for their kind encouraging me both openly and secretly to complete the effort. I also thank my daughter Yuko and my wife Akiko, for their understanding and sacrifice in behalf of this effort.

List of Figures

Figure	Contents	Page
2.2.1	Design layout of Nagawado Dam	26
2.2.2	General geologic plan and representative cross-section of the dam foundation	27
2.2.3	Location of accelerographs	28
2.2.4	Amplitude-Frequency characteristics of accelerograph (No. 595); Open triangles and open circles are for excitations by portable shaker at 150 and 110 gal in AGC active status. Solid circles are for 50 gal excitations. Double open circles denote the results obtained by oscilating built-in coil at 1 Hz	29
2.2.5	Linearity test result of overall recording system before and after AGC is activated (No. 595).	29
2.2.6	Corrected accelerograms of the dam and computed displacement time histories of 1/4 point and the crown of the crest arch (radial inward direction as positive).	31
2.2.7	Corrected accelerograms of the foundation (North and East direction as positive).	32
2.2.8	Fourier spectra of corrected accelerograms.	33
2.2.9	Spatial and Temporal displacement diagram of Band - a (1.0 - 1.3 Hz)	34
2.2.10	Spatial and Temporal displacement diagram of Band - c (2.0 - 2.35 Hz)	34
2.2.11	Spatial and Temporal displacement diagram of Band - e (3.1- 3.4 Hz)	35
2.2.12	Spatial and Temporal displacement diagram of Band - e (3.45- 3.75 Hz)	35
2.2.13	Spatial and Temporal displacement diagram of Band - e (4.0- 4.4 Hz)	36
2.2.14	Spatial and Temporal displacement diagram of Band - e (4.55- 4.85 Hz)	36
2.2.15	Spatial and Temporal displacement diagram of Band - e (5.35- 5.65 Hz)	37
2.2.16	Comparison of corrected accelerograms recorded across the D fracture zone	38

2.2.17 Comparison of computed displacement time histories across the D fracture zone. 38

2.2.18 Finite element model with far-field impedance along the dam-foundation interface 39

2.2.19 Comparison of three types of input ground motions on Fourier spectra; Solid, broken, and chained lines denote the type I, Type II, and Type III input ground motion, respectively 39

2.2.20 Spatially varied scheme of three types of input ground motions represented by Y-direction (upstream-downstream) 40

2.2.21 Displacements according to the three types of quasi-static input motions, in X (N - S) direction 42

2.2.22(a) Comparison between the observed and simulated motions by final model(FM); Solid and dotted lines denote the observed and simulated, respectively. 43

2.2.22(b) Comparison between the observed and simulated motions on Fourie spectra; Line type is same as Figure 2.2.22(a) 44

2.2.23(a) Comparison between the observed and simulated motions when the horizontal input motions of N-S direction are multiplied by 1.5 in the final model(FM); Line type is same as Figure 2.2.22 (a) 45

2.2.23(b) Comparison between the observed and simulated motions in Figure 19(a) on Fourie spectra; Line type is same as Figure 2.2.22(a). 46

2.2.24(a) Comparison of the simulated results obtained by using the in-phase motion (a) with the final result; For time histories, line type is same as Figure 2.2.22. For spectra, solid, dotted, and chained lines are for those of the observed, the final results, and the results with the in-phase motion (a) 47

2.2.24(b) Comparison of the simulated results obtained by using the in-phase motion (b) with the final result; For time histories, line type is same as Figure 2.2.22. For spectra, solid, dotted, and chained lines are for those of the observ-ed, the final results, and the results with the in-phase motion (b). 48

2.2.25 Comparison of the simulated results obtained by the fixed boundary model with the final result; For time histories, line type is same as Figure 2.2.22. For spectra, solid, dotted, and chained lines are for

those of the observed, the final results , and the results by the fixed boundary model 50

2.2.26 Comparison of the simulated results obtained by the model without reservoir water with the final result; For time histories, line type is same as Figure 2.2.22. For spectra, solid, dotted, and chained lines are for those of the observed, the final results , and the results by the model of this case. . . . 51

2.3.1 Modeling concept of HASSI-4 72

2.3.2 Substructuring scheme of Near-Field soil region 72

2.3.3 Soil condition of the sub-surface layers 73

2.3.4 Absolute and normalized dynamic shear modulus and absolute damping ratio versus shear strain relationship for the first and second layer 74

2.3.5 Configuration of models 75

2.3.6 A representative forced vibration test results 75

2.3.7 Numerical model of forced vibration test at Model 2c by HASSI-4 and the observed and the calculated results 76

2.3.8 Seismic instrumentation at Model 2C and triangular seismic array 77

2.3.9 Observed response of Model 2C and free-field ground motions on Jan. 17, 1987 78

2.3.10 Observed response of Model 2C and free-field ground motions on Dec. 17, 1987 79

2.3.11(a) Input ground motions for simulation: The upper and lower accelerograms are the free-field motions observed at points S1 and A1, each apart from the model 1.5 m and 30 m, respectively 80

2.3.11(b) Comparison of acceleration time histories (NS components) between the observed and simulated: The upper is the observed motion of the roof top of the model, the middle the simulated motion by using the S1 motion, and the lower that by using the A1 motion (r=1.8 t/cu.m, Vs=275 m/s, h=0.5%). 80

2.3.11(c) Input ground motions for simulation: The upper and lower accelerograms are the free-field motions observed at points S1 and A1, each apart from the model 1.5 m and 30 m, respectively 81

2.3.11(d) Comparison of acceleration time histories (EW components) between the observed and simulated: The upper is the observed motion of the roof top of the model, the middle the simulated motion by using the S1 motion, and the lower that by using the A1 motion (r=1.8 t/cu.m, Vs=275 m/s, h=0.5%) 81

2.3.12(a) Fourier spectra of the observed and simulated acceleration time histories in case of NS components (with Parzen's window of the band width 0.2Hz) 82

2.3.12(b) Fourier spectra of the observed and simulated acceleration time histories in case of EW components (with Parzen's window of the band width 0.2Hz) 82

2.3.12(c) Comparison of the simulated results on Fourier spectra 82

2.3.13 Comparison of the recorded motions with calculated motions in case of the 1987 December 17th earthquake records by linear analysis by using HASSI-6: The thick solid lines denote the observed motions and the fine chained lines the calculated motions; the first two figures are the comparison for NS components by using the input ground motion at S1 and A1, and the next two figures are for those of EW components by S1 and A1 motions 83

2.3.14 Fourier spectra of the recorded motions and the calculated motions by linear analysis by HASSI-6 84

2.3.15(a) Comparison of the recorded motions at the roof top of the model 2C with the calculated motions by the non-linear analysis with using HASSI-7 and three orthogonal ground motions at S1 point: The upper figure compares those of NS component and the lower for EW component 85

2.3.15(b) Comparison of the recorded and calculated results by HASSI-7 on the acceleration spectra; The upper is for NS components and the lower for EW components. 85

2.3.16 Converged soil properties in non-linear zone and adjacent soil; the converged values of shear wave velocities and damping values (in parentheses) across the I/N interface show very close values. 86

2.3.17 Numerical model in case of the two-dimensional analysis by FLUSH-VB 87

2.3.18 Comparison of the observed and simulated response motion (NS components); from the upper to lower, the observed motion, the simulated motion by three-dimensional HASSI-4, two-dimensional HASSI-2D, and FLUSH-VB codes 88

2.3.19 Comparison of the recorded and calculated response motions on Fourier spectra; (a), (b), (c) and (d) stands for the recorded motion, the calculated by HASSI-4, HASSI-2D and FLUSH-VB, respectively 89

2.3.20 Comparison of the absolute acceleration amplitude transfer functions of the roof top motions by HASSI-4, HASSI-2D, and FLUSH-VB 90

2.3.21 Comparison of the absolute acceleration amplitude transfer functions(approximated) of the ground surface motions at the points shown in (a); (b) and (c) stand for HASSI-4 and FLUSH-VB, respectively 91

2.3.22 Simulation results by the stick model with soil springs of circular disc(the third and fourth) and single degree of freedom (rocking) model (the fifth); The first and the second time histories are for reference and the soil properties are shown in the parentheses) 92

3.2.1 Fit of Donovan curve;
$A=1080\cdot\exp(0.5M)(R+25)^{-1.32}$ (gal) 118

3.2.2 Fit of Ang and Newmark curve;
$A=1.35\cdot\exp(0.67M)(D+15)^{-1.75}$ (G) 119

3.2.3 Fit of T.Katayama curve;
$A=203.3\cdot\exp(0.948M)(R+30)^{-1.637}$ (gal) 120

3.2.4 Fit of T.Katayama curve;
$A=9.60\cdot\exp(1.073M)D^{-1.290}$ (gal) 121

3.2.5 Fit of Orphal et al curve;
$A=0.66\cdot10^{0.40M}\cdot R^{-1.39}$ (G) 122

3.2.6 Fit of Combined Kanai-Seed curve;
$A_0=(1/Tp)\cdot10^{B}$ (gal), $Tp=(0.000512M-0.00143)\cdot(X+100)+0.02$; $B=0.61M-P\log_{10}X+Q$; $X=(D^2+H^2)^{1/2}$;
$P=1.66+3.6/X$; $Q=0.167-1.83/X$ 123

3.2.7 Fit of Joyner and Boore curve;
$\log_{10}A=-1.02+0.249M-\log_{10}(r)$
$-0.00255\cdot r$ (G), $r=(D^2+7.32^2)^{1/2}$ 124

3.2.8 Fit of Milne and Davenport curve;
$A=0.69\cdot\exp(1.64M)/[D^2+1.1\cdot\exp(1.1M)]$ (G) 125

3.2.9 Fit of Campbell curve;
$A=0.0159\cdot\exp(0.868M)[D+0.0606\cdot\exp(0.7M)]^{-1.09}$ (G) 126

3.2.10 Fit of Campbell curve;
$A=0.0185\cdot\exp(1.28M)[D+0.147\cdot\exp(0.732M)]^{-1.75}$ (G) 127

3.2.11 Fit of I.Katayama(Type I) curve;
$A=0.0302\cdot\exp(1.281M)[D+0.300\cdot\exp(0.752M)]^{-1.513}$ (G) . . . 128

3.2.12 Fit of Nakamura et al curve;
$\log_{10}A=0.168M-0.50\cdot\log_{10}(D+H)$
$-0.0551\cdot D\cdot 10^{-0.156M}+1.86$ (gal) 129

3.2.13 Fit of I.Katayama (Type II) curve;
$\log_{10}A=0.180M-0.193\cdot\log_{10}(D+H)$
$-0.0558\cdot D\cdot 10^{-0.157M}-1.333$ (G) 131

3.3.1 Iso-seismal maps for 75 and 100 years of expectancy; (a) and (b) for the case of Type I curve, and (c) and (d) for Type II curve are used, respectively 139

3.3.2 Examples of the observed propagation speed at the ground surface (After Toki, 1981) 140

3.3.3 Result of regression analysis for Type I curve;
$A=0.0652\cdot\exp(0.494M)(R+0.58)^{-0.656}$ (G) 143

3.3.4 Result of regression analysis for Type II curve;
$A_0=(1/Tp)\cdot 10^{B}$; $Tp=(0.000512M-0.00143)\cdot (X+100)+0.02$; $B=0.339M-P\log_{10}X+Q$; $X=(D^2+H^2)^{1/2}$
$P=-0.217-13.08/X$; $Q=-4.37-3.4/X$ (gal) 144

3.3.5 Result of regression analysis for Type III curve;
$A=0.0284\cdot\exp(1.285M)\cdot[D+0.300\cdot\exp(0.752M)]^{-1.54}$ (G) . . . 145

3.3.6 Result of regression analysis for Type IV curve;
$A=0.1125\cdot\exp(0.269M)[D+H]^{-0.339}\cdot$
$\exp[-0.480\cdot\exp(-0.694M)\cdot D]$ (G) 146

3.3.7 Proposed formula of PGA for structures on the ground surface of ordinary soil 148

3.3.8 Proposed formula of PGV for structures on the

ground surface of ordinary soil. 149

3.3.9 Proposed formula of PGA for structures buried in the ground of ordinary soil 150

3.3.10 Proposed formula of PGV for structures buried in the ground of ordinary soil 151

3.3.11 Distribution of maximum acceleration amplification factor of the surface layer of 55 substaions in the Kanto area 152

3.4.1 Inter-relationship among Tectonic Features (After Tsumura,1973) 164

3.4.2(a) Distribution of hypocenters in the Kanto area; showing the double seismic planes (After ERI, 1982) 164

3.4.2(b) Distribution of hypocenters in the Kanto area; showing the double seismic planes (After ERI, 1982) 165

3.4.2(c) Distribution of hypocenters in the Kanto area; showing the double seismic planes (After ERI, 1982) 165

3.4.3 Illustration of the tectonic model by Hamada and Kasahara (1981) 166

3.4.4 The earthquake nests in the Kanto area by Usami and Watanabe (1976) 167

3.4.5(a) Distribution of epicenters in the Kanto area for the range of the earthquake magnitude greater than 2.0 and focal depths from 40 to 80 km. The earthquakes plotted here have been determined by four or more stations of ERI with standard erros less than 7.5 km. (After Maki and others, 1980) 168

3.4.5(b) Distribution of earthquakes along the sections passing through the southwestern part of Ibaragi Prefecture (a) in the direction of northwest-southwest and (b) in the direction of southwest-northeast, within 25 km on the both sides of the lines plotted. (same) 169

3.4.5(c) Distribution of the earthquakes along the section passing through the middle part of Chiba Prefecture in the direction of east-west. (same) 169

3.4.6(a) Map used for specifying the upper surface planes of seismically active regions in PHP and PAC; Epicenter distribution of microearthquakes (After Ishida, 1984) 170

3.4.6(b) Map used for specifying the upper surface planes of seismically active regions in PHP and PAC; Plane and

vertical section of the area shown in the inserted map (After Ishida, 1984) 170

3.4.6(c) Map used for specifying the upper surface planes of seismically active regions in PHP and PAC; Plane and vertical section of the area shown in the inserted map (After Ishida, 1984) 171

3.4.6(d) Map used for specifying the upper surface planes of seismically active regions in PHP and PAC; Plane and vertical section of the area shown in the inserted map (After Ishida, 1984) 171

3.4.6(e) Map used for specifying the upper surface planes of seismically active regions in PHP and PAC; Plane and vertical section of the area shown in the inserted map (After Ishida, 1984) 172

3.4.7 Illustrative evaluation of seismic hazard point P_A caused by sources B and C on three-dimensional seismic surface defined in subducting plates 172

3.4.8(a) The configuration of the seismically active surface of the Pacific Plate(PAC) 173

3.4.8(b) The configuration of the seismically active surface of the Philippine Sea Plate(PHP) 173

3.4.9(a) Epicenter distributions of earthquakes located at a depth of 0 to 100 km by JMA from 1961 through 1982 used for dividing seismically active regions. I, II, III denote seismically active fields and those with suffices are respective seismically active regions in each field 174

3.4.9(b) Epicenter distributions of earthquakes located at a depth of 0 to 20 km by JMA from 1961 through 1982 used for dividing seismically active regions. I, II, III denote seismically active fields and those with suffices are respective seismically active regions in each field. 175

3.4.9(c) Epicenter distributions of earthquakes located at a depth of 21 to 30 km by JMA from 1961 through 1982 used for dividing seismically active regions. I, II, III denote seismically active fields and those with suffices are respective seismically active regions in each field. 176

3.4.9(d) Epicenter distributions of earthquakes located at a depth of 31 to 100 km by JMA from 1961 through 1982 used for dividing seismically active regions. I, II, III denote seismically active fields and those with suffices are respective seismically active regions in each field. 177

3.4.10 Truncated M-log(N) relation of total area and each seismically active field; (a) stands for the fields I+II+III, (b), (c), and (d) seismically active field I, II, and III, respectively 178

3.4.11 Hypocenter distribution of the earthquakes greater than 5.5 by magnitude during the period from 1885 through 1982 and used for determining the seismicity parameters of each seismically active region 179

3.4.12 Isoseismal map for the mean return periods of 25 years; (a) and (b) are for surface and buried structure 181

3.4.13 Isoseismal map for the mean return periods of 50 years; (a) and (b) are for surface and buried structure 182

3.4.14 Isoseismal map for the mean return periods of 75 years; (a) and (b) are for surface and buried structure 183

3.4.15 Isoseismal map for the mean return periods of 100 years; (a) and (b) are for surface and buried structure 184

3.4.16 Annual probability of exceedance versus PGM at the sites shown here; (a) and (b) are for PGA and PGV, respectively 185

4.2.1 Numerical model scheme of quasi-static analysis method GRAMBS 194

4.3.1 The model of one storied multi-cell concrete duct 202

4.3.2 Strain dependent dynamic properties of the soil and the soft rock 202

4.3.3 Input ground motions used for analyses; the upper figure shows the strong motion originated from Taft records (1957) and the lower from Lake Hughes array No. 9 (1971) 204

4.3.4 Numerical models for the free-field soil response analysis and the two-dimensional finite element dynamic analysis and the quasi-static analysis; the lowest boundaries are at 80 meters depth and only the first 40 meters portions are shown in this figure 204

4.3.5 The cross-sectional force distribution of Model-1 (T_M=4.02 sec.); (a) the results by FLUSH-VB and (b) the results by GRAMBS 206

4.3.6 The cross-sectional force distribution of Model-2 (T_M=4.06 sec.); (a) the results by FLUSH-VB and (b) the results by GRAMBS 207

4.3.7 The cross-sectional force distribution of Model-9 (T_M=6.82 sec.); (a) the results by FLUSH-VB and (b) the results by GRAMBS 208

4.3.8 Comparison of the end-moment distribution of Model-2 obtained by various analysis methods; the evaluating position of the end-moments is in the figure attached 209

4.3.9 Comparison of the end-moment distribution of Model-9 obtained by various analysis methods; the evaluating position of the end-moments is same as is in Figure 4.3.8 209

4.3.10 Comparison of the stress distribution at the outer surface of the duct by FLUSH-VB and GRAMBS in case of Model-9; (a) and (b) shows the normal stress and shear stress, respectively 210

4.3.11 Comparison of the acceleration response spectra of the free-field soil response motion of the top of the layer No. 8 and the response obtained by FLUSH-VB of the nodal point No. 193 at the center of the top slab of the duct for the Model-9 210

4.3.12 Plastic duct and shear soil column used in the experiment (After Tohma and others, 1985) 212

4.3.13 Frequency characteristic of the input motion and the measured response of the soil column surface motion (After Tohma and others, 1985) 213

4.3.14 Maximum bending moment distribution of the duct walls obtained by the experiment ("shallow case"; After Tohma and others, 1985) 213

4.3.15 Numerical model used in the simulation of the experimental results by FLUSH (After Tohma and others, 1985) 214

4.3.16 Strain-dependent properties of the sand used in the experiment (After Tohma and others, 1985) 214

4.3.17 Acceleration response spectra of the free-field surface response and the acceleration response of the top slap of the duct (After Tohma and others, 1985) 214

4.4.1 Vertical section of shaft, location of seismometers, re-bar extensometers, soil pressure meters of the shaft, soil profile and properties of surrounding

soil 218

4.4.2 Plan of shaft and the location of vertical array; the location of the seismometers is in Figure 4.4.1) 219

4.4.3 The examples of the soil response motions recorded at the vertical array and the response of the shaft in the event of the Southern Ibaragi Prefecture Earthquake on October 4, 1985 219

4.4.4 Simulated time history and the recorded motion of the point GL. -44.81 m and the respective Fourier spectrum ratios 220

4.4.5 Deconvolved outcrop motion at the depth of 82.55 m and Fourier spectrum used as the input motion of the numerical model shown in Figure 4.4.6(a) 220

4.4.6 Numerical model and the simulated soil response; (a) Numerical model used for the simulation of the shaft by FLUSH-VB and (b) the simulated and the observed maximum accelerations of the shaft, the surrounding soil and the free-field soil 221

4.4.7 The results of the simulation by FLUSH-VB compared by the absolute maximum indications of re-bar extensometers and soil pressure meters observed 222

4.4.8 The details of free-field soil and the response result at t_m=5.75 sec 223

4.4.9 The determination of the time t_m 224

4.4.10 Finite element model of the system consisting the shaft and the surrounding soil for the quasi-static analysis by GRAMBS 225

4.4.11 Shear stress distribution by GRAMBS of the soil at the contact surface of the shaft coplotted with that obtained by FLUSH-VB 224

4.4.12 Comparison of the results obtained by GRAMBS with the observed and calculated by FLUSH-VB at the time t_m=5.75 sec 226

4.5.1 Cavern assembly and the modeling concept 230

4.5.2 Control motion and input motion for dynamic analyses . . . 231

4.5.3 The comparison of the response acceleration time histories at the invert of caverns and the time history at the same level by one dimensional wave propagation analysis 231

4.5.4 Comparison of dynamic stresses of the inner concrete lining wall obtained by FLUSH and GRAMBS 232

4.5.5 Input seismic intensity distribution and quasi-static analysis model 233

4.5.6 Principal stress states surrounding the parallel caverns by overburden pressure and seismic force (by GRAMBS) 234

4.5.7 Principal stress states around the parallel caverns and the fiber and shear stress of the inner concrete lining wall of the cavern A for combined loads (by GRAMBS) 235

List of Tables

Table	Contents	
2.2.1.	Dimension of Dams and Reservoirs	26
2.2.2	List of maxima of corrected accelerograms and of computed velocity and displacement time histories	30
2.2.3	Comparison of significant modes of vibration between obsevation and laboratory test	37
2.2.4	Relation between the predominant frequencies and the material properties used for dynamic models	41
2.2.5	Damping values obtained by the final model (FM) in percent	49
2.3.1	Dimension and weight of model	75
2.3.2	Results of cross-correlation analysis of observed motions	77
3.2.1	Change of peak ground acceleration by filtering	114
3.2.2(a)	Contents of the Japanese strong motion data used	114
3.2.2(b)	Soil classification and the data	114
3.2.3	The peak acceleration and velocity data used for regfression analysis (Non-filtered record; NONFSEL)	115
3.2.4	Fit of original empirical formulas with Japanese Data	117
3.3.1	The peak acceleration and velocity data used for regression analysis (Filtered; FLTDSEL)	140
3.3.2	Results of regression analysis using the Japanese strong motion data (Non-filtered; NONFSEL)	142

Tables

3.4.1 The seismicity parameters of each seismically active source region 180

4.3.1 Installation conditions of the duct and the case number of the analyses 202

4.3.2 Dynamic material properties used for the model 203

4.3.3 Comparison of the maximum cross-sectional forces obtained through the analyses by FLUSH - VB and GRAMBS (Vs=200 m/s;Taft record) 205

4.3.4 Comparison of the maximum end-moments obtained by FLUSH-VB and GRAMBS with the models analyzed by using Vs=200 m/s and Taft record 211

4.3.5 Comparison of the maximum end-moments obtained at Model-3 when the shear wave velocity of the surface soil layer and the input ground motioncompares were changed 212

CHAPTER 1. INTRODUCTION

1.1 OBJECTIVES AND SCOPE

We have already constructed many heavy structures and facilities such as high-dams and nuclear power plants that are very critical for generating electricity needed by the industrial activity of our modern society. These structures and facilities have been very productive; however, at the same time some structures have had very high-potential hazard over the population in case of their failures. In this regard, these structures have been designed and constructed with the best analytical tools or model experiments, materials and construction practice available at the time, and have been keeping good operational records not causing any significant failure.

Further, recent development of electronic technology and communication networks in highly populated cities has given increasing importance on the reliability of power transmission facilities that include many types of underground structures such as tunnels and ducts extending over distance in the longitudinal directions.

With also recent advances in computer technology and finite element analysis modeling, large scale numerical models gradually became popular in the analyses of these critical structures by two-dimensional and three-dimensional finite element method; however, there are still little studies on the validity of these codes. Validation of the inherent assumptions and the effectiveness of the sophistication that have been implemented within these codes needs to be examined.

In practice, there are still not a few problems to be resolved that bar us in reaching a complete satisfaction especially in the area of dynamic analyses and designs against earthquakes; problems in implementing advanced theories into practical computation, limit of computer core size, wide fluctuation of input ground motions and foundation material properties, seismic soil-structure interaction problems and non-linear behavior effect of soft foundation media on structures, etc.

On the other hand, some extensive observations of behaviors of these structures have been accumulating and have given us a good chance to reflect the observations on the validation of available computer codes or new development of computer codes for refining our design analyses.

Under the circumstances described above and being motivated by increasing demands for more rational and reliable seismic safety design

of critical structures and facilities such as dams, nuclear power plants and lifeline systems as represented by buried structures, some of the fundamental problems included in the seismic design and analyses of the representative structures above described are studied primarily based on observational facts.

The first item looked into in Chapter 2 is the seismic soil-structure interaction (SSI) effects significant for the seismic analyses and design of heavy structures like dams and nuclear reactor buildings.

In Chapter 2.2, the author examines the significance of the radiation damping effects in the foundation impedance problem, as one of the fundamental components regarding SSI problem, through the comparison of the recorded response motions with the predicted response motions of an arch dam analyzed by a three-dimensional finite element code attached with a far-field impedance boundary and a reservoir water boundary.

As the second subject of Chapter 2, the significance of three-dimensional SSI analysis for truly three-dimensional structures is reaffirmed in Chapter 2.3 through the comparison of the recorded motions obtained at a small scale model during the forced vibration test and two earthquakes of different ground motion intensities with the numerical simulation of these records.

Subsequent two items to be described in Chapters 3 and 4 are the subjects primarily very familiar to practicing engineer's community in the design analyses of not only the critical structures described above but also conventional structures:

The item which is studied extensively and described in Chapter 3 is the development of new attenuation curves and seismic hazard maps that are more rational to be applied in the earthquake environment of us and meaningful for various structures constructed on the ground and underground.

The last item discussed in Chapter 4 is the development and validation of the quasi-static two-dimensional analysis method GRAMBS to provide the practicing engineering community with a more rational and reliable design analysis tool for buried structures. The theoretical aspect and the application procedure are described, and the validation study are performed using experimental results of a simple duct and response records of an actual shaft during an earthquake.

1.2 RELATED PREVIOUS STUDIES AND PRESENT APPROACH TO SOLVE PROBLEMS

It is the fundamental attitude of the author's that all the items selected for the study on and evaluation of the significance in engineering analyses will be supported by observational facts relevant to the appropriate items in case such facts are available. Therefore, in each item relating to dynamic analysis, each analytical procedure or computer code hired will be tested by the facts first and then the fundamental problems are pointed out and discussed.

In the seismic safety evaluation and design of critical structures such as dams and nuclear power facilities, a variety of sophisticated dynamic analysis codes have been applied; however, as already described above there are only limited studies on the validity of these codes including the inherent assumptions and the effectiveness of the sophistication that have been implemented within these codes, and at the same time most of these treat the basically three-dimensional soil-structure interaction problem in two-dimensions, mainly because of practical limitation of computer core size and computer economy.

The author selects SSI problem among dynamic analysis problems and examines some fundamental components for SSI analysis and SSI analysis codes based on the correlation results between analytical results and actually recorded response motions obtained at an arch dam and a model structure of nuclear reactor buildings.

Presently, such codes that can consider the seismic response of a dam and its foundation with the reservoir water upstream by finite element analysis techniques exist already; however, the foundation was considered as elastic media of limited volume neglecting its mass. Dependent on the volume idealized by the finite elements, such assumption of finite foundation causes not only many insignificant modes of vibrations for the dam response but also unrealistic refracted waves from the fixed boundary to the dam as clearly shown in Chapter 2.2. The reservoir water boundary is also an another important mathematical and engineering subject to be extensively studied separately and needs observational validation.

Including the both above, there were almost no reports that compared the computed response of dam and water response of arch dams with the observed response during earthquakes. As a set of precious response records was obtained at a high arch dam, the first item above, the radiation damping effects in the foundation impedance problem, was studied as one of the fundamental components regarding SSI problem by

comparing the recorded response motions with the predicted response motions obtained by a three-dimensional finite element code having been modified to consider the foundation scattering problem, soil impedance problem and reservoir water interaction problem. Because dynamic water pressures were not measured, the detail of the reservoir water acting on the upstream face of the dam can not be clarified, however, its effect on the response of the dam as a whole may be examined through the parametric approach varying these significant assumptions of boundary conditions as will be shown later.

Even the seismic safety evaluation and design of critical structures such as nuclear power plants, in most cases, basically three-dimensional soil-structure interaction problems have been treated in two-dimensions, mainly because of practical limitation of computer core size and computer economy. However, it is well known that the conversion of a three-dimensional problem into two-dimension has usually caused serious modulation of the dynamic characteristics of a structural system. Especially for such a vibration system that has to consider seriously the effect of soil compliance on the fundamental vibration characteristics of the system, this two-dimension simplification should be avoided unless the results can be guaranteed by some supplemental measures.

There are some reports on the validation study of dynamic analysis procedures used in the design analysis of reactor buildings through the comparison of the predicted response and observed records, however, the contribution of SSI over the whole response has not been thoroughly clarified due to fairly high rigidity of the foundation rocks relative to that of reactor buildings. And there was a report describing a good agreement between the observed response and the predicted results by a two-dimensional finite element code where the SSI effect on the response of the reactor building was not major.

Under the situation above, in order to make clear the significance of three-dimensional analyses in SSI problem, the recorded motions at an experimental model constructed at an open air site are compared with the predicted response motions obtained by the two-dimensional finite element codes, FLUSH-VB - a modified version of FLUSH with bi-directional viscous dampers at bottom boundary, HASSI-2D - the two-dimensional version of HASSI-4 having an equivalent soil impedance functions of infinite strip foundation, and the three-dimensional finite element linear and non-linear analysis codes, HASSI-4 and HASSI-7. A classical dynamic model is also employed for understanding the characteristics of the response motions.

Based on the validation study of the HASSI codes and the correlation study above, some significant characteristics of three-dimensional features of SSI phenomena will be shown. By extracting appropriate results from the numerical results successfully reproducing the observed response motions and comparing them with the results obtained by the two-dimensional analysis and classical analysis codes, the importance of three-dimensional treatment of SSI problem for truly three-dimensional structures is clarified.

The subject to be described in Chapters 3, e.g. the development of new attenuation curves and seismic hazard maps, is primarily very familiar to practicing engineer's community and similar results have been already given elsewhere; however, those attenuation curves and seismic hazard maps are almost none which were developed using Japanese strong motion data carefully corrected, considering the appropriate contribution of focal depths on the resultant peak ground motions and the application to buried structures.

The last item discussed in Chapter 4, e.g. the development and validation of the quasi-static two-dimensional analysis method GRAMBS, is first proposed by the author and is unique. Similar simplified method called "Response Displacement Method" is available but this method can not be deemed as unique because there are some types of methods under the same name that hire different analytical assumptions and procedures.

The author again validates his method through the comparison of the computed results with experimental results and observed structural response records during an earthquake. The fundamental difference between GRAMBS and other simplified method described above is clearly described.

Most of the conclusions to be derived for these items described in this dissertation may be already well known, however, it is the basic stance of the author to clarify what were already pointed out in most cases theoretically with the support of facts actually observed. Through this, the author intends to provide some key, even if it be small, leading to new insight in the fundamental problems left unclear or unresolved in the area of seismic design analyses for special but critical structures.

CHAPTER 2. IMPORTANCE OF THREE-DIMENSIONAL ANALYSIS IN SOIL-STRUCTURE INTERACTION ANALYSIS

2.1 OBJECTIVES AND SCOPE

Seismic soil-structure interaction (SSI) effects are important for the seismic analyses and design of critical facilities such as heavy structures like dams, nuclear reactor buildings and some lifeline structures.

Recent advance in the area has made available for us some computer analysis codes by two-dimensional and three-dimensional finite element method; the two-dimensional finite element code FLUSH, the three-dimensional finite element codes such as CLASSI by the continuum half space impedance method, SASSI, and HASSI by hybrid method.

These computer codes have been used in various analyses of the critical facilities, however, there are only limited studies on the validity of these codes including the inherent assumptions and the effectiveness of the sophistication that have been implemented within these codes.

The author examines the fundamental components required for SSI analysis and SSI analysis codes based on the correlation results between analytical results and actually recorded response motions obtained at an arch dam and a model structure of nuclear reactor buildings.

First, as for the radiation damping effects in the foundation impedance problem as one of the fundamental components regarding SSI problem, the recorded response motions of an arch dam in the event of an intermediate earthquake are compared with the predicted response motions obtained by a three-dimensional finite element code having been modified to consider the foundation scattering problem, soil impedance problem and reservoir water interaction problem. Through the correlation study, the importance of radiation damping effect in the foundation impedance problem is confirmed and a practical approach is proposed.

Secondly, as for the significance of three-dimensional analysis in SSI problem, the recorded motions at an experimental model used for the validation study of the hybrid analysis code for soil-structure interaction, HASSI, are compared with the predicted response motions obtained by the two-dimensional finite element codes, FLUSH-VB - a modified version of FLUSH with bi-directional viscous dampers at bottom boundary, HASSI-2D - the two-dimensional version of HASSI-4 having an

equivalent soil impedance functions of infinite strip foundation, and the three-dimensional finite element linear and non-linear analysis codes, HASSI-4 and HASSI-7. Based on the validation study of the HASSI codes and the correlation study, the importance of three-dimensional treatment of SSI problem for truly three-dimensional structures is clarified.

2.2 ANALYTICAL REPRODUCTION OF THREE-DIMENSIONAL BEHAVIOR OF AN ARCH DAM

2.2.1 INTRODUCTION

On September 14th, 1984 at 8:48 a.m., in the western part of Nagano prefecture, an intermediate earthquake of magnitude 6.8 occurred at the epicenter 35.82 N, 137.56 E and the depth 2 km. The Naganoken Seibu earthquake caused devastating landslides and subsequent debris flows around the epicentral area, resulting in 29 fatalities and 10 injured.

The accelerograph array installed in 1969 at Nagawado dam, 37 km northeast of the epicenter, recorded the response of the dam and the foundation rock. When the earthquake occurred the water level of Nagawado reservoir was at elevation 961 m (24 m below the crest).

The recorded motions in the above earthquake are first shown. Next, the significant modes of vibration of the dam, obtained through waveform analyses of the processed data, are analyzed and the fundamental modes of vibration of the dam are compared with those results having been obtained by the laboratory test of a small-scale model. Finally, by using the recorded motions in three-dimensional dynamic analyses of the dam response, the author confirms the significant feature of far-field soil effect with combination of some available assumptions in three-dimensional dynamic finite element model.

2.2.2. PROFILE OF NAGAWADO DAM AND GEOLOGY OF THE SITE

The Azusa River Hydropower Project, which includes three arch dams of Nagawado, Midono, and Inekoki, facilitates 960 MW electrical output. The construction of these dams started in 1965 and was completed in 1970. Table 2.2.1 summarizes the dimensions of these dams and relevant reservoirs.

Nagawado arch dam is the highest of the three arch dams. The dam axis lies approximately north-south. As shown in Figure 2.2.1, the dam is a double-curvature circular arch dam, i.e., curved in both the vertical (cantilever) and horizontal (arch) planes. The height of the dam is 155 m and the thicknesses at the crest and the base of the crown cantilever are 5 and 35 m, respectively. The crest length along the axis is 355.5 m, subtending a total of 97 deg. The dam is three-centered in each arch planes, i.e., one for the circular extrados and intrados curves of the central uniform section, and the other two for fillets at the two ends of the intrados curves. It has a vertical "open-joint" 35 m long from the

crest to the foundation rock in the north fillet section.

Figure 2.2.2 shows a representative geologic section of the foundation rock. The foundation rock consists primarily of sound granites with a small amount of lamprophyre covered by fractured hornfels, predominantly at the right bank near the crest level.

The in situ rock deformability tests and the elastic wave speed measurements were carried out in the test adits dug along the dam abutments. Allowing a considerable fluctuation, the elastic modulus of the foundation rock tends to increase from the upper to the lower level of the gorge; the static and the dynamic modulus increase from 30×10^3 to 120×10^3 and from 180×10^3 to 500×10^3 kg/cm^2 , respectively (TEPCO, 1966).

In the geologic investigation stage, some fracture zones were found in the periphery of the dam abutments, most of which had east-west strikes and nearly vertical dips. They were treated with plugs or dental works using ordinary concrete before placing the dam concrete. Their locations are shown in Figure 2.2.2.

2.2.3 SEISMIC MOTION INSTRUMENTATION

2.2.3.1 Location of accelerographs

Figure 2.2.3 shows the locations of accelerographs. Six accelerographs in the dam structure measure the radial motions of the crest arch (D_2, D_4) and its abutment (D_1), and the mid-height arch (D_3, D_5) and its wing (D_6) where an "open-joint" directs the thrust force to the foundation rock of the level. Nine similar accelerographs were installed at four locations in the foundation galleries for recording the foundation rock motion; these are one set(G_1) of three orthogonal components and three sets (G_2, G_3, G_4) of two horizontally orthogonal components. One component of each set is parallel to the upstream-downstream (E-W) direction. Another four sets (S_1 and S_2, S_3 and S_4, S_6 and S_7, S_8 and S_9) of accelerographs, each with horizontally orthogonal components, are installed across the treated portion of four fracture zones in the foundation rock.

All the accelerographs mentioned above are of the electromagnetic type. For cross-checking these accelerographs, the electromagnetic accelerographs at the crown and the left abutment of the crest arch were partnered with SMAC-B triaxial accelerographs next to them.

2.2.3.2 Overall response characteristics of accelerographs

The recording system has an Automatic Gain Control(AGC) system, which suppresses the amplitudes of input signals from accelerographs by one-half when a signal level of any given accelerograph exceeds the nominal level equivalent to 100 gal. This control function lasts for several seconds, and then the system restores its initial recording condition.

As the actual data on how the AGC system worked during the earthquake were not available, we performed an in situ test to examine the actual response of the AGC to accurately recover the suppressed portions of the records after the earthquake. The test verified the response characteristics of full signal line from accelerograph to dry photo paper recorder by shaking some representative accelerographs on a portable shaker. This test was limited to two radial components at the crest arch and one component in the inspection gallery. We also tested all accelerographs by driving, at 1 Hz, the built-in calibration coil of each accelerograph using a test oscillator.

Figure 2.2.4 shows that the amplitude-frequency curves of the acceleration recording system are flat over the frequency range of significant dam response (1 Hz-10 Hz) and that the amplitudes at 1 Hz obtained by built-in calibration coils are in good agreement with those from the portable shaker tests. The linearity of the output signal on the recorder for varied accelerations is well maintained over the range from 50 to 280 gal as clearly shown in Figure 2.2.5. The actual acceleration that activates AGC system was found to be 80 gal, 20 gal less than the nominal value originally specified. The duration of signal suppression by AGC was 4.7 seconds, precisely common for all signal lines.

2.2.4 OUTLINE OF THE RECORDED MOTIONS

2.2.4.1 Processing and correction of records

The earthquake motions were carefully traced and digitized from the paper records by using a time increment of 0.01 second during 12 seconds of record, where the earthquake signals maintained a level sufficiently larger than that of the noise. The digitized data were then corrected for slight fluctuations of the paper speed among the recorders by using the simultaneously recorded standard time codes. Further, the wave heights during the time of activation of the AGC were adjusted to give correct amplitudes in accordance with the test results described above.

These digitized records were then filtered by a band-pass filter with the low and high cut-off frequencies of 1.0 and 30 Hz for the subsequent analyses. These filtered acceleration records were numerically integrated twice to obtain the absolute displacements in the limited frequency band.

2.2.4.2 Characteristics of the recorded motions

The maximum values of the corrected digital acceleration records of the dam and the foundation rock are listed in Table 2.2.2. The acceleration time histories, except those recorded at the treated fracture zones, are shown in Figures 2.2.6 and 2.2.7, with the computed displacement time histories of the points on the crest arch. From the table and the figures of these records, the following features can be pointed out:

1. The three seconds between 2.8 and 5.8 contains the major part of the acceleration records; the initial one second duration of each record is the most intense portion.

2. The recorded maxima of the acceleration time histories of the points in the foundation rock, including those of abutments, lie within the range of 18 to 35 gal. Those of the right bank are larger than those of the left bank.

3. Acceleration amplitudes obtained at the deeper point in the foundation rock (G_4) are smaller than at points near the surface (G_1, G_2). This seems consistent with the trend in elastic constants shown by in situ tests of the foundation rock.

4. The maximum accelerations of the points of the crest arch are 193 and 242 gal for the crown (D_4) and 1/4 point (D_2), respectively. This suggests that the antisymmetric mode of vibration is dominant on the response of the crest arch.

5. Assuming that the records obtained at the points G_1 and G_2 are the input ground motions for the dam, the ratios of the maximum accelerations of these points to the input motion accelerations lie in the range 7 to 9.

2.2.5 ANALYSES OF THE RECORDED MOTIONS

2.2.5.1 Fourier analysis

We calculated Fourier spectra for three groups of records, one for the crown(D_4; No. 597) and the 1/4 point (D_2; No. 595) of the dam, and the other two for the north-south components (No. 1116 in left bank and No. 1118 in right bank) of the points (G_1 and G_2) and for the east-west components (No. 1115 in left bank and No. 1117 in right bank) in the foundation rock at the crest level. They are plotted in Figure 2.2.8, in which some peaks are denoted by the letters "a" to "j" for convenience of subsequent analyses.

In the frequency bands denoted by a and c, the amplitudes of the dam and the foundation responses are almost of the same order. This could be attributed to the fundamental modes of vibration of the foundation rock. The difference in the foundation motion spectra across the gorge (N-S components) could have affected possibly the response of the dam.

At the crown point of the crest arch (D_4; No. 597), those components of 3.6 Hz (f), 4.1 Hz (g) and 4.7 Hz (h) have large Fourier amplitudes. On the other hand, at the 1/4 point (D_2; No. 595) of the crest arch, the Fourier amplitudes show large peaks at 5.5 Hz (j) and 3.3 Hz (e).

2.2.5.2 Characteristics of the dam and foundation responses

To examine the overall response of the dam and the foundation rock and the relationship between them, we filtered the computed displacement time histories with band-pass filters. The frequency bands of these filters were selected to take into account those peaks on the Fourier spectra previously noted. Then we drew the temporal and spatial diagrams of displacements of the dam and the foundation for each frequency band at selected time intervals during a half cycle of the most significant portion in the filtered time history. Figures 2.2.9 to 2.2.15 are examples of those diagrams which showed significant response modes of the dam and the foundation rock.

From the comparison of the Fourier amplitudes and the time dependent spatial variations for each selected band, we conclude that the frequency bands a and c are those of the foundation response modes and the bands e,f,g, and j show the response modes of the dam, as described below.

1. a (1.0-1.3 Hz): The dam and the foundation rock were found displaced in the same manner, as shown in Figure 2.2.9.

2. c (2.0-2.35 Hz): The foundation motions in EW direction were small. In contrast, the foundation motions in NS direction were in phase but their magnitudes were unequal at the banks(Figure 2.2.10).

3. e (3.1-3.4 Hz): The dam showed large deformations relative to those of the foundation rock at 3.36 s, in an antisymmetric manner, as shown in Figure 2.2.11. This mode may correspond to the first antisymmetric mode of the dam.

4. f (3.45-3.75 Hz): The dam showed significant deformations in this band at 3.48 s which could be attributed to the first symmetric arch mode, as shown in Figure 2.2.12.

5. g (4.0-4.4 Hz): The crest arch alone showed a large relative deformation. However, the mid-height arch did not show significant displacement. In this mode, the second cantilever mode of vibration seems to be represented(figure 2.2.13).

6. h (4.55-4.85 Hz): The crest arch showed a large deformation, and the phases of motion at the crown and the 1/4 point were reversed during a half cycle. This mode may correspond to the second symmetric mode (Figure 2.2.14).

7. j (5.35-5.65 Hz): The deformation of the crest arch was significant but that of the mid-height arch was negligibly small. The dam may show antisymmetric arch and cantilever type of the second mode (Figure 2.2.15).

A small scale model was tested during the design stage of the dam, and the measured frequencies of the first antisymmetric arch mode, the first symmetric arch mode, and the second symmetric arch mode were 3.08, 3.50, and 4.67 Hz, respectively, as is shown in Table 2.2.3 (Takahashi et al, 1964). These correspond respectively to the peak frequencies of the antisymmetric first mode in band e (3.1-3.4 Hz), the symmetric first mode in band f (3.45-3.75 Hz), and the symmetric second mode in band h (4.55-4.85 Hz).

As for the observed records across the treated fracture zones, we take, as representative, a complete set of orthogonal records obtained at both sides of the treated fracture zone along D fault (S_8 and S_9). We slightly rotated the corrected records into the normal and parallel

directions to the strike of the fracture zone. Each pair of records is compared in Figure 2.2.16. The major portions of the computed displacements are shown similarly in Figure 2.2.17. Significant differential motions did not occur during this earthquake, as evident from these figures. A similar result has been reported for another earthquake(Fujii, 1973).

2.2.6 NUMERICAL MODELING OF THE DAM AND FOUNDATION

The deformability of the foundation rock supporting the dam can have significant effect on the dynamic response of the structure during an earthquake. We idealized the dam and the foundation rock with a finite element model for the dam surrounded by boundary springs and viscose dampers as shown in Figure 2.2.18. The input ground motions of the dam are defined in a multiple and spatially varied input scheme.

2.2.6.1 Formulation of equation of motion

The equations of motion of the combined dam-foundation system with the reservoir water on the upstream face in Figure 2.2.18 can be written as

$$\begin{bmatrix} M_s & M_{sb} & 0 \\ M_{sb}^T & M_b & 0 \\ 0 & 0 & M_\phi \end{bmatrix} \begin{Bmatrix} \ddot{U}_s \\ \ddot{U}_b \\ \ddot{\phi} \end{Bmatrix} + \begin{bmatrix} C_s & C_{sb} & C_{s\phi} \\ C_{sb}^T & C_b & C_{b\phi} \\ C_{s\phi}^T & C_{b\phi}^T & C_\phi \end{bmatrix} \begin{Bmatrix} \dot{U}_s \\ \dot{U}_b \\ \dot{\phi} \end{Bmatrix} + \begin{bmatrix} K_s & K_{sb} & 0 \\ K_{sb}^T & K_b & 0 \\ 0 & 0 & K_\phi \end{bmatrix} \begin{Bmatrix} U_s \\ U_b \\ \phi \end{Bmatrix}$$

$$= \begin{Bmatrix} 0 \\ f_b \\ C_{v\phi} \cdot \dot{U}_{b\phi} \end{Bmatrix} \qquad (1)$$

where U_s, U_b are the total displacement vectors of the dam and the dam-foundation interface. M, C, and K denote the mass, damping, and stiffness, respectively. The suffix s denotes the degree-of-freedom(DOF) of the dam excluding that of the dam-foundation interface. The suffix b refers to the DOF of the interface. The right-hand side(RHS) term, f_b,

is the interaction force acting at the dam-foundation interface.

The reservoir water was taken into consideration as was shown in the third of Eq.(1), where ϕ, M_ϕ, K_ϕ, and C_ϕ denote, respectively, velocity potential, mass, stiffness, and damping of free water. $C_{b\phi}$ and $C_{s\phi}$ denotes damping related to the bottom and side boundary of the reservoir and to the boundary of the upstream face of the dam.

The RHS term, $[C_{v\phi}]\cdot \dot{U}_{b\phi}$, is the force acting at the boundary of the water.

$$\text{Let} \quad \begin{Bmatrix} U_s \\ U_b \end{Bmatrix} = \begin{Bmatrix} U_s^{qs} \\ U_b^{qs} \end{Bmatrix} + \begin{Bmatrix} U_s^{d} \\ U_b^{d} \end{Bmatrix} \tag{2}$$

where the vector U_b^{qs} and U_b^{d} are, respectively, quasi-static displacements and the dynamic interaction displacements at the boundary.

The prescribed multiple input motions, $\underline{a}_l(t)$, $\underline{a}_c(t)$, and $\underline{a}_r(t)$, which are measured accelerations along x, y, and z axes in the foundation rock, are assumed as those of the free-field. They are related to $\ddot{U}_b^{qs}$ by

$$\begin{Bmatrix} \\ \ddot{U}_b^{qs} \\ \\ \end{Bmatrix} = \begin{bmatrix} & & \\ & \underline{A} & \\ & & \end{bmatrix} \begin{Bmatrix} \underline{a}_l(t) \\ \underline{a}_c(t) \\ \underline{a}_r(t) \end{Bmatrix} \tag{3}$$

where

$$\underline{a}_l(t) = \begin{Bmatrix} a_{lx}(t) \\ a_{ly}(t) \\ a_{lz}(t) \end{Bmatrix}, \quad \underline{a}_c(t), \text{ and } \underline{a}_r(t) \text{ are similar.} \tag{4}$$

and matrix $\underline{A}$ is defined by the interpolation functions as described later; thus $\ddot{U}_b^{qs}$ becomes known.

Substituting Eq.(2) into Eq.(1) to get

$$\begin{bmatrix} M_s & M_{sb} & 0 \\ M_{sb}^T & M_b & 0 \\ 0 & 0 & M_\phi \end{bmatrix} \begin{Bmatrix} \ddot{U}_s^d \\ \ddot{U}_b^d \\ \ddot{\phi} \end{Bmatrix} + \begin{bmatrix} C_s & C_{sb} & C_{s\phi} \\ C_{sb}^T & C_b & C_{b\phi} \\ C_{s\phi}^T & C_{b\phi}^T & C_\phi \end{bmatrix} \begin{Bmatrix} \dot{U}_s^d \\ \dot{U}_b^d \\ \dot{\phi} \end{Bmatrix} + \begin{bmatrix} K_s & K_{sb} & 0 \\ K_{sb}^T & K_b & 0 \\ 0 & 0 & K_\phi \end{bmatrix} \begin{Bmatrix} U_s^d \\ U_b^d \\ \phi \end{Bmatrix} =$$

$$-\begin{bmatrix} M_s & M_{sb} & 0 \\ M_{sb}^T & M_b & 0 \\ 0 & 0 & M_\phi \end{bmatrix}\begin{Bmatrix} \ddot{U}_s^{qs} \\ \ddot{U}_b^{qs} \\ 0 \end{Bmatrix}-\begin{bmatrix} C_s & C_{sb} & C_{s\phi} \\ C_{sb}^T & C_b & C_{b\phi} \\ C_{s\phi}^T & C_{b\phi}^T & C_\phi \end{bmatrix}\begin{Bmatrix} \dot{U}_s^{qs} \\ \dot{U}_b^{qs} \\ 0 \end{Bmatrix}-\begin{bmatrix} K_s & K_{sb} & 0 \\ K_{sb}^T & K_b & 0 \\ 0 & 0 & K_\phi \end{bmatrix}\begin{Bmatrix} U_s^{qs} \\ U_b^{qs} \\ 0 \end{Bmatrix}+\begin{Bmatrix} 0 \\ f_b \\ C_{v\phi}\cdot\dot{U}_{b\phi} \end{Bmatrix} \quad \cdots\cdots(5)$$

Taking quasi-static terms into account, we obtain the following relations from Eq.(1).

$$\begin{bmatrix} K_s & K_{sb} \\ K_{sb}^T & K_b \end{bmatrix}\begin{Bmatrix} U_s^{qs} \\ U_b^{qs} \end{Bmatrix}=\begin{Bmatrix} 0 \\ 0 \end{Bmatrix} \tag{6}$$

Because of Eq.(6), the stiffness terms on RHS of Eq.(5) drop out. The damping terms on the RHS of the first and second of Eq.(5) are small and can be deleted, but the hydrodynamic damping terms on the RHS of the third of Eq.(5) are retained.

Fourier transforming Eq.(5) to the frequency domain and noting f_b becomes, with the frequency dependent far-field foundation impedance matrix, $I_f(iw)$, and the interaction boundary displacements, $U_b^d(iw)$,

$$f_b(iw) = - I_f(iw)\cdot U_b^d(iw) \tag{7}$$

then we obtain

$$\left\{ -w^2\begin{bmatrix} M_s & M_{sb} & 0 \\ M_{sb}^T & M_b & 0 \\ 0 & 0 & M_\phi \end{bmatrix} + iw\begin{bmatrix} C_s & C_{sb} & C_{s\phi} \\ C_{sb}^T & C_b+I_f^I(w) & C_{b\phi} \\ C_{s\phi}^T & C_{b\phi}^T & C_\phi \end{bmatrix} + \begin{bmatrix} K_s & K_{sb} & 0 \\ K_{sb}^T & K_b+I_f^R(w) & 0 \\ 0 & 0 & K_\phi \end{bmatrix}\right\}\begin{Bmatrix} U_s^d(iw) \\ U_b^d(iw) \\ \phi(iw) \end{Bmatrix}$$

$$= -\begin{Bmatrix} \begin{bmatrix} M_s & M_{sb} \\ M_{sb}^T & M_b \end{bmatrix}\begin{Bmatrix} \ddot{U}_s^{qs}(iw) \\ \ddot{U}_b^{qs}(iw) \end{Bmatrix} \\ C_{s\phi}^T\cdot\dot{U}_s^{qs}(iw) + C_{b\phi}^T\cdot\dot{U}_b^{qs}(iw) - C_{v\phi}\cdot\dot{U}_{b\phi}(iw) \end{Bmatrix} \tag{8}$$

where $\ddot{U}_s^{qs}(iw) = -K_s^{-1}\cdot K_{sb}\cdot\ddot{U}_b^{qs}(iw)$, from the first of Eq.(6).

Now the RHS of Eq.(8) is completely known, so one can solve for

$$\left\{ U_s^d(iw),\ U_b^d(iw),\ \phi(iw) \right\}^T,$$

then $$\left\{ \ddot{U}_s^d(iw),\ \ddot{U}_b^d(iw),\ \ddot{\phi}(iw) \right\}^T = -w^2 \left\{ U_s^d(iw),\ U_b^d(iw),\ \phi(iw) \right\}^T,$$

and finally we can obtain

$$\begin{Bmatrix} \ddot{U}_s(iw) \\ \ddot{U}_b(iw) \end{Bmatrix} = \begin{Bmatrix} \ddot{U}^{qs}_s(iw) \\ \ddot{U}^{qs}_b(iw) \end{Bmatrix} + \begin{Bmatrix} \ddot{U}^d_s(iw) \\ \ddot{U}^d_b(iw) \end{Bmatrix} \tag{9}$$

The normal modes of the above dynamic displacements can be obtained from the eigen problem

$$\begin{bmatrix} M_s & M_{sb} & 0 \\ M_{sb}^T & M_b & 0 \\ 0 & 0 & M_\phi \end{bmatrix} \begin{Bmatrix} \ddot{U}^d_s \\ \ddot{U}^d_b \\ \ddot{\phi} \end{Bmatrix} + \begin{bmatrix} K_s & K_{sb} & 0 \\ K_{sb}^T & K_b + I_f^R(w) & 0 \\ 0 & 0 & K_\phi \end{bmatrix} \begin{Bmatrix} U^d_s \\ U^d_b \\ \phi \end{Bmatrix} = \begin{Bmatrix} 0 \\ 0 \\ 0 \end{Bmatrix} \tag{10}$$

where $I_f^R(w)$ is the real part only of the foundation impedance matrix $I_f(iw)$ evaluated for a particular frequency.

2.2.6.2 Definition of input ground motions

The horizontal input ground motions in form of acceleration were varied by bank and depth. On the other hand, the vertical motion was always defined uniquely and uniformly because we have only one vertical component observed at G_1 of the left bank.

By following the observed records, the contributions of the in-phase and out-of-phase motions calculated from the horizontal records obtained at G_1 and G_2 were almost equal as displayed by the Fourier spectra of Figure 2.2.19. In contrast, the intensity of the group of records at G_4, S_3, and S_4 relative to that of G_1 and G_2 was smaller as can be seen also in the figure.

Hence, we defined the horizontal input ground motions at the

boundary of the dam which are composed of three types of free-field motions as illustrated in Figure 2.2.20.

(I) in-phase motion uniform at the whole boundary based on the records at G_1 and G_2
(II) out-of-phase motion, defined by the records at G_1 and G_2, linearly varies vertically to zero at the bottom of the dam
(III) in-phase motion decreasing from the crest to the bottom of the dam in parabolic curves and defined independently at both banks by using the pairs of records G_1 to (S_3, S_4) and G_2 to (S_3, S_4).

2.2.6.3 Material properties

The specific weight, shear wave velocity, dynamic Young's modulus, and Poisson's ratio of the dam concrete and the foundation were chosen respectively as (2.3 t/m^3, 2800 m/sec, $4.3 \cdot 10^6$ t/m^2, and 0.17) and (2.6, 2000, $2.9 \cdot 10^6$, and 0.32). The specific weight and dilatational wave velocity of the water as 1.0 t/m^3 and 1500 m/sec, respectively. These values were finally adopted after comparing the calculated eigen frequencies of the dam response with the significant frequencies derived from observed records. As shown in Table 2.2.4, various parameters were varied to obtain reasonable results within the limit considered as permissible. A material damping ratio of 2 % was used for both the dam concrete and foundation rock as the value appropriate in small strain level, compatible with the recorded response of the dam.

2.2.7 SIMULATION OF THE DAM RESPONSE

2.2.7.1 Application of equations

In applying the preceding formulation of dynamic analysis, the following assumptions and procedures were introduced to meet practical requirements in computation;

(1) First, the normal modes, eigen frequencies, and participation factors were calculated for the dam and foundation system model in which the foundation is fixed at its boundary. Then, the foundation impedance $I_f(iw)$ (real spring and imaginary dash-pot) for rocking, normal, transverse, and longitudinal motions were approximately estimated from two-dimensional compliance functions derived with the assumption of an infinite rigid massless strip of finite width lying on an elastic half space. With the results of the preceding eigen value

analysis, the frequency independent springs along the boundary of the dam were determined by averaging the frequency dependent springs over the significant frequency range of the dam response in order to make subsequent calculations easier.

(2) Next, the normal modes and eigen frequencies of the dam and foundation spring system model were calculated and used for calculating the total modal damping constant for the jth mode of the dam and dam-foundation interface, h_j^t, by

$$h_j^t = h_j^m + h_j^r \tag{11}$$

$$h_j^r = [1/(2w_j \cdot M_j)] \cdot [\phi_j]^T [C_f] [\phi_j]$$

where h_j^m : material damping constant of the dam and foundation

h_j^r : radiation damping constant according to the radiation effect at the dam-foundation interface

M_j : $= [\phi_j]^T [M] [\phi_j]$ relating to j th mode

$[M]$: mass matrix of the dam

$[C_f]$: $= [0 + I_f^I(w)]$

$[\phi_j]$: = eigen modes of the dam and foundation system

(3) The condition of infinity at the most upstream boundary and discontinuity at the side boundary of the water reservoir were implemented by making respective impedance ratio equal to 1 and 5.

(4) When solving Eq.(8), by taking the approximation;

Let $\left\{U_r\right\}^T = \left\{U_s^{qs} + U_s^d, \quad U_b^{qs} + U_b^d\right\}^T$

and taking the upper two equations of Eq.(10), the separation of variance as $U_r^d = [\phi] \cdot \{q\}^T$ was performed, where $[\phi]$ and $\{q\}^T$ are respectively the eigen vectors and normalized coordinates of dynamic displacements of the dam-foundation system, and performing appropriate operation, we obtain the final form of Eq.(8) as

$$-w^2\left(\begin{bmatrix}[I] & 0\\ 0 & [M\phi]\end{bmatrix}+iw\begin{bmatrix}[2h_j^t\cdot w_j] & [\phi]^T\cdot[C_{d\phi}]\\ [C_{d\phi}]^T\cdot[\phi] & [C_\phi]\end{bmatrix}+\begin{bmatrix}[w_j{}^2] & 0\\ 0 & [K_\phi]\end{bmatrix}\right)\begin{Bmatrix}q(iw)\\ \phi(iw)\end{Bmatrix}$$

$$=-\begin{Bmatrix}\begin{bmatrix}\phi\end{bmatrix}^T\cdot\begin{bmatrix}M_s & M_{sb}\\ M_{sb}{}^T & M_b\end{bmatrix}\begin{Bmatrix}\ddot{U}^{qs}_s\ (iw)\\ \ddot{U}^{qs}_b\ (iw)\end{Bmatrix}\\ (1/iw)\cdot[C_{s\phi}{}^T\cdot\ddot{U}^{qs}_s\ (iw)+C_{b\phi}{}^T\cdot\ddot{U}^{qs}_b\ (iw)-C_{v\phi}\cdot\ddot{U}_{b\phi}(iw)]\end{Bmatrix} \qquad (12)$$

In solving Eq.(12), first, the eigen modes and frequencies of the dam-foundation system were calculated up to the 30th mode equivalent to 15 Hz and the equation was fixed. Then, the relative displacement response of the dam were solved, using discrete frequency w convenient for subsequent Fourier inverse transformation to obtain the time domain response, for the frequency range up to 10Hz. The absolute displacement and acceleration response were calculated using the relationship in Eq.(2).

2.2.7.2 Results

The response to the quasi-static input motions at the dam-foundation interface for each loading type are shown in Figure 2.2.21, which was used to verify the adequacy of the computer source code.

Figure 2.2.22 shows the calculated results of the dynamic response of the dam-foundation system by the final model(hereafter denoted by FM) in the form of acceleration time histories and Fourier spectra, and comparison with respective observed motions.

For the crest arch, the calculated response at the crown(D_4) and the abutment(D_1) nicely simulate the observed motions, where the 1st antisymmetric and symmetric modes are observed around 3.4 Hz. However, at the left 1/4 point(D_2), the calculated response is much smaller than the observed and this mainly comes from shortness in the calculated response of frequency components of the 2nd symmetric and antisymmetric modes around 5 to 6 Hz and unidentified mode of 2.7 Hz in the observed record, as evident from the comparison of the Fourier spectra.

Regarding the mid-height arch, the fitness between the calculated and observed is poor and the frequency components both around 2.7 Hz and 5 to 7 Hz in the observed records are not sufficiently reproduced.

The input ground motions in the cross canyon direction (N-S direct-

ion), which have been recorded under the environment of the gorge but assumed here as those of free-field, might be affected by the shape of the gorge. Here, we assume that the the shape of the gorge affected these ground motions, resulting in suppressing these motions by about two third, and therefore we alter these ground motions by a multiplying factor of 1.5. Then, ,as is shown in Figure 2.2.23, the results becomes much improved generally. As for this assumption, some appropriate analysis is needed for verification.

2.2.8 IMPORTANT ASSUMPTIONS IN SIMULATION ANALYSIS

As described above, we have tried dynamic analysis in order to simulate the recorded motions of a dam, based on the three-dimensional hybrid model which presumes spatially varying multiple input free-field ground motions acting at the dam-foundation interface and allows the radiation of the wave to the far-field from the interface.

The results are not completely satisfactory if we compare the results with the author's experience in the simulation of other structures. However, by utilizing the model and the simulation procedure, the author will examine the importance of the modeling concept and assumptions which might generate different results.

2.2.8.1 Spatial variation of input motion

The first question is the spatial variation of input ground motions. Figure 2.2.24 shows the calculated results when the input motions were defined as unvaried with space. We take two representative input motions, namely, (a) the horizontal ground motions at (S_3 and S_4) and (b) the horizontal motions averaged from those at (G_1, G_2, and G_3). The vertical motion is always the same that was obtained at G_1. The results are shown for those obtained at D_4 and D_2 in forms of time histories and Fourier spectra.

The case (a), in Figure 2.2.24(a), is not better than the previous results and also the case (b), in Figure 2.2.24(b), is worth especially for the response of the crown of the crest arch where the best fitting has been obtained in the previous model(FM).

From this, we may suggest that the spatially varied input motions are necessary.

2.2.8.2 Fixed boundary or far-field boundary

This question whether to use the fixed boundary or the far-field boundary is somewhat controversial, because it also refers to the problem of basic definition of input ground motion; free-field motion or motion within a profile. Regardless of the latter problem, we compare the results obtained by two models; one with limited volume of foundation rock modeled by finite elements with fixed boundary and the other with far-field boundary along the dam and foundation interface, e.g. the final model(FM) used in the previous analysis.

The results are shown for two points of the crest arch in Figure 2.2.25. When the boundary of the foundation rock is fixed, the damping in the calculation is limited to the material damping of 2 % for the dam and foundation rock. The resultant response at D_4 became much larger than the observed, whereas the model with far-field impedance could provide much more adequate results with a fairly large modal damping values including radiation damping, as shown Table 2.2.5. Though the maximum acceleration at the 1/4 point of the crest arch obtained in the fixed boundary model seems a little closer to the observed, the phase lag is significant and the damping at high frequency range is clearly insufficient. The acceleration level of the observed records can not correspond to material damping value much larger than 2 %, even though higher material damping might result in improved results with this model.

From this, we may say that the model with far-field impedance will provide more rational evaluation of dynamic characteristic as a whole, with a more reasonable material damping.

2.2.8.3 Reservoir water

As for the interaction of reservoir water on the dynamic response of arch dams, several assumptions regarding the reservoir water upstream has recently been proposed(the additional mass method is one of them, for example) but we considered the contribution of reservoir water interaction throughout the preceding calculations by idealizing the water by finite elements as has been already described. Here, we simply display the contribution of the reservoir water to the final simulation results and emphasize its significance on the final results.

Figure 2.2.26 compares the results obtained with and without water on the upstream face of the dam. When the water is neglected, the

response at the crown of the crest arch(D_4), where the 1st symmetric mode dominates, becomes very large. On the other hand, at the 1/4 point of the crest arch where the 1st and 2nd anti-symmmetric modes are dominant, the Fourier spectrum peaks at around the 1st symmetric and 2nd symmetric modes show remarkable shift to higher frequency but at around the 2nd antisymmetric mode, such shift does not occur.

From this, as easily understandable, it is evident that the water strongly suppresses the response of the dam in the upstream and downstream directions. The shift of frequency observed may also depend on the assumption used for determining material properties of the model, since our final model properties have been chosen to make the model hold comparable frequency characteristics of the proto-type under the presence of the reservoir water.

2.2.8.4 Free-field motion

In the foregoing analyses, we have skipped the examination on how the free-field input ground motions were selected among the recorded motions in the foundation rock of the dam. In practice, it seems very difficult to acquire at any arch dam site the true free-field ground motions needed for rigorous analysis because of the complicated nature of the gorge suitable for arch dams. Therefore, even if the importance of the spatial variation of input motions was examined above, the spatially varying free-field input ground motions were replaced by the ground motions recorded in depth and from this they can not be said as true free-field motions. Further, it is possible to obtain the true free-field ground motions by performing the deconvolution analysis by a three-dimensional model of the gorge without dam structure. However, this is not practical, because the properties of the foundation material of the entire foundation area are usually not explored to the extent required for a deconvolution analysis.

In this regard, even if we performed some parametric studies to estimate the free-field motions along the surface of the abutment by a two dimensional model that takes the configuration of the gorge into account, the apparent lack of dynamic properties of the foundation rock area necessary for such a deconvolution analysis precludes us from obtaining reasonable results.

2.2.9 CONCLUSION

The author clarified some reasonably practical modeling methods to simulate the response recorded for an arch dam. Through the study, the author found some significant conditions required for performing a rational three-dimensional dynamic analysis of arch dams.

The reservoir water was found to suppress the upstream-downstream response of the dam; however, there is no effect on the antisymmetric modes of vibration.

When the dam was modeled with limited volume of foundation rock with fixed boundary, the dam response became unreasonablly large unless unreasonably large values of material damping for the dam and the foundation rock are used.

The analytical model capable of reflecting the far-field boundary effect along the dam abutment will give more reasonable response of the dam.

To get a good fit to the recorded motions of the dam, it was required to take the spatial variation of input ground motions into account. This fact suggests the need for observing reliable spatially varied input ground motions preferably in the form of free-field motions.

2.2.10 REFERENCES

(1) Fujii, T., K. Egawa, and I. Katayama, (1987). Dynamic Behavior of Nagawado Arch Dam in the Event of 1984 Naganoken Earthquake, Earthquake Spectra, Earthquake Engineering Research Institute, Vol. 3, No.2, pp.347-364.

(2) Fujii, T., K. Egawa, and I. Katayama, (1987). Seismic Response of Nagawado Arch Dam, International Conference on Large Dams, Beijin, May 17-25.

(3) Tokyo Electric Power Co., Inc. (1966), Design and Foundation Treatment of Nagawado, Midono, and Inekoki Arch Dams (in Japanese).

(4) Takahashi, C. and Y. Mashiko (1964), "The dynamic model test on Nagawado Arch dam", the report to Tokyo Electric Power Co., Inc., the Central Research Institute for Electric Power Industries (in Japanese).

(5) Fujii, T. (1973), On the Treatment of Faults in Dam Foundation by Using Replacement with Concrete, Cement Grouting together with Prestressing Steel Bars, Doctoral Thesis (in Japanese).

Table 2.2.1. Dimension of Dams and Reservoirs

Item		Nagawado	Midono	Inekoki
Catchment area	(km^2)	380.5	431.0	470.4
Dam				
Type		arch	arch	arch
Height	(m)	155	95.5	60
Crest length	(m)	355.5	343.3	192.8
Concrete volume	(10^3m^3)	660	304	65.4
Reservoir				
Surface area	(10^4m^2)	274	57	51
Total capacity	(10^6m^3)	123	15.1	10.7
Effective capacity	(10^6m^3)	94	4	6.1
Available depth	(m)	55	8	14
High water level	(m)	982	853.5	787

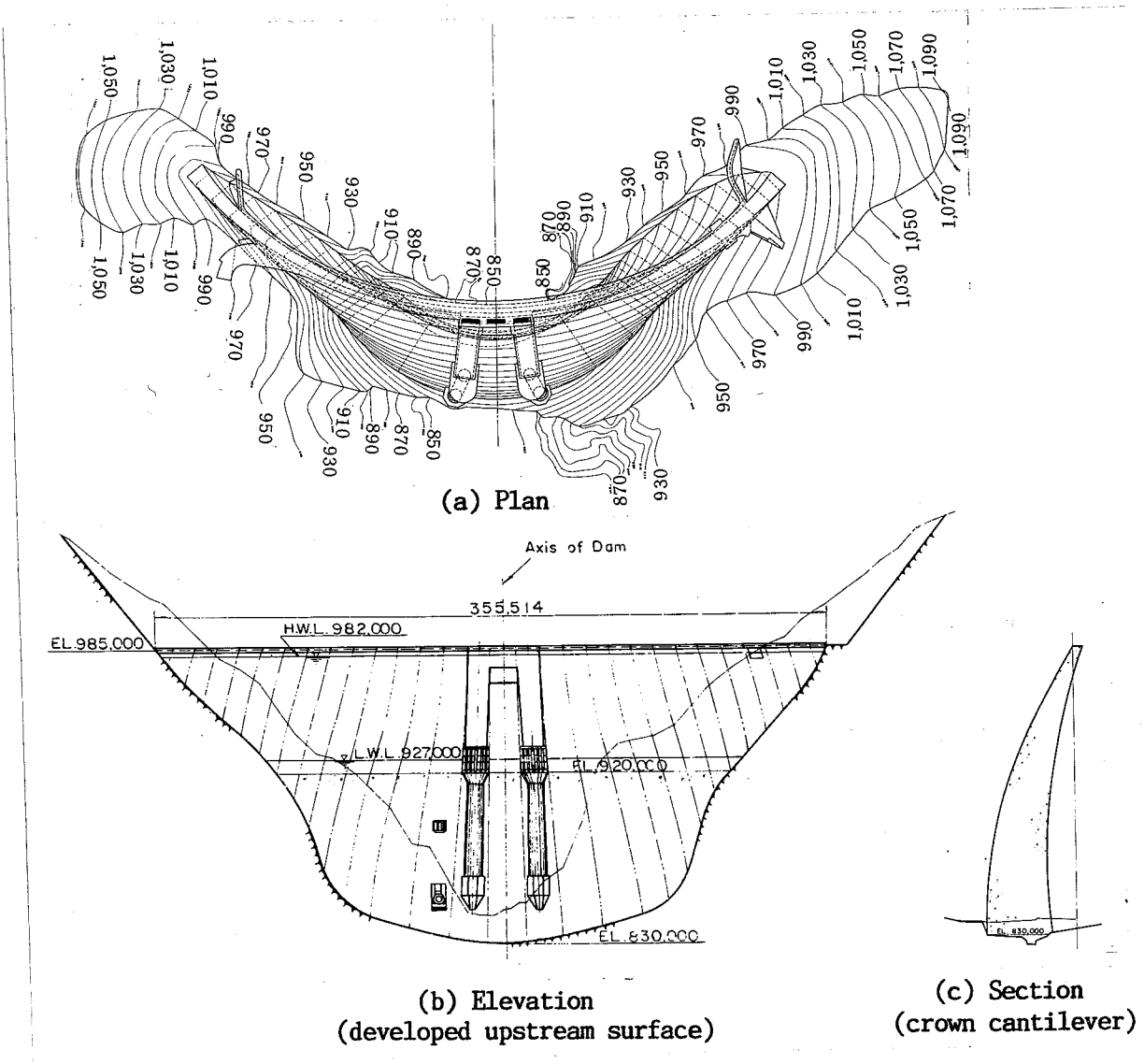

(a) Plan

(b) Elevation
(developed upstream surface)

(c) Section
(crown cantilever)

Figure 2.2.1 Design layout of Nagawado Dam

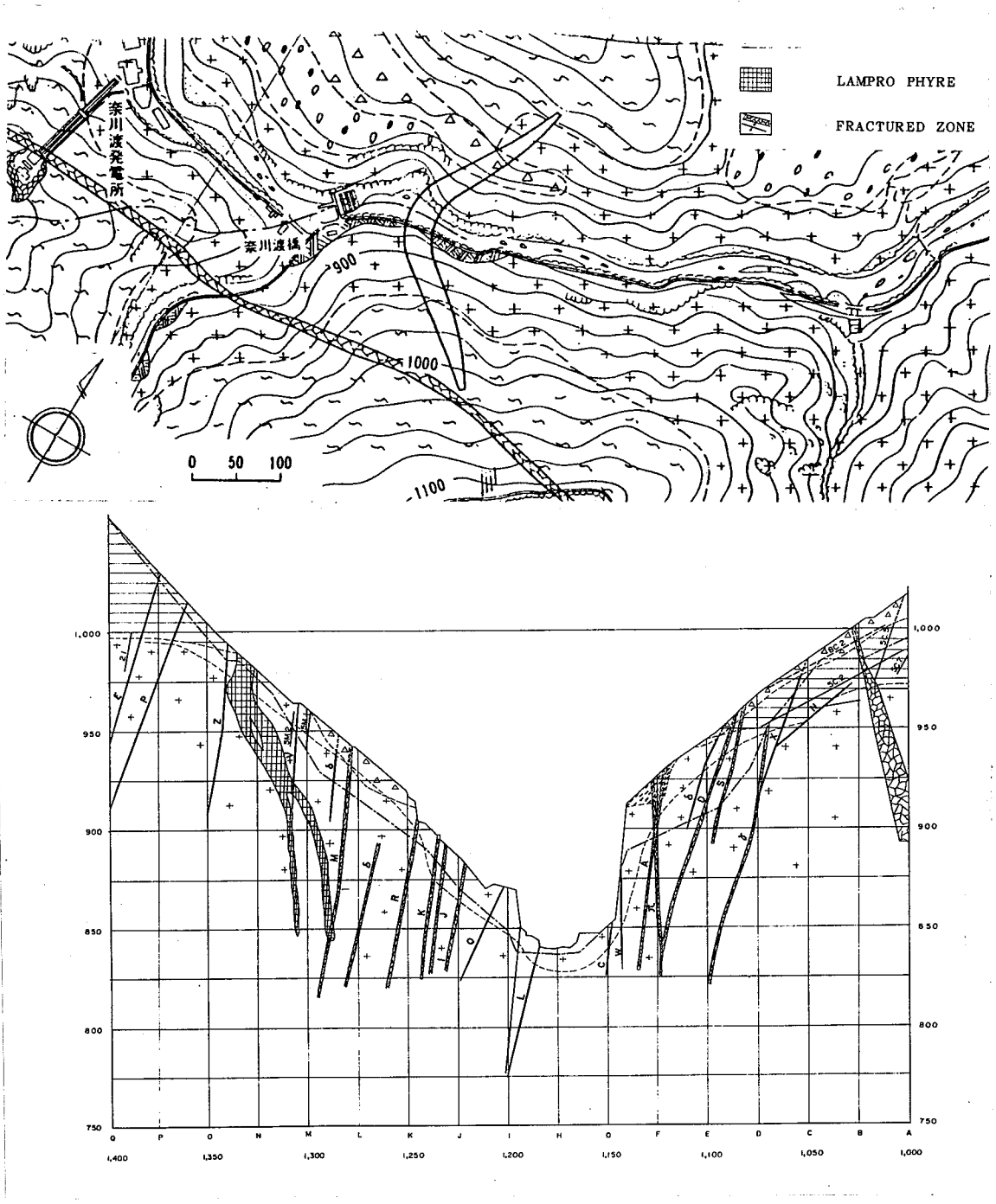

Figure 2.2.2 General geologic plan and representative cross-section of the dam foundation

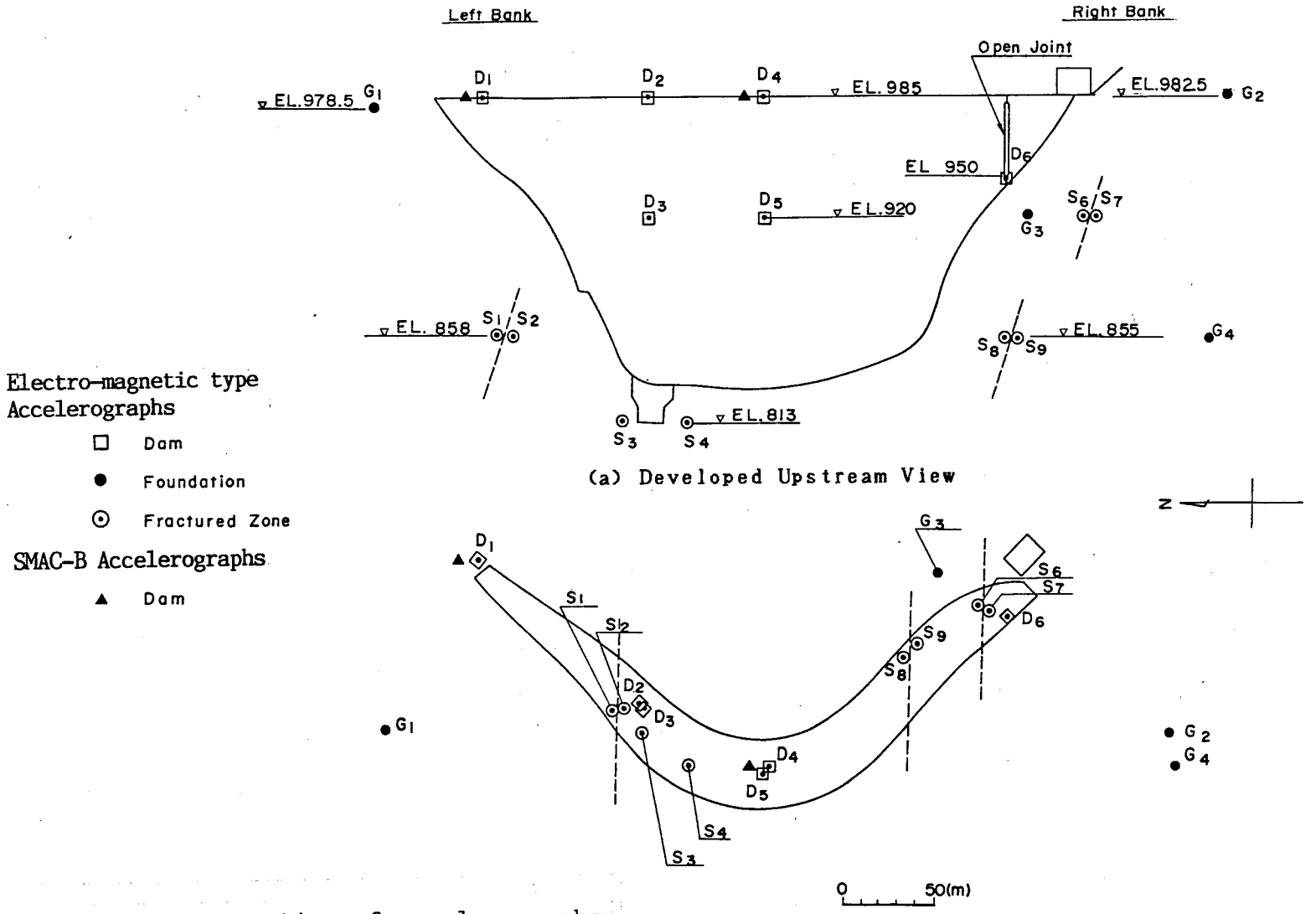

Figure 2.2.3 Location of accelerographs

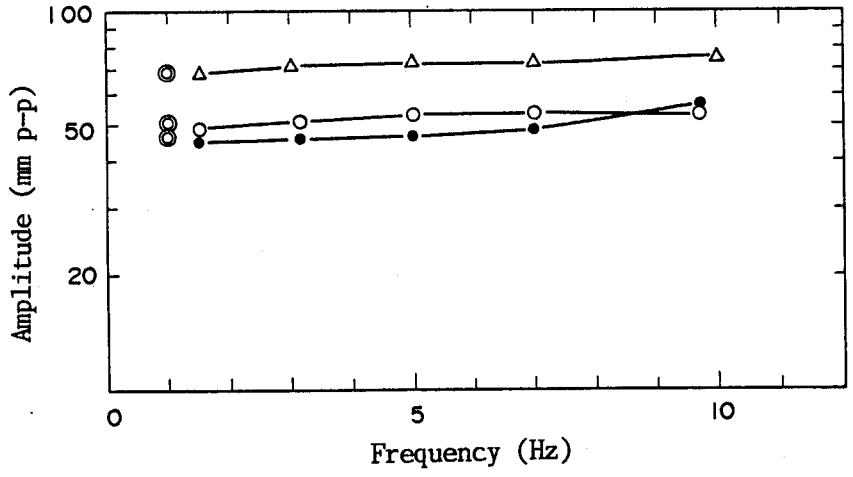

Figure 2.2.4 Amplitude-Frequency characteristics of accelerograph (No. 595); Open triangles and open circles are for excitations by portable shaker at 150 and 110 gal in AGC active status. Solid circles are for 50 gal excitations. Double open circles denote the results obtained by oscilating built-in coil at 1 Hz.

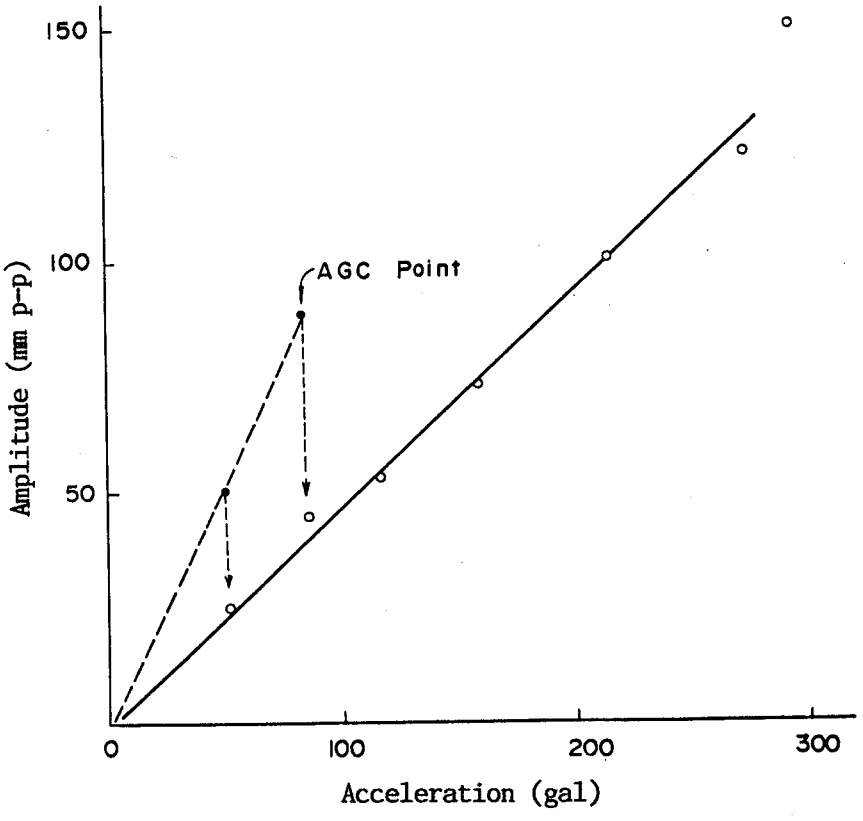

Figure 2.2.5 Linearity test result of overall recording system before and after AGC is activated (No. 595).

Table 2.2.2 List of maxima of corrected accelerograms and of computed velocity and displacement

	Observation Point	Instrument		Filtered Maxima (band pass 1.0-30.0 Hz)		
		No.	Direction	Acceleration (Obs.):gal	Velocity (comp.):kine	Displacement (comp.):mm
Dam	D_1	594	(R)	34.5(2.95)	1.59(2.87)	0.89(4.26)
	D_2	595	(R)	242.3(3.14)	8.68(3.18)	3.59(3.23)
	D_3	596	(R)	48.2(3.25)	2.04(3.14)	1.34(3.06)
	D_4	597	(R)	192.7(3.02)	6.08(2.98)	3.45(3.03)
	D_5	598	(R)	72.3(3.07)	3.25(3.11)	1.75(3.05)
	D_6	599	(R)	35.8(3.17)	1.48(2.72)	1.25(3.17)
Ground	G_1 (left)	1114	(U-D)	12.7(2.89)	0.70(2.80)	0.59(2.90)
		1115	(N-S)	26.4(2.93)	1.32(3.00)	0.97(2.92)
		1116	(E-W)	20.5(2.80)	1.23(2.73)	1.14(3.35)
	G_2 (right)	1117	(N-S)	30.7(2.85)	1.85(2.92)	1.30(2.83)
		1118	(E-W)	26.4(3.81)	1.61(3.13)	1.48(4.30)
	G_3 (right)	942 *3)	(S52°35'W)	36.7(3.39)	1.46(3.08)	1.02(2.88)
		943 *2)	(N35°49'W)	-	-	-
	G_4 (right)	1119	(N-S)	18.3(3.33)	0.79(3.27)	0.71(3.07)
		1120	(E-W)	21.0(3.08)	1.04(3.04)	0.84(2.95)
Fractured Zone at Dam Base	S_3	940	(N-S)	16.9(3.17)	0.78(2.87)	0.66(2.80)
	S_4	941	(E-W)	28.5(3.00)	0.96(3.04)	0.72(4.23)
δ-Fractured Zone	S_1 (Bank Side)	938	(N-S)	20.8(2.84)	0.92(2.90)	0.72(2.83)
		939	(E-W)	28.3(3.02)	1.07(3.05)	0.75(4.24)
	S_2 (River Side)	936 *3)	(S8°2'W)	20.1(2.85)	0.82(2.90)	0.76(2.83)
		937 *1)	(N79°42'W)	-	-	-
D-Fractured Zone	S_9 (Bank Side)	950	(N-S)	22.6(3.36)	0.84(3.16)	0.72(3.11)
		951	(E-W)	20.1(3.02)	0.93(3.05)	0.77(3.79)
	S_8 (River Side)	948	(N-S)	21.8(3.26)	0.86(3.16)	0.72(3.11)
		949	(E-W)	24.4(3.02)	1.11(3.05)	0.82(3.81)
γ-Fractured Zone	S_7 (Bank Side)	946	(N-S)	26.7(3.39)	1.28(2.91)	0.98(2.82)
		947	(E-W)	16.1(3.76)	1.19(3.09)	1.05(3.81)
	S_6 (River Side)	944 *2)	(S26°24'W)	-	-	-
		945 *1)	(N63°45'W)	-	-	-

*1) Not recorded.
*2) Fraction of record not available.
*3) Not transformed into NS-EW component due to imperfection of record of orthogonal pairs.

Note: Numerals in parantheses are reference onset time (sec) of maxima.

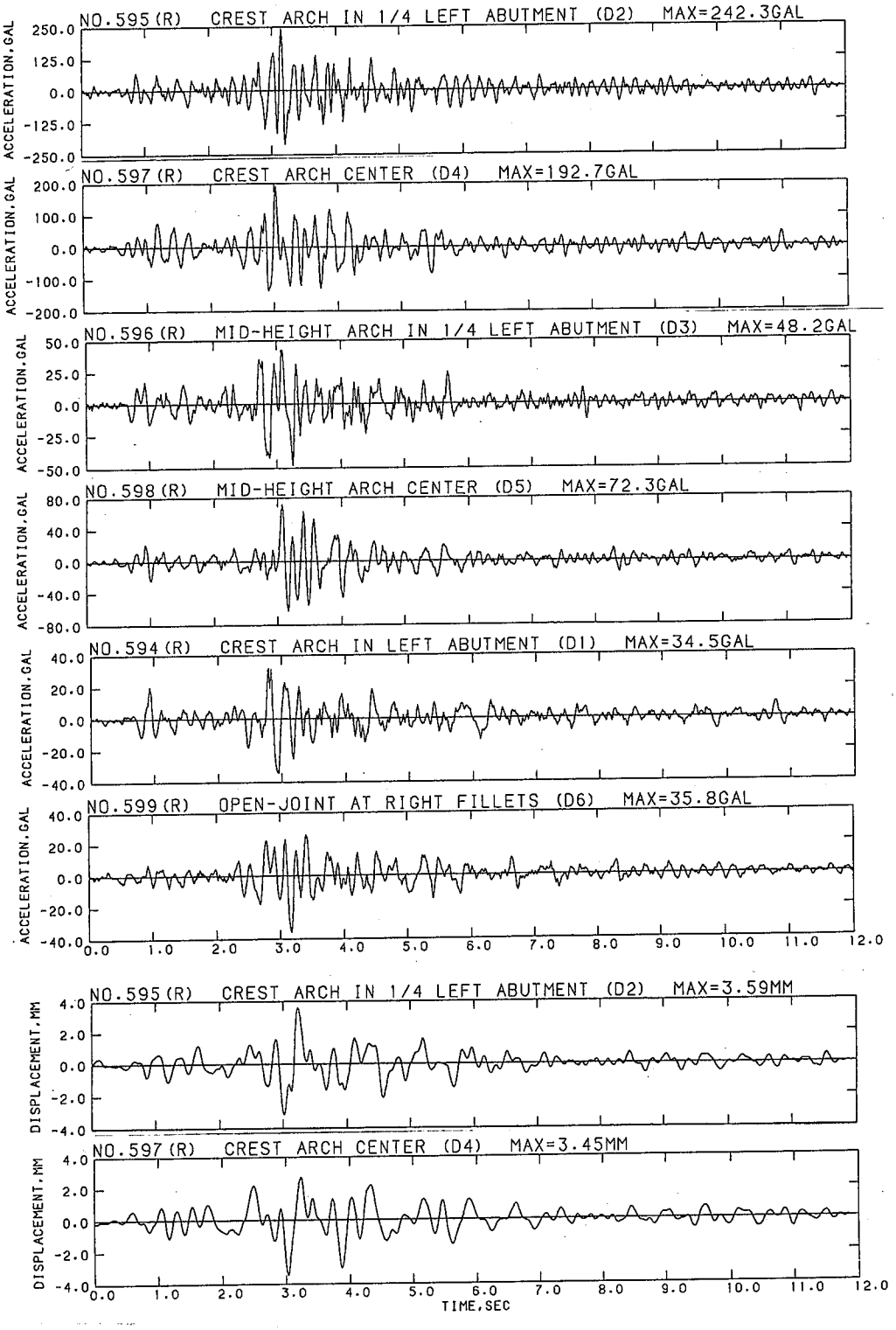

Figure 2.2.6 Corrected accelerograms of the dam and computed displacement time histories of 1/4 point and the crown of the crest arch (radial inward direction as positive)

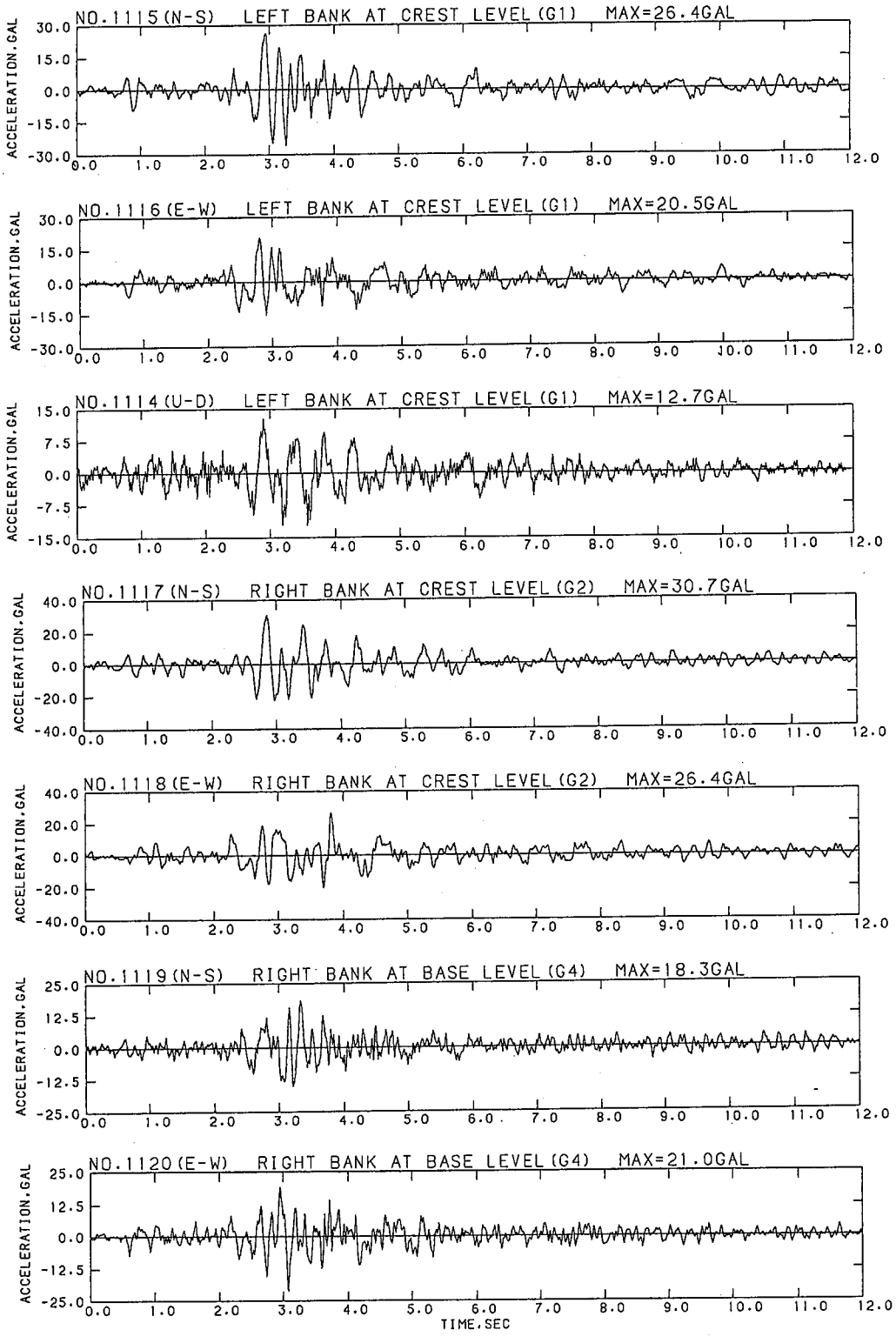

Figure 2.2.7 Corrected accelerograms of the foundation (North and East direction as positive)

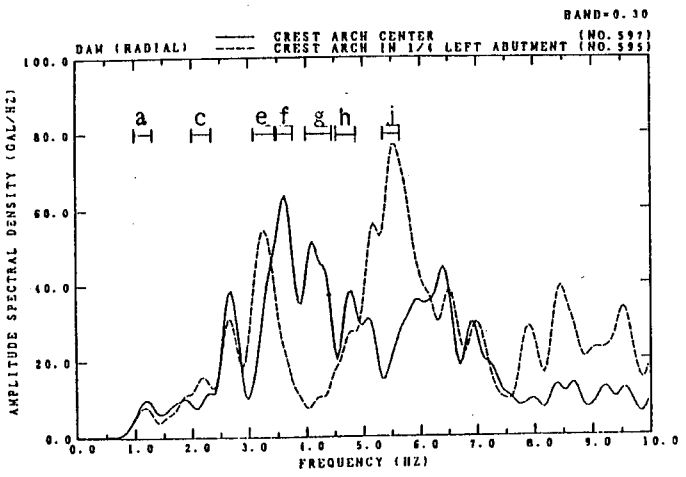

(a) Dam (radial)

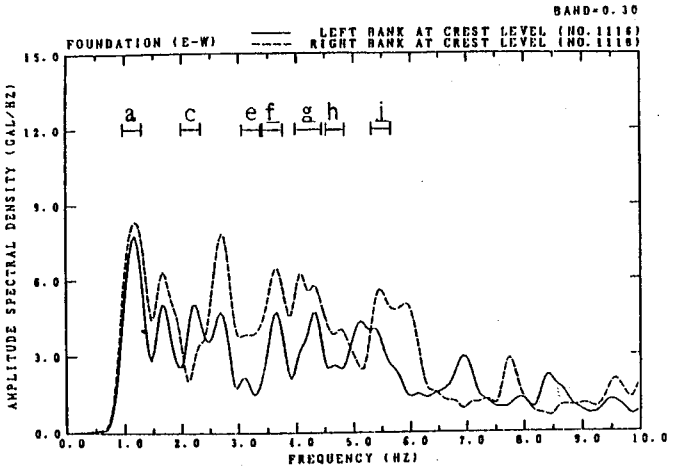

(b) Foundation (E-W)

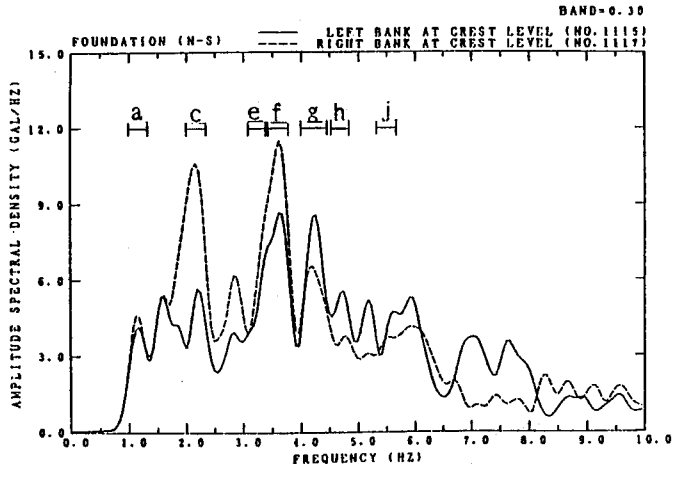

(c) Foundation (N-S)

Figure 2.2.8 Fourier spectra of corrected accelerograms

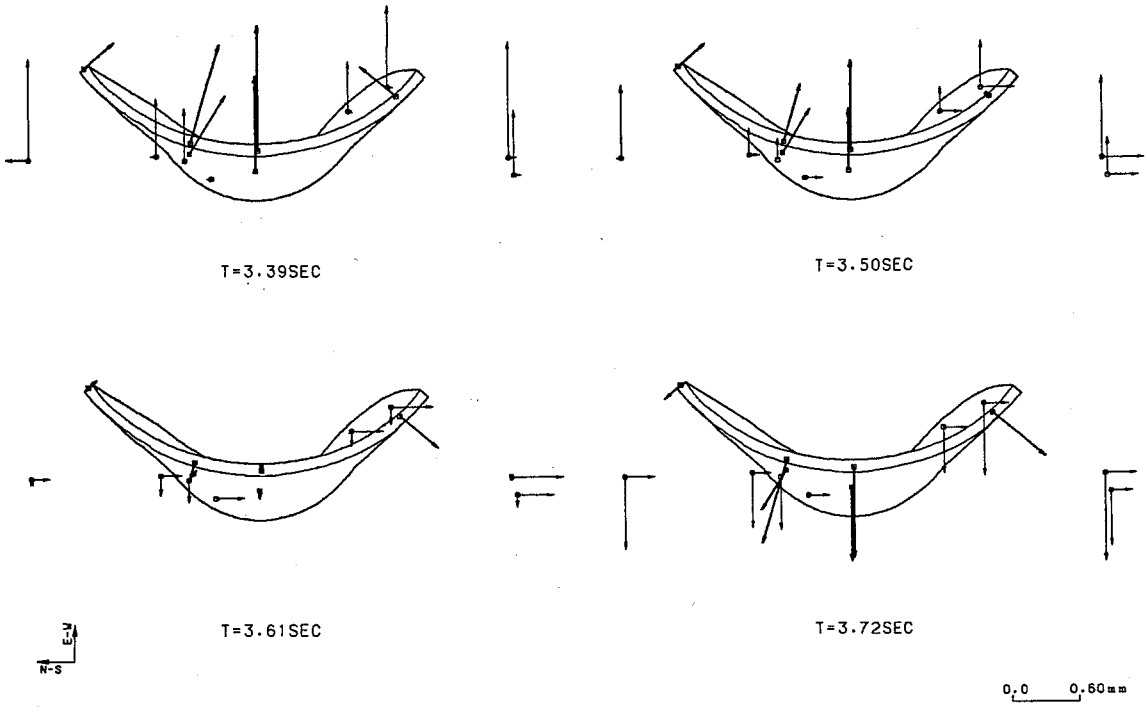

Figure 2.2.9 Spatial and Temporal displacement diagram of Band - a (1.0 - 1.3 Hz)

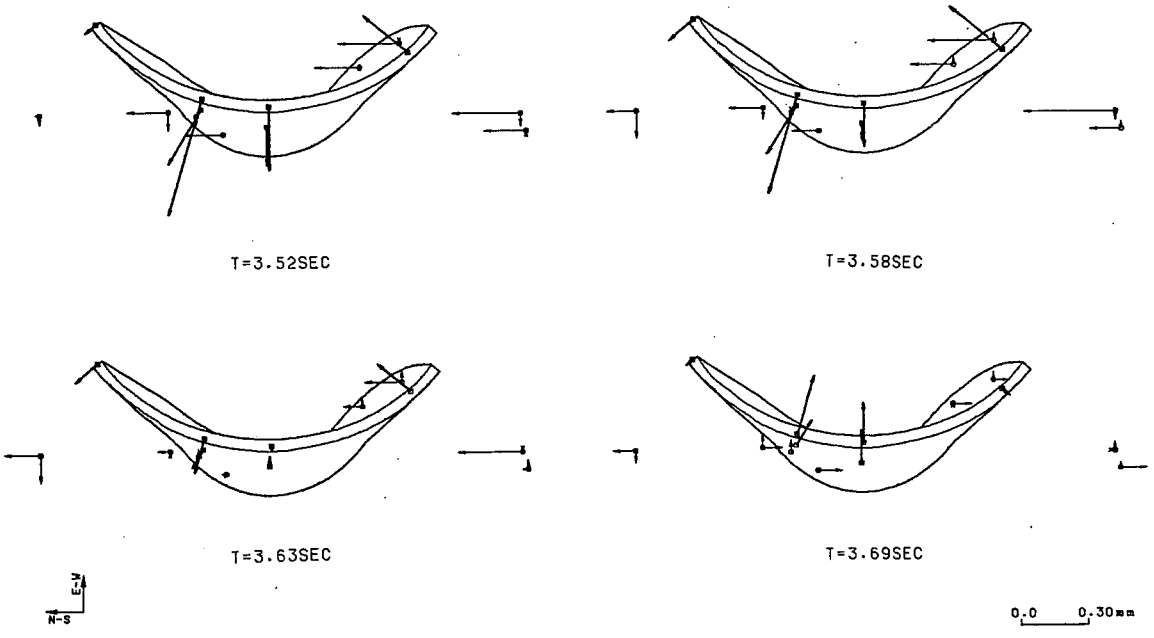

Figure 2.2.10 Spatial and Temporal displacement diagram of Band - c (2.0 - 2.35 Hz)

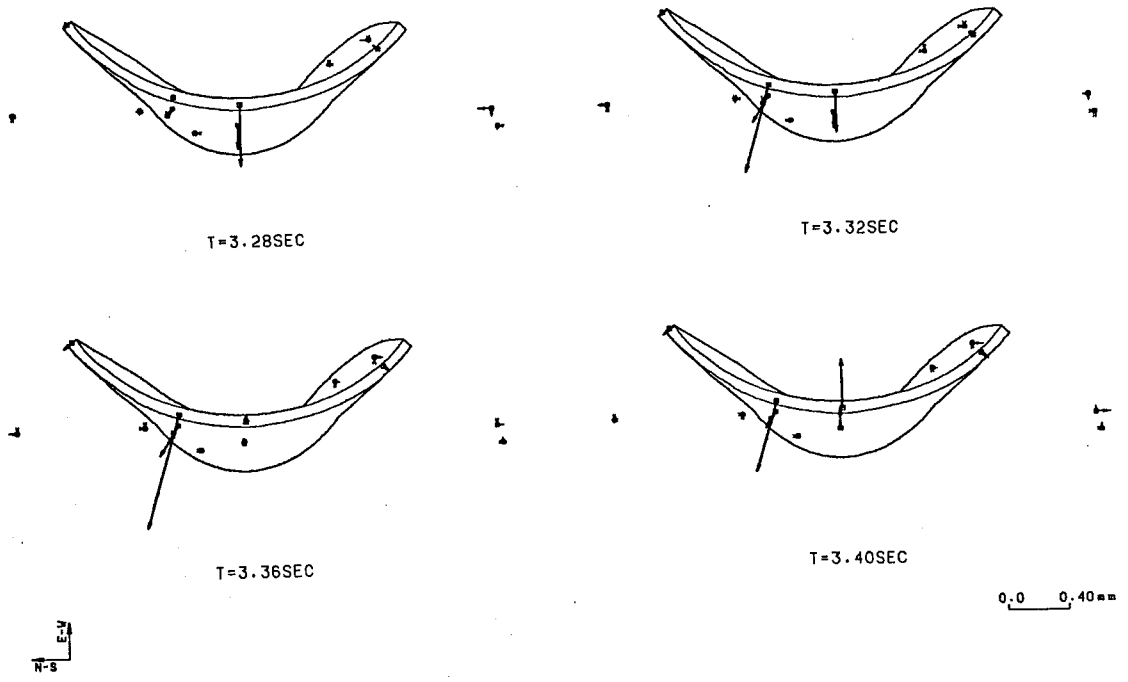

Figure 2.2.11 Spatial and Temporal displacement diagram of Band - e (3.1- 3.4 Hz)

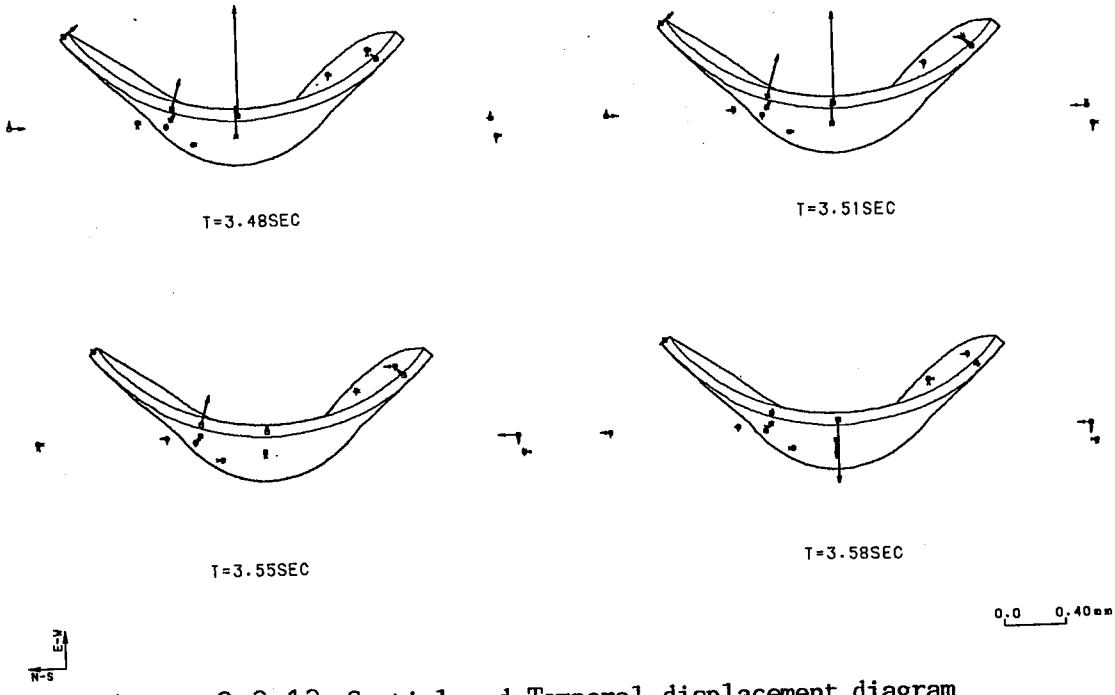

Figure 2.2.12 Spatial and Temporal displacement diagram of Band - f (3.45 - 3.75 Hz)

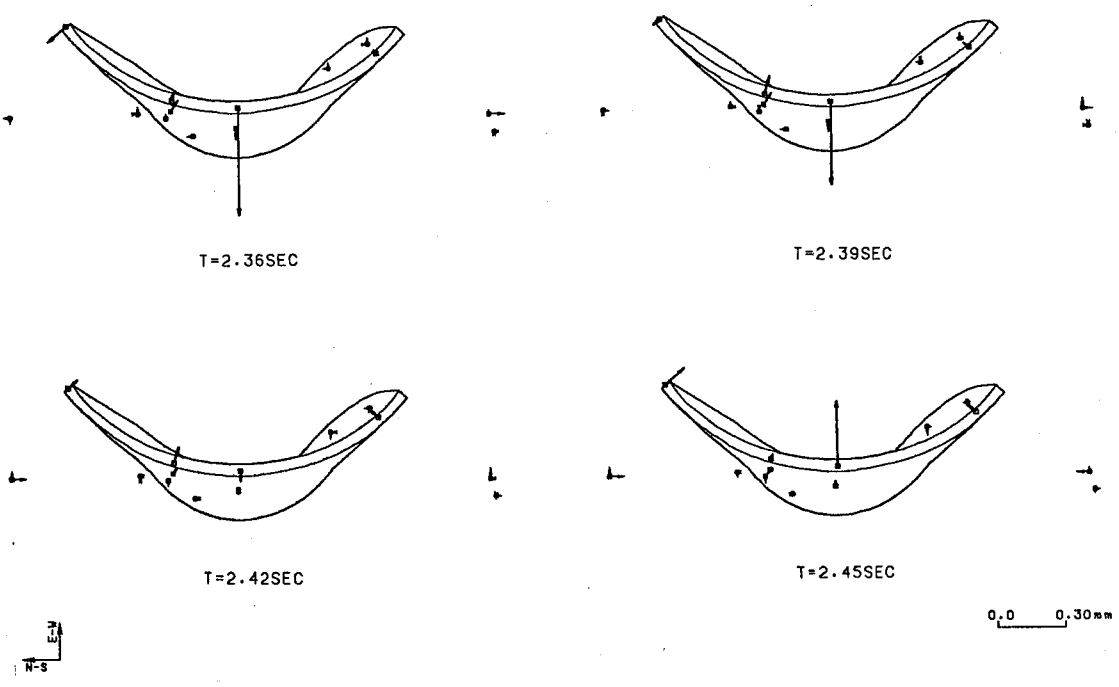

Figure 2.2.13 Spatial and Temporal displacement diagram of Band - g (4.0 - 4.4 Hz)

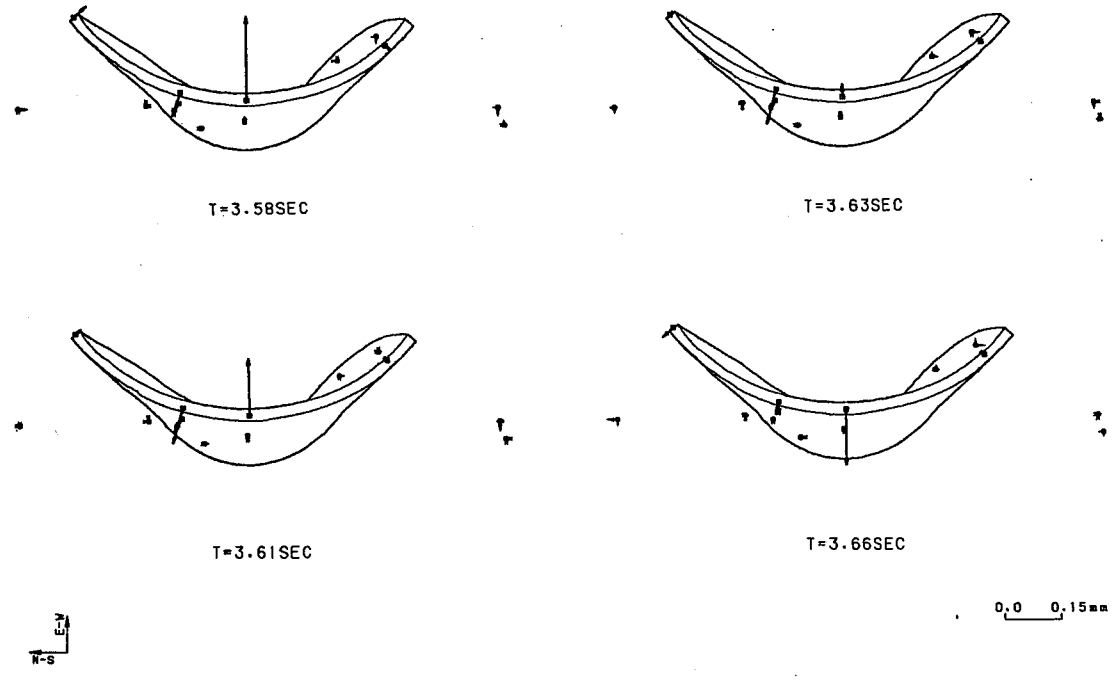

Figure 2.2.14 Spatial and Temporal displacement diagram of Band - h (4.55 - 4.85 Hz)

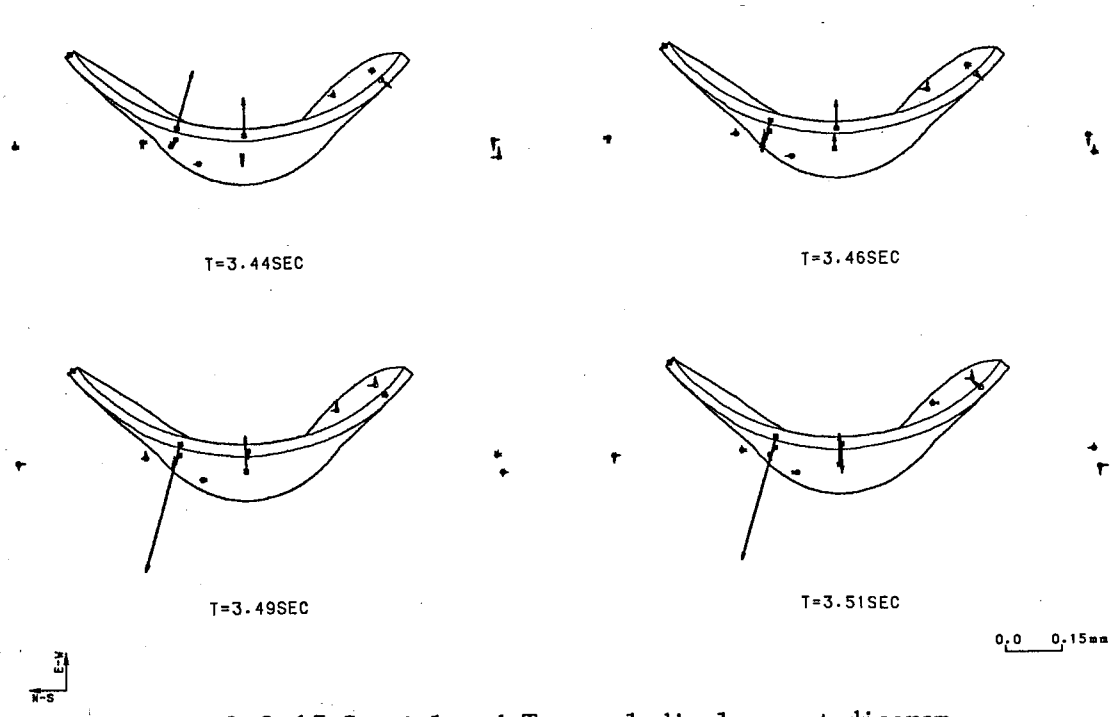

Figure 2.2.15 Spatial and Temporal displacement diagram of Band - j (5.35 - 5.65 Hz)

Table 2.2.3 Comparison of significant modes of vibration between observation and laboratory test.

Mode	Observation			Laboratory Test (Hz)
	Band	Frequency Band (Hz)	Peak Frequency (Hz)	
	a	1.0 -1.3	1.2	
	c	2.0 -2.35	2.2	
Antisymmetric 1st	e	3.1 -3.4	3.3	3.08
Symmetric 1st	f	3.45-3.75	3.6	3.50
	g	4.0 -4.4	4.1	
Symmetric 2nd	h	4.55-4.85	4.7	4.67
Antisymmetric 2nd	j	5.35-5.65	5.5	

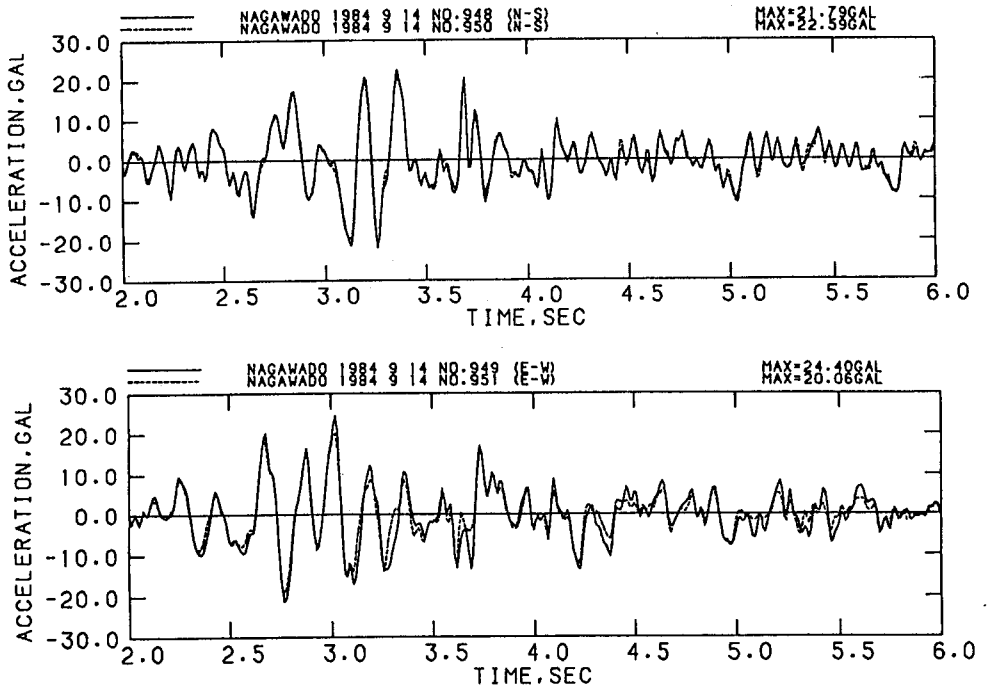

Figure 2.2.16 Comparison of corrected accelerograms recorded across the D fracture zone

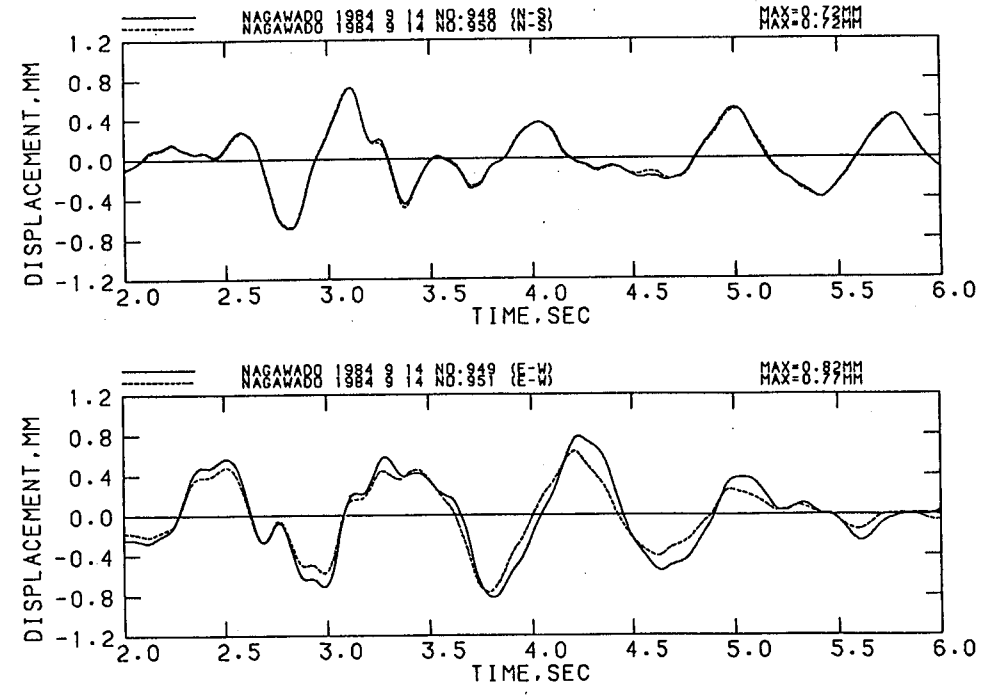

Figure 2.2.17 Comparison of computed displacement time histories across the D fracture zone

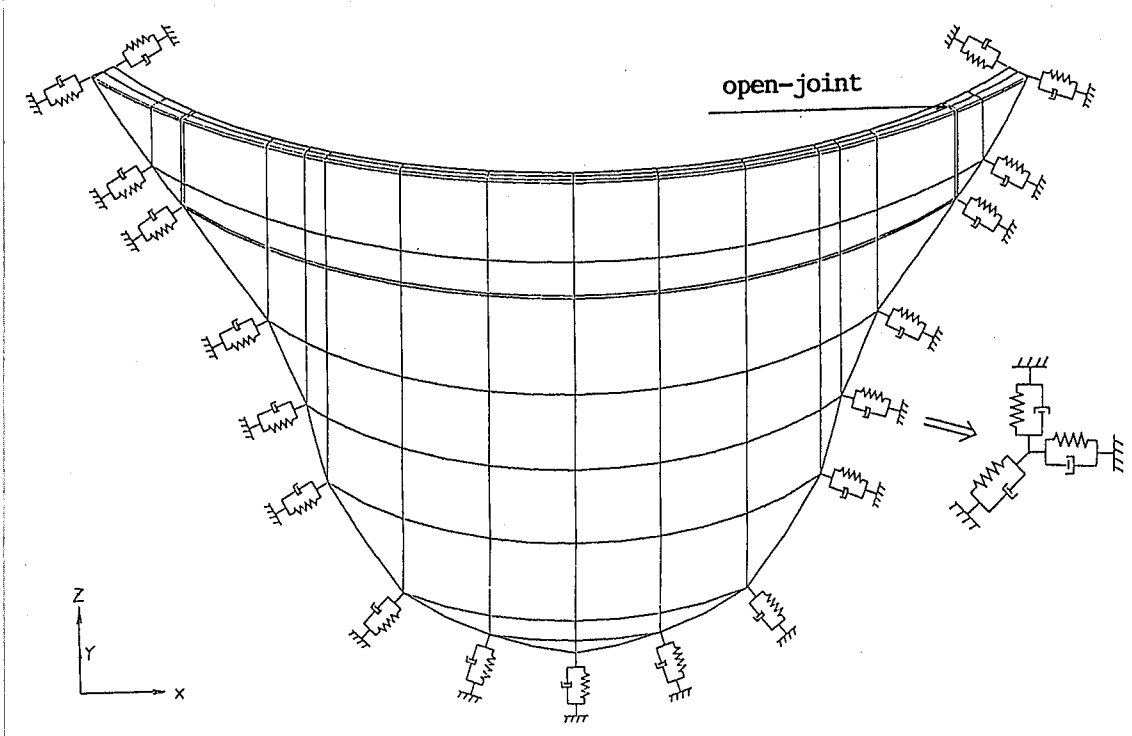

Figure 2.2.18 Finite element model with far-field impedance along the dam-foundation interface

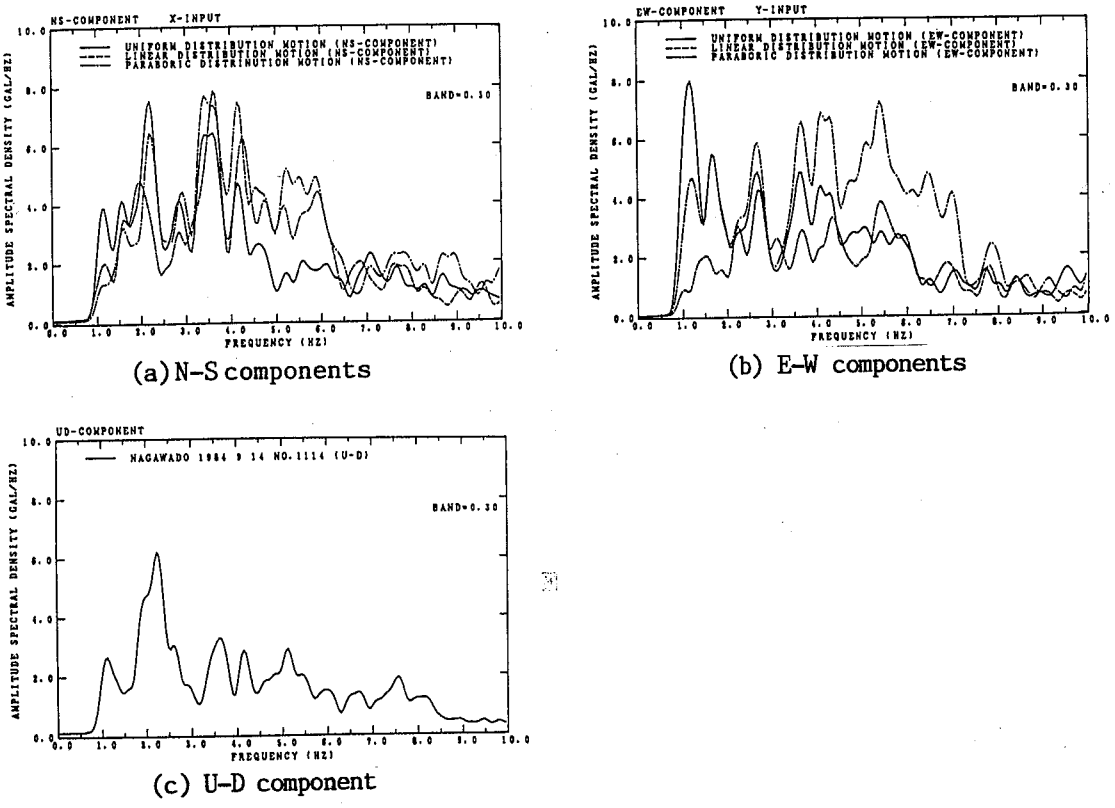

(a) N-S components

(b) E-W components

(c) U-D component

Figure 2.2.19 Comparison of three types of input ground motions on Fourier spectra; Solid, broken, and chained lines denote the type I, Type II, and Type III input ground motion, respectively.

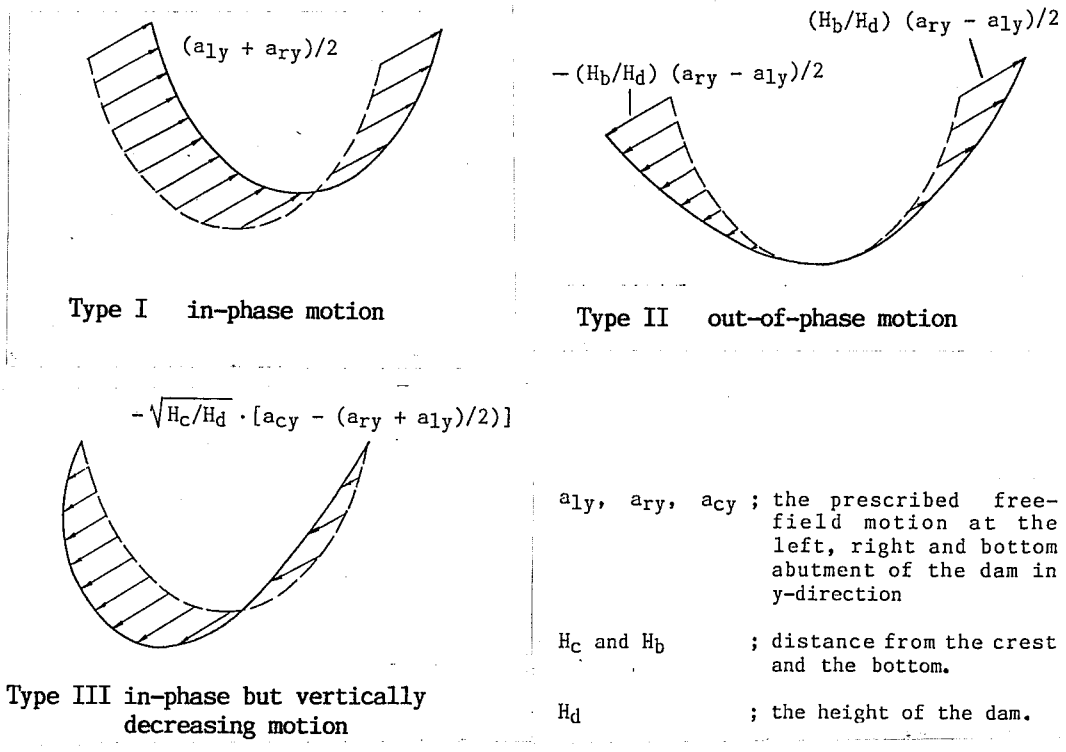

Figure 2.2.20 Spatially varied scheme of three types of input ground motions represented by Y-direction (upstream-downstream)

Table 2.2.4 Relation between the predominant frequencies and the material properties used for dynamic models.

Rock Model	Reservoir	Mode Type	Observed	Rock Vs=1400 (m/s)			Rock (m/s) Vs=2000	Rock (m/s) Vs=2600
				Dam (t/m^2) $E=3.6\times10^6$	Dam (t/m^2) $E=4.3\times10^6$	Dam (t/m^2) $E=5.1\times10^6$	Dam (t/m^2) $E=4.3\times10^6$	Dam (t/m^2) $E=3.4\times10^6$
Rock Modeled by FEM	Without Reservoir	Antisymmetric 1st		3.3 Hz	3.6 Hz		3.8 Hz	3.6 Hz
		Symmetric 1st		3.5 Hz	3.8 Hz		4.0 Hz	3.7 Hz
		Symmetric 2nd		5.1 Hz	5.5 Hz		6.0 Hz	5.5 Hz
		Antisymmetric 2nd		6.1 Hz	6.4 Hz		7.2 Hz	6.7 Hz
	With Reservoir	Antisymmetric 1st	3.3 Hz	3.0 Hz			3.6 Hz	3.3 Hz
		Symmetric 1st	3.6 Hz	3.2 Hz			3.7 Hz	3.5 Hz
		Symmetric 2nd	4.7 Hz	4.8 Hz			5.7 Hz	5.2 Hz
		Antisymmetric 2nd	5.5 Hz	6.1 Hz			7.0 Hz	6.5 Hz
Rock Modeled by Spring	Without Reservoir	Antisymmetric 1st			3.3 Hz	3.5 Hz	3.7 Hz	3.5 Hz
		Symmetric 1st			3.4 Hz	3.4 Hz	3.8 Hz	3.6 Hz
		Symmetric 2nd			5.1 Hz	5.4 Hz	5.7 Hz	5.4 Hz
		Antisymmetric 2nd			6.0 Hz	6.1 Hz	6.8 Hz	6.5 Hz
	With Reservoir	Antisymmetric 1st	3.3 Hz		3.0 Hz	3.2 Hz	3.3 Hz	3.2 Hz
		Symmetric 1st	3.6 Hz		3.0 Hz	3.1 Hz	3.4 Hz	3.3 Hz
		Symmetric 2nd	4.7 Hz		———	———	———	5.1 Hz
		Antisymmetric 2nd	5.5 Hz		5.6 Hz	5.5 Hz	5.8 Hz	6.3 Hz

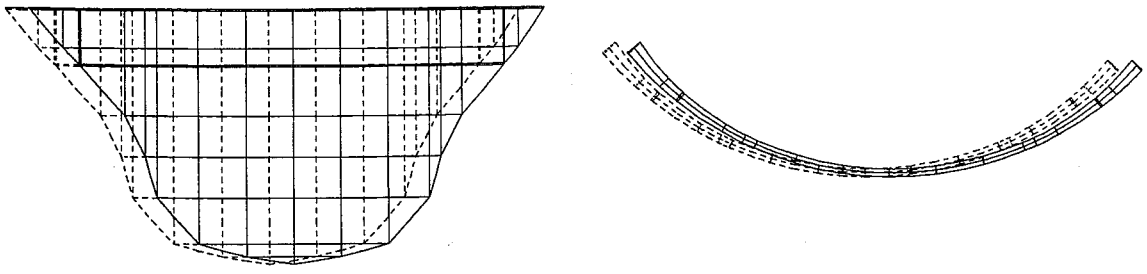

(a) Displacement by Type I motion

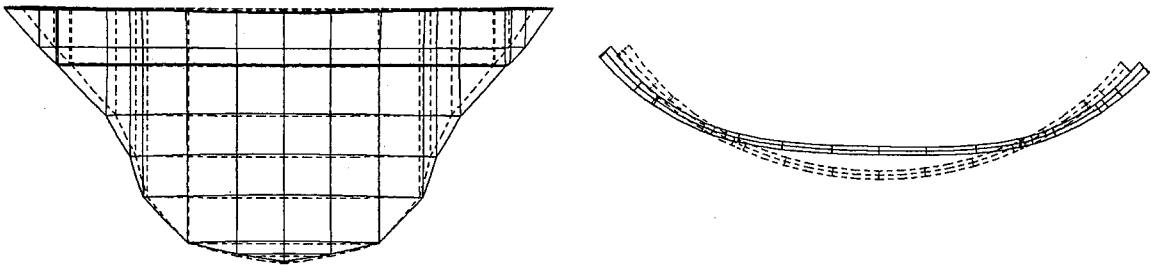

(b) Displacement by Type II motion

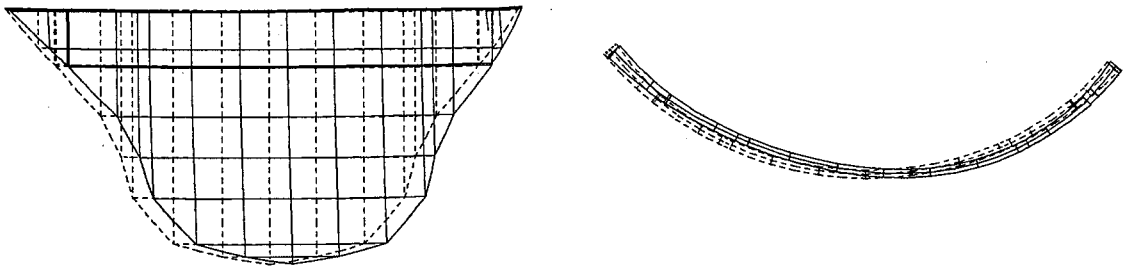

(c) Displacement by Type III motion

Figure 2.2.21 Displacements according to the three types of quasi-static input motions, in X (N - S) direction.

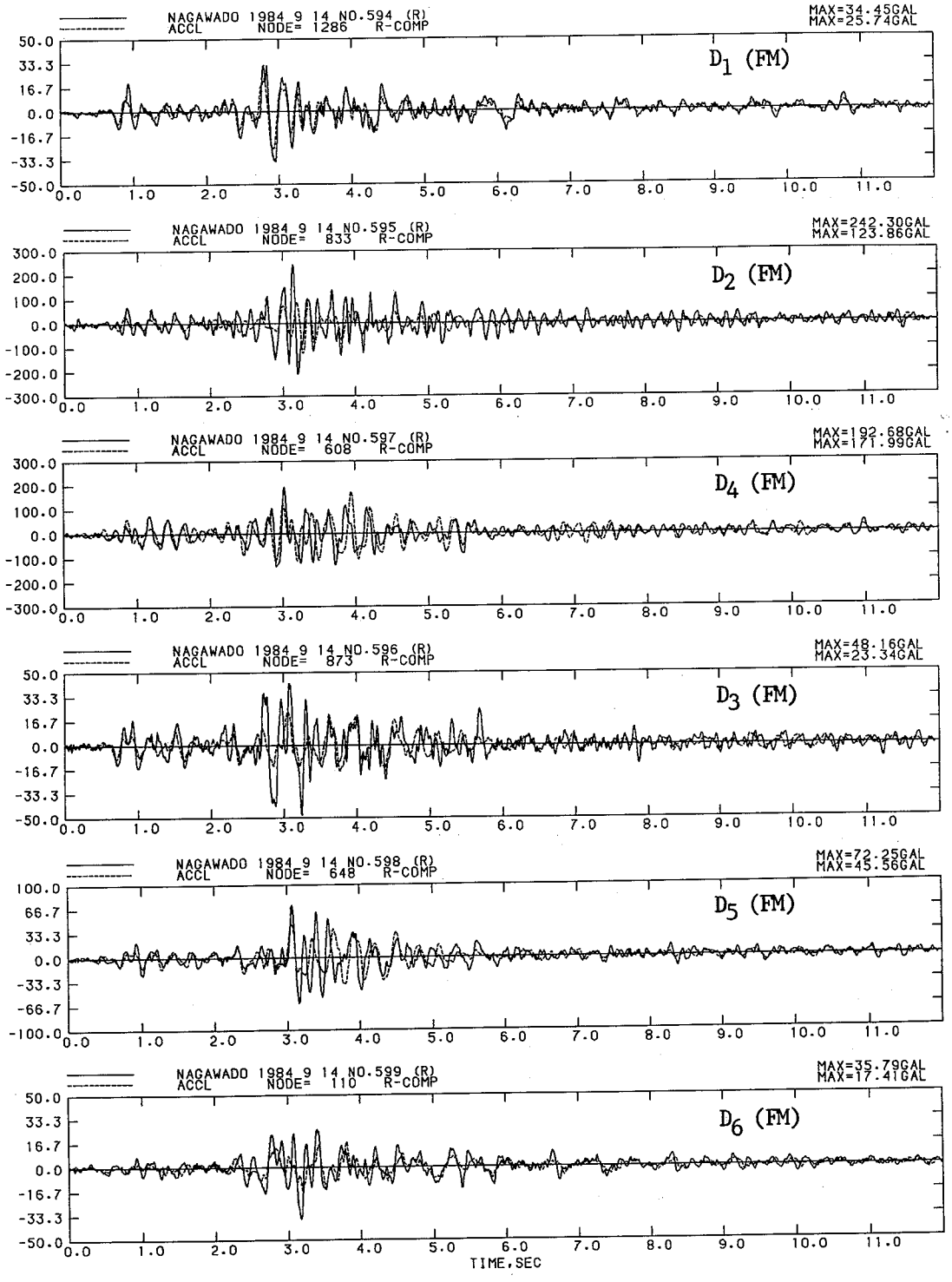

Figure 2.2.22(a) Comparison between the observed and simulated motions by final model(FM); Solid and dotted lines denote the observed and simulated, respectively.

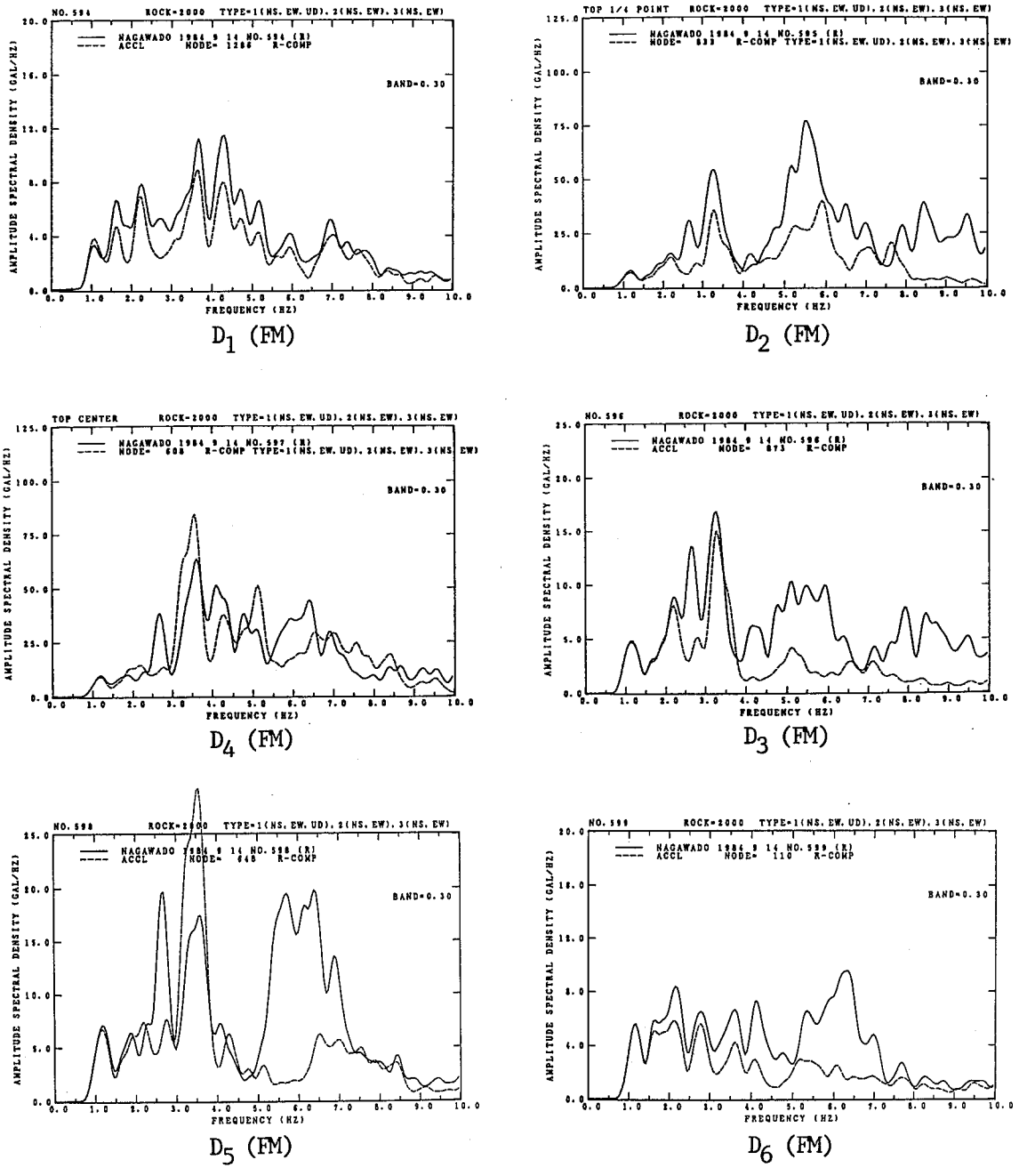

Figure 2.2.22(b) Comparison between the observed and simulated motions on Fourie spectra; Line type is same as Figure 2.2.22(a).

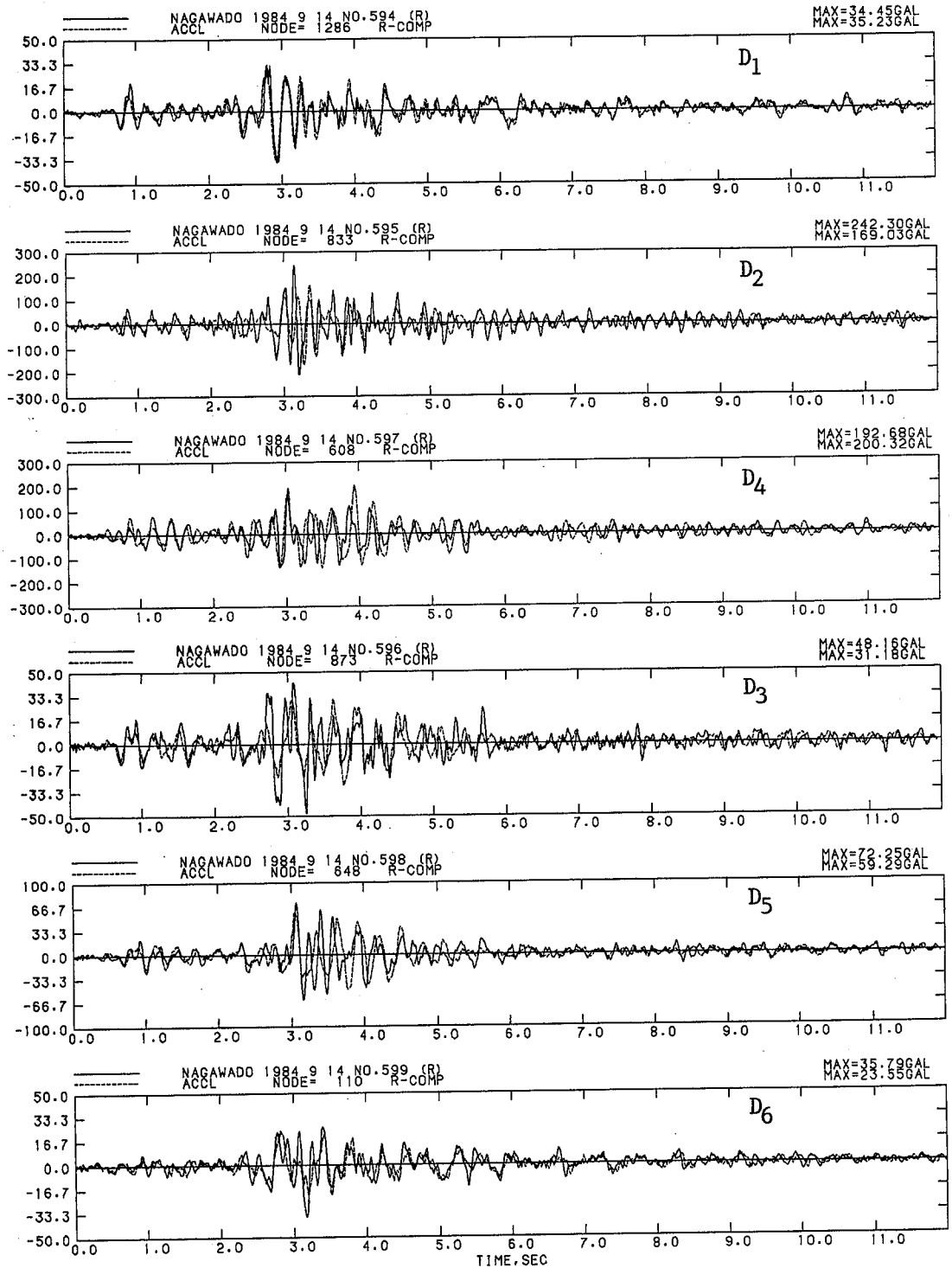

Figure 2.2.23(a) Comparison between the observed and simulated motions when the horizontal input motions of N-S direction are multiplied by 1.5 in the final model(FM); Line type is same as Figure 2.2.22(a).

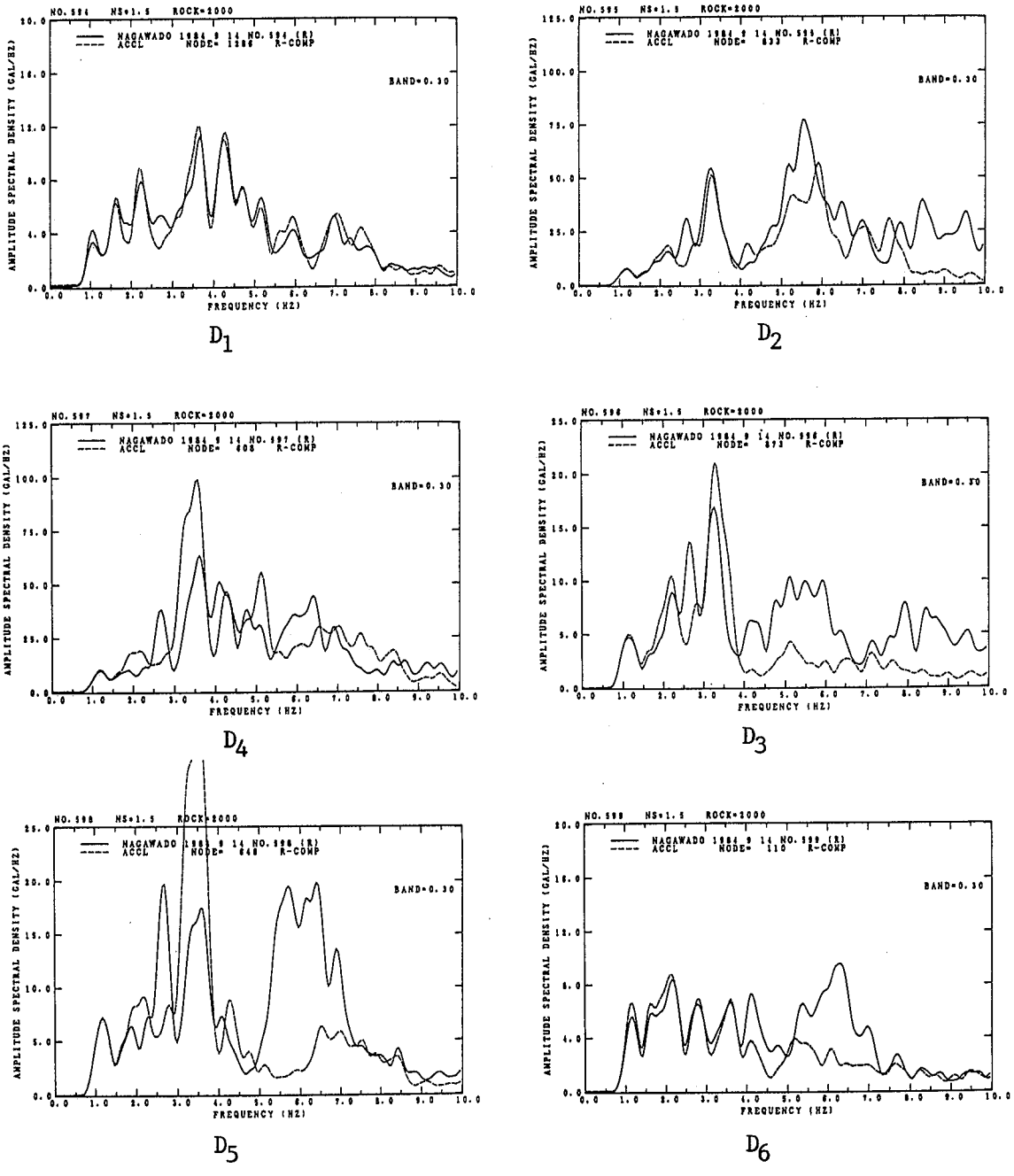

Figure 2.2.23(b) Comparison between the observed and simulated motions in Figure 19(a) on Fourie spectra; Line type is same as Figure 2.2.22(a).

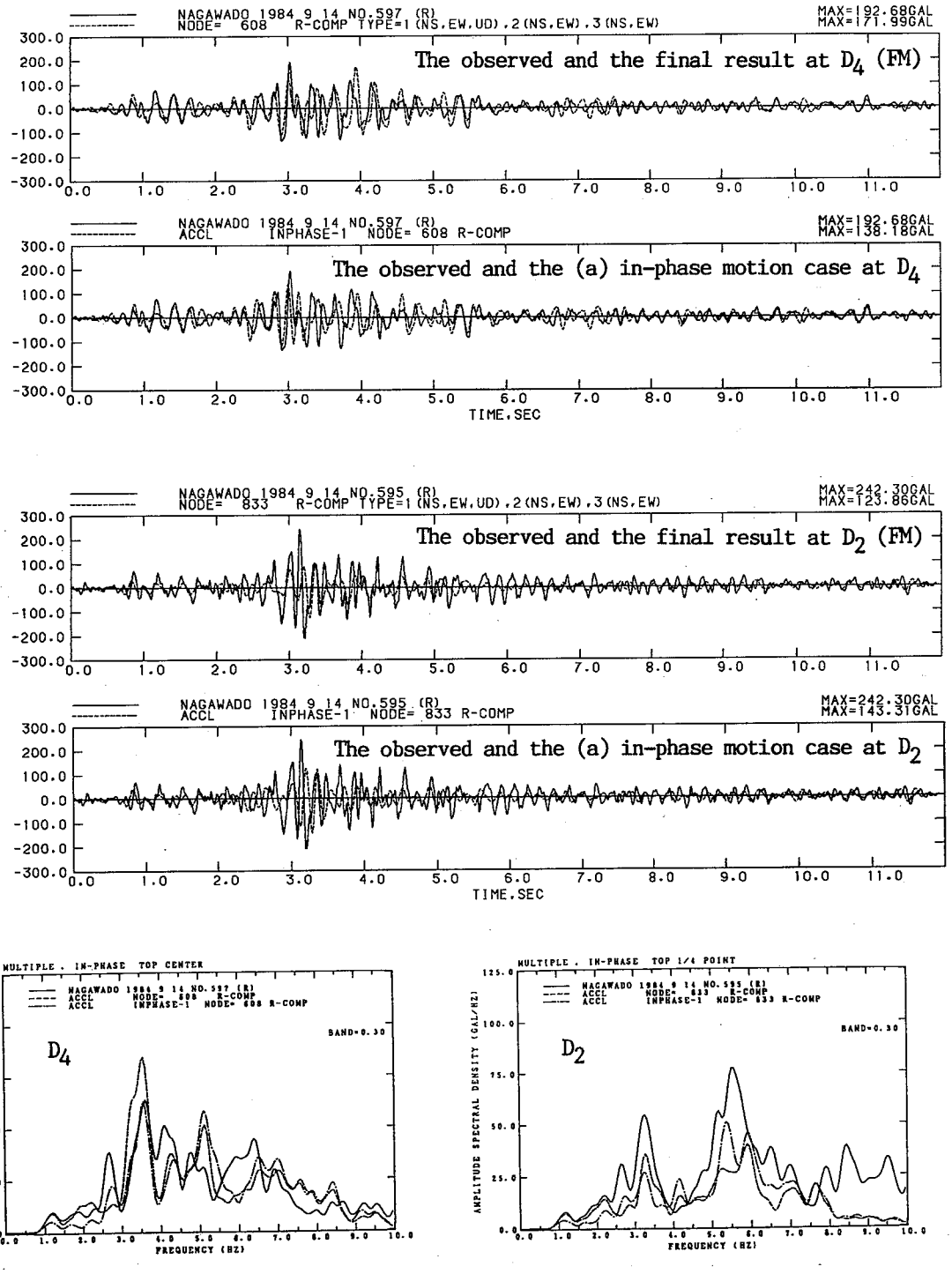

Figure 2.2.24(a) Comparison of the simulated results obtained by using the in-phase motion (a) with the final result; For time histories, line type is same as Figure 2.2.22. For spectra, solid, dotted, and chained lines are for those of the observed, the final results , and the results with the in-phase motion (a).

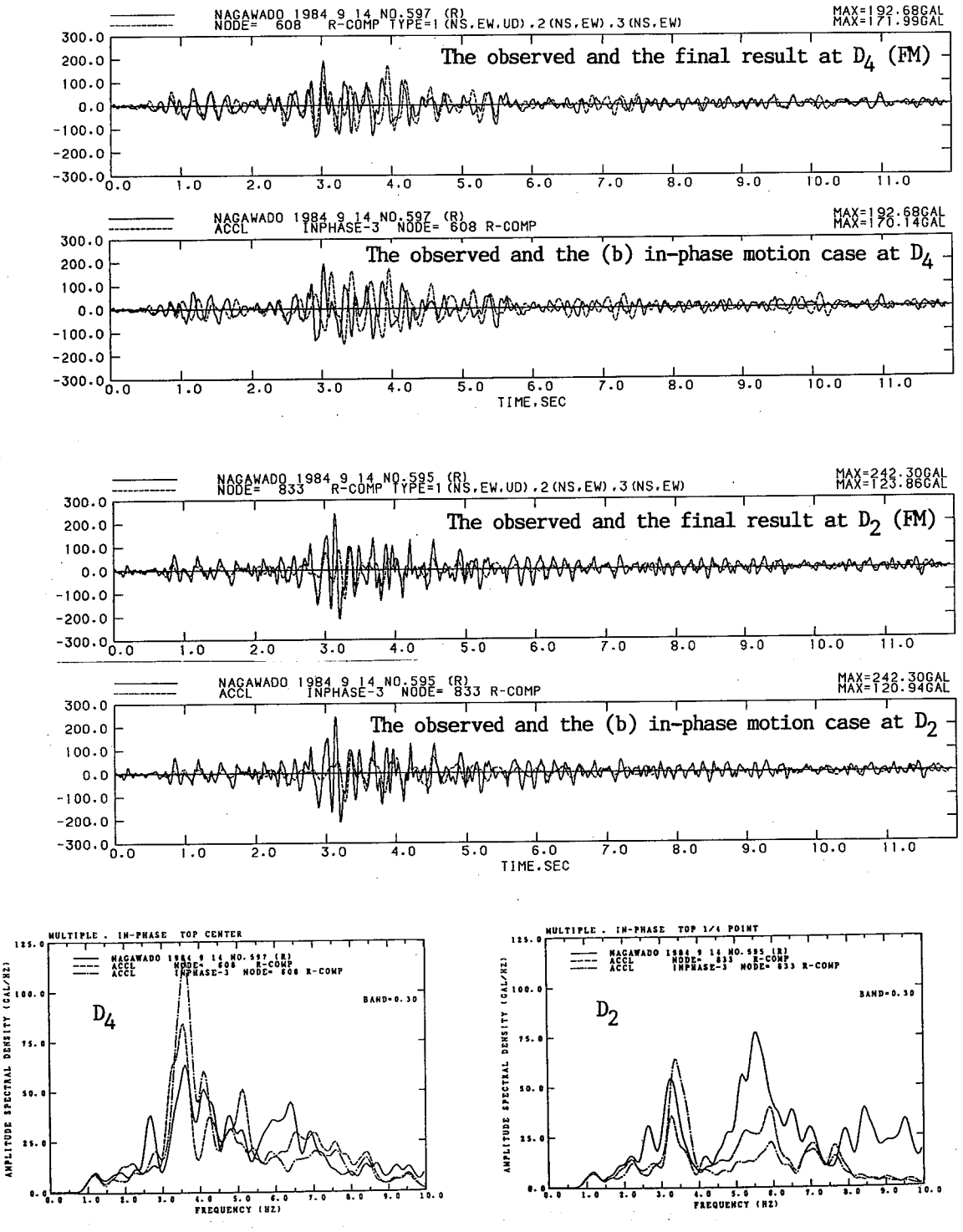

Figure 2.2.24(b) Comparison of the simulated results obtained by using the in-phase motion (b) with the final result; For time histories, line type is same as Figure 2.2.22. For spectra, solid, dotted, and chained lines are for those of the observed, the final results , and the results with the in-phase motion (b).

Table 2.2.5 Damping values obtained by the final model (FM) in percent

Mode	Freq.(Hz)	Material damping	Radiation damping	Total damping
1	3.65	2.00	2.73	4.73
2	3.78	2.00	4.67	6.67
3	5.75	2.00	6.13	8.13
4	6.37	2.00	6.24	8.24
5	6.80	2.00	8.96	10.96
6	7.07	2.00	10.54	12.54
7	7.56	2.00	27.38	29.38
8	8.48	2.00	6.31	8.31
9	8.90	2.00	24.35	26.35
10	9.95	2.00	27.49	29.49
11	9.96	2.00	15.36	17.36
12	10.36	2.00	8.99	10.99
13	10.70	2.00	13.01	15.01
14	11.88	2.00	16.47	18.47
15	12.52	2.00	5.75	7.75
16	12.65	2.00	35.38	37.38
17	13.69	2.00	21.51	23.51
18	13.83	2.00	21.22	23.22
19	14.33	2.00	25.52	27.52
20	14.81	2.00	27.03	29.03

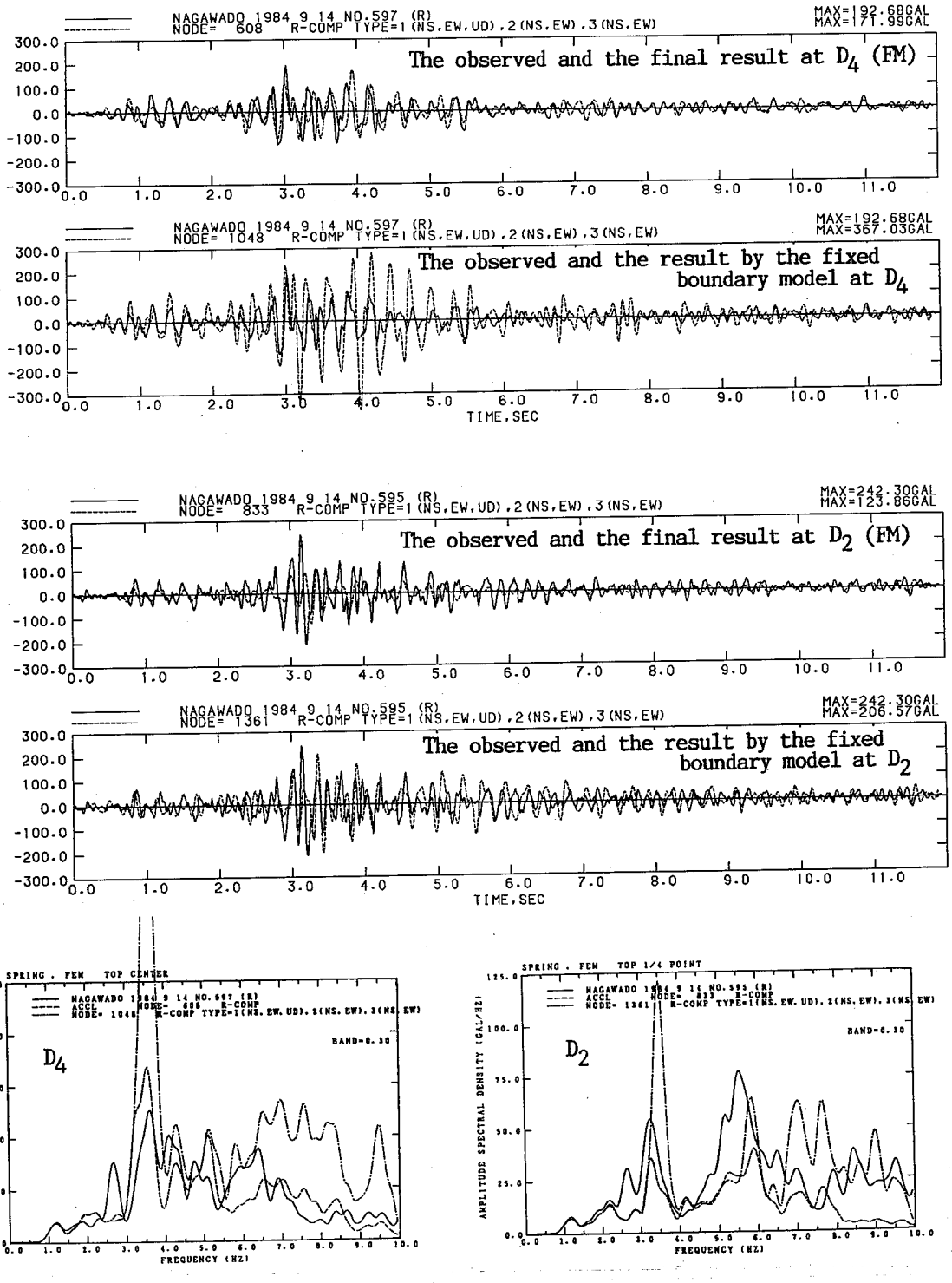

Figure 2.2.25 Comparison of the simulated results obtained by the fixed boundary model with the final result; For time histories, line type is same as Figure 2.2.22. For spectra, solid, dotted, and chained lines are for those of the observed, the final results , and the results by the fixed boundary model.

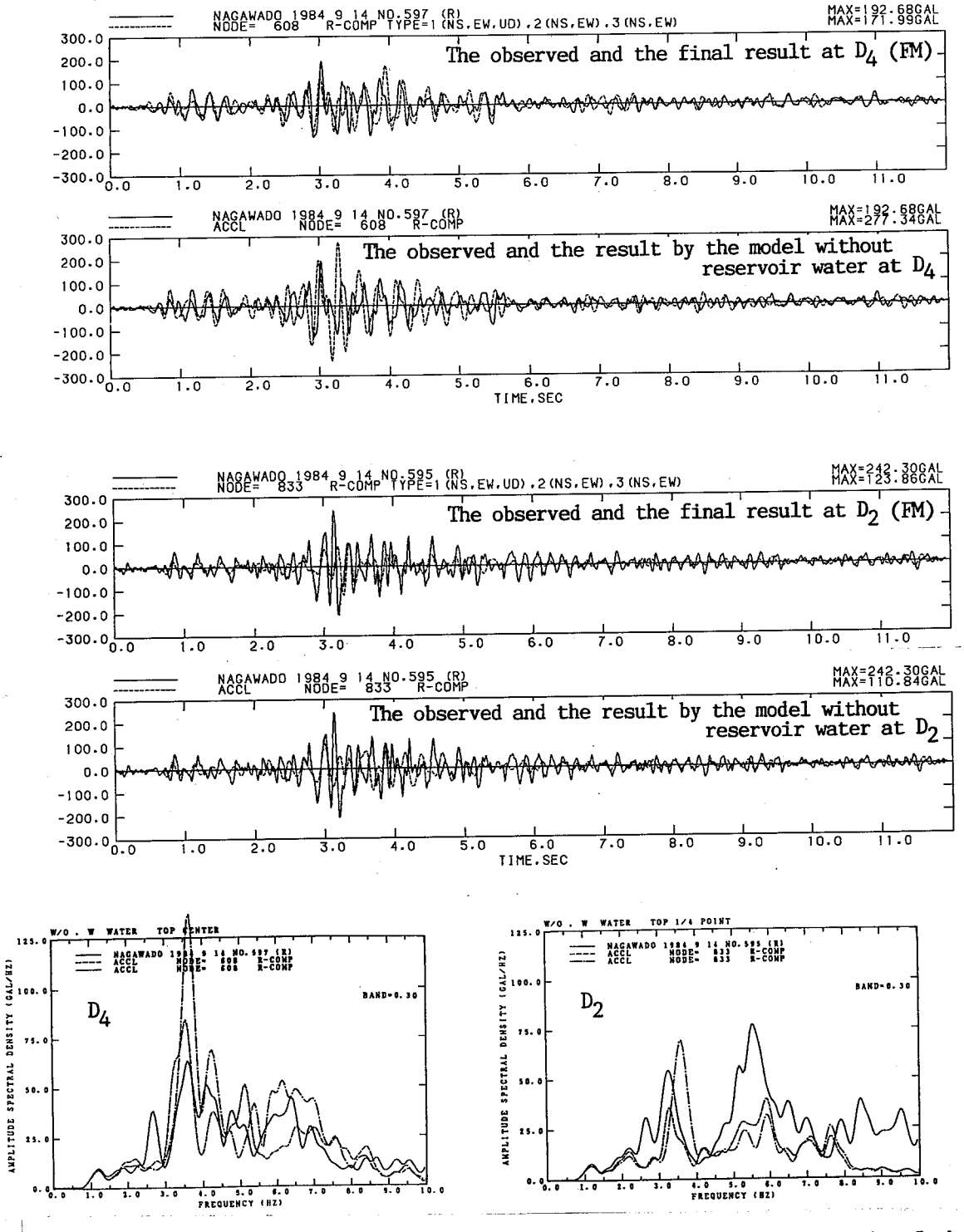

Figure 2.2.26 Comparison of the simulated results obtained by the model without reservoir water with the final result; For time histories, line type is same as Figure 2.2.22. For spectra, solid, dotted, and chained lines are for those of the observed, the final results , and the results by the model of this case.

2.3 ANALYTICAL REPRODUCTION OF THREE-DIMENSINAL BEHAVIOR OF A NUCLEAR REACTOR BUILDING MODEL

2.3.1. INTRODUCTION

In the seismic safety evaluation and design of nuclear power facilities, a variety of sophisticated dynamic analysis codes have been applied; however, most of these treat the basically three-dimensional soil-structure interaction problem in two-dimensions, mainly because of practical limitation of computer core size and computer economy. However, the conversion of a three dimensional problem into two dimension has usually caused serious modulation of the dynamic characteristics of a structural system. Especially for such a vibration system that has to consider seriously the effect of soil compliance on the fundamental vibration characteristics of the system, this two-dimension simplification should be avoided unless the results can be guaranteed by some supplemental measures.

To make clear the needs for true three-dimensional dynamic analyses, the author first tested a series of newly developed three dimensional dynamic analysis codes based on a hybrid finite element method through comparative analyses with using recorded motions obtained in forced vibration tests and real earthquake response observations of a small scale concrete structural model constructed at an open air site for the study.

Next, the author will explain how the three-dimensional response will be distorted by some typical two-dimensional analysis codes and confirm the need for true three-dimensional analysis. Finally the author discuss some valuable insight on three-dimensional soil-structure interaction features.

2.3.2 VALIDATION STUDY OF HASSI-4 AND HASSI-7

For the purpose of testing the validity of the developed HASSI codes, the correlation studies as described in the followings has been performed. A series of small scale concrete structural models were constructed at a stiff soil site and the dynamic soil properties were explored by in-situ and laboratory tests. Then the response of the structures were measured under sinusoidal vibration forces and to real earthquakes. Finally, these measured response records were compared with the results obtained in simulation analyses of these experimental data

and earthquake response records.

2.3.2.1 Outline of HASSI-4

The hybrid modeling approach to seismic soil-structure interaction analysis is basically a substructure method. However, instead of partitioning the total soil-structure system along the interface of the soil and the structure, it partitions the system (Figure 2.3.1(a)) into the near-field and the far-field soil region, by using a hemispherical interface which cuts through the soil region under the structure(Gupta and Penzien, 1981).

One substructure (the near-field) consists of the structure to be analyzed under prescribed loading conditions and a finite portion of soil encompassing its base as shown in Figure 2.3.1(b). The second substructure (the far-field) is a semi-infinite half-space which shares a common interface with the near-field as in Figure 2.3.1(c). This interface is hemispherical in form so that it provides a smooth surface along which mathematical boundary conditions to permit radiation of energy away from the foundation of the structure into the half-space can easily be satisfied. This modeling uses a far-field impedance matrix which relates far-field forces at the interface nodes to the corresponding nodal displacements by the system identification technique(Gupta and Penzien, 1981).

Chronology of HASSI-series computer codes

The HASSI series computer codes evolved from Version-1 to Version-8, the chronological development of which are as follow:

HASSI-1: Linear response analysis of the soil-structure system subjected to the prescribed uniform triaxial free-field surface acceleration input motions at the hemispherical boundary of near-field soil region. Frequency response analysis of the system subjected to simultaneous forced vibration forces prescribed at multiple locations (Niwa, Katayama, and Penzien 1983).

HASSI-2: Input free-field acceleration motions were expanded to various type of waves; vertically incident shear waves, inclined shear waves, and surface waves(Penzien, 1983).

HASSI-3 & HASSI-4: The control point of the prescribed triaxial free-field surface acceleration input motions was changed to be defined uniformly at the structure and soil interface (Katayama,

1987).

HASSI-5: The function to treat the structures having deep embedment was added to the previous version by providing a cylindrical near-field boundary in place of the hemispherical boundary.

HASSI-6: Except for the additional capability included in HASSI-5, the previous version, HASSI-4 was refined and at the same time has the added capability to generate the total stress response of the near-field soil by both free-field response of soil and soil-structure interaction.

HASSI-7: To take account of non-linear response of the soil surrounding the structure foundation, an equivalent linear algorithm was applied to a limited region within the near-filed soil inside the hemi-spherical near-field soil region(Katayama et al,1989). A non-linear and linear soil interface was defined as an additional substructure.

HASSI-8: The previous uniform triaxial free-field surface acceleration input motions at the structure-soil interface were changed to be defined at the non-linear and linear boundary within the the hemi-spherical near-field soil region. Spatial variation of the input motions was taken into account by condensation of the basic equations of motion at the boundary.

Linear hybrid modeling and HASSI-4

The HASSI series have reached a practical application level at the stage of HASSI-4 (Katayama, 1988), in which modelling of the near-field makes use of the following types of linear finite elements:

(1) three-dimensional beam element,
(2) three-dimensional spring element, and
(3) three-to-nine-node axisymmetric solid element.

The stiffness and damping properties of each element are modeled using the complex modulus method; thus element damping is represented in hysteretic form. This modeling concept has been incorporated into HASSI-4 and permits the following calculations assuming linear and homogeneous soil property, (1) response analysis of the soil-structure system subjected to the prescribed triaxial free-field surface acceleration input motions at the structure and soil interface, and (2) time domain response or frequency response analysis of the system subjected to simultaneous forced vibration forces prescribed at multiple locations.

This HASSI-4 is fundamentally usable for the case where the

structures are supported on a uniform elastic half-space or embedded in very shallow depth. To refine this constraint, an extended version, HASSI-5, has also been developed based on the hybrid technique of attaching equivalent complex impedances calculated by Green's functions along the cylindrical interface between the near-field soil and the far-field region(Tzong and Penzien, 1983). This version can be applied to the case of a structure supported on or embedded in a horizontally-layered viscoelastic soil medium overlying rigid bed rock. However, this version still assumes linear analysis scheme and the validation of this capability has not been completed.

The HASSI-4 was refined to become HASSI-6 in which the routine to calculate the stress response of the near-field soil was added and its solver was refined to realize better computer economy.

HASSI-6 was refined recently to HASSI-7 which allows non-linear soil condition by equivalent linear technique and significantly improved computer time over that of HASSI-4 by introducing another substructures within the near-field soil boundary; limited soil region of non-linear response and linear soil region. The validity of limiting the soil region of non-linear response was examined through simulation analyses of the recorded motions obtained at each model located in Taiwan and Japan (Katayama et al;1989).

Non-linear hybrid modeling and HASSI-7

Through many correlation studies of field test data under either forced vibration or earthquake excitation, it has been shown that the HASSI programs can effectively predict the dynamic response of a soil-structure system, if realistic soil parameters are adopted (Katayama et al., 1987(a) and 1987(b); Penzien et al., 1987; Katayama, 1988; Chen et al., 1988).

In the above general and simplified formulations of the seismic soil-structure interaction effects, the entire structure-foundation system is considered to respond in a linear fashion. However, when strong vibration forces or earthquake ground motions are assumed, non-linear behavior will be experienced in the near-field soil region, due to the large strains produced close to the base of the structure.

Since the dissipation of the reflected waves at the soil-structure interface seems very fast (Katayama and et al, 1987(a), Katayama, 1988), the response of the soil close to the base of the structure may greatly

affect the response of the structure, proper modeling of nonlinear soil characteristic is essential. The nonlinear behavior of the near-field soil has been taken into consideration in HASSI-7 by such standard equivalent linearization procedures as already used in programs SHAKE and FLUSH.

The procedures used in treating such nonlinearity by the hybrid modeling method including efficient substructuring and condensation procedures are described below.

Controlling strain of soil In applying the standard equivalent linearization technique, the selection of the shear strain to control the strain dependent stiffness and damping properties of the near-field soil becomes important. This controlling (effective) strain of a soil element as experienced during three-dimensional seismic response was represented by its octahedral shear strain at the mid point of the element.

First, the displacement due to soil-structure interaction, u^i, is calculated and the total displacement of a soil element, u^t, is obtained by adding the displacement, u^f, induced by the free-field ground excitation; i.e.

$$u^t = u^f + u^i$$

By using the constitutive law for the given displacement and shear strain in the free-field soil response analysis, the octahedral shear strain can be expressed by non zero strain components e_{zz}, e_{yz}, and e_{xz} as:

$$r_{oct} = \sqrt{\frac{8}{3} \cdot [\frac{1}{3} e_{zz}^2 + e_{yz}^2 + e_{xz}^2]} ,$$

where x, y, and z denotes two orthogonal horizontal axis, and vertical axis, respectively.

This octahedral strain is calculated so that the soil properties can be modulated to give the strain dependent shear moduli and damping ratios compatible with the fraction of this strain in the free-field soil response analysis and the subsequent soil-structure interaction analysis.

Substructuring of hybrid system In hybrid modeling, the hemispherical interface is chosen to pass through the soil region at a distance of approximately three to four times the radius of the structure. It is

assumed that the ground motions outside the hemispherical interface will be essentially the same as the free-field motions produced by the earthquake and only the motions at the region very close to the structure will be influenced by the effects of soil-structure interaction.

Therefore, the near-field soil region separated from the far-field soil by a hemispherical interface is again subdivided into two subregions I and N as shown in Figure 2.3.2 From what has been described, this region I with artificial interface having $\underline{U}_e$ nodal degrees of freedom is introduced as the region considered to be seriously affected by soil-structure interaction effect. This interface can be of arbitrary shape and located anywhere between the structure-soil interface and the hemispherical NF/FF interface; however, appropriate consideration of the excitation characteristics of the complete soil-structure system is required. The region S is the structure itself which is assumed to remain linear throughout its time-history of seismic response.

The last refinement is to provide the HASSI-7 with the capability to consider the scattering effect or kinematic effect due to the modification of the input motions by the excavated profile of the foundation soil where the foundation structure is located. This capability was already implemented in the latest HASSI-8.

2.3.2.2 Site investigation and soil properties

The test field selected for the forced vibration test is located on the eastern coast of Tokyo bay 50 km to the south-east from Tokyo. The thick deposits of medium to coarse diluvial sand have formed low rise hills of the area after the regression of sea water in the early alluvial age. A 50 ^{m} x 60 ^{m} yard in the bare plain of 2 ^{km} x 2 ^{km} which was graded by excavation to the height about 40 m above sea level was selected for the forced vibration test. The layer of medium clean sand with fine traces of deposited ore were underlain by well cemented mudstone in the depth more than 70 m within the yard. The total thickness of the sand layers was considered sufficient to form an elastic half-space for the models of forced vibration tests.

The identification of the stratigraphy, velocity measurement to the depth of 40 m were performed by drilling a pilot bore hole at a corner of the yard. The complex bedding of the sand formation due to frequent cycles of sea progression and regression of the gracial age did not affect practically the dynamic properties of the r wave velocity of the layer. The natural water table was 14 m deep; at this level a remarkable

contrast in soil impedance between the upper and lower sand layers was found.

Velocity measurement of both P and S waves of the underlying soil layer were performed in-situ by the Suspended Probe Method. The undisturbed sand samples were collected by rotary boring of 300 mm diameter from a bore hole drilled 3 m apart from and parallel to the pilot bore hole. These un-disturbed samples were used for physical property measurements and cyclic torsional tests using hollow cylinders. In the cyclic torsional test, confining pressures were varied assuming the difference of in-situ overburden pressure. The resonant column test was also performed for covering the wide fluctuation of shear modulus measurements at very small strain level. The stratigraphic classification, S and P wave velocity profiles, equivalent S-wave velocity by laboratory test and distribution of natural unit weight used for subsequent analyses are summarized in Figure 2.3.3. Figures 2.3.4(a) and (b) show the shear modulus and damping ratio versus shear strain relationships of the first and second layer from the ground surface, respectively. The shear wave velocity of 300 m/sec for very small shear strain level was assumed for the first layer.

2.3.2.3 Simulation of forced vibration tests

Models

As shown in Table 2.3.1 and Figure 2.3.5, five models were constructed at the yard. Each A and B series differs in height, but has a common radius of 3 m. The different heights for the same type of models are designed to improve the resolution in decomposing the test results into translational and rotational soil compliance functions. Because the present underground water table was found to be deep and the diluvial unsaturated soil, which was originally submerged under ground water and retained a very weak cementation that provided the soil with high shear wave velocity and mechanical strength, were considered to be subject to deterioration even by a minor disturbance of drying up (Katayama et al, 1986). Therefore, in constructing these models, some special cares were paid in excavation and placing of the underground portion of the models, not to loosen the upper surface of the base soil and surrounding soil of each model. The details of instrumentation and tests were described by Niwa et al (1987).

Tests and results

The forced vibration tests were performed by carefully limiting the exciting loads in the linear range of response of each model and the forces at various frequencies were kept within practicably small variation. The velocity response records were converted into displacement responses per unit exciting load and were plotted, as in Figure 2.3.6 for the case of model 2C as representative, on the force, amplitude and phase vs. frequency diagrams.

Simulation of forced vibration tests

The experimental case of model 2C was selected for the correlation study by HASSI-4, because this model can be further simulated for its response to earthquake excitations. The forced vibration test of the model 2C was idealized by the numerical model as shown in Figure 2.3.7 (a), where far-field interface was chosen at four times the radius of the cylinder. The size of the mesh used can generate the response to the highest frequency of 20 Hz.

As the near-field soil belongs to the first layer, the soil properties of the layer were degraded for the analysis by taking strain dependent nature into account; e.g. by approximately estimating the working shear strain of the soil near the ground surface just close to the side wall of the model, the shear moduli of the soil were varied.

By estimating the shear force acting at the model from the recorded motion at the resonant frequency of 4.2 Hz, the initial soil modulus was calculated by a simple iterative procedure on the curve as shown in Figure 2.3.4(a) as 48 % of the initial value, 7,950 t/m^2(V_S=216 m/s), and the material damping was obtained as 6 % of critical damping from the same curve. The unit weight of the soil 1.8 t/m^3 was used from Figure 2.3.3. The Poisson's ratio of 0.211, determined from in-situ wave velocity data, was used.

The resultant displacement amplification curves and the experimental data are simultaneously plotted by solid lines in Figures 2.3.7(b) and (c), for the observation points, T and B. These figures show a good agreement between the calculated and the observed values in the range higher than the peak frequency.

However, in the lower frequency range, the coincidence is poor. Because the working load capacity is proportional to the exciting

frequency and changes in the vibration characteristic of the model, the shear modulus and damping ratio of the soil were varied following the same procedure described above for the two lower frequency ranges where the estimated working strain level were very small. The resultant values are plotted by solid triangles in these figures. Obviously the resonant curves were shifted down forward to the observed data points.

2.3.2.4 Simulation of earthquake response motion of model 2C

Earthquake response observation

The seismic observation system for earthquake response of the model 2C has been maintained after a series of forced vibration test until the end of February, 1988, with seismometers installed as schematically shown in Figure 2.3.8. Until now over twelve sets of response motions have been recorded. Among them, two sets of earthquake response records were selected for validation study of the HASSI series computer codes.

The first set of the records was obtained in a small local earthquake with focal depth of about 50 km which occurred just beneath the site on January 17, 1987. The maximum acceleration of 20.6 gals was recorded at the roof top of the model and 3.9 to 6.7 gals at the ground surface points. We use the records as representative of the response of the model in the linear range in this simulation study. The recorded horizontal components of acceleration records have been filtered by band-pass from 0.4 - 40 Hz and are shown in Figure 2.3.9.

The second set of the records, with much stronger earthquake response records than the previous one, was recorded on December 17th in the event of 1987 Off Bousou Pennisula Earthquake which occurred some 10 kilometers off the coast of Bousou Peninsula with a focal depth of about 40 kilometers. This earthquake severely shaked the Kanto area and caused many soil liquefactions at the sea front industrial complex sites along the Tokyo Bay and some damages of transformers of a high voltage substation important for the central part of the Pennisula. On this occasion, the maximum acceleration of 301.2 gals at the roof top and 73.5 gals at the ground surface were recorded as shown in Figure 2.3.10. Judging from the large accelerations obtained and through the preliminary evaluation of the apparent frequency transition of the roof top response motion on the the time history, the set of records was selected for the simulation study as representative of the case where the soil surrounding the model structure might have behaved as non-linear material.

Reproduction of 1987 January 17th earthquake response records

Input free-field ground motions The cross correlation coefficients of the recorded motions are shown in Table 2.3.2. From this table, the spatial variation among every free-field ground motion is evident and the cross correlation coefficients of the roof top components with S1 and A1 components are sufficiently smaller than the coefficient between S1 and A1 motions. These facts suggest that the S1 and A1 motions may reasonably be used as the input ground motions to the model.

Computer codes applied The HASSI-4 code was used for the simulation. The numerical model is the same as that shown in Figure 2.3.7(a) but the input ground motions are applied instead of the sinusoidal vibration force.

Material properties used Similarly as mentioned in the forced vibration test case, the strain dependent shear modulus was used, based on the estimated maximum shear strain near the ground surface close to the wall of the model 2C. The material damping of the structure was set as 0.5 %.

Results The recorded and calculated horizontal NS and EW components of the roof top motions for the NS and EW components of input ground motions at S1 and A1 points and the corresponding Fourier spectra are shown respectively in Figures 2.3.11 and 2.3.12.

With the shear wave velocity and material damping ratio of the soil, respectively assumed as 275 m/s and 0.5 %, amazingly good fit to the time history and the Fourier spectrum of the recorded NS response motion was obtained when the input ground motion at S1 was used, as evident from Figures 2.3.11(b) and 2.3.12(a). In case the ground motion at A1 was used as the input motion, the fit on the Fourier spectrum was quite good whereas the fit on the time history was poor. The distance between two points, S1 and A1, is 30 m and this distance seems large enough to generate spatial variation of ground motions. Regarding the EW component, the resultant simulated motions gave a poor fit as evident both from the comparison of corresponding time histories and Fourier spectra shown in Figures 2.3.11(d) and 2.3.12(b).

These two orthogonal components of the recorded roof top motions are essentially those of rocking motion and, even if the structure itself is symmetric and the soil property was derived as homogeneous, have shown

remarkably different predominant peaks of 5.5 Hz and 5.2 , respectively for the NS and EW components as shown in Figure 2.3.12(c). As a result, it may be said that the assumed shear modulus based on the soil investigation is valid only for the NS components. The soil properties may be adjusted to get good fit also for the EW component; however, as the soil properties could not be given directionally, such a directional adjustment of the properties were not performed.

Reproduction of 1987 December 17th earthquake response records

Preliminary analysis As a preliminary study, the HASSI-6, a revised version of HASSI-4 with improved solver for computer efficiency, was used for the linear analysis.

For this analysis, similar to the previous case, both the surface ground motions obtained at S1 and A1 points shown in the previous Figure 2.3.10 were used as input motions.

The recorded motions are considered essentially as the rocking motions of the rigid structure on soft soil and the peak frequency of the recorded motions of the roof top of the model show the same frequency of 4.2 Hz obtained by the forced vibration test previously described, as shown in Figure 2.3.14. Therefore, the equivalent uniform shear wave velocity and the damping ratio were estimated as close to those used in the forced vibration test.

Considering this and using the shear wave velocity and material damping ratio of soil, 210 m/s and 5 % respectively, the response time histories and their Fourier spectra as shown in Figures 2.3.13 and 2.3.14 were obtained.

From the comparison of the recorded and predicted motions at the predominant frequency on the Fourier spectra of Figure 2.3.14 and the frequency dependent soil properties given in Figure 2.3.4, the above damping value of 5 % seems still too large as the equivalent damping value used for linear analysis. To avoid this, the initial shear wave velocity of 300 m/s obtained from in-situ seismic profiling seemed to be changed to the value obtained by the resonant column test in the laboratory, leading to the lowering of the corresponding working shear strain in the subsequent equivalent linear method.

Input free-field ground motions The triaxial free-field input ground motions at S1 point were selected.

Computer codes applied Non-linear analysis by equivalent linear method was performed by HASSI-7.

Material properties used For the reason described above, the initial shear wave velocity at very small strain was selected as 250 m/s based on the resonant column test of the soil of the first layer in the non-linear analysis. The strain dependent shear modulus and damping ratio were calculated by using the previous strain dependent soil properties in the iteration process having been implemented in HASSI-7.

Results For the site response analysis, the low strain shear modulus corresponding to the shear wave velocity of 250 m/s and the damping ratio of 2 % were used as the initial soil properties for each layer of the numerical model. Adopting 0.6 as the fraction of the effective shear strain to the maximum octahedral shear strain, the iterative calculation was performed until the response converged within a tolerance of 5 % adjustment for both shear modulus and damping ratio of each element in the non-linear region (the Region I in Figure 2.3.2). The number of iterations required to assure the convergence limit were from 3 to 5.

The resultant time histories of motion and corresponding response spectra of 5 % damping of the roof top of the model are shown in comparative form in Figure 2.3.15. The coincidence of the calculated and observed response of the model structure are fair as a whole, however, the predicted maximum accelerations became smaller than the observed; this may be attributed to the high-cut nature usually found in the complex modulus method.

The converged average shear wave velocity and damping ratio of the presumed non-linear soil region I and those adjacent soil are shown in Figure 2.3.16. From the figure, it is evident that the strain levels of the free-field soil and the soil near the foundation structure are remarkably different. Also the extent of degradation of shear wave velocity and increase of material damping of the soil by the soil-structure interaction recovered quickly to those of the free-field within the distance of two times the radius of the foundation structure which approximately corresponds to the radius of the presumed non-linear soil region. Therefore, it can be said that the soil strongly affected by

soil-structure interaction is limited to a fairly small region.

2.3.2.5 The importance of three-dimensional approach to SSI analysis

Simulations by two-dimensional codes

Based upon the previous successful simulation results of the Jan. 17th earthquake response records obtained by the three-dimensional code HASSI-4, similar simulation analyses were performed by other two dimensional dynamic analysis codes in order to compare the fundamental difference between three dimensional and two dimensional approaches.

Input motion applied The NS component of S1 ground motions was chosen as the input motion for these computer codes.

Computer codes applied In this analysis, two types of codes, HASSI-2D and FLUSH-VB, were used. The former is HASSI-2D, the two dimensional version of HASSI-4, which was also modified to have far-field impedance expression of plain strain case by using the results given by Tzong and Penzien(1983). The numerical model is the same as was used in the previous three-dimensional analysis but the equivalent cross section and rigidity per unit width were used for the super structure and the near-field soil was controlled to be that of plane strain. The latter is FLUSH-VB, the modified FLUSH code which was attached with viscous dampers at the bottom boundary of the near-field soil to realize far-field effect there. The numerical model of this case is shown in Figure 2.3.17.

Material properties used As for the analysis by HASSI-2D, the strain dependent shear wave velocity and the damping ratio of the soil were assumed respectively as 275 m/s and 0.5 %, as used in the analysis by HASSI-4. The material damping of the structure was set as 0.5 %. In the case of FLUSH-VB, the previous strain dependent shear modulus and damping ratio curve in Figure 2.3.4 were applied and automatic convergence function was utilized.

Results The resultant time histories of NS component obtained by the above two two-dimensional codes and the simulated motion of the same component by HASSI-4 (the same one already shown in Figure 2.3.11(b)) are compared with the recorded NS motion of the roof top of the Model 2C

in Figure 2.3.18. The Fourier spectra of these time histories are presented in Figure 2.3.19.

From these figures, it is evident that the predicted motions by these two-dimensional analysis codes differed greatly from the recorded motion in both time history and Fourier spectrum. The poor simulation results by these two-dimensional codes could be well displayed by the transfer functions shown in Figure 2.3.20(a).

The frequency shift is not so significant but the over-damping is very serious, resulting in an excessive underestimate of the response of the structure. The over-damping by HASSI-2D and FLUSH-VB in this case were 8.4 and 4.9 times respectively of the damping expected by HASSI-4, as are known from Figures 2.3.20(b) and (c).

The possibility of such slight shift of the primary frequency (Figure 2.3.20(a)) and significant over-damping of the response of the system, as is clearly shown in Figure 2.3.20, has been analytically estimated first by Luco and Hadjian(1974) and recently by Wolf(1985).

The structure is sufficiently rigid against the surrounding soil and so far the above distortion of the response characteristics of the structure is considered to come from the generic feature of soil impedance incorporated in these 2-dimensional codes, explicitly in HASSI-2D and implicitly in FLUSH-VB.

To look at this type of over-damping inherent in these codes from another aspect, Figure 2.3.21 was prepared. The figure shows how the horizontal components of the reflected waves generated by interaction at the soil-structure interface were dissipated with distance from the side wall of the foundation of the model in the form of the (approximate) amplitude transfer functions (the ratio of Fourier amplitude spectra) of the surface ground motions. The points and their distance from the wall for the case of HASSI-4 are shown in Figure 2.3.21(a) and the corresponding points will be found in Figure 2.3.17 for FLUSH-VB; the mesh size of the ground surface is common to both numerical models.

The transfer functions of the surface motions at a series of the points located in the near-field soil region show a very rapid and sharp decay in case of the three-dimensional code, HASSI-4 (Figure 2.3.21(b)), whereas the transfer functions of the two-dimensional code, FLUSH-VB (Figure 2.3.21(c)), show slower decay and are dispersive.

Damping value estimate in two-dimensional analyses

As already above described, the two-dimensional codes caused a small shift of the primary frequency and significant over-damping to the system response. The over-damping is more serious than the frequency shift, because it always leads to the underestimate of the structural response.

In order to clarify the working damping values of the above three computer codes with reference to the 1987 January 17th earthquake, the NS component of the recorded roof top motion was reproduced by the classic stick model with soil springs.

Since the fundamental response characteristic of the model 2C can be explained largely by the rocking response and is significantly controlled by the soil compliance, the previous finite element model of the model 2C may well be replaced by a stick model with soil springs (SMSS: rocking and translational springs) and a single degree of freedom model (SDOF).

To obtain the most reliable results, the recorded NS motion was simulated by both SMSS and SDOF by using the NS motion of the point S1 as the input ground motion of the systems. The static soil springs of circular disc were attached to the base mass of these models, by using the shear modulus and damping values derived from previous analyses as initial values for these analyses.

The results of simulation are shown in Figure 2.3.22 by time histories. For the SMSS, the case where the shear wave velocity of 275 m/sec and 0.5 % damping ratio were used from the results obtained by HASSI-4, the fit to the recorded motion was very poor. This fit was improved by raising the shear wave velocity to 420 m/sec and assuming modal damping of 2.1 % as the sum of radiation and material damping. For the case of SDOF, by the combination of the shear wave velocity and damping ratio of 340 m/sec and 2.0 %, a fairly good fit was obtained. The increase of the shear wave velocity of the soil required to get good fit may be explained partly by the assumption of using the static spring constant independent of on frequency; however, these values are still within the deviation of the soil properties derived from in-situ and laboratory test data.

As already described in the analysis using HASSI-4, the material damping of the soil was assigned as 0.5 %, based on the estimated maximum shear strain near the ground surface by the wall of the model 2C. From this and the above simulation results by both SMSS and SDOF model, the total damping in the simulation by HASSI-4 may be approximately estimated

as about 2 % and consequently the radiation damping of the model becomes 2 - 0.5 = 1.5 %.

In the previous analyses using FLUSH-VB and HASSI-2D, the maximum working damping in FLUSH-VB and HASSI-2D relative to that in HASSI-4 were respectively 8.4 and 4.9 times as shown in the previous Figures 2.3.20(b) and 2.3.20(c). Therefore, in the case of HASSI-2D, the material damping of the soil was also assigned as .5 % and therefore the radiation damping may be estimated as 4.9 x 2.0 - 0.5 = 9.3 %; the radiation damping by this two-dimensional code will become 9.3 / 1.5 = 6.2 times of the one by three-dimensional code. On the other hand, in the case of FLUSH-VB, the effective damping can not be clearly separated into the material damping and the radiation damping; however, it may be approximately considered as material damping. On this basis, in the case of FLUSH-VB, the effective damping value may be estimated as 8.4 x 2.0 = 16.8 %.

The difference of the damping values estimated for HASSI-4 and HASSI-2D comes from the fundamental difference in the nature of energy dissipation by radiation damping inherent to the infinite half-space and infinite strip assumption of the far-field soil. Wolf(1985) has discussed the controversial matter of modeling a three-dimensional problem with a two-dimensional model by showing the over-damping nature of the two-dimensional modeling approach and the significant underestimation of the true three-dimensional dynamic response. On his figure (Figure 7-27 in pp. 309), as the non-dimensional frequency of this case becomes 2 x 3.142 x 5.5^{Hz} / 275 $^{m/s}$ = 0.19, the ratio of damping for the half-plane/half-space is estimated as close to 4 for the case of rocking motion. This ratio is valid for the case in which both systems have the same rocking frequency and no material damping; however, his result gives a close value of over-damping ratio (including the contribution of the frequency shift) of 4.9 in this study.

As for the case of FLUSH-VB, similar comparison may not be appropriate, because we can not distinguish between the material damping and the radiation damping in this system. However, it may be pointed out that it gives us significant underestimate of the three-dimensional response of the truly three-dimensional structure to the extent larger than the results of the two-dimensional code HASSI-2D, which has better theoretical basis as a computer code.

2.3.3 CONCLUSION

The linear and non-linear three-dimensional soil-structure interact-

ion analysis codes, HASSI-4 and HASSI-7, were tested their validity through correlation studies using the forced vibration test data and earthquake response records of a small scale reactor building model.

The predicted results obtained by three-dimensional codes successfully reproduced the recorded motions which essentially represented the rocking motions of a rigid structure on soft soil. The soil properties obtained by in-situ and laboratory test have been used in the analyses. Some ambiguous nature inherent in to these soil properties affected the results, however, the properties used to reproduce the records remained within a reasonable range of the variation of soil properties actually observed.

By using the predicted result by HASSI-4 of 1987 January 17th earthquake, the rapid decaying nature of the wave due to soil-structure interaction was examined with the comparative results obtained by representative two-dimensional finite element analysis codes. The frequency shift is not so significant but the over damping is very serious, resulting into an excessive underestimate of response of the structure. The effective dampings in the two-dimensional codes, HASSI-2D and FLUSH-VB, were estimated as 8.4 and 4.9 times, respectively, of those in the three-dimensional code, HASSI-4.

The structure was sufficiently rigid against the surrounding soil and so far the above distortion of the response characteristics of the structure are considered as being solely caused by the generic feature of the soil impedance incorporated in these two-dimensional codes, explicitly in HASSI-2D and implicitly in FLUSH-VB.

Based upon this feature, the excessive damping existed in the above two two-dimensional finite element codes was analyzed through the simulation of the recorded motion by stick models with soil springs and the comparison of the resultant total dampings among the above three computer codes. The total damping in the simulation by the three-dimensional code, HASSI-4, was estimated as about 2 %, whereas in the simulation by the two-dimensional codes, HASSI-2D and FLUSH-VB, corresponding dampings were estimated as 9.8 % and 16.8 %, respectively.

As pointed out earlier by Luco and Hadjian(1974) and Wolf(1985), it is almost impossible to model a three-dimensional structure with a two-dimensional model. Any two-dimensional model will significantly underestimate the true three-dimensional response by a small shift in frequency and significant over-damping of the vibration system.

In the case of HASSI-2D, the over-damping can be explained by the inadequacy of converting the truly infinite half-space problem into the infinite strip problem. For the case of FLUSH-VB, the interpretation comparable to the above may not be appropriate, because we can neither distinguish between the material damping and the radiation damping nor give clear explanation of the mechanism of damping in this system. However, it may be pointed out that FLUSH-VB will give significant under-estimation of the three-dimensional response of the truly three-dimensional structure.

The transfer functions of the surface motions at a series of points located in the near-field soil region show a very rapid and sharp decay of the response with distance from the side wall of the structure foundation in the case of three-dimensional code, HASSI-4, whereas those transfer functions by the two-dimensional code, FLUSH-VB, shows slow and dispersive nature.

Taking far stronger earthquake response records obtained in the 1987 December 17th earthquake which recorded the maximum acceleration of 301.2 gals at the roof top and 73.5 gals at the ground surface, HASSI-7, the non-linear version of HASSI-4, was tested for its validity.

The coincidence of the calculated and observed response of the model structure are fair as a whole; however, the predicted maximum accelerations were smaller than the observed; this may be attributed to the high-cut nature usually found in the complex modulus method.

However, through the simulation, it was clearly shown that the strain levels of the free-field soil and the soil near the foundation structure are remarkably different and that the soil strongly affected by the soil-structure interaction was limited to a fairly small region the radius of which was less than two times the radius of the structure. This also indicates that only a three-dimensional analysis can reproduce the rapid decaying nature of the wave generated at the soil-structure interface of truly three-dimensional structures.

As a conclusion, it can be clearly stated that we should avoid to treat soil-structure interaction phenomena of truly three-dimensional structures with two-dimensional models, in order not to underestimate the true response of three-dimensional structures.

2.3.4 REFERENCES

(1) Gupta, S., Penzien, J., Lin, T. W., and Yeh, C. S., (1980), "Hybrid

Modeling of Soil-Structure Interaction", Report No. UCB/EERC-80/09, Earthquake Engineering Center, University of California, Berkeley, California.

(2) Gupta, S. and Penzien, J., (1981), "Hybrid Modeling of Soil-Structure Interaction for Embedded Structures", Proc. Sixth Conference on Structural Mechanics in Reactor technology, Paris, France.

(3) Gupta, S., Penzien, J., Lin, T. W., and Yeh, C. S., (1982), "Three-Dimensional Hybrid Modeling of Soil-Structure Interaction", Earthquake Engineering and Structural Dynamics, Vol. 10, No. 1, Jan.-Feb..

(4) Niwa, A., I. Katayama, & J. Penzien, (1983), A Quantitative Evaluation of Radiation Damping in Soil-Structure Interaction Effects. 7th SMiRT: K 8/9.

(5) Penzien, J., (1983), Soil-structure Interaction Considering Multiple Traveling Wave Input, International Symposium on Earthquake Engineering to mark the occasion of Professor K. Kubo retirement, July 29, Tokyo, pp.34-43.

(6) Tzong, T. J. and J. Penzien, (1983), Hybrid Modeling of Soil-Structure Interaction in Layered Media. Report No. UCB/EERC-83/22.

(7) Katayama, I, Ohsumi, T., Kubo, Y., Nakase, H., and Penzien, J., (1987a), "Experimental Validation of Soil-Structure Interaction Analysis", Proc. of US-Korea Joint Seminar on Critical Engineering Systems, Vol. 1, pp. 495-506, Seoul, Korea, May 11-15.

(8) Katayama, I., S. Fukui, and others. (1986). Comparison of Dynamic Soil Properties between Undisturbed and Disturbed Dense Sand Samples. Annual Meet. Soil. Found., Sapporo.

(9) Niwa, A., I. Katayama, T. Ohsumi, Y. Kubo, H. Nakase, and J. Penzien, (1987), "Verification of Hybrid Analysis Concept of Soil-Foundation Interaction by Field Vibration Tests (1) - Experimental Phase", Trans. of the 9th Structural Mechanics in Reactor Technology, Vol. K1, pp. 229-234, Lausanne, Aug. 17-21.

(10) Katayama, I., A. Niwa, Y. Kubo, and J. Penzien, (1987b), "Verification of Hybrid Analysis Concept of Soil-Foundation Interaction by Field Vibration Tests (2) - Analytical Phase", Trans.

of the 9th Structural Mechanics in Reactor Technology, Vol. K1, pp. 235-240, Lausanne, Aug. 17-21.

(11) Penzien, J. et al., (1987), Soil-Structure Interaction Correlations of EPRI/TPC Field Test Results with Analytical Predictions. Workshop on Validation of Seismic Soil-Structure Interaction Analysis Techniques Using Lotung Experiment Data, Palo-Alto.

(12) Katayama, I., (1988), "The Importance of Three Dimensional Approach in Soil-Structure Interaction Analyses", Proc. ANS/ROC International Workshop in Seismic Design, pp. 139-175, Taipei, Taiwan, R.O.C., May 26-27.

(13) Chen, C. et al, (1988), Soil-Structure Interaction-Correlation of Field Test Results with Analytical Predictions. Proc. of 9th WCEE, Tokyo-Kyoto, Aug. 4-8.

(14) Katayama, I., Ohsumi, T., Teramura, Y., (1988), Experimental Validation of Soil-Structure Interaction Analysis, Proc. of 9th WCEE, Tokyo-Kyoto, Aug. 4-8.

(15) Luco, J. E. and A. H. Hadjian, (1974), Two-Dimensional Approximations to the Three-Dimensional Soil-Structure Interaction Problem, Nuclear engineering and Design 31.

(16) Wolf, John P., (1985), Dynamic Soil-Interaction, Chapter 7, 7.4.2 Two-Dimensional versus Three-Dimensional Modeling, Prentice-Hall.

(17) Katayama, I., Chen, C. H., Lee, Yang-Jye, Jean Wen-Yu, and Penzien, J., (1989), Near-field soil-structure interaction analysis using nonlinear hybrid modeling, 10th International Conference on Structural Mechanics in Reactor Technology, Anaheim, California, K05/2, Aug. 14-18.

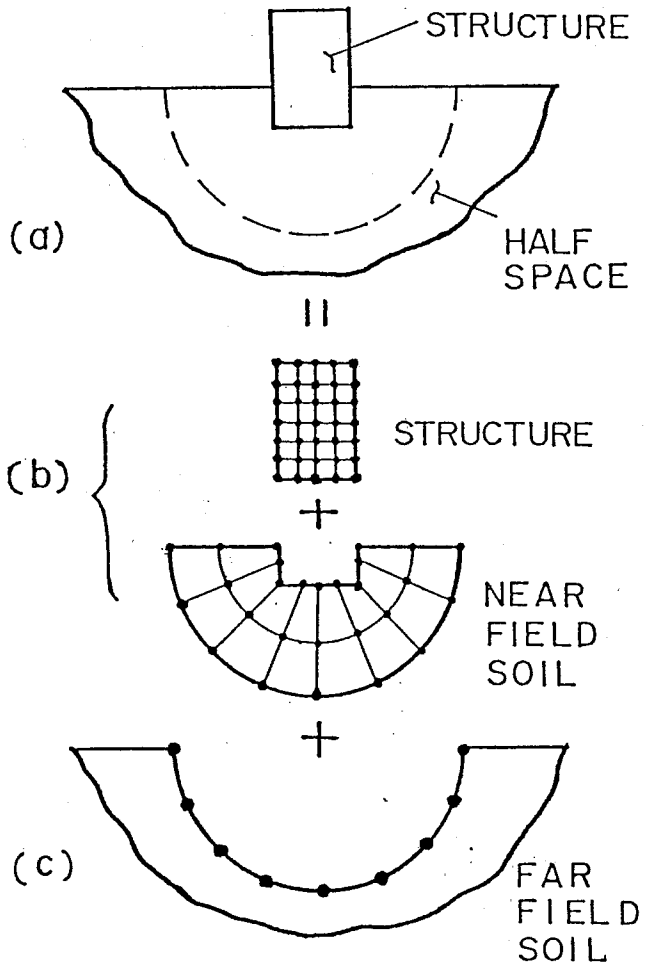

Figure 2.3.1 Modeling concept of HASSI-4

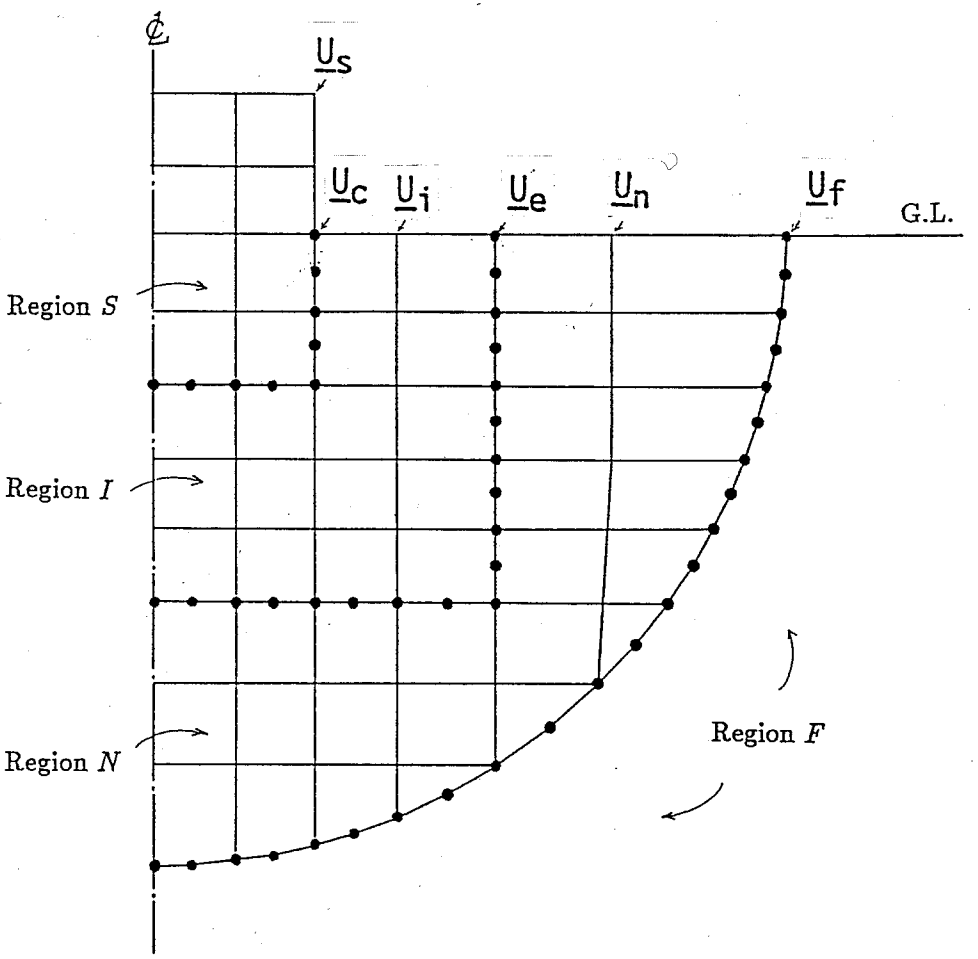

Figure 2.3.2 Substructuring scheme of Near-Field soil region

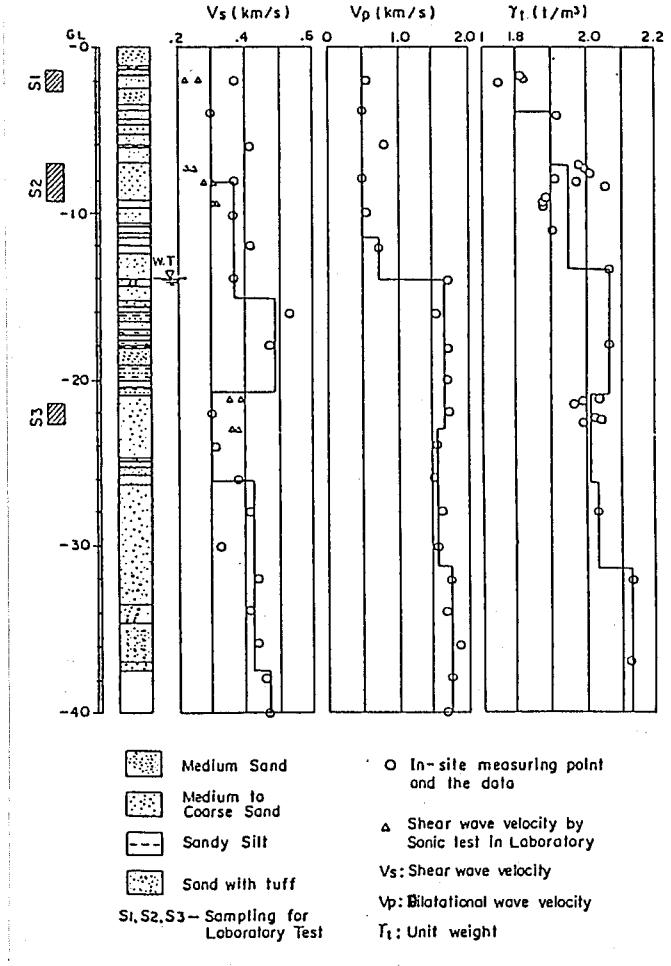

Figure 2.3.3 Soil condition of the sub-surface layers

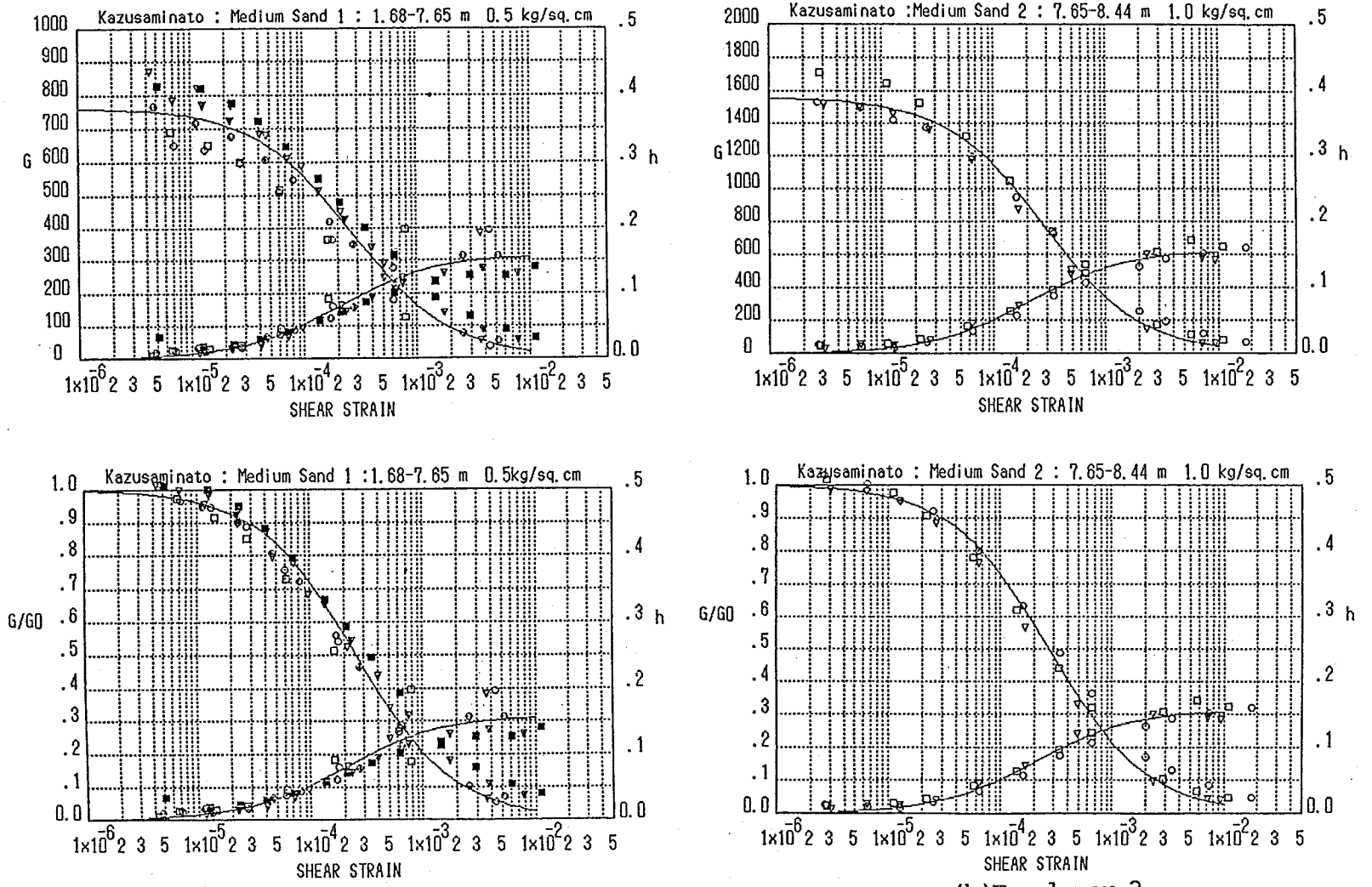

(a)For layer 1

(b)For layer 2

Figure 2.3.4 Absolute and normalized dynamic shear modulus and absolute damping ratio versus shear strain relationship for the first and second layer

Table 2.3.1 Dimension and weight of model

No.	Radius (m)	Height (m)	Embedment (m)	Weight (t)
1A	3.0	0.55	---	38.8
1B	3.0	3.55	---	104.8
2A	3.0	3.55	3.0	104.8
2B	3.0	6.00	3.0	135.1
2C	1.5	10.00	1.5	98.0

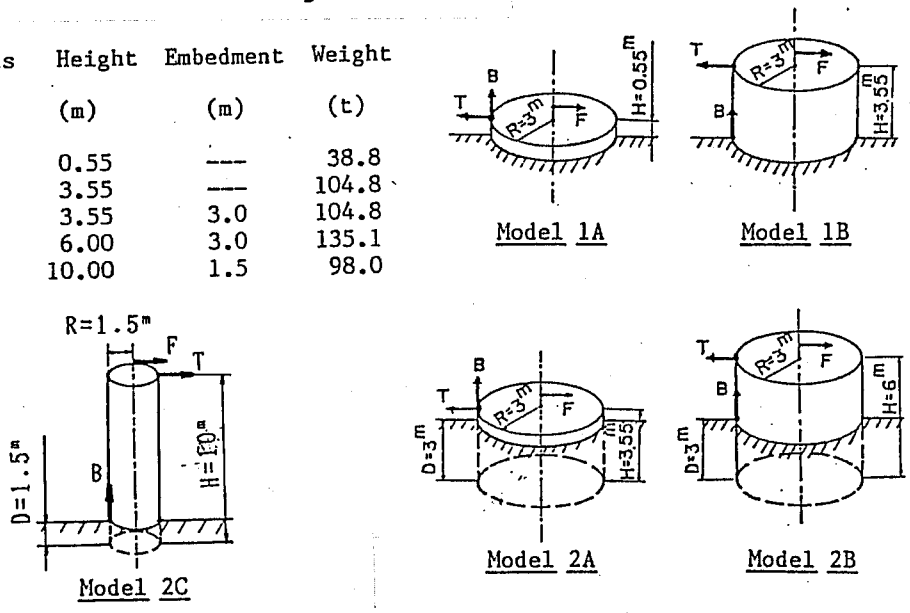

Figure 2.3.5 Configuration of models

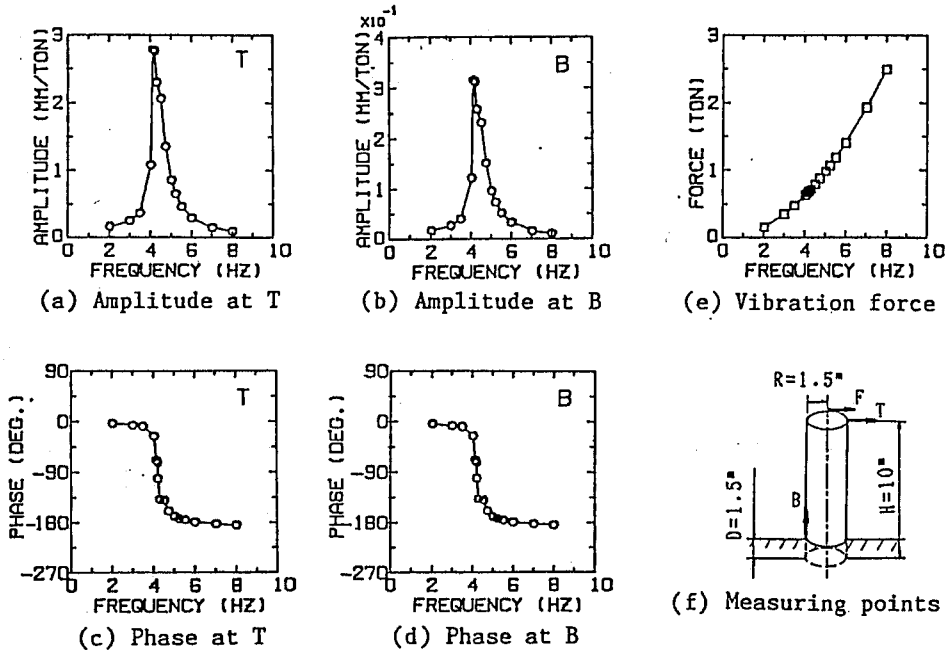

Figure 2.3.6 A representative forced vibration test results

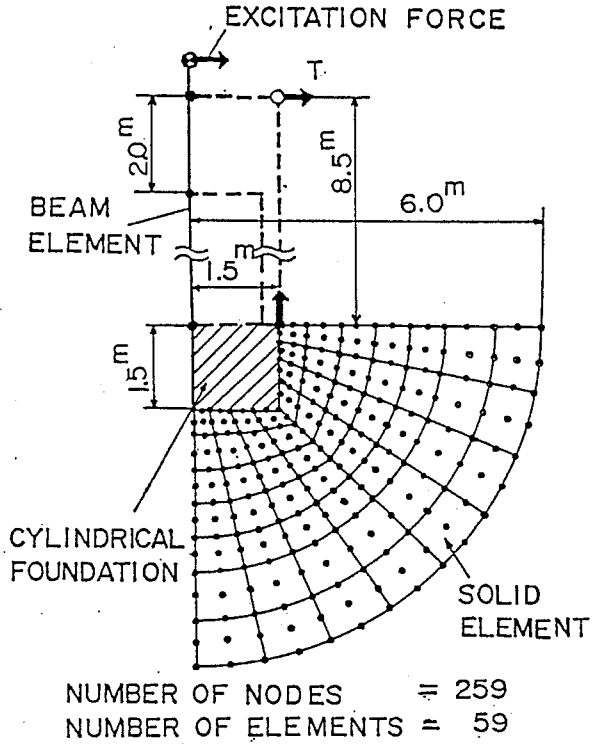

(a) Numerical model

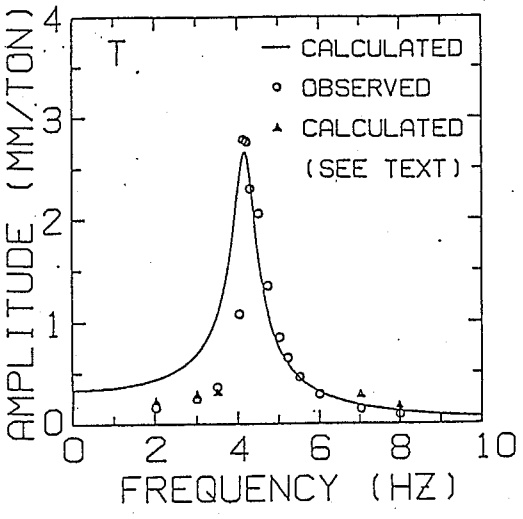

(b) Amplitude at T

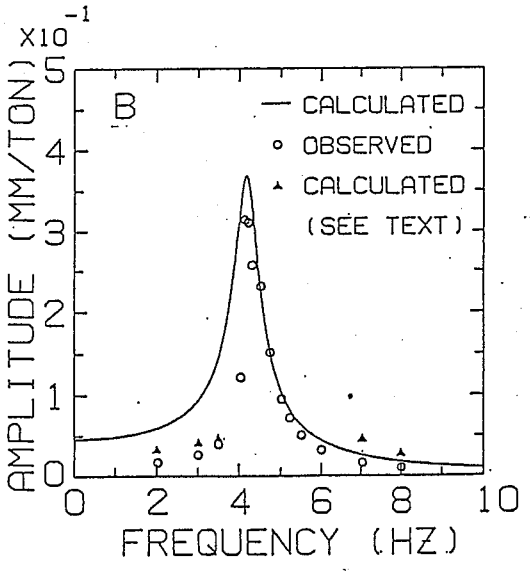

(c) Amplitude at B

Figure 2.3.7 Numerical model of forced vibration test at Model 2c by HASSI-4 and the observed and the calculated results

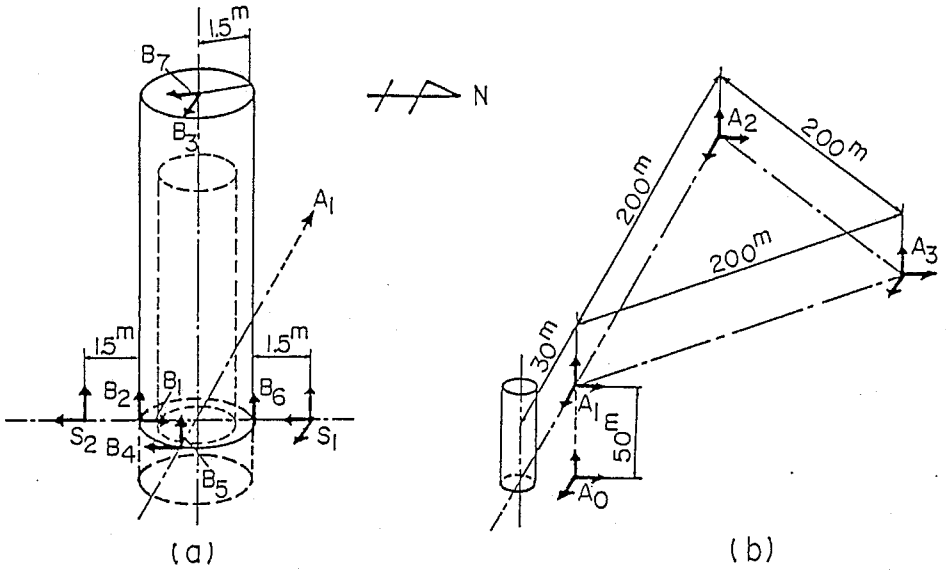

Figure 2.3.8 Seismic instrumentation at Model 2C and triangular seismic array

Table 2.3.2 Results of cross-correlation analysis of observed motions

January 14 (Upper half) and January 17(Lower half), 1987 Earthquake

	St. NS	St. EW	S1 NS	S1 EW	A1 NS	A1 EW	A2 NS	A2 EW
St. NS	*	-0.047	0.238	-0.025	0.150	0.022	0.031	0.088
St. EW	-0.058	*	0.094	0.265	0.084	0.157	-0.088	0.065
S1 NS	0.052	-0.096	*	0.193	0.821	0.249	0.223	0.191
S1 EW	-0.039	0.027	-0.001	*	0.171	0.830	-0.216	0.333
A1 NS	0.035	-0.048	0.599	-0.115	*	0.273	0.253	0.192
A1 EW	0.125	-0.078	-0.026	0.460	-0.039	*	-0.228	0.372
A2 NS	-0.097	0.005	0.143	-0.067	0.123	-0.078	*	-0.058
A2 EW	0.082	-0.117	0.059	0.025	0.106	0.102	-0.166	*

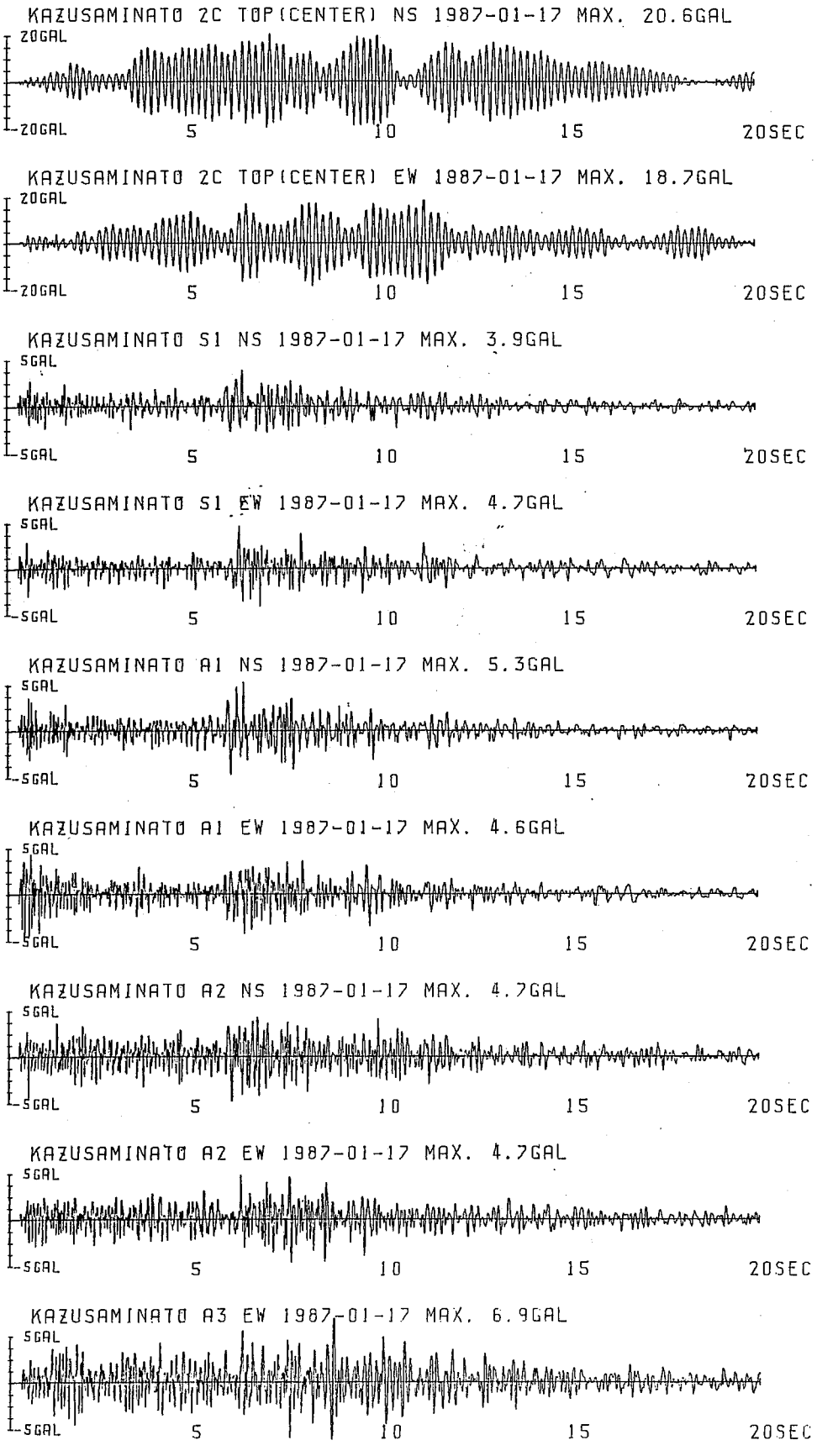

Figure 2.3.9 Observed response of Model 2C and free-field ground motions on Jan. 17, 1987

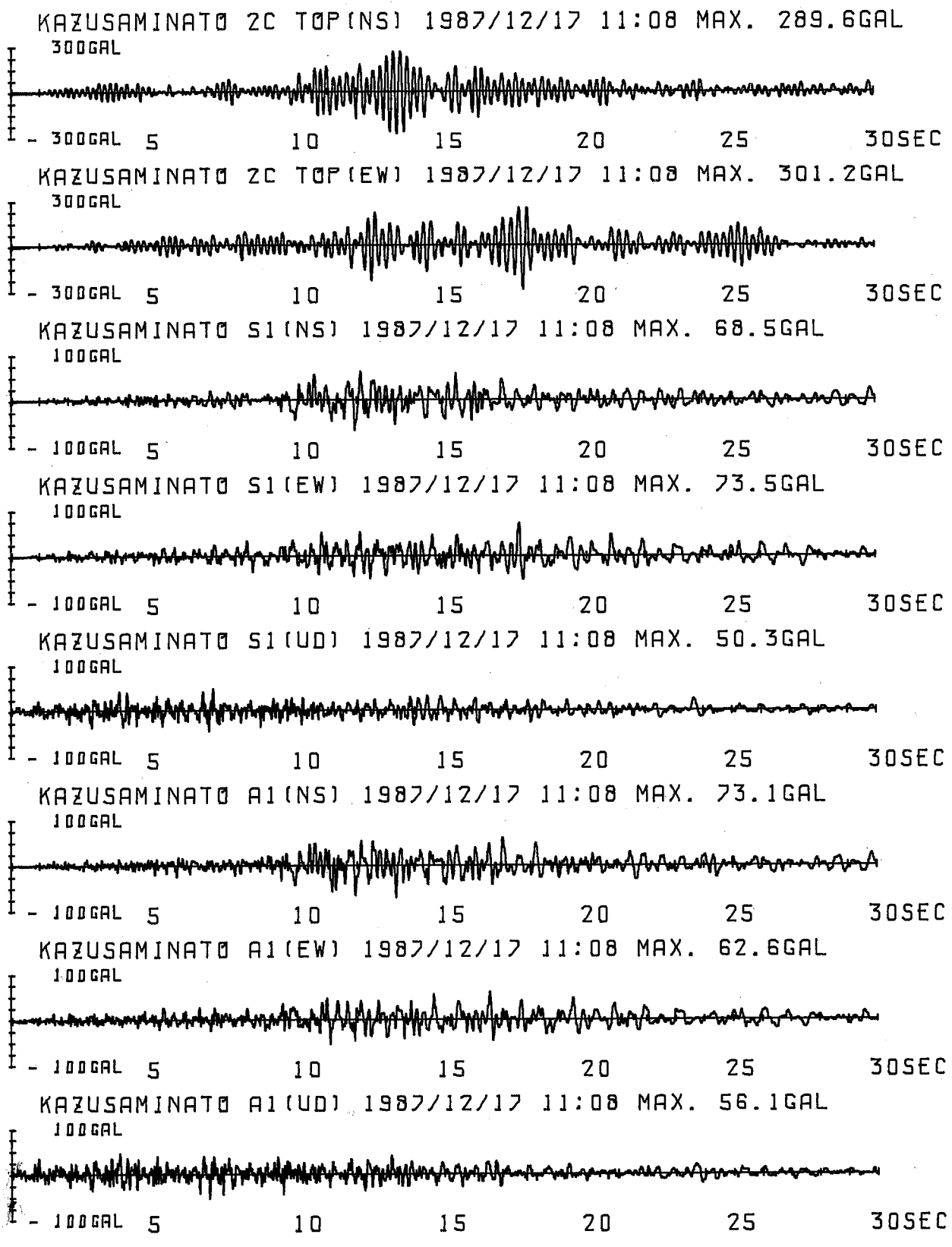

Figure 2.3.10 Observed response of Model 2C and free-field ground motions on Dec. 17, 1987

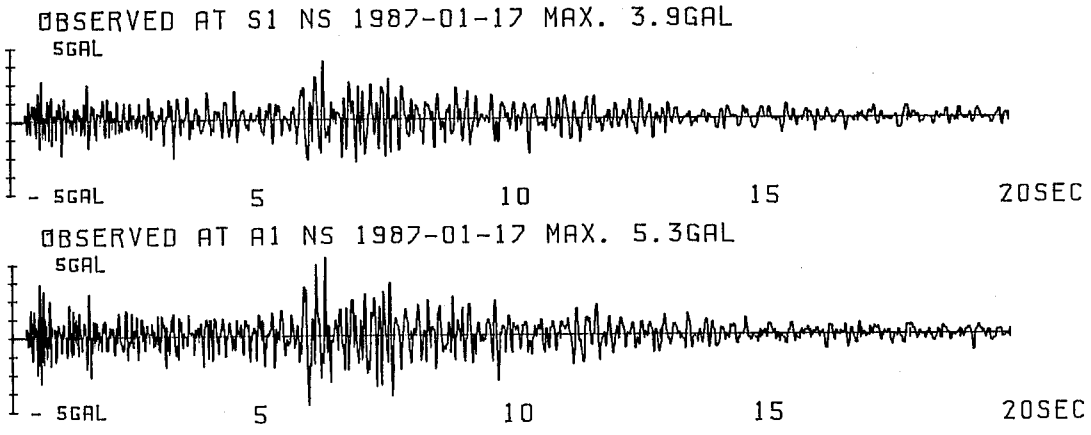

Figure 2.3.11(a) Input ground motions for simulation: The upper and lower accelerograms are the free-field motions observed at points S1 and A1, each apart from the model 1.5 m and 30 m, respectively.

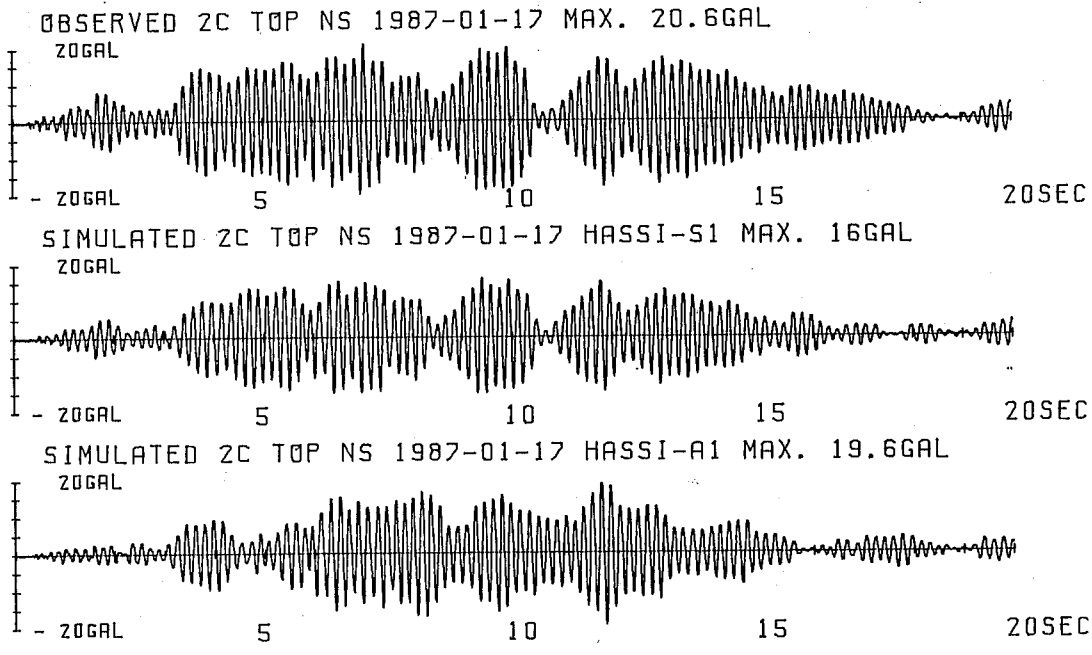

Figure 2.3.11(b) Comparison of acceleration time histories (NS components) between the observed and simulated: The upper is the observed motion of the roof top of the model, the middle the simulated motion by using the S1 motion, and the lower that by using the A1 motion (r=1.8 t/cu.m, Vs=275 m/s, h=0.5%).

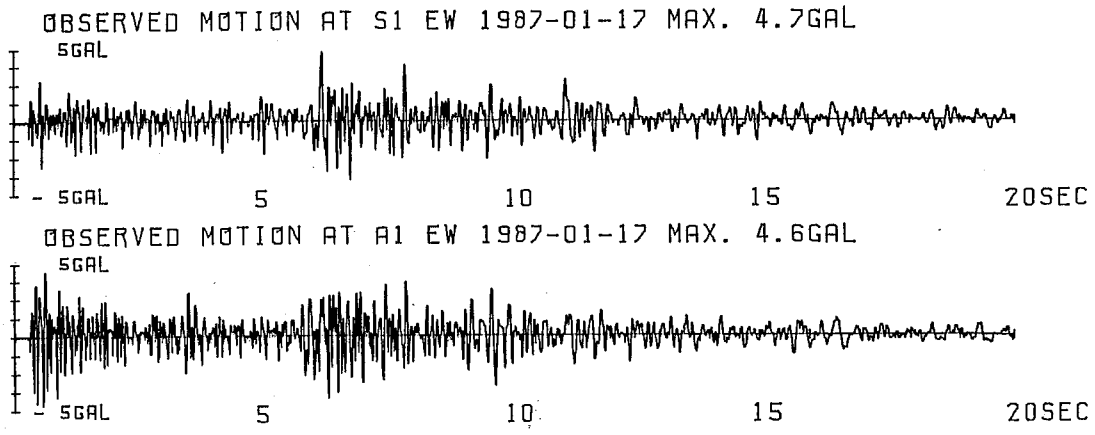

Figure 2.3.11(c) Input ground motions for simulation: The upper and lower accelerograms are the free-field motions observed at points S1 and A1, each apart from the model 1.5 m and 30 m, respectively.

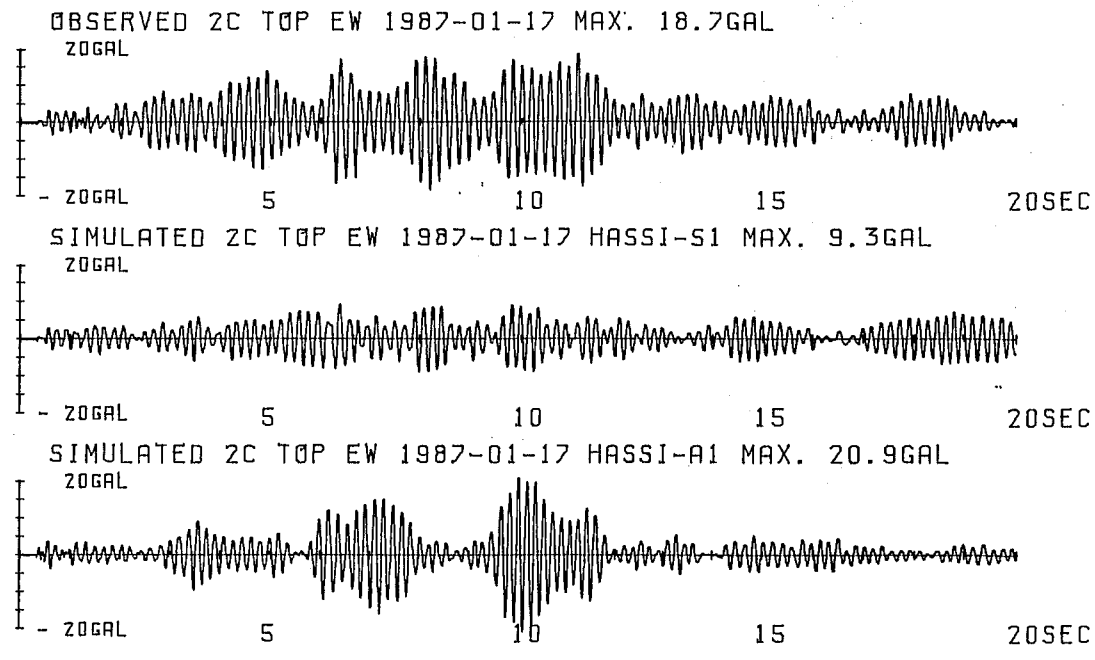

Figure 2.3.11(d) Comparison of acceleration time histories (EW components) between the observed and simulated: The upper is the observed motion of the roof top of the model, the middle the simulated motion by using the S1 motion, and the lower that by using the A1 motion (r=1.8 t/cu.m, Vs=275 m/s, h=0.5%).

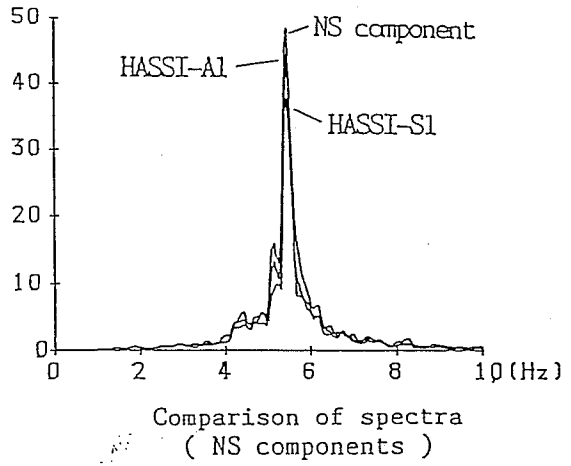

Figure 2.3.12(a) Fourier spectra of the observed and simulated acceleration time histories in case of NS components (with Parzen's window of the band width 0.2Hz)

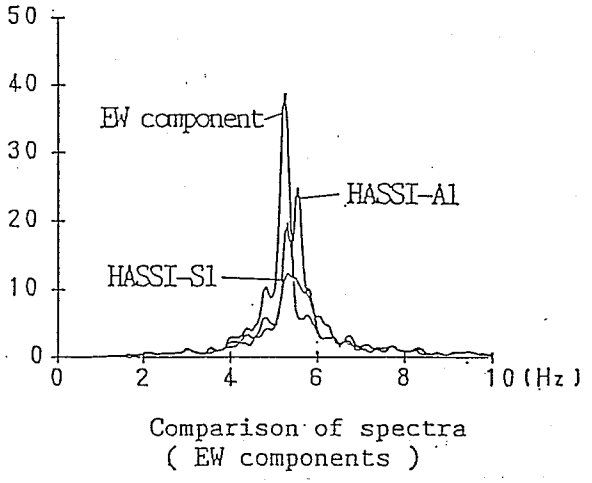

Figure 2.3.12(b) Fourier spectra of the observed and simulated acceleration time histories in case of EW components (with Parzen's window of the band width 0.2Hz)

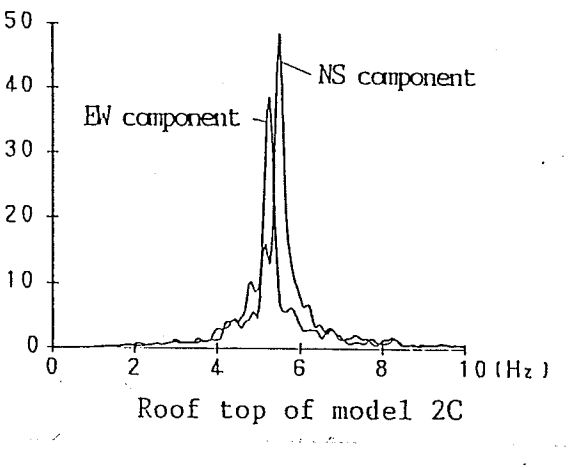

Figure 2.3.12(c) Comparison of the recorded motions on Fourier spectra

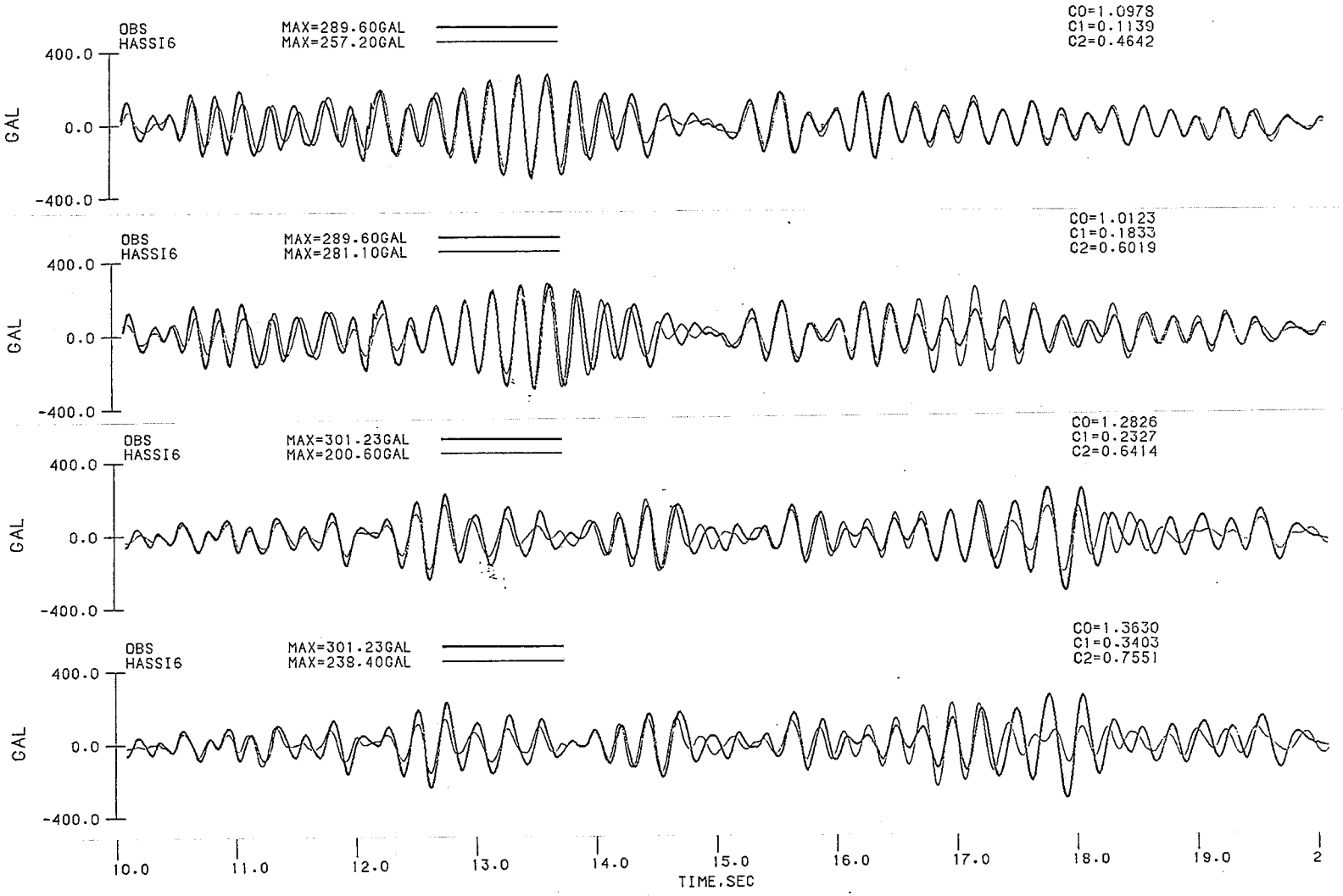

Figure 2.3.13 Comparison of the recorded motions with calculated motions in case of the 1987 December 17th earthquake records by linear analysis by using HASSI-6: The thick solid lines denote the observed motions and the fine chained lines the calculated motions; the first two figures are the comparison for NS components by using the input ground motion at S1 and A1, and the next two figures are for those of EW components by S1 and A1 motions.

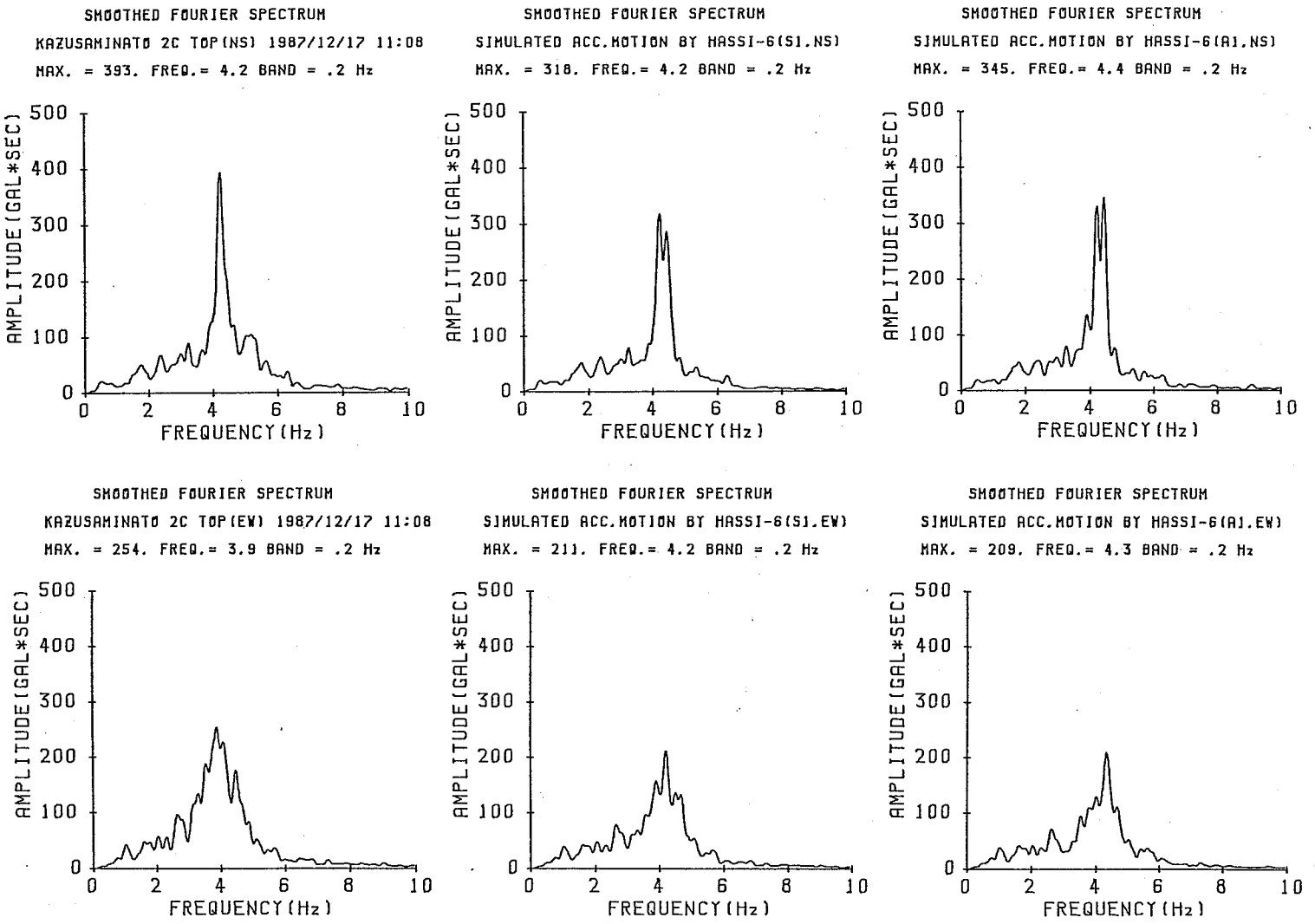

Figure 2.3.14 Fourier spectra of the recorded motions and the calculated motions by linear analysis by HASSI-6

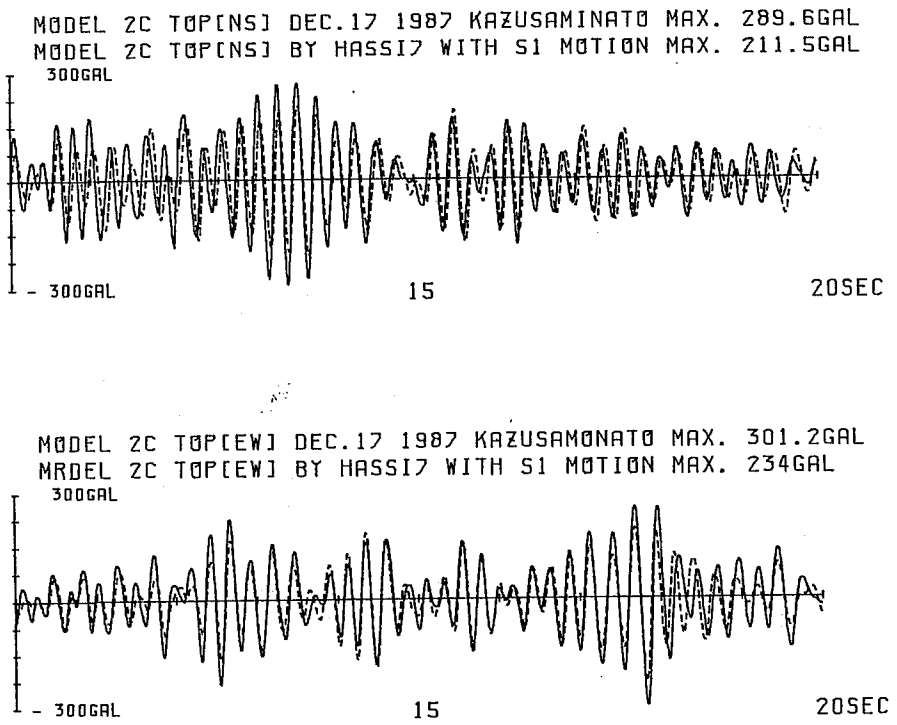

Figure 2.3.15(a) Comparison of the recorded motions at the roof top of the model 2C with the calculated motions by the non-linear analysis with using HASSI-7 and three orthogonal ground motions at S1 point: The upper figure compares those of NS component and the lower for EW component.

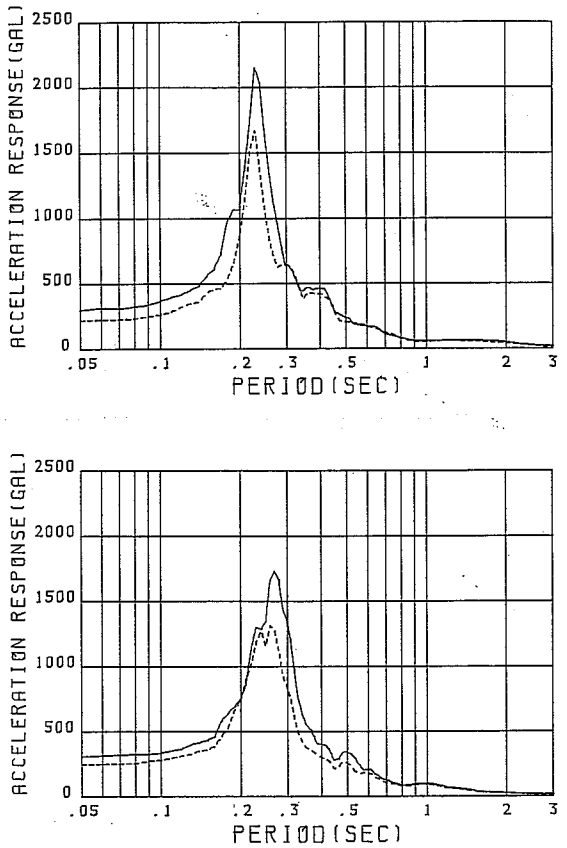

Figure 2.3.15(b) Comparison of the recorded and calculated results by HASSI-7 on the acceleration spectra; The upper is for NS components and the lower for EW components.

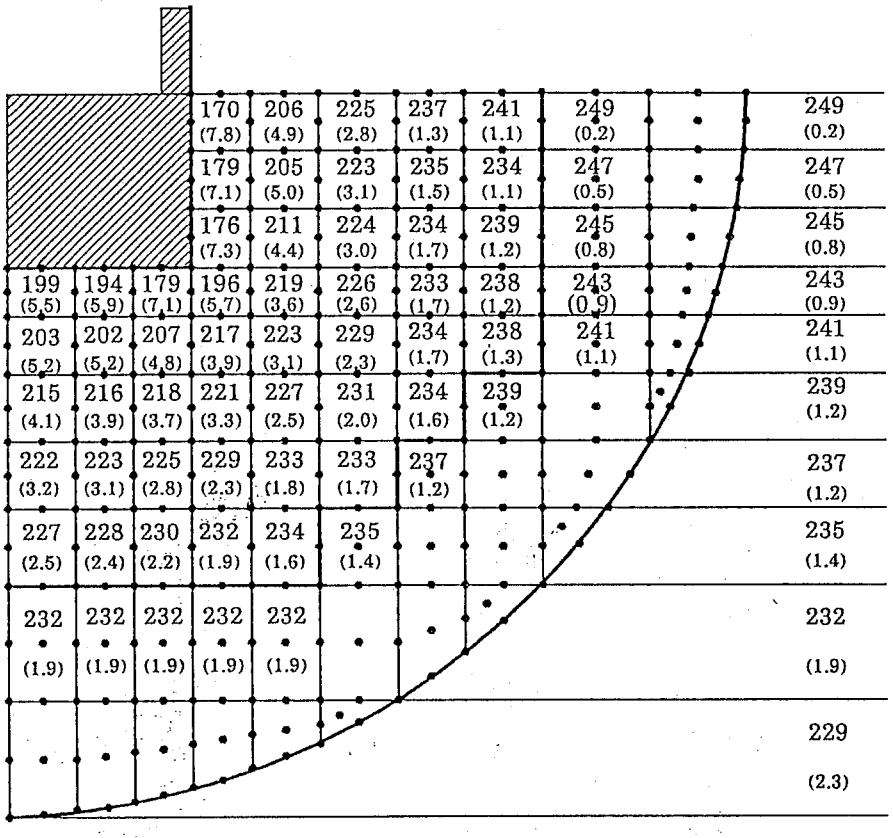

Figure 2.3.16 Converged soil properties in non-linear zone and adjacent soil; the converged values of shear wave velocities and damping values (in parentheses) across the I/N interface show very close values.

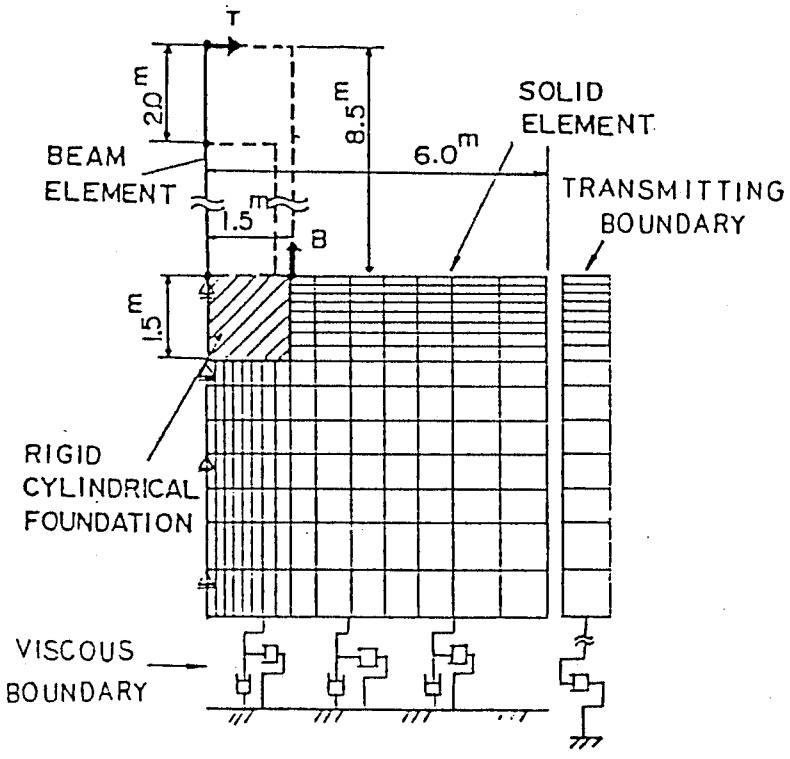

Figure 2.3.17 Numerical modeling in case of the two-dimensional analysis by FLUSH-VB

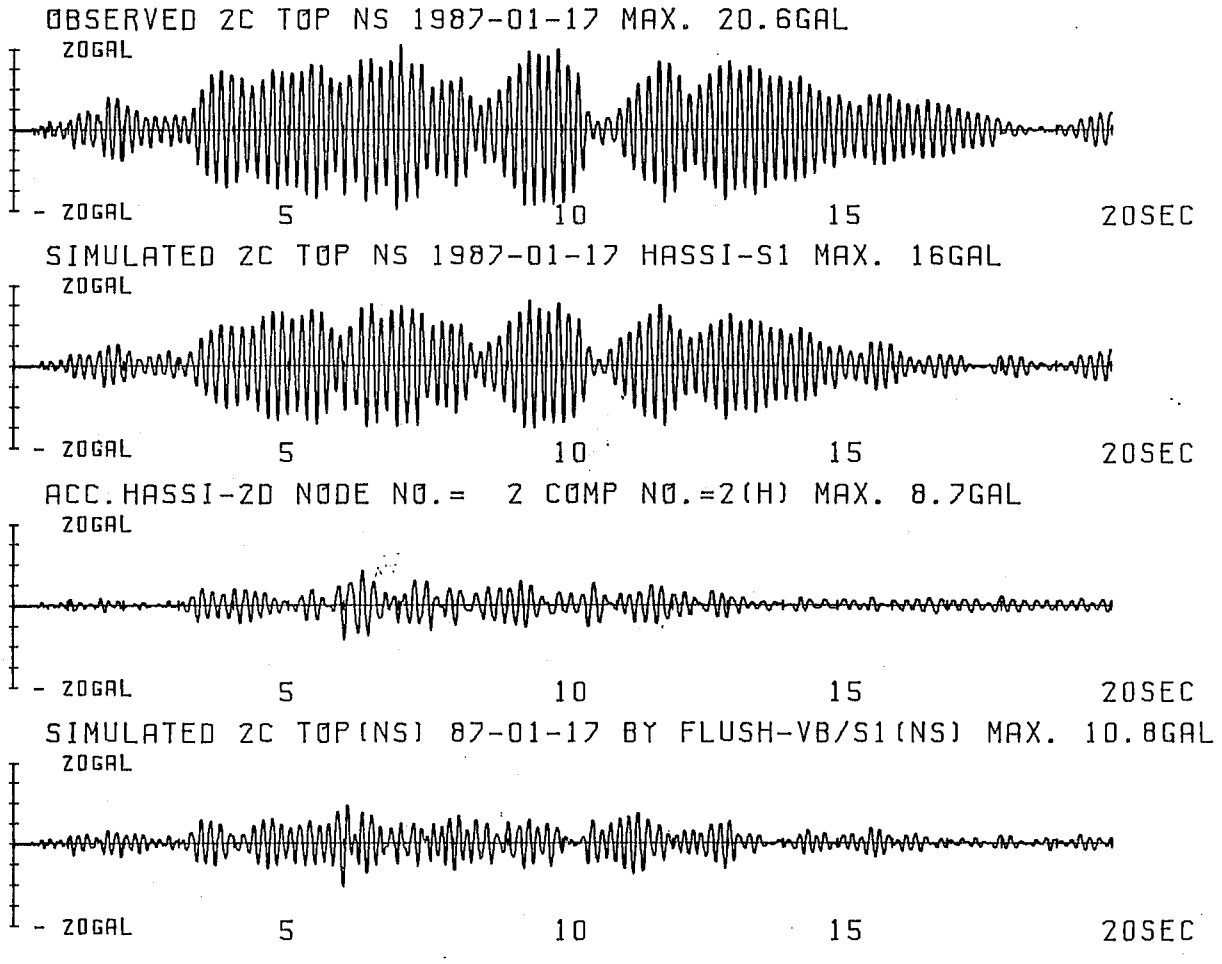

Figure 2.3.18 Comparison of the observed and simulated response motion(NS components); from the upper to lower, the observed motion, the simulated motion by three-dimensional HASSI-4, two-dimensional HASSI-2D, and FLUSH-VB codes.

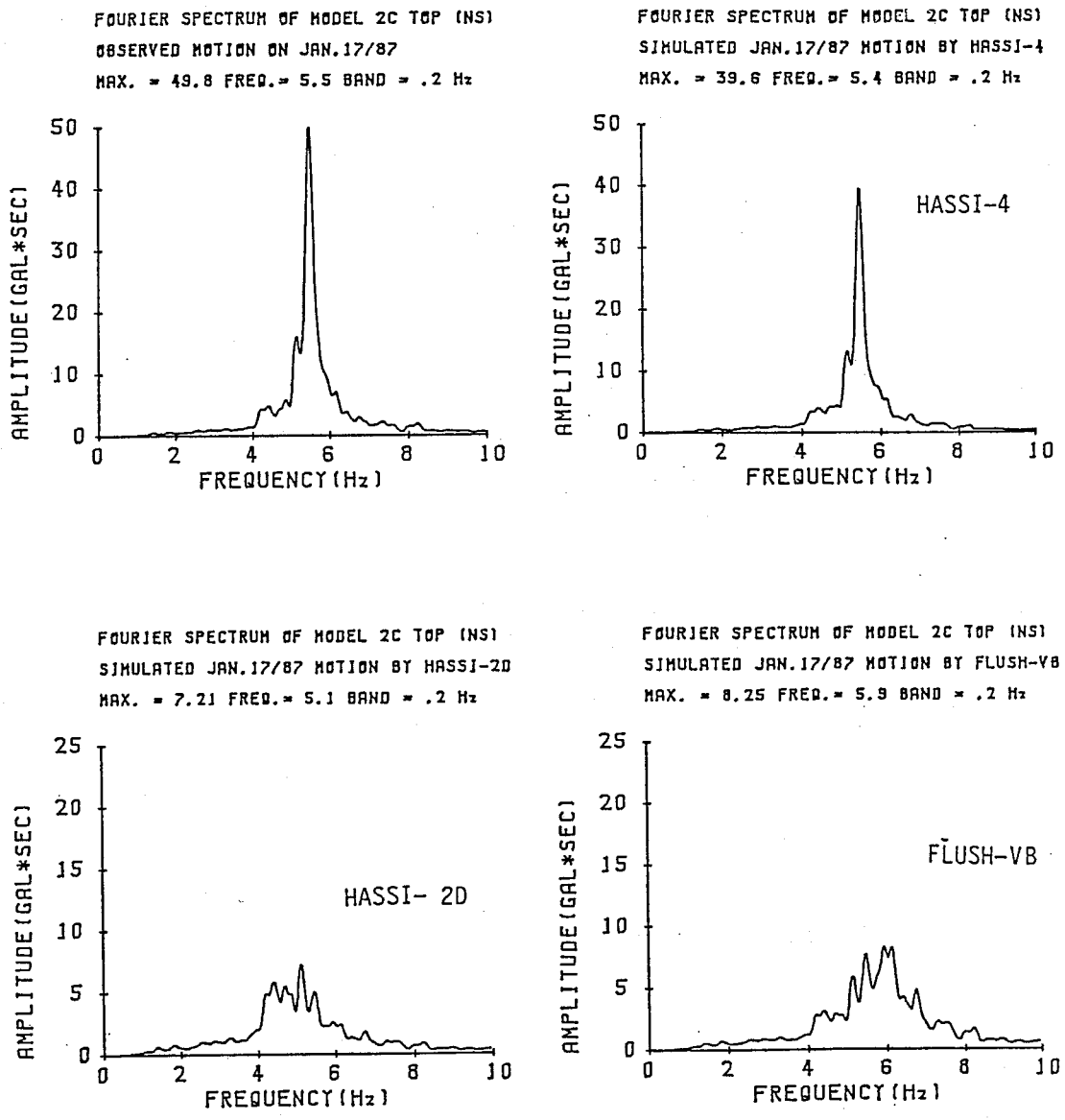

Figure 2.3.19 Comparison of the recorded and calculated response motions on Fourier spectra; (a), (b), (c) and (d) stands for the recorded motion, the calculated by HASSI-4, HASSI-2D and FLUSH-VB, respectively.

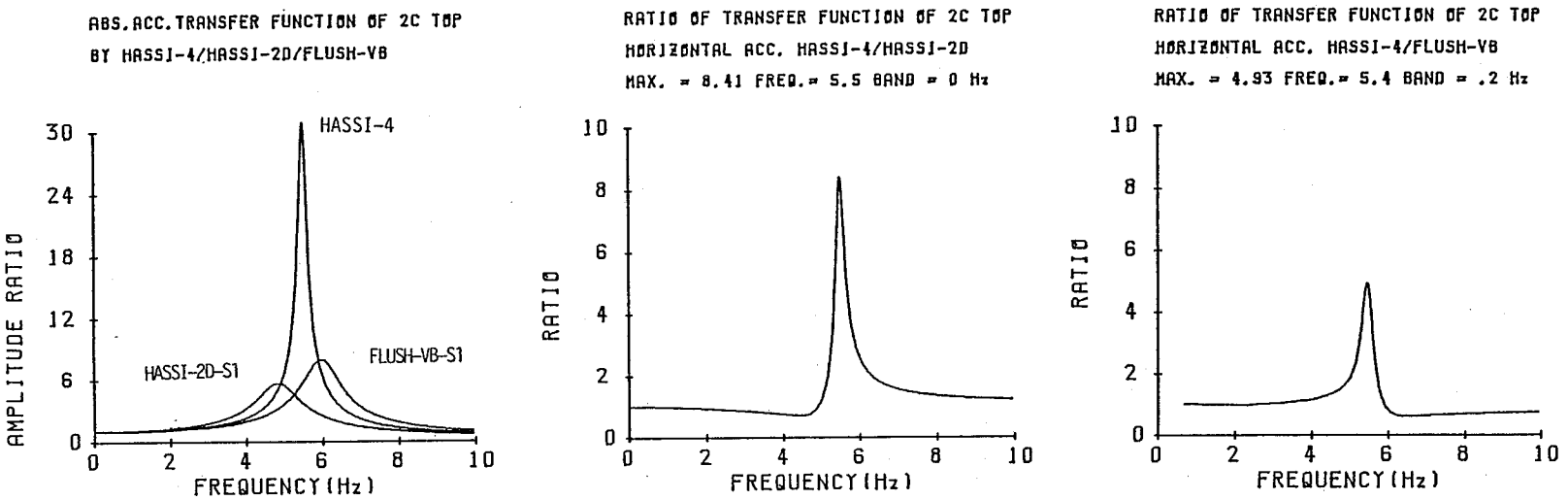

(a) Comparison between three codes

(b) Ratio; HASSI-4 vs. HASSI-2D

(c) Ratio; HASSI-4 vs. FLUSH-VB

Figure 2.3.20 Comparison of the absolute acceleration amplitude transfer functions of the roof top motions by HASSI-4, HASSI-2D, and FLUSH-VB

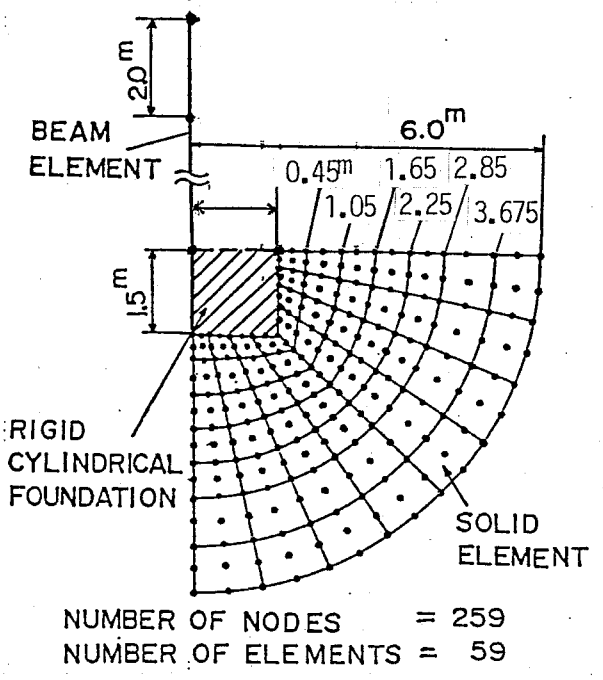

(a) Location of calculated points

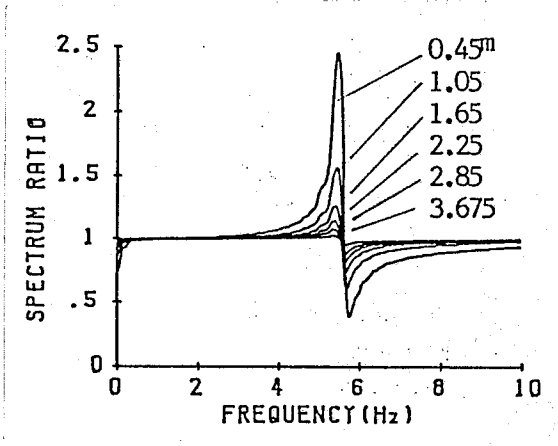

(b) Spectrum ratio in HASSI-4

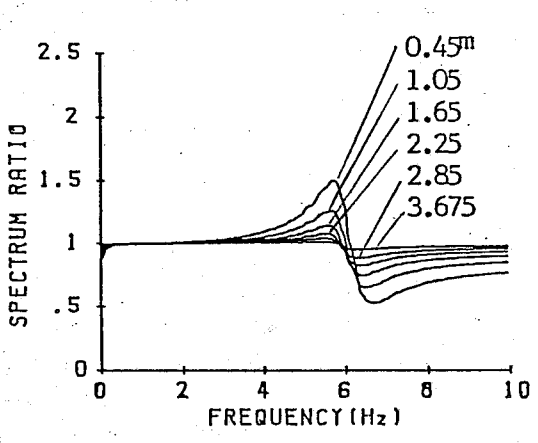

(c) Spectrum ratio in FLUSH-VB

Figure 2.3.21 Comparison of the absolute acceleration amplitude transfer functions(approximated) of the ground surface motions at the points shown in (a); (b) and (c) stand for HASSI-4 and FLUSH-VB, respectively.

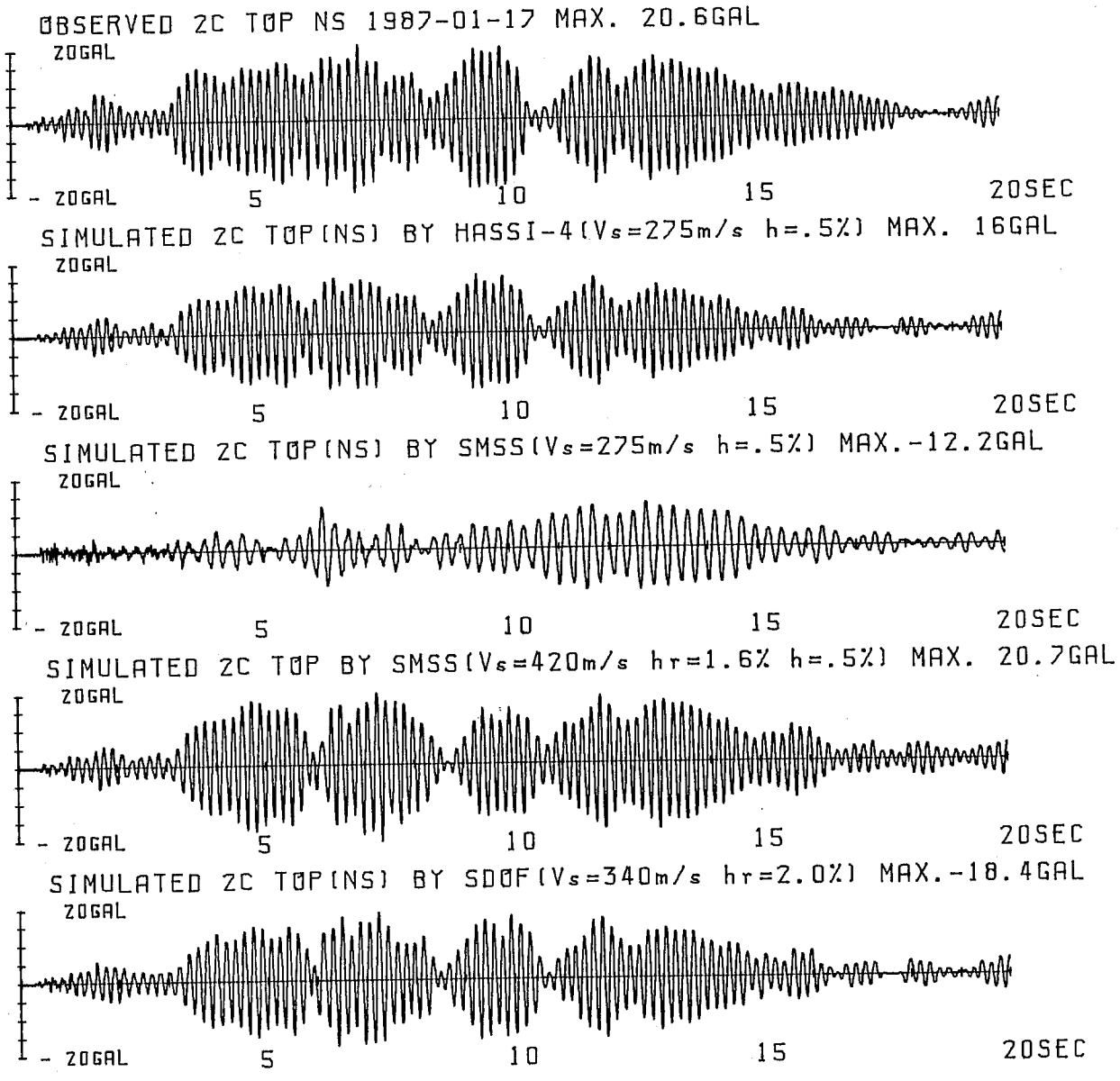

Figure 2.3.22 Simulation results by the stick model with soil springs of circular disc(the third and fourth) and single degree of freedom (rocking) model (the fifth); The first and the second time histories are for reference and the soil properties are shown in the parentheses).

2.4 CONCLUSIONS

The author tested a practical modeling concept to reasonably simulate the actual dam response recorded at an arch dam. The modeling concept consists of the three-dimensional finite dam elements with far-field impedances of infinite strips along the abutment which are constant for significant frequency range of the dam and foundation modes, with the reservoir water elements upstream and transmitting boundaries defined by impedance ratios at the water-water boundary and the water-gorge and bottom boundary, and frequency domain analysis scheme. Through the analysis, the author found the following significant conditions to be selected for successfully explaining the recorded response of the dam.

(1) The analytical model capable to represent the far-field boundary effect by an approximate impedance function along the dam abutment will give an acceptable response of the dam.

(2) When the dam was modeled with limited volume of foundation rock with fixed boundary, the dam response became very large when a reasonable value of material damping is used respectively for the dam and the foundation rock.

(3) The reservoir water was found to have suppressed the upstream-downstream response of the dam; however, this does not contribute to its antisymmetric mode of vibration.

(4) To obtain a good fit of the recorded motions of the dam, it was required to take the spatial variation of input ground motions into account. This fact suggests the need for observing reliable spatially varied input ground motions in the form of free-field motions.

The linear and non-linear three-dimensional soil-structure interaction analysis codes, HASSI-4 and HASSI-7, were tested for their validity by the correlation studies using the forced vibration data and earthquake response records of a small scale reactor building model. The soil properties needed for the prediction were those which have been obtained by in-situ and laboratory tests. Some ambiguity inherent in these soil properties affected the results; however, the properties used for reproducing the records remained within a reasonable range of the variation of soil properties actually observed.

From the predicted results of 1987 January 17th earthquake by the

three-dimensional analysis code, two-dimensional analyses, and the stick model with soil springs, the following SSI features were found;

(1) The transfer functions of the surface motions at a series of points located in the near-field soil region show a very rapid and sharp decay with distance from the side wall of the structure foundation in the case of the three-dimensional code, HASSI-4, whereas those transfer functions by the two-dimensional code, FLUSH-VB, shows slow and dispersive nature.

(2) In the two-dimensional analyses, the frequency shift was not so significant but the over damping is very serious resulting in an excessive underestimate of the response of the structure. The effective dampings in HASSI-2D and FLUSH-VB were estimated as 8.4 and 4.9 times that in HASSI-4, respectively.

(3) The total damping in the simulation by the three-dimensional code, HASSI-4, was estimated as about 2 %, whereas in the simulation by the two-dimensional codes, HASSI-2D and FLUSH-VB, corresponding damping was estimated as 9.8 % and 16.8 %, respectively.

(4) In the case of HASSI-2D, the over-damping can be explained by the inadequacy of converting the truly infinite half-space problem into the infinite strip problem. For the case of FLUSH-VB, the interpretation comparable to the above may not be appropriate, because we can neither distinguish between material damping and radiation damping nor give clear explanation of the mechanism of damping in this system. However, it may be pointed out that FLUSH-VB will give significant underestimate of the three-dimensional response of a truly three-dimensional structure.

Taking far stronger earthquake response records which were obtained during the 1987 December 17th earthquake and recorded the maximum acceleration of 301.2 gals at the roof top and 73.5 gals at the ground surface, the non-linear version, HASSI-7, was tested for its validity.

The coincidence of the calculated and observed response of the model structure are fair as a whole; however, the predicted maximum accelerations became smaller than the observed. This may be attributed to the high-cut nature usually found in the complex modulus method.

However, through the simulation, it was clearly shown that the strain levels of the free-field soil and the soil near the foundation structure are remarkably different and that the soil strongly affected by

the soil-structure interaction was limited to a fairly small region the radius of which was less than twice the radius of the structure. This also indicates that only the three-dimensional analysis can reproduce the rapidly decaying nature of the wave generated at the soil-structure interface of truly three-dimensional structures.

As already pointed out earlier by Luco and Hadjian(1974) and Wolf(1985), it is almost impossible to model a three-dimensional structure with two-dimensional modeling, and any two-dimensional model will significantly underestimate the true three-dimensional response by small shift in frequency and significant over-damping of the vibration system.

As a conclusion, it can be clearly stated that we should avoid to treat the soil-structure interaction phenomena of truly three-dimensional structures with two-dimensional modeling, in order not to underestimate the true response of three-dimensional structures.

CHAPTER 3. PROBLEMS IN ESTIMATING PEAK GROUND MOTIONS FOR USE IN SEISMIC DESIGN ANALYSIS

3.1 OBJECTIVES AND SCOPE

The ground motion parameter such as peak acceleration or peak velocity of ground motion time histories is one of the important factors in establishing the design ground motion time histories expected from design earthquakes at a particular site.

There are many arguments on the validity of empirical formulas to predict the peak ground motions, because they have been constructed from seismologically simple parameters like earthquake magnitude and distance parameters (e.g., epicentral distance or hypocentral distance or the distance to the fault). However, it is also true that we have relied upon some empirical formulas in various areas of engineering.

In most regions in Japan, earthquakes have been occurring both in the crust and the upper-most mantle and we have experience that those earthquakes which have occurred at intermediate depths scarcely caused significant damages even around their epicentral regions, whereas very shallow earthquakes of magnitude larger than medium size have caused strong ground motions and serious damages.

Therefore, such empirical formulas that will be used in our country for predicting peak ground motion parameters are desirable to at least take into account the influence of focal depth on the resultant peak values with some reasonable distance from the site to the earthquake source. And when a very shallow earthquake should occur, a severe ground motion and its consequence should be reasonably predicted, in contrast to damages caused by an earthquake of intermediate depth described by the type of empirical formula mentioned above.

Recent development of electronic technology and communication networks in highly populated cities has given increasing importance on the reliability of lifeline systems that include many types of underground structures such as tunnels and ducts. In the case of a buried structure extending over distance in the longitudinal direction, the relative displacement along the structure can cause axial stress and bending moment. Therefore, the new empirical formulas are also expected to provide the information regarding those peak ground motions which are meaningful for the structures extending over distance in longitudinal direction, to which the surface wave components or horizontally

propagating wave components rather than the vertically traveling body wave components are of primary concern.

In this regard, previous empirical formulas are reviewed and classified into some groups and discussed their adaptability to a Japanese strong motion data. A preferable type of formula is selected and new sets of empirical formulas for predicting both peak ground acceleration and velocity are proposed.

By using these formulas and combining the three-dimensional seismic sources of the Kanto area, the seismic hazard maps in the form of the iso-seismal maps of expected maximum accelerations and velocities for various exposure times are presented in order to provide a design data base applicable for both structures built on the ground and buried underground in the central Kanto area.

3.2 REVIEW OF EMPIRICAL FORMULAS FOR ESTIMATING PEAK GROUND MOTIONS

3.2.1 INTRODUCTION

In this chapter, available empirical formulas are reviewed first and discussed in terms of their characteristics through the test of their fitness for a Japanese strong motion data set carefully selected by the author. Then, a suitable form of skeleton curve is chosen to construct the empirical formulas to predict both peak ground acceleration and velocity of earthquakes occurring at various depths.

3.2.2 CLASSIFICATION OF EMPIRICAL FORMULAS

There are numerous empirical formulas proposed since the 1971 San Fernando Earthquake, however including those formulas proposed before the event, they could be classified into categories regarding the nature of the skeleton curve as follows;

(1) $A=a\cdot\exp(bM)(R+c)^{-n}$ (3.2.1)

(2) $A=a\cdot\exp(bM)R^{-n}\cdot\exp(-dR)$ (3.2.2)

(3) $A=a\cdot\exp(bM)[R+c_1\cdot\exp(c_2M)]^{-n}$ (3.2.3)

(4) $A=a\cdot\exp(bM)R^{-n}\cdot\exp[-d_1\cdot\exp(d_2M)\cdot R]$ (3.2.4)

where: A = peak acceleration

M = earthquake magnitude

R = distance measure

a,b,c,c_1,n,c_2,d,d_1 and d_2 = constant parameters

In these equations, the maximum acceleration is defined usually in gal or in fraction of percentage of the gravitational acceleration G. The earthquake magnitude is given mostly by surface magnitude M_S which is approximately equal to M_J the magnitude scale being used in Japan. In some equations this is defined in local magnitude M_L or in moment magnitude M_W which is, interrelated with the seismic moment M_O, which is almost equivalent to M_S if the value does not reach that of a great earthquake. R is defined as the distance parameter which takes various forms such as the closest distance from the site to the fault rupture surface, the closest distance to the surface projection of the fault, the traditional epicentral distance and the focal distance.

3.2.3 REVIEW OF EACH FORMULA

The representative past empirical formulas are briefly described below in the order of the categories described above. The notations of the variables are basically common with that previously described, however, additional explanation will be given when needed.

3.2.3.1 Type I curves - $A=a\cdot\exp(bM)(R+c)^{-n}$

Most of the past empirical formulas may be classified in this type; this type of formula does not consider the anelastic attenuation effects on the peak acceleration and only the geometrical attenuation is taken into account.

Donovan(1973) obtained the following relation from 550 worldwide strong motion records with peak acceleration greater than 10 gals including the data obtained in the event of 1971 San Fernando Earthquake;

$$A=1080\cdot\exp(0.5M)(R+25)^{-1.32} \qquad (3.2.5)$$

where A is peak acceleration in gals and R is the distance to the energy

center in km.

Ang and Newmark(1977) formulated the following formula using the specially selected data set presented by Page et al(1972);

$$A=1.35\cdot\exp(0.67M)(R+15)^{-1.75} \qquad (3.2.6)$$

where: A = maximum peak acceleration in fraction of G

R = the closest distance to the surface projection of the fault in km.

They used this formula for predicting the maximum peak acceleration of the ground motion on hard rock in the case of Diablo Canyon nuclear power plant seismic hazard analysis.

Katayama, T.(1974) showed for the average maximum acceleration of 330 records recorded on the ground of various soil classes;

$$A=203.3\cdot\exp(0.948M)(R+30)^{-1.637} \qquad (3.2.7)$$

and

$$A=9.60\cdot\exp(1.073M)D^{-1.290} \qquad (3.2.8)$$

where: A = average maximum peak acceleration, in gal

M = M_J

R = focal distance, in km

D = epicentral distance, in km.

The second equation by Katayama.T lacks a constant c in order to avoid division by zero when D becomes zero and should suppress the acceleration values in the near field. Similar type of curves have been given also by Orphal et al (1974), S.C. Liu (1972), and Saheki et al (1977).

Orphal et al(1974), based on the peak acceleration data reported by Wiggins(1964) which contained 27 observations of peak acceleration

recorded at the El Centro and Ferndale stations from earthquakes ranging from 4.1 to 7.0 with focal depths of earthquakes assumed to be 15 km, proposed the following formula in a more general form in which the closest distance to faults is replaced by the focal distance R in their regression analysis and the formula was tested for its validity with recorded strong motions in the 1971 San Fernando Earthquake;

$$A=0.66\cdot10^{0.40M}\cdot R^{-1.39} \quad \text{(st.dev. 1.99)} \qquad (3.2.9)$$

where A is in G.

They also suggested that epicentral accelerations of earthquake ground motions could reasonably be estimated by the relation, letting R be 15 km in the above formula as;

$$A_0=0.015\cdot10^{0.40M} \qquad (3.2.10)$$

where A is in G.

Saheki et al(1977) used 301 records larger than 50 gals recorded in the event of Japanese earthquakes of magnitude larger than 5.0 and focal depth shallower than 60 km and obtained;

$$A=28.5\cdot10^{0.207M}\cdot D^{-0.598} \quad \text{(1st class soil)} \qquad (3.2.11a)$$

$$A=13.2\cdot10^{0.330M}\cdot D^{-0.806} \quad \text{(2nd class soil)} \qquad (3.2.11b)$$

$$A=32.1\cdot10^{0.254M}\cdot D^{-0.757} \quad \text{(3rd class soil)} \qquad (3.2.11c)$$

and $$A=6.47\cdot10^{0.430M}\cdot D^{-0.977} \quad \text{(4th class soil)} \qquad (3.2.11d)$$

where: A = maximum acceleration in gal

D = epicentral distance in km.

3.2.3.2 Type II curves - $A=a\cdot\exp(bM)R^{-n}\cdot\exp(-dR)$

This type of formula contains anelastic attenuation term in the form of exp(-dR) in addition to the geometrical attenuation terms in the form similar to the previous types of curves, where d is a constant and R is a distance parameter.

Those formulas by Kanai et al(1969), Katayama, I.(1975) and Joyner et al (1981) are basically classified under this type though they differs a little with each other.

Kanai et al(1969) proposed a semi-empirical formula to predict maximum velocity at bed rock and as an extension of the formula showed the form to calculate corresponding maximum acceleration on bed rock with limiting condition of the corresponding period of ground motion giving maximum velocity.

Also, they showed the formula for predicting the maximum accelerations on ordinary ground by introducing an empirical amplification factor for surface layers and the fitness of their formula to strong motion records obtained in the Matsushiro area in Nagano Prefecture where earthquake swarms of magnitude less than 6.0 occurred during 1965-1970 and the strong motion records in the Western United States available at that time.

The formula to be applied to bed rock is

$$V_0=10^B \qquad (3.2.12)$$

where: $B=0.61M-P\log_{10}(X)+Q$

$P=1.66+3.6/X$; $Q=-0.631-1.83/X$

$T=0.02 - (10^{0.39M-1.70})$

$X=(D^2+H^2)^{1/2}$

and

$$A_0=(1/T)10^B \qquad (3.2.13)$$

where $B=0.61M-P\log_{10}(X)+Q$

$P=1.66+3.6/X$; $Q= 0.167-1.83/X$ (3.2.13b)

The formula to be applied to general surface ground is

$$A =[5/(T_g)^{1/2}]\cdot 10^B \qquad (3.2.14)$$

where: $B=0.61M-P\log_{10}(X)+Q$

$$P=1.66+3.6/X \quad ; \quad Q= 0.167-1.83/X$$

and T_g= predominant period of surface layer

Combined Kanai-Seed formula In order to estimate the maximum acceleration of the design ground motion on hard rocks, the author combined Kanai's formula for maximum velocity amplitude at bed rocks in eq.(3.2.12) with the predominant period of rock motions T_p given in Fig.7 of Seed et al(1969). The formula becomes similar to eq.(3.2.13) by replacing T with T_p as follows;

$$A_0=(1/T_p)10^B \qquad (3.2.15)$$

where: $B=0.61M-P\cdot\log_{10}(X)+Q$

$$P=1.66+3.6/X \; ; \; Q= 0.167-1.83/X$$

and $$T_p=(0.000512M-0.00143)(X+100)+0.02 \qquad (3.2.16)$$

This combined formula was first used in the seismic design of Ikata nuclear power plant and later called for convenience as the combined Kanai-Seed formula, in the licensing application documents of Ikata Nuclear Power Plant of Shikoku Electric Power Co., Ltd. submitted to the Advisory Committee for Reactor Safeguard of Science and Technology Agency.

This method of application of Kanai's empirical formula has become very popular in nuclear power plant design in Japan since then.

The predominant period T_p having been given in the form of a figure by Seed et al was later converted into functional form by some utility engineers as shown in eq.(3.2.16).

Joyner and Boore(1981) proposed the following formula using the data obtained in the North Western United States;

$$\log A=-1.02+0.249M-\log(r)-0.00255r \qquad (3.2.17)$$

where: $r = (d^2+7.3^2)^{1/2}$

M = moment magnitude (M_W) which is interrelated with the seismic moment M_0 by Kanamori and Anderson(1975)

d = the closest distance to the surface projection of the fault rupture, in km

3.2.3.3 Type III curves - $A=a\cdot\exp(bM)[R+c_1\cdot\exp(c_2M)]^{-n}$

The characteristic of this type lies in the magnitude dependent term $c_1\cdot\exp(c_2M)$, which is added in the geometrical attenuation term and contributes in suppressing the peak accelerations with the size of the earthquake source area for the entire range of distance.

Milne and Davenport(1969) proposed the following formula using recorded strong motions in Canada;

$$A=0.69\cdot\exp(1.64M)/[D^2+1.1\cdot\exp(1.1M)] \qquad (3.2.18)$$

where: A= maximum acceleration, in percent of G

D= epicentral distance, in km

Campbell(1981) derived his formulas using the data base collected from worldwide earthquakes with shallow rupture, the accuracy of the location of which is within 5 km in the distance to the fault rupture surface. His data base includes available published peak acceleration data recorded in the United States through at least March 1979 including most recent events such as the 1979 Imperial Valley(M_S=6.9) and selected data outside the United States, e.g. 1967 Coyna, India(M_S=6.5), 1972 Managua, Nicaragua(M_S=6.2), 1974 Lima, Peru(M_S=7.6) and so on. He proposed the following formulas for predicting near field accelerations (Campbell, 1981), and when the dependency of the near source peak accelerations was modulated artificially by adjusting the ratio of this term and the magnitude dependent term exp(bM), the formula was referred to as the one with constraint.

Without constraining the near field acceleration;

$$A=0.0159\cdot\exp(0.868M)[R+0.0606\cdot\exp(0.700M)]^{-1.09} \qquad (3.2.19)$$

With constraint of the near field acceleration;

$$A=0.0185\cdot\exp(1.28M)[R+0.147\cdot\exp(0.732M)]^{-1.75} \quad (3.2.20)$$

where A is the mean of two peak horizontal values of a recording in fraction of G. If an estimate of the maximum value is required, an additional factor of 1.13 should be applied to the predicted values. R is the closest distance to the fault rupture computed from either the surface expression of faulting or the distribution of after shocks. The data used are those with distances within 30 km for $M\leq 6.25$ and within 50 km for $M>6.25$. The condition of constraining the accelerations at the fault rupture surface as to be approximately independent of magnitude is accomplished by the condition;

$$c_2=b/n \text{ in } A=a\cdot\exp(bM)[R+c_1\cdot\exp(c_2M)]^{-n} \quad (3.2.21)$$

Campbell described that the residuals of regression was not changed regardless of inclusion of those data obtained at rock sites; however, those records obtained at the sites underlain by shallow soil deposit or extremely soft soils were excluded in the regression analysis because these data usually showed anomalous peak values.

In evaluating his formulas, care must be exercised in the assumption of data weights used. Namely, each data point was multiplied with a weight which was designated to make every set of data within a selected distance range have the same weight over the whole data set. This data weight scheme seems to strongly affect the contribution of the near field data in the regression analysis.

Katayama, I.(1985) derived the following formula(Type I) by using the data set consisting of processed peak acceleration data that have been collected from the corrected strong motion accelerograms published by the World Data Center A and the peak ground motion list published by Seismic Load Research Group of Kyoto university(SLG,1984). The scheme of the data processing and the contents of the data base are similar to the current Japanese strong motion data set which will be described in detail later, except that there is some difference in the standard for rejecting records and the choice of two horizontal peak accelerations from each record.

The skeleton curve used here is basically the same as that of Campbell (1981); however the closest distance to the surface of the fault rupture as used by Campbell was replaced by the epicentral distance. The

following curve with standard deviation of 1.78 was proposed as the best result among available types of curves obtained through regression analysis, under the condition that any contribution of focal depth on the resultant peak accelerations were neglected;

Katayama Type I curve

$$A=0.0302\cdot\exp(1.28M)[D+0.300\cdot\exp(0.752M)]^{-1.513}\cdot(1.78)^{y} \quad (3.2.22)$$

where A is in G; when y=0 it gives the mean value and with y=1 it gives the mean plus one standard deviation value.

3.2.3.4 Type IV curves - $A=a\cdot\exp(bM)R^{-n}\cdot\exp[-d_1\cdot\exp(d_2M)\cdot R]$

This type of curve modulates the anelastic attenuation term exp(-dR) of the previous Type II curves to the form dependent on earthquake magnitude by replacing d with $d_1\cdot\exp(d_2M)$.

Nakamura et al(1984) derived an equation using strong motion records obtained at the ground surface by SMAC-B_2 strong motion accelerographs in implicit form as;

$$\log_{10}A=0.168M-0.5\log(D+H)-0.0551\ 10^{-0.156M}\cdot D+1.86 \quad (3.2.23)$$

where: A = maximum acceleration, in gal

D = epicentral distance, in km

H = focal depth, in km

Katayama,I.(1985) also derived, using the same data base used for constructing the Katayama Type I curve previously described, the following Type II curve with standard deviation of 1.84 as the most promising form of the attenuation curve that can take into account an appropriate effect of focal depth on the predicted peak accelerations by following the skeleton curve of Nakamura et al(1984);

Katayama Type II curve

$$A=10^{P}\cdot(1.84)^{y}$$

$$\log_{10}P=0.180M-0.193\ \log(D+H)-0.0558\cdot10^{-0.157M}D-1.333 \quad (3.2.24)$$

where A is in G, and when y=0 it gives the mean value and with y=1 it gives the mean plus one standard deviation value.

3.2.4 ANALYSIS OF REPRESENTATIVE FORMULAS

The author has already recommended a suitable form of attenuation curve for Japanese seismic environment(I. Katayama: 1985), however it may give us a more general information useful in constructing such empirical formulas that is fundamentally suitable for the Japanese seismic environment to test the characteristics of the past empirical formulas with the Japanese strong motion data. From this reason, first a Japanese strong motion data set is constructed and then the data set is directly applied to each of the preceding formulas in its original form. The fit of each formula to the Japanese data is displayed by the mean ratio of observed and calculated peak accelerations(O/C) and the standard deviation from the mean. Finally, through these values and the comparison of the predicted value and the data in terms of each parameter included in the attenuation curve, each empirical formula is evaluated for its native adaptability to the Japanese strong motion data.

3.2.4.1 Strong motion data base

A new data set is prepared for this study from two strong motion data bases; these are the Japanese strong motion corrected accelerograms compiled by World Data Center A (Mori et al,1981) and that by the Design Seismic Load Research Group(SLG, 1984).

The former strong motion accelerograms published in two series of data sets by the World Data Center A contains a total number of 177 component digitized records of 75 earthquakes which occurred in and around the Japan Island during 1956 through 1978. These accelerograms were recorded mostly by SMAC type strong motion accelerographs and were compiled separately in two volumes, the uncorrected digitized records (Volume 1) and the corrected digitized records (Volume 2), respectively. The uncorrected records of this data base have been adjusted for distortions of tracing due to initial pen offset and arc, and processed with base line correction. On the other hand, the corrected accelerograms were further processed by band pass filter with frequency ranges of 0.05-0.1 to 23 Hz the lowest end of which depends on the situation of the individual records using the instrument frequency characteristics which

were experimentally determined by the organization.

The latter strong motion record data base that have been collected by SLG contains 400 components of earthquake records that occurred from 1962 through 1983, recorded mostly by three types of accelerographs; SMAC-A, SMAC-B_2 and SMAC-M accelerographs at stations having been maintained by the Port and Harbour Research Institute, Ministry of Transport, and the Public Works Research Institute, Ministry of Construction. The digitized records compiled in this data base have been processed for both baseline and instrument correction using the so-called Goto-Kameda's filtering method (Goto et al,1978a and 1978b), so that all the resultant time histories are valid within an identical frequency range of 0.15-10Hz.

To obtain as many peak ground motion data as possible and to have the resultant data set with a common band width, the data from the above two data bases were processed as follows.

Since the correction scheme of the two data bases are quite different with each other from the arc and base line correction to the instrument correction, only adjustment of valid frequency range were thought practically justifiable for the purpose of improving the consistency in the data collected from the above two data bases. Because the frequency range of the latter data base was narrower than the former, the corrected records of the former data base were processed with the band-pass filter the lowest and the highest cut-off frequency of which were chosen respectively to the 0.15 Hz and 10 Hz which are the corresponding valid frequency range for both data bases. Table 3.2.1 demonstrates some examples of the change of peak values of the records in the former data base due to the filtering described above.

The information regarding earthquake magnitudes and locations of the latter data base were given based on what the Japan Meteorological Agency had given periodically in published earthquake catalogues (JMA catalogues).

The location data of earthquakes published in the JMA catalogues are not necessarily accurate but generally thought to be a kind of standardized results dependent on the routine location method that was employed by the agency, and the focal depths have been given in every 10 km for the earthquakes during the whole period of both data bases concerned. This degree of accuracy of the focal depth sometimes gives not a small problem in performing certain detailed analysis using these data. On the other hand, the earthquakes contained in the former data base have been

determined for their focal mechanisms based on worldwide data including recorded seismograms obtained at the networks of microearthquake observatories maintained by universities in Japan. In determining the focal mechanism of an earthquake, the focal depth is one of the parameter that must have the best available accuracy. On this point, in most cases, the JMA catalogue will not give us focal depths which can be used for determining the focal mechanism of earthquakes. Therefore, those earthquake data especially of focal depths given in the former data base are judged basically more accurate than those given in the latter data based of the JMA data.

Considering the above, the records commonly included in the above two data bases were represented by the data in the former data base. Those records that were without a soil classification, or were obtained on deep alluvial deposit (Class 4 soil), or lack the necessary information on the earthquake, or give an apparently anomalous peak values were excluded.

The final data set was thus obtained and contains 125 horizontal component time histories of acceleration, velocity and displacement of 52 earthquakes obtained with epicentral distance less than 200km and focal depth shallower than 100km and recorded on the ground surface classified by soil type 1 to 3, and was named as the "Non-filtered data set(NONFSEL)". Table 3.2.2(a) shows the distribution of records in terms of magnitude and epicentral distance and Table 3.2.2(b) gives the statistics on the numbers by soil condition. The peak acceleration and velocity of each record included in the data set is shown in Table 3.2.3 with relevant data needed for the subsequent analysis.

3.2.4.2 Fit in original form to the Japanese strong motion data

All empirical formulas previously shown were first tested their fit in original forms directly with the peak acceleration data in Table 3.2.3. In applying each formula, the distance parameters that had been specifically defined in each formula could not always be followed but either the epicentral distance or the hypocentral distance and the focal depth was used. The total number of peak accelerations effectively used was 125.

The results are shown in terms of the mean O/C value and the standard deviation around the mean in Table 3.2.4.

In evaluating the fit of the formulas derived using US data, the

mean O/C value is of the order of 1.5, which is considered not unusual leading to the devaluation of the formulas for the following reason; (1) the peak accelerations used here are those obtained for ordinary soil ground and (2) since the 55 ordinary soil sites in the Kanto region showed the mean acceleration amplification factor of 1.5 to the stiff soil layer having a shear wave velocity of 300 to 500 m/s (TEPSCO, 1987) and the ordinary soil sites in the western United States are considered largely comparable to the above stiff layer, the mean O/C value of the order of 1.5 might not be unusual in case of those empirical formulas derived by using the US data. However, in case of the Japanese empirical formulas, the above bias may not be allowable except when a formula was derived from only the data recorded on the stiff soil layer such as described above.

Therefore, the mean O/C value is not always the critical factor in evaluating the fundamental adaptability of each formula to the Japanese data base. On the contrary, the standard deviation from the mean O/C and the characteristic of the deviation with the value of the parameters that constitute the formula is considered more important. If the standard deviation is small and there is no irregular deviation of data with the parameters involved, it will be possible that the skeleton curve will reflect appropriately the Japanese data as a whole with new parameters determined by regression analysis using the data and will give a smaller mean O/C value.

Each figure of Figs. 3.2.1 to 3.2.13 shows the characteristic shape of each original empirical formula with the peak accelerations of the Japanese non-filtered data(NONFSEL) plotted, overall comparison on observation and calculation (O/C) curve, O/C curves in terms of magnitude, epicentral distance or hypocentral distance and/or focal depth dependent on parameters involved in the formula.

First from the table, the following points can be pointed out:

1) Donovan's skeleton curve among Type I curves is better than those by Ang and Newmark as well as by Orphal et al. T.Katayama's formula with (R+c) is fundamentally the same as Donovan's.

2) Type II curves are probably inadequate because of large O/C and standard deviation value.

3) Campbell's formula is essentially the same as the one by Milne and Davenport and will be as good as the Type I curve. This is evident from the extent of fit that has been obtained in the curve by the

I.Katayama formula(1985), where almost similar data base was used in obtaining the formula.

4) Type IV curve by Nakamura et al is good to the extent of fit obtained for the above Type III curves. Similarly this is evident from the extent of fit that has been obtained for the curve, Katayama Type II. This type of curve is among the curves previously shown only for the curve that includes the term focal depth, giving the same degree of fit as the Type III curve.

Referring to Figures 3.2.1 through 3.2.13, the above general feature of the curves can be described in more detail:

1) Among the Type I curves, the skeleton that has the term (R+c) as the geometrical attenuation term as represented by Donovan's curve seems to result in a fairly good fit to the Japanese data, whereas the curves that lack the term c or use only D seems to be incapable of fitting the Japanese data. Moreover, it seems that both curves by T. Katayama(R+c) and Nakamura, may have an obvious bias. In fact, the data used by them were not corrected for the frequency characteristics of the seismographs.

2) The Type II curves seem unsuitable in view of the large mean O/C with the large standard deviations and a peculiar trend found in the O/C curves with magnitude and hypocentral distance.

3) The Milne and Davenport's Type III curves seems inadequate for the Japanese data because of the term D^2. The others except Campbell's constrained curve shows favorable fit with both parameters of magnitude and epicentral distance. The curve by Campbell(unconstraint) gives almost twice the O/C value of that given by Katayama, I.(1985) but the standard deviations of both are almost the same. This indicates that this type of curve may have the capability to represent appropriately the Japanese strong motion data, even if it lacks the focal depth term. The Katayama Type I curve(1985) was constructed by using the maximum peak of two horizontal peaks of each record which is almost common with current data. Therefore, it is possible that this formula can be one solution in its present form. In fact, the fit of the curve to the maximum of two horizontal peak accelerations showed the mean O/c and the standard deviation of 1.04 and 1.49, respectively. The ratio of this O/C and the value of 0.88 in Table 3.2.4 becomes 1.2 and this value is comparable to the average ratio of the two peak accelerations of each record.

4) Type IV curves are essentially one skeleton curve, in which Nakamura et al controlled the coefficient of $\log_{10}(D+H)$ which represent the slope of the geometrical attenuation with somewhat special form as -0.5 considering the attenuation law of surface wave component, because their data contained mostly the data obtained for far distant earthquakes. From this reason, the fit of the curve with epicentral distance and with the focal depth are poor as a whole, if compared with the case of the Katayama Type II curve in which the coefficient of $\log_{10}(D+H)$ was determined from the data used and does not have a particular function to attenuate a particular wave component. From a similar situation as described in 3) above, the Katayama Type II curve also has a probable solution for the maximum acceleration data of the current Japanese strong motion data. In this case, the similar mean O/C and standard deviation becomes 0.95 and 1.48, respectively. The ratio of this O/C and the value of 0.80 in Table 3.2.4 becomes also 1.2; this value is again comparable to the average ratio of the two peak accelerations of each record.

3.2.5 CONCLUSION

As a conclusion of the above analysis, the skeleton curves of the Type III or the Type IV can be a candidate formula to construct some reasonable formula appropriate for the Japanese data. The data contains earthquakes having focal depths less than 80 km and the above two types of curve showed almost the same level of fit to the Japanese data regardless of the number of terms included. If so and if it is desirable to include the focal depth as a term in the empirical formula, the last Type IV curve can be said to be the best among them.

3.2.6 REFERENCES

(1) Donovan, Neville C., A Statistical evaluation of strong motion data including the February 9, 1971 San Fernando Earthquake, 5th World conference on Earthquake Engineering, Rome, Italy, 1973.

(2) Ang, A. H.-S. and Newmark, N. M., A Probabilistic Seismic Safety Assessment of the Diablo Canyon Site, California, prepared for ACRS, U.S. NRC, 1977.

(3) Page, Robert A., David M. Boor, William B. Joyner,and Henry W. Coulter, Ground Motion Values for Use in the Seismic Design of the Trans-Alaskan Pipeline System, Geological Survey Circular 672, U.S.

Geological Survey, U.S. Department of the Interior, 1972.

(4) Katayama, Tsuneo, Statistical Analysis of Peak ground Accelerations of Recorded Earthquake Ground Motions, Seisan Kenkyu, Vol.26, No.1, pp.18-20, 1974.

(5) Orphal, D. L. and J. A. Lahoud, Prediction of peak ground motion from earthquakes, Bulletin of the Seismological Society of America, Vol.64, No.5, pp.1563-1574, October 1974.

(6) Saheki et al, Characteristics of strong motion accelerograms obtained on the ground in Japan, Proceedings of the annual meeting on Japan Society of Civil Engineers, Vol.1, 1977.

(7) Kanai, Kiyoshi, Kintaro Hirano and Shizuyo Yoshizawa, Observation of Strong Earthquake Motions in Matsushiro Area. Part 1. (Empirical Formulae of Strong earthquake Motions), Bulletin of the Earthquake Research Institute, Vol.44, pp.1269-1296, 1966.

(8) Kanai, Kiyoshi, Katsuyoshi Yamabe, Masayuki Sawada and Shigeru Shimosaka, On the results of investigation of Los Angeles Earthquake, 8th Symposium on Natural Disaster Science, 69, October 1971.

(9) Shikoku Electric Power Company, On the design earthquake and design time hitories, Reference Documents for Licensing Application Documents for Construction Permit of Ikata Nuclear Power Plant Unit 1, B1-7, Subcommittee No.86 of Advisory Committee for Reactor Safegurd, Japan AEC, pp. 20-22, 1972(in Japanese).

(10) Seed, H. Bolton, I.M. Idriss and Fred W. Kiefer, Characteristics of rock motions during earthquakes, Journal of the Soil Mechanics and Foundations Division, Proceeding of the American Society of Civil engineers, SM 5, September 1969.

(11) Joyner, William B. and David B. Boor, Peak acceleration and velocity from strong-motion records including records from 1979 Imperial valley, California, Earthquake, Bulletin of the Seismological Society of America, Vol.71, No.6, pp.2011-2038, December 1981.

(12) Milne, W. G. and A. G. Davenport, Distribution of earthquake risk in Canada, Bulletin of the Seismological Society of America, Vol.59, pp.729-754, April 1969.

(13) Campbell, K. W., Near-source Attenuation of Peak Horizontal Acceler-

ation, BSSA, Vol.71, No.6, pp.2039-2070, 1981.

(14) Katayama, I., Microzoning of the central Kantou area considering ground motion intensity on practical design base layer, Proceedings of the Trilateral Seminar-Workshop on Lifeline Earthquake Engineering, pp. 135-152, Taipei, Taiwan, November 1985.

(15) Nakamura, Y. and Tomita, K., Empirical Formula for Estimating Maximum Ground Motion Acceleration, Abstr. Ann. Mt., JSCE, Vol. 1, 1984 (in Japanese).

(16) Katayama, I., A Model for microzoning of the central Kanto area considering ground motion intensity on practical design base layer, Proc. of the seventh Japan Earthquake Engineering Symposium, 16, pp. 91-96, Dec., 1986.

(17) Mori, A. W. and C. B. Crouse, Strong Motion Data From Japanese Earthquakes, World Data Center A, REPORT SE-29, NOAA, 1981.

(18) Kameda, H. and Sugito, S., Corrected and Integrated Earthquake Motion Accelerograms (Graphical Information), Revised Edition, Design Seismic Load Research Group, Department of Civil Engineering, Department of Transportation Engineering, Kyoto University, July 1984 (in Japanese).

Table 3.2.1 Change of peak ground acceleration by filtering

Event & site	Component	WDC. A original		WDC. A filtered		S. L. G. Data	
1970/04/01	Acceleration	189. 7	161. 8	190. 2	162. 6	170. 6	152. 7
M=5. 8 H=75	Velocity	4. 4	3. 3	4. 4	3. 3	5. 6	4. 5
TH014 S=1	Displacement	0. 3	0. 3	0. 3	0. 3	1. 0	0. 6
1973/06/17	Acceleration	200. 9	126. 9	199. 8	127. 7	186. 8	135. 0
M=7. 4 H=41	Velocity	27. 5	15. 7	26. 8	15. 1	26. 7	15. 6
HK004 S=2	Displacement	6. 4	4. 6	6. 1	2. 6	6. 2	2. 8

Table 3.2.2(a) Contents of the Japanese strong motion data used

Magnitude	Epicentral distance (km)						
	0-19	20-39	40-59	60-99	100-139	140-200	Sum
4. 0 - 4. 9	4	2	0	2	0	0	8
5. 0 - 5. 9	11	10	4	8	0	0	33
6. 0 - 6. 9	0	12	14	16	10	0	52
7. 0 - 7. 4	0	0	0	8	4	10	22
7. 5 - 7. 9	0	0	0	4	2	4	10
Sum	15	24	18	38	16	14	125

Table 3.2.2(b) Soil classification and the data

Soil condition	Number
1st class	20
2nd class	38
3rd class	67
Sum	125

Table 3.2.3 The peak acceleration and velocity data used for regfression analysis (Non-filtered record; NONFSEL)

Date of Event	M	H (km)	Observation Site	Epic. Dist. (km)	S C	Max. Acc. (gal)		Max. Vel. (kine)	
						Comp 1	Comp 2	Comp1	Comp 2
1963/08/04 20:43	5.1	39	KT014	35.0	2	.0768	.0700	4.3	2.7
1966/04/05 17:51	5.4	4	CB020	8.0	3	.2132	.0000	8.4	0.0
1966/04/05 17:51	5.4	4	(2)	4.0	2	.3989	.2571	21.1	11.1
1966/04/05 17:51	5.4	4	(3)	3.0	2	.2775	.2634	20.4	17.3
1966/04/17 10:22	4.7	6	(2)	4.0	2	.2511	.1023	7.3	3.2
1968/04/01 09:42	7.5	37	KS002	60.0	3	.2809	.2312	27.3	16.5
1968/04/01 09:42	7.5	37	SK006	80.0	3	.2020	.1889	19.9	13.3
1968/05/16 09:48	7.9	20	HK013	159.0	3	.0972	.0722	5.8	5.4
1968/05/16 09:48	7.9	20	TH014	187.0	1	.1609	.1445	6.1	5.3
1968/ 5/16 19:39	7.4	20	AOMORI	193.0	3	.1006	.0824	9.8	9.2
1968/05/16 19:39	7.4	20	HK013	75.0	3	.0834	.0625	5.2	3.8
1968/05/23 04:29	6.3	50	TH014	78.0	1	.0850	.0760	2.3	1.6
1968/06/12 22:42	7.2	31	TH014	81.0	1	.1606	.1365	6.0	5.0
1968/07/01 19:45	6.1	68	TK056	58.0	3	.1323	.0835	8.8	7.6
1968/07/05 20:28	6.4	44	TH005	62.0	3	.0599	.0372	4.8	2.7
1968/08/07 17:00	5.7	68	HK004	32.0	2	.0886	.0498	5.5	3.1
1968/10/08 09:50	5.3	73	KT004	38.0	3	.0758	.0342	3.8	1.7
1968/11/14 03:42	6.0	40	TH014	83.0	1	.0845	.0558	2.2	1.3
1969/04/21 16:19	6.5	39	KS002	43.0	3	.1136	.0896	6.2	5.8
1969/09/09 14:15	6.6	29	AC017	101.0	3	.0795	.0552	5.6	4.4
1970/ 1/21 2:33	6.7	25	CHIYODA BRIDGE	87.9	3	.1544	.1149	10.9	7.8
1970/01/21 02:33	6.7	25	HK013	46.0	3	.1375	.1329	6.9	6.9
1970/04/01 23:23	5.8	75	TH014	17.0	1	.1641	.1424	4.4	3.4
1970/07/26 07:41	6.7	47	KS002	21.0	3	.1393	.1280	13.4	8.7
1970/07/26 16:10	6.1	47	KS002	21.0	3	.0638	.0607	3.4	2.8
1970/10/16 14:26	6.2	5	YUUHEI BRIDGE	24.1	3	.2496	.1604	12.7	9.2
1970/10/16 14:26	6.2	5	YUUHEI BRIDGE	24.1	3	.2051	.1964	13.1	10.5
1971/ 1/ 5 6: 9	6.1	44	KINUURA	54.2	3	.0914	.0894	9.5	6.7
1971/ 1/ 5 6: 9	6.1	44	TOYOHAMA BRIDGE	42.3	3	.1987	.1451	8.6	5.7
1971/01/05 06:09	6.1	44	KK026	64.0	3	.1060	.0914	6.9	6.2
1971/02/26 04:27	5.5	37	CB030	27.0	2	.1523	.1430	8.4	6.0
1971/ 7/23 7: 7	5.3	10	SAKAIGAWA BRIDGE	16.3	1	.1765	.1016	6.5	4.1
1971/08/02 16:25	7.0	45	HK004	196.0	2	.0894	.0785	7.0	6.8
1971/10/11 19:16	5.2	40	KT050	12.0	2	.1652	.0507	6.8	2.0
1972/05/11 09:45	5.8	63	HK004	33.0	2	.1382	.0835	6.0	5.6
1972/10/26 22: 2	4.3	10	OCHIAI BRIDGE	10.6	3	.1486	.0680	5.4	2.3
1973/ 3/27 11: 8	4.9	60	KANNONZAKI	34.0	1	.1173	.0497	6.3	2.2
1973/06/17 12:55	7.4	41	HK004	112.0	2	.1832	.1353	27.0	15.3
1973/11/19 22:02	6.4	56	TH033	107.0	3	.0631	.0526	5.2	4.3
1974/03/03 13:50	6.1	49	KT036	39.0	2	.1111	.0393	10.5	5.2
1974/07/08 14:45	6.3	45	KT036	73.0	2	.0668	.0476	3.5	3.3
1974/09/04 18:20	5.6	52	TH029	42.0	2	.0717	.0711	3.9	3.1
1974/11/16 8:32	6.1	44	P.W.R.I KASHIMA	55.0	3	.1737	.1661	12.3	11.6
1974/11/16 08:32	6.1	44	KT036	38.0	2	.0866	.0736	7.2	5.9

Table 3.2.3 (Continued)

Date of Event	M	H (km)	Observation Site	Epic. Dist. (km)	S C	Max. Acc. (gal)		Max. Vel. (kine)	
						Comp 1	Comp 2	Comp1	Comp 2
1975/04/21 02:35	6.4	12	KSO14	41.0	2	.1054	.0831	3.4	3.0
1978/ 1/14 12:24	7.0	5	SHIMIZU-MIHO	71.4	2	.0944	.0517	11.4	6.8
1978/ 1/14 12:24	7.0	5	YAMASHITA-HEN	80.9	3	.0640	.0554	7.2	4.6
1978/ 1/15 7:31	5.8	20	SHIMIZU-MIHO	41.0	3	.0565	.0241	5.5	2.1
1978/ 2/20 13:37	6.7	50	KAIHOKU BRIDGE	85.8	1	.1742	.0990	8.0	6.1
1978/ 6/12 17:14	7.4	40	TAIRA BRIDGE	165.4	3	.0967	.0841	15.5	12.9
1978/ 6/12 17:14	7.4	40	ONAHAMA	175.8	3	.0592	.0574	7.5	6.3
1982/ 3/ 6 19:16	5.3	30	HOSOSHIMA-S	70.0	3	.0498	.0319	2.7	2.1
1982/ 3/ 7 8:14	5.5	60	KASHIMA-ZOKAN-S	61.0	3	.0644	.0344	2.2	1.5
1982/ 4/19 11:25	4.7	50	KAWASAKI-DAIGO	66.0	3	.0289	.0235	0.9	0.6
1982/ 6/ 1 5:13	6.1	40	OFUNATO-BOCHI	63.0	1	.0545	.0290	2.9	1.4
1982/ 6/ 1 5:13	6.1	40	MIYAKO-S	110.0	1	.0548	.0471	2.1	1.4
1982/ 7/23 23:23	7.0	30	KASHIMA-ZOKAN-S	118.0	3	.0876	.0827	5.1	4.9
1982/ 8/12 13:33	5.7	30	YAMASHITA-HEN	64.0	3	.0432	.0238	3.4	2.4
1982/ 8/23 14:50	5.3	80	SHIOGAMA-KOJYO	79.0	3	.0557	.0218	3.7	2.9
1983/ 5/26 12: 2	7.7	14	AKITA-S	107.0	2	.2311	.2181	28.9	26.5
1983/ 6/ 9 21:49	6.1	23	AKITA-S	113.0	2	.0507	.0461	5.1	4.1
1983/ 6/ 9 22: 4	6.0	14	AKITA-S	115.0	2	.0498	.0406	2.4	2.0
1983/ 6/21 15:26	7.1	6	AOMORI-S	160.0	3	.0742	.0602	8.8	7.0

Table 3.2.4 Fit of original empirical formulas with Japanese Data

Reference	Proposed Empirical Formula	(O/C) av.	(O/C) σ
Type I curves Donovan (1973)	$A=1080\cdot\exp(0.5M)(R+25)^{-1.32}$ (gal)	1.52	1.59
Ang and Newmark (1977)	$A=1.35\cdot\exp(0.67M)(D+15)^{-1.75}$ (G)	1.79	1.90
Katayama, T. (1974)	$A=203.3\cdot\exp(0.948M)(R+30)^{-1.637}$ (gal)	2.32	1.71
	$A=9.60\cdot\exp(1.073M)D^{-1.290}$ (gal)	1.81	1.87
Orphal et al (1974)	$A=0.66\cdot10^{0.4M}\cdot R^{-1.39}$ (G)	3.02	2.44
Type II curves Kanai-Seed Combination	$A0=(1/Tp)\cdot10^{B}$ (gal) $Tp=(0.000512M-0.00143)(X+100)+0.02$ (After Seed et al, 1968) $B=0.61M-P\log_{10}X+Q$; $X=(D^2+H^2)^{1/2}$ $P=1.66+3.6/X$; $Q=0.167-1.83/X$	4.80	2.00
Joyner and Boore (1981)	$\log_{10}A=-1.02+0.249M-\log_{10}(r)-0.00255\cdot r$ (G) $r=(D^2+7.3^2)^{1/2}$	3.41	2.09
Type III curves Milne and Davenport (1969)	$A=0.69\cdot\exp(1.64M)/(D^2+1.1\cdot\exp(1.1M))$ (G)	2.06	1.88
Campbell (1981)	$A=0.0159\cdot\exp(0.868M)\cdot(D+0.0606\cdot\exp(0.700M))^{-1.09}$ (G)	1.82	1.62
	$A=0.0185\cdot\exp(1.28M)\cdot(D+0.147\cdot\exp(0.732M))^{-1.75}$ (G)	2.35	1.85
Katayama, I. (1985) (Type I)	$A=0.0302\cdot\exp(1.281M)\cdot(D+0.300\cdot\exp(0.752M))^{-1.513}$ (G)	0.88	1.58
Type IV curves Nakamura et al (1984)	$\log_{10}A=0.168M-0.50\cdot\log_{10}(D+H)$ $-0.0551\cdot D\cdot10^{-0.156M}+1.86$ (gal)	2.36	1.73
Katayama, I. (1985) (Type II)	$\log_{10}A=0.180M-0.193\cdot\log_{10}(D+H)$ $-0.0558\cdot D\cdot10^{-0.157M}-1.333$ (G)	0.80	1.59

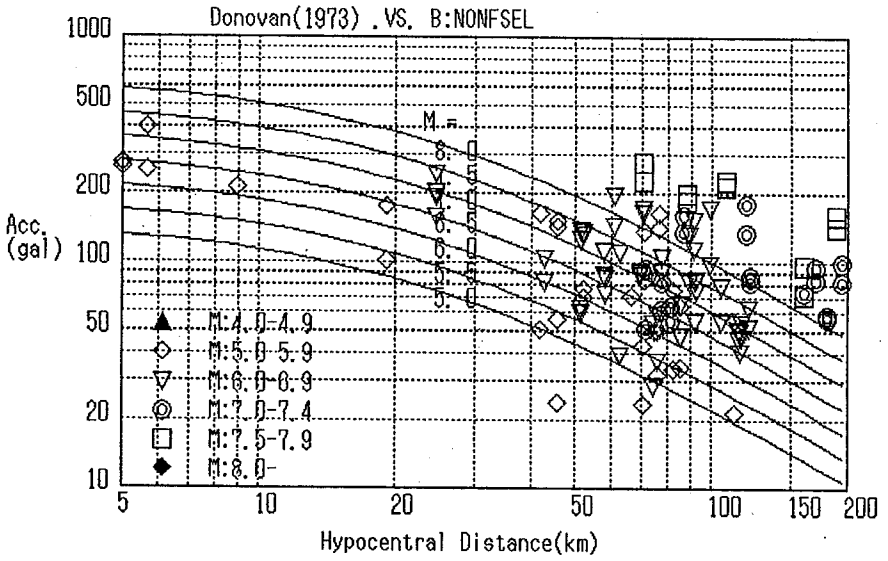

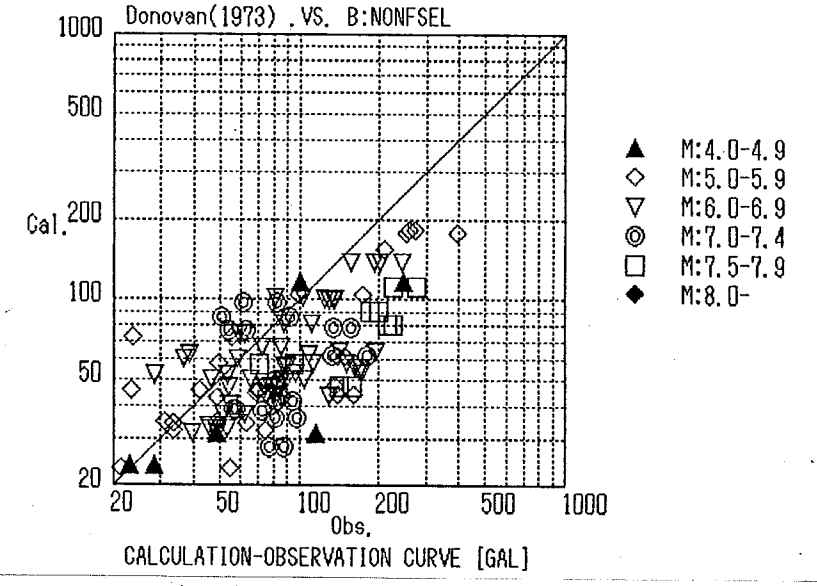

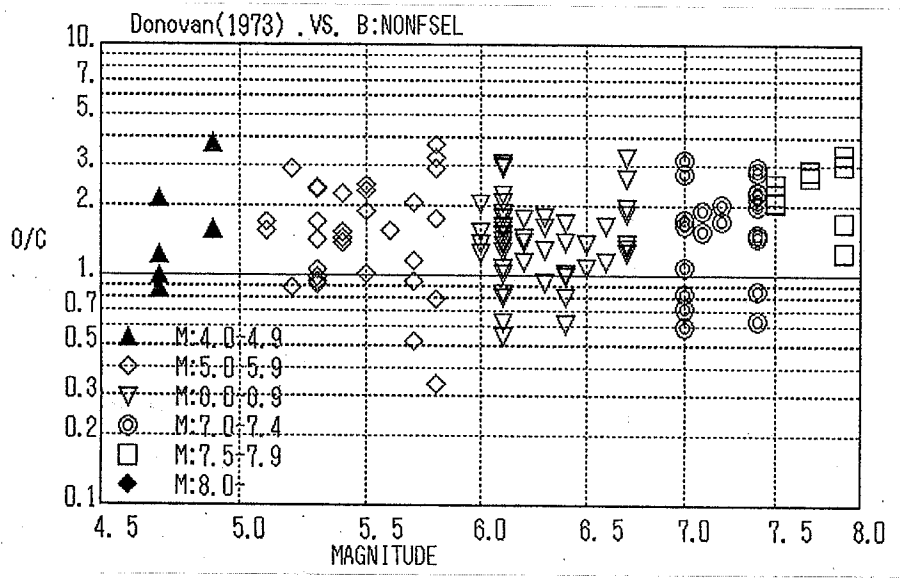

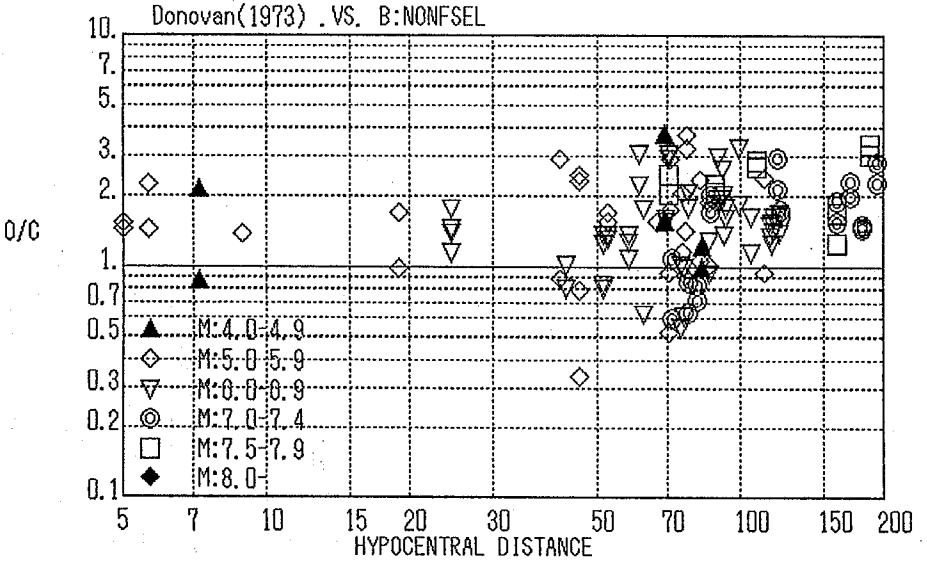

Figure 3.2.1 Fit of Donovan curve;
$A=1080 \cdot \exp(0.5M)(R+25)^{-1.32}$ (gal)

NUMBER OF DATA = 125
AVERAGE FITTNESS(O/C) = 1.52486
STANDARD DEVIATION = 1.59462

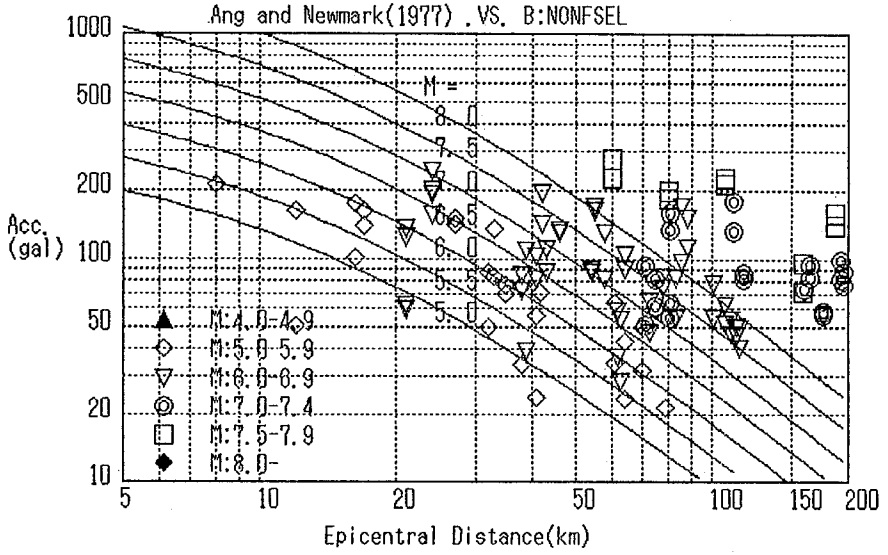

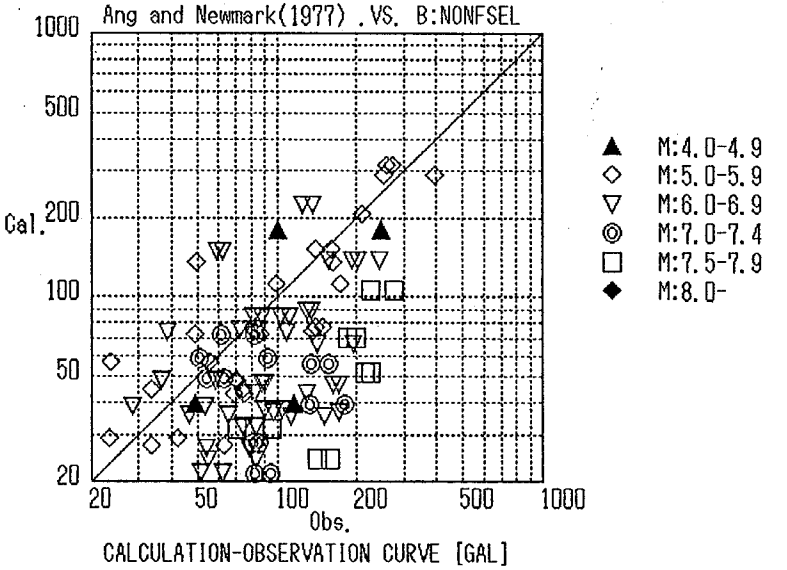

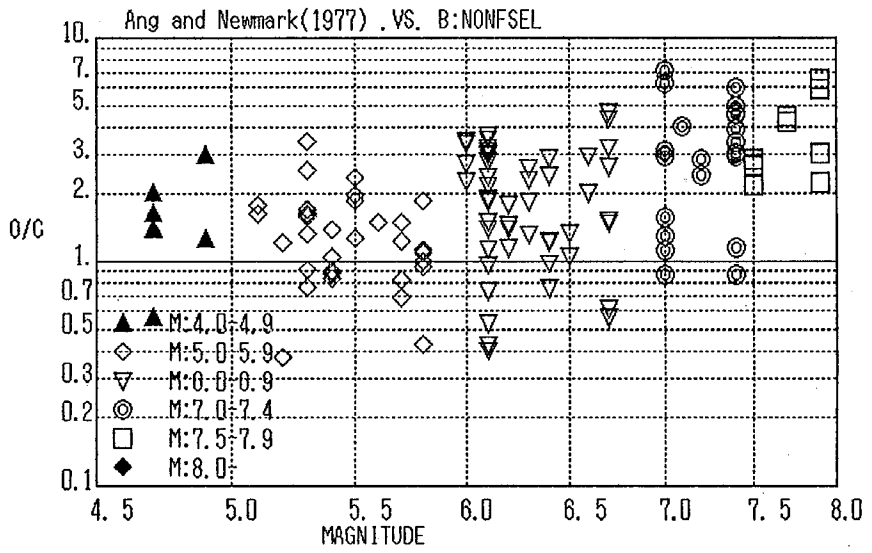

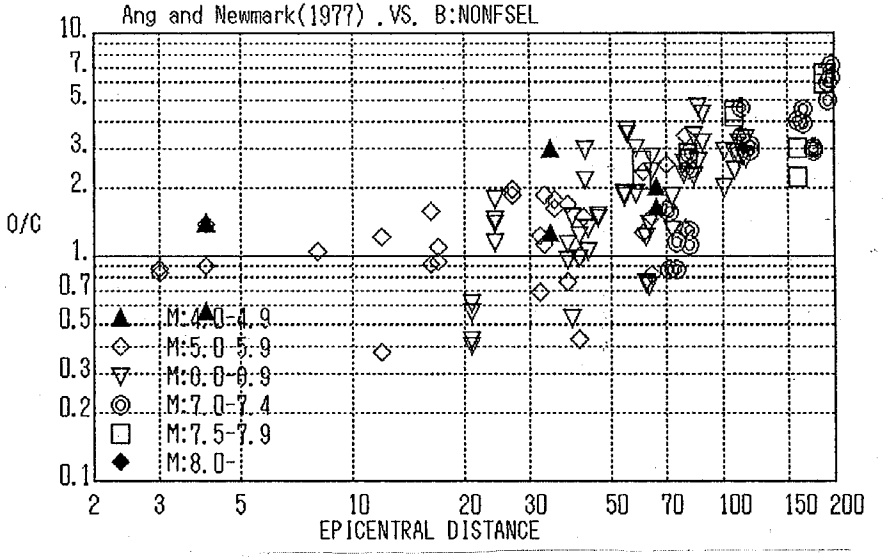

Figure 3.2.2 Fit of Ang and Newmark curve;
$A=1.35 \cdot \exp(0.67M)(D+15)^{-1.75}$ (G)

NUMBER OF DATA = 125
AVERAGE FITTNESS(O/C) = 1.78598
STANDARD DEVIATION = 1.90185

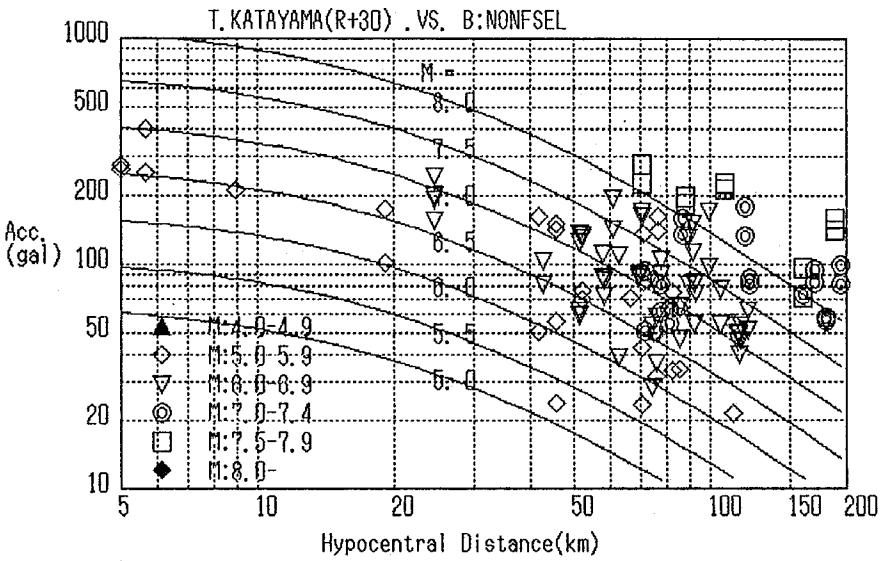

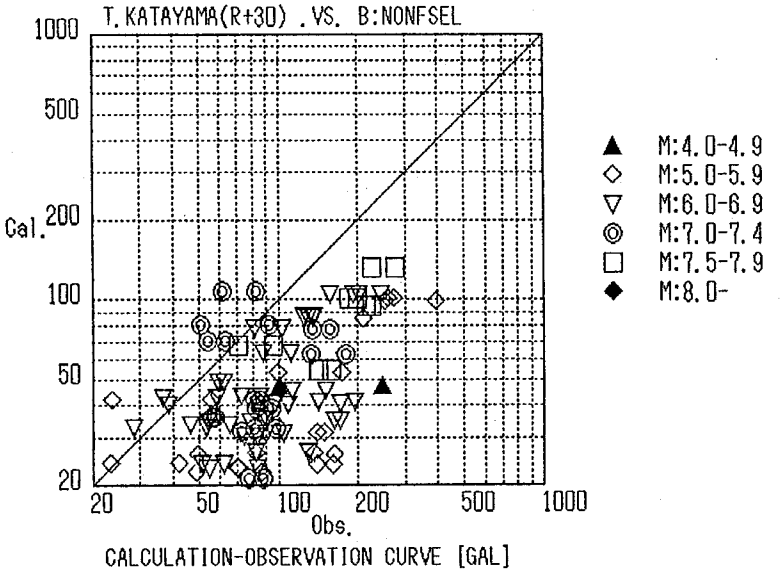

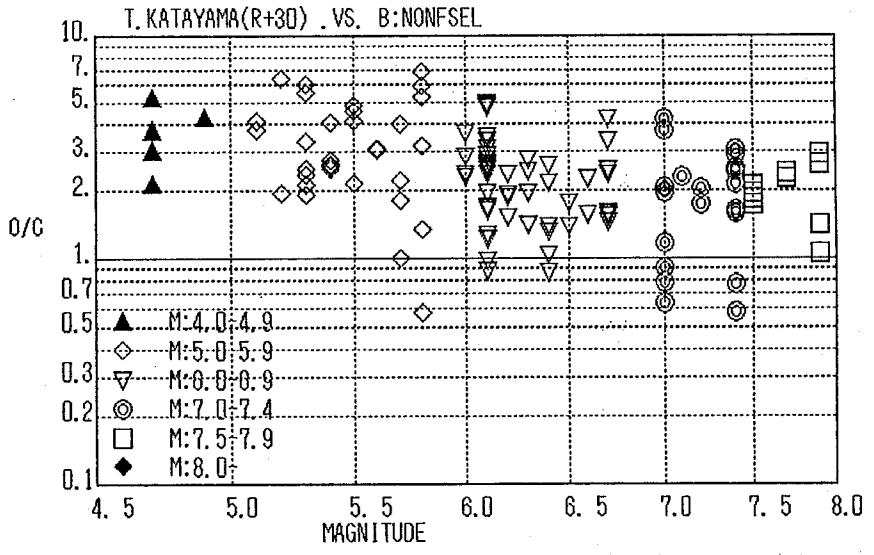

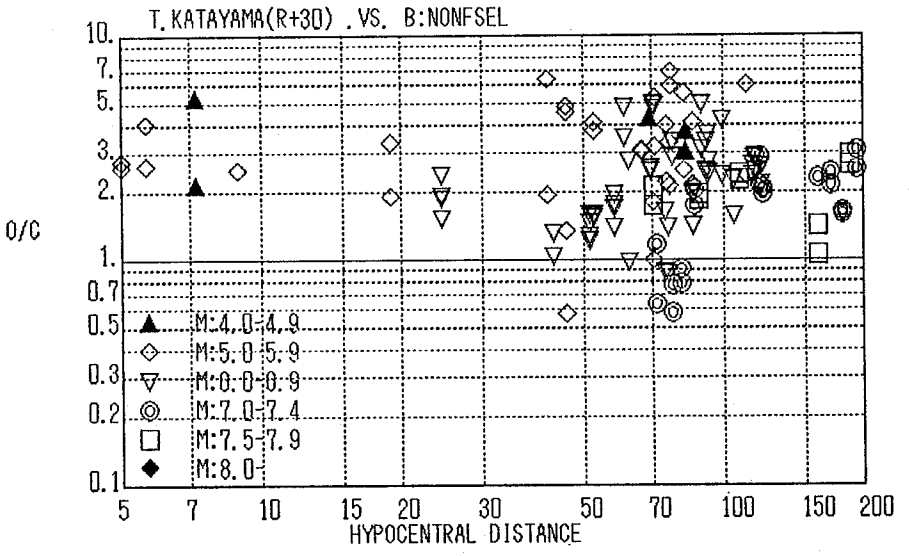

Figure 3.2.3 Fit of T.Katayama curve;
$A=203.3 \cdot \exp(0.948M)(R+30)^{-1.637}$ (gal)

NUMBER OF DATA = 125
AVERAGE FITTNESS(O/C) = 2.31758
STANDARD DEVIATION = 1.71013

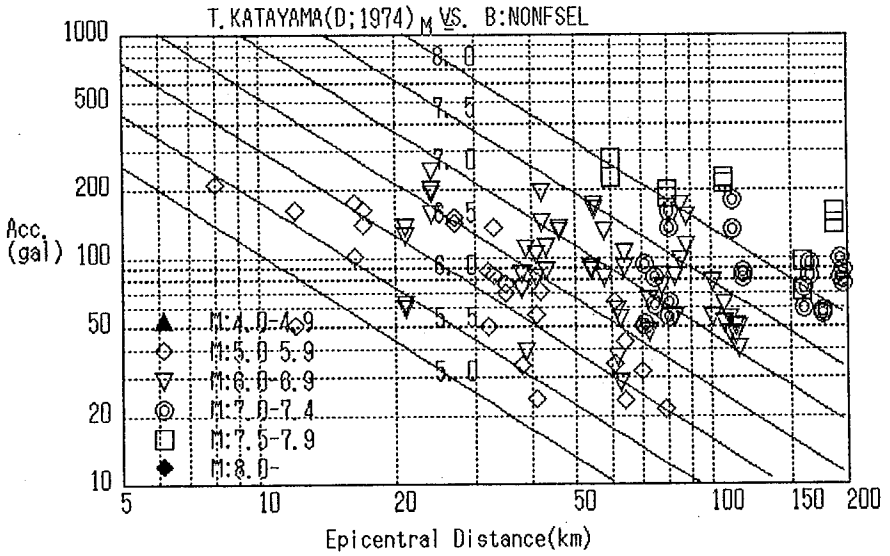

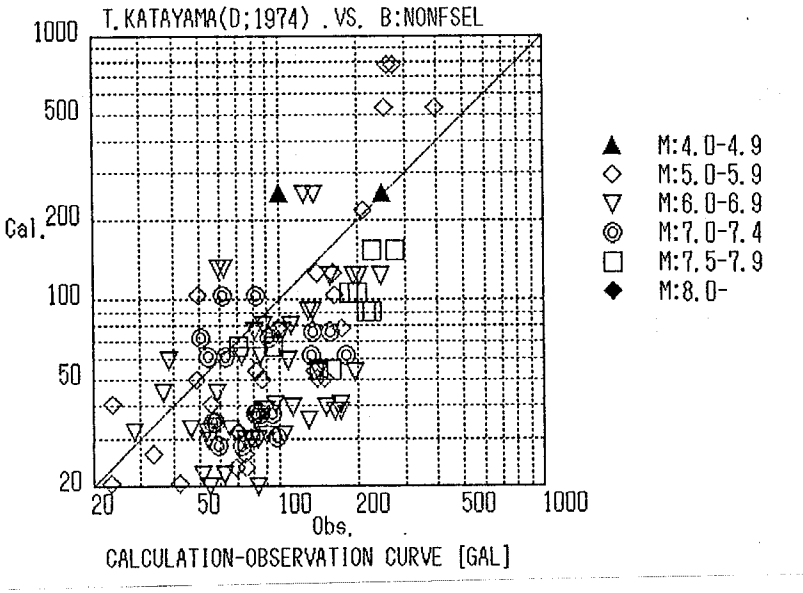

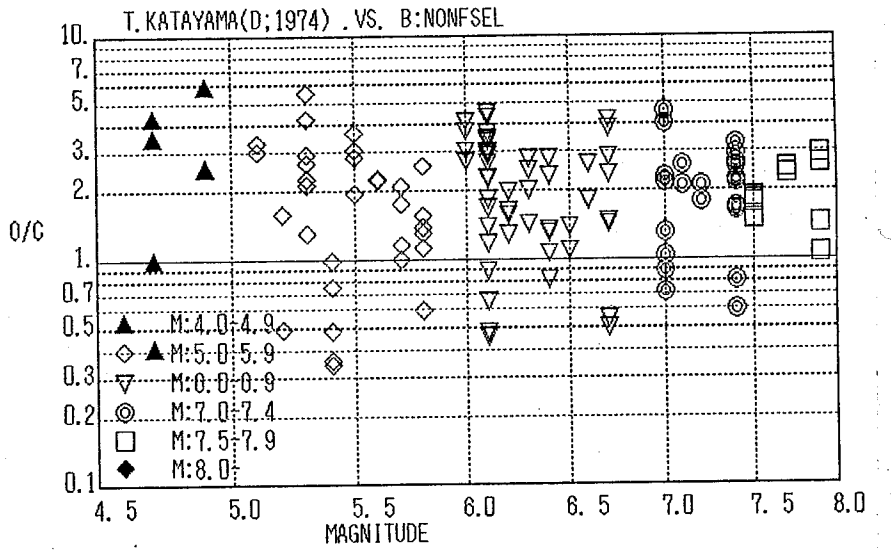

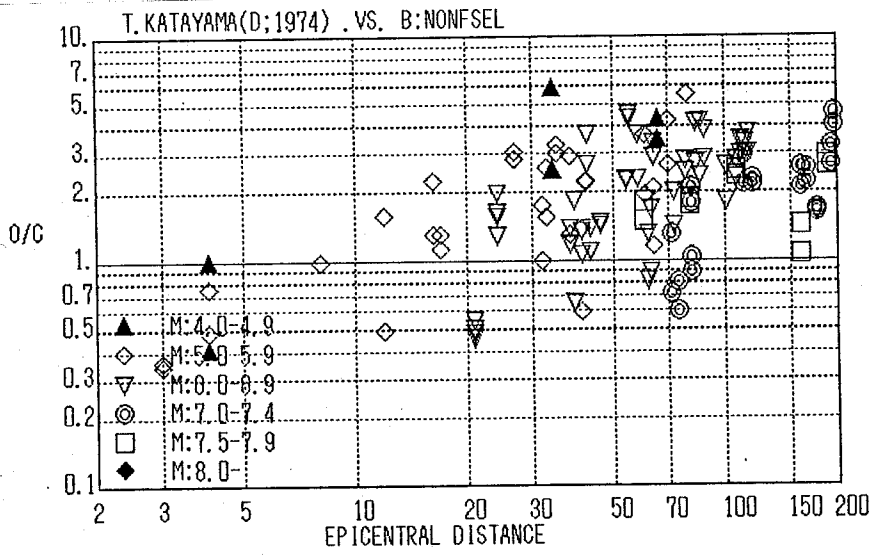

Figure 3.2.4 Fit of T.Katayama curve;
$A=9.60 \cdot \exp(1.073M) D^{-1.290}$ (gal)

NUMBER OF DATA = 125
AVERAGE FITTNESS(O/C) = 1.80507
STANDARD DEVIATION = 1.87031

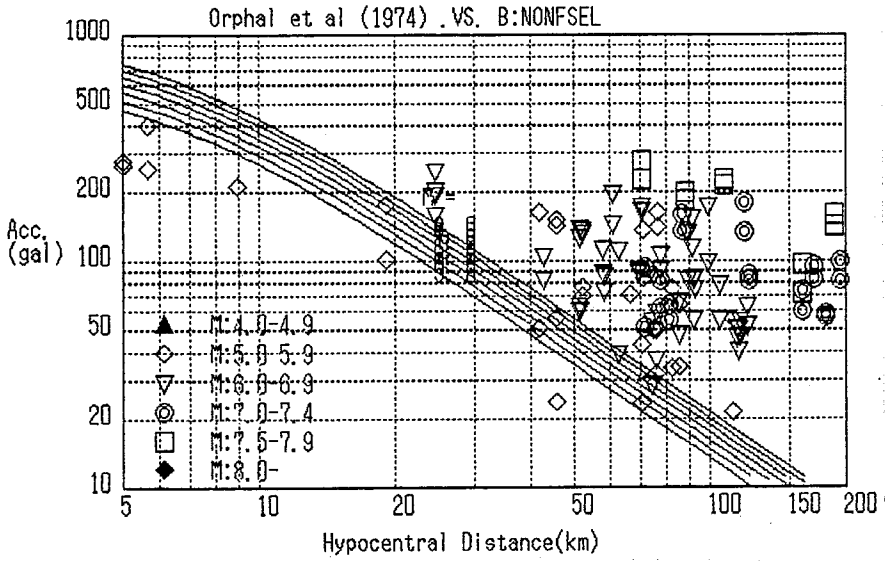

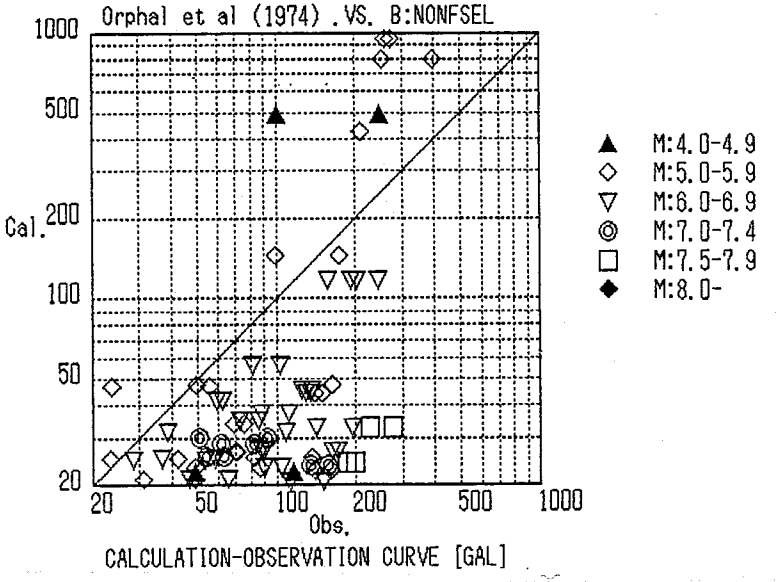

CALCULATION-OBSERVATION CURVE [GAL]

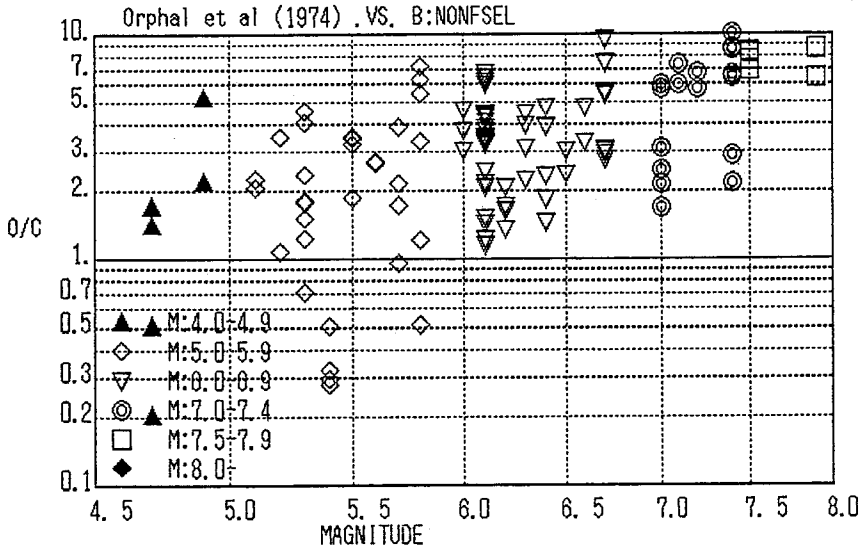

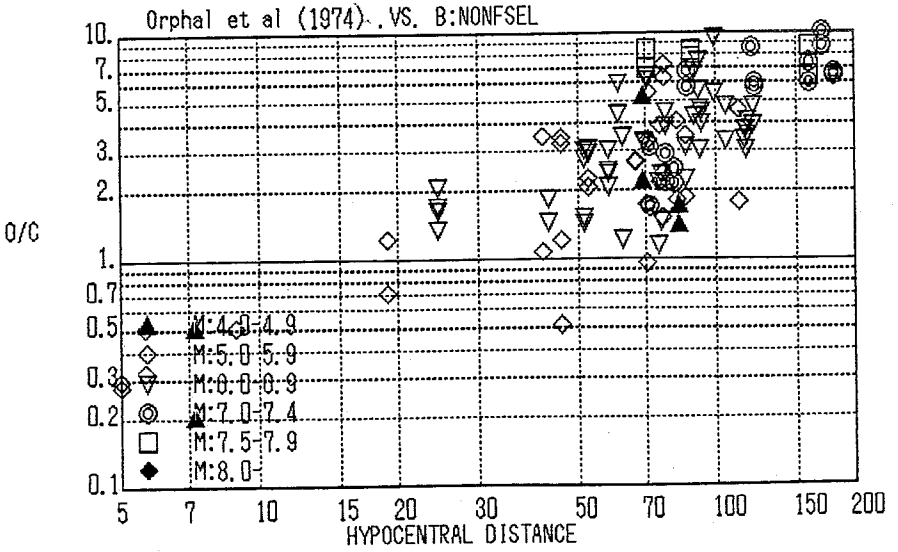

Figure 3.2.5 Fit of Orphal et al curve;
$A=0.66 \cdot 10^{0.40M} \cdot R^{-1.39}$ (G)

NUMBER OF DATA = 125
AVERAGE FITTNESS(O/C) = 3.0156
STANDARD DEVIATION = 2.43908

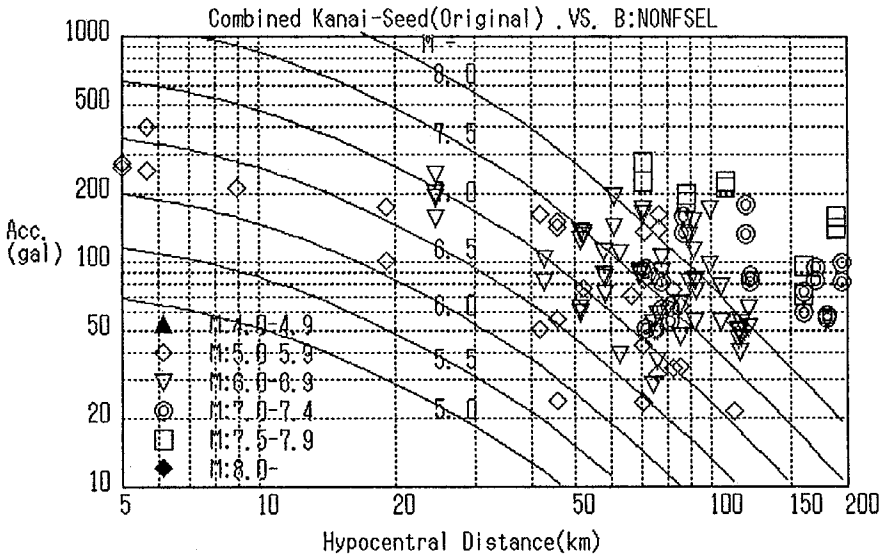

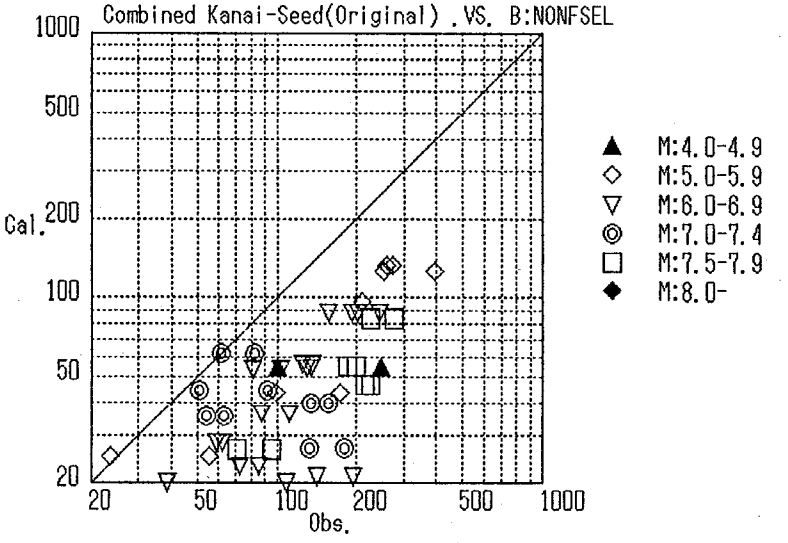

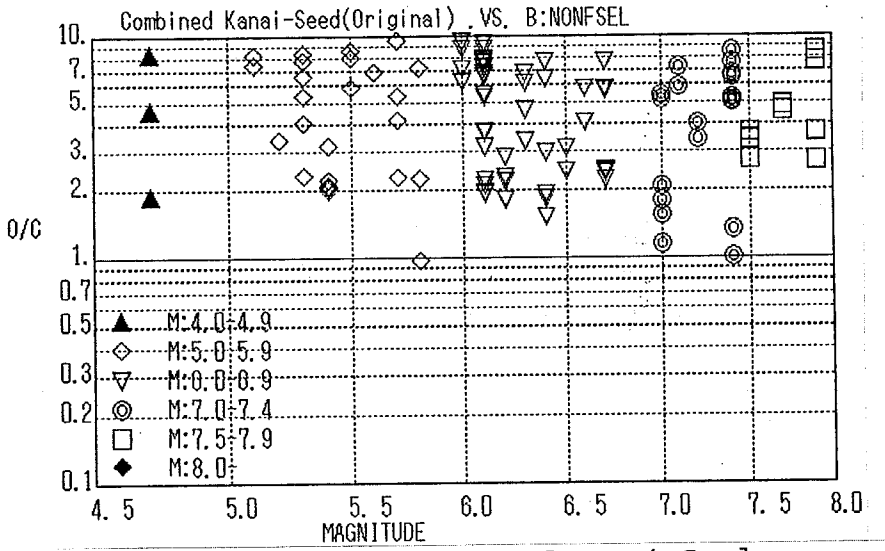

CALCULATION-OBSERVATION CURVE [GAL]

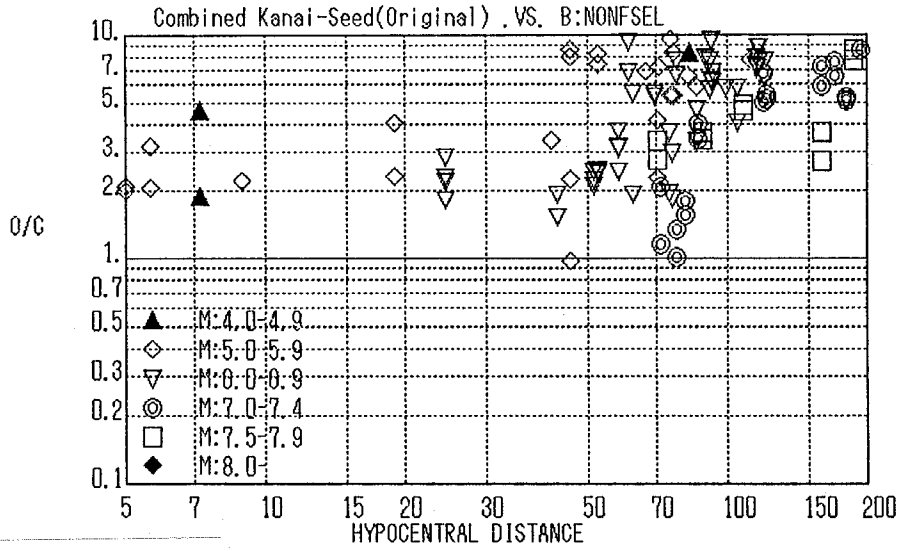

Figure 3.2.6 Fit of Combined Kanai-Seed curve;
$A_0=(1/Tp)\cdot 10^B$ (gal), $Tp=(0.000512M-0.00143)\cdot(X+100)+0.02$; $B=0.61M-P\log_{10}X+Q$; $X=(D^2+H^2)^{1/2}$;
$P=1.66+3.6/X$; $Q=0.167-1.83/X$

NUMBER OF DATA	=	125
AVERAGE FITTNESS(O/C)	=	4.80187
STANDARD DEVIATION	=	1.96624

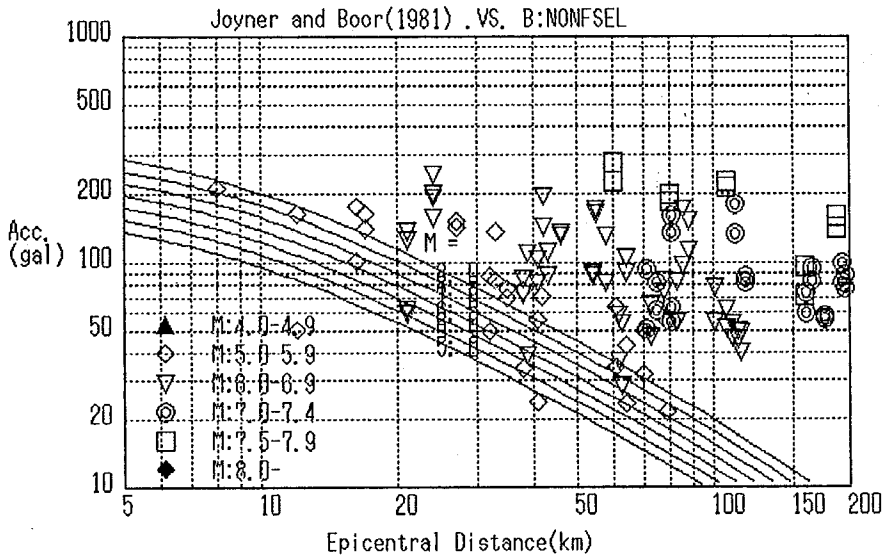

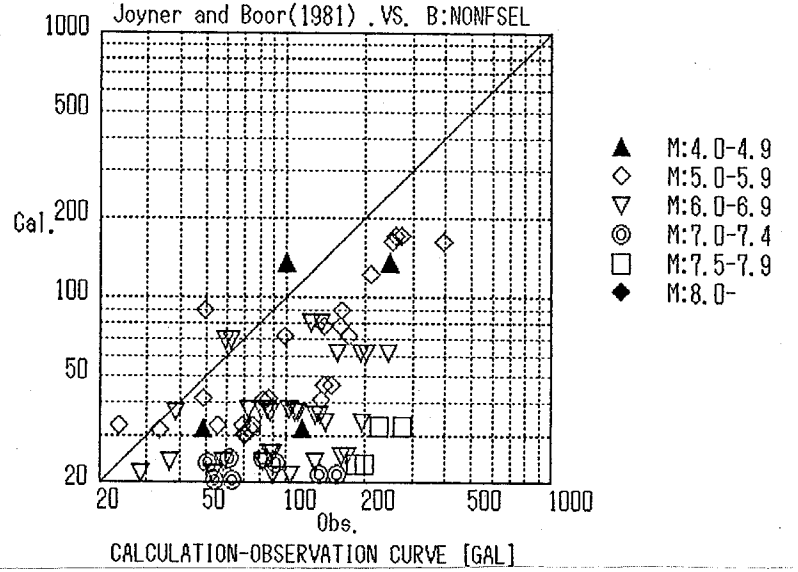

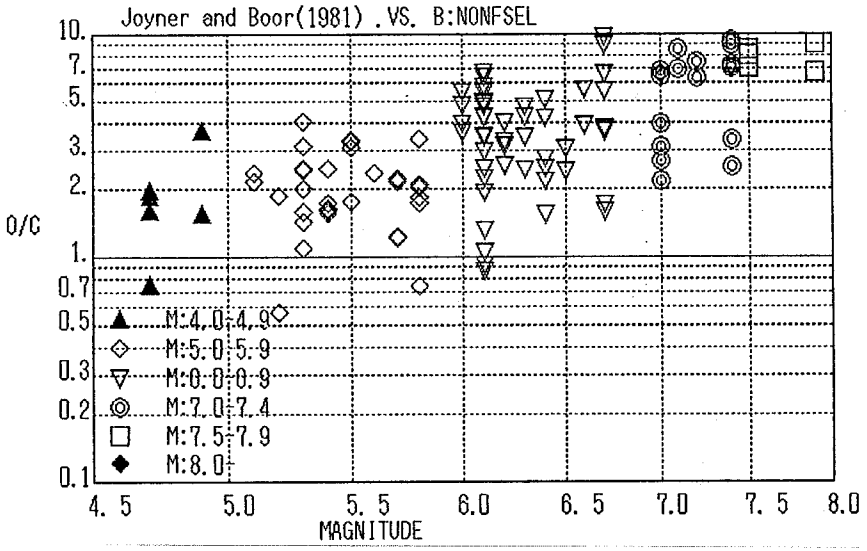

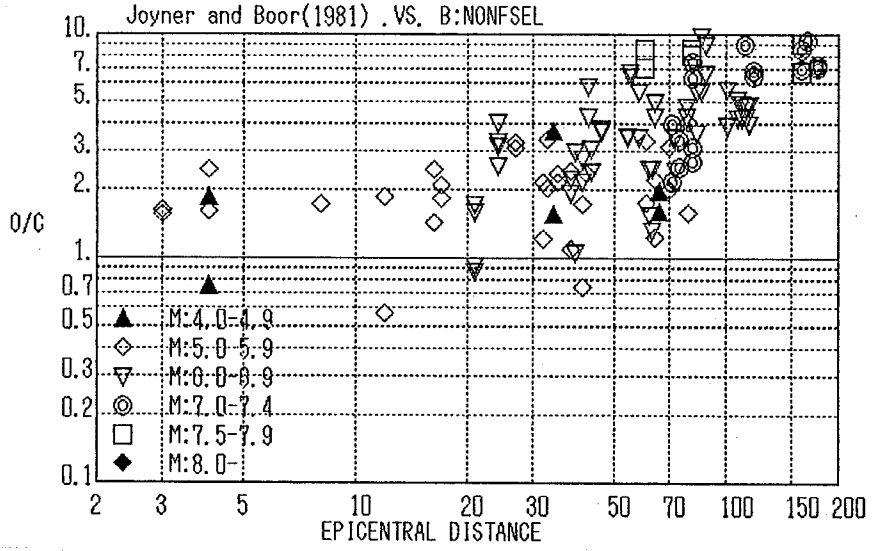

Figure 3.2.7 Fit of Joyner and Boore curve;
$\log_{10}A=-1.02+0.249M-\log_{10}(r)$
$-0.00255 \cdot r$ (G), $r=(D^2+7.32^2)^{1/2}$

NUMBER OF DATA = 125
AVERAGE FITTNESS(O/C) = 3.4076
STANDARD DEVIATION = 2.09324

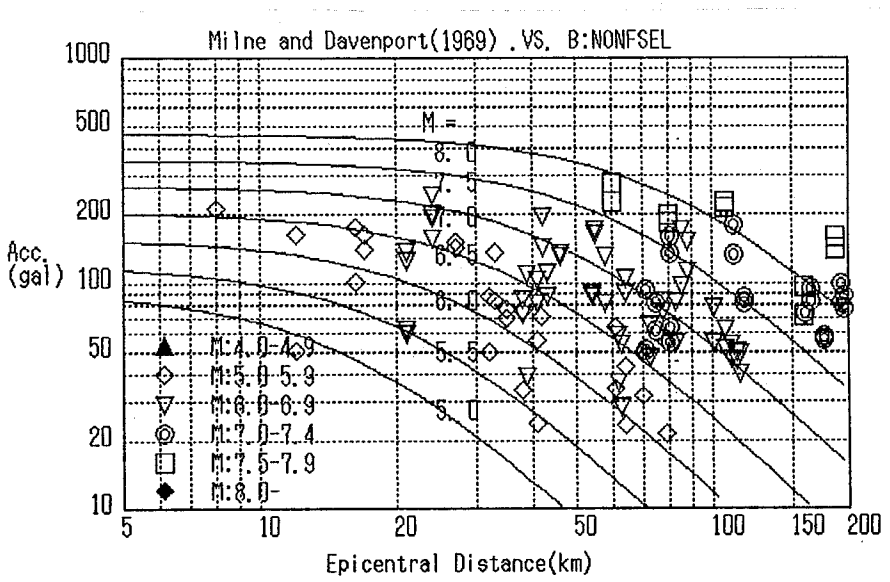

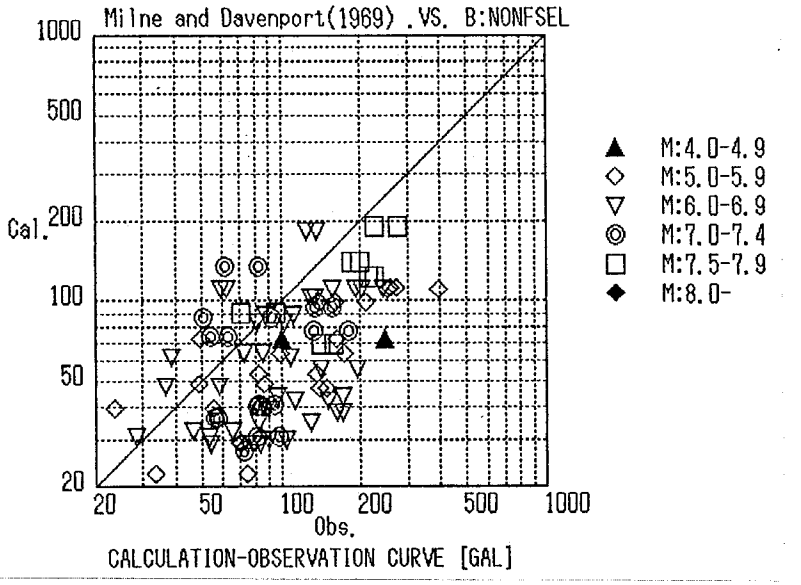

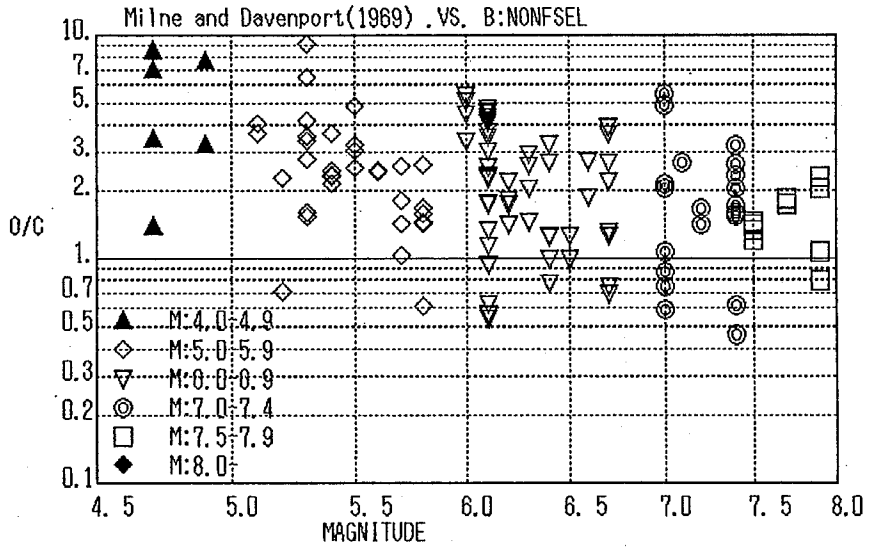

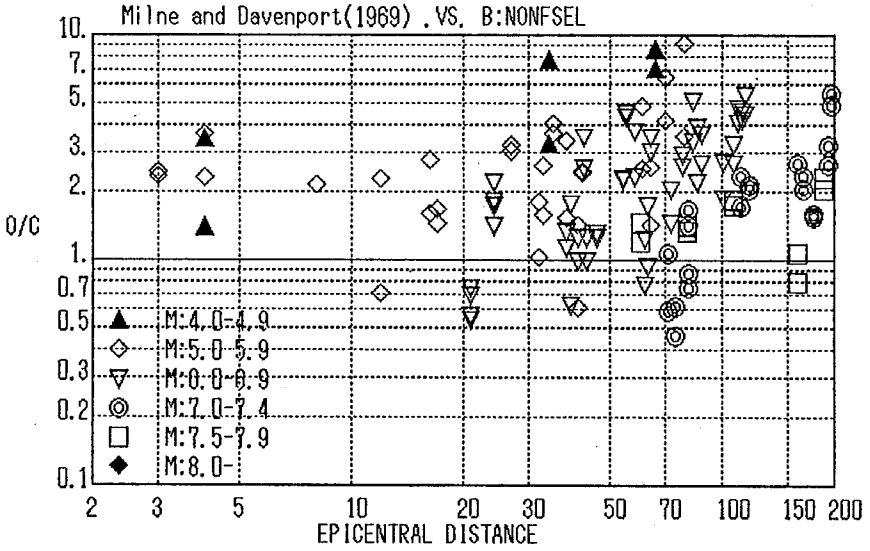

Figure 3.2.8 Fit of Milne and Davenport curve;
$A=0.69 \cdot \exp(1.64M)/[D^2+1.1 \cdot \exp(1.1M)]$ (G)

NUMBER OF DATA = 125
AVERAGE FITTNESS(O/C) = 2.06266
STANDARD DEVIATION = 1.88379

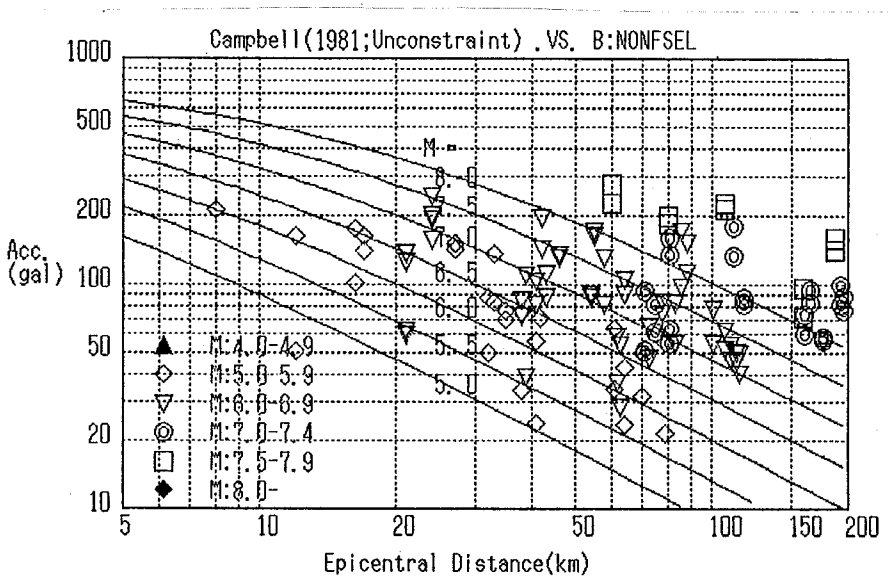

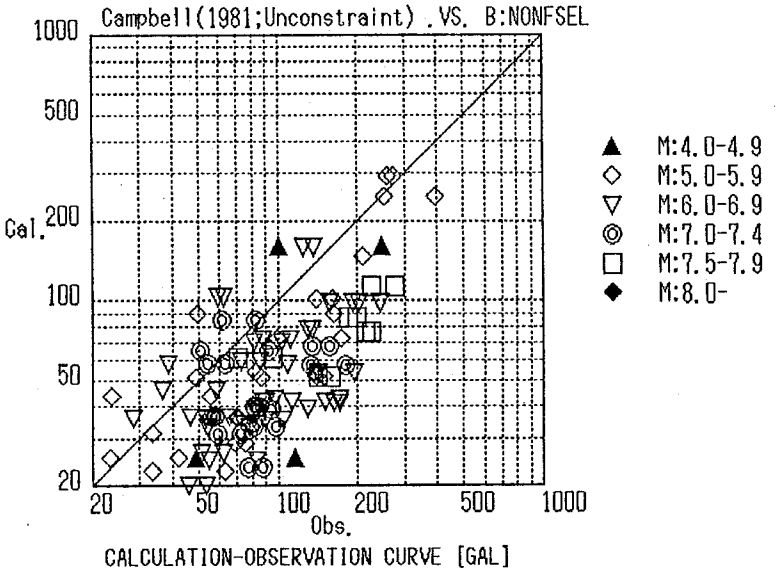

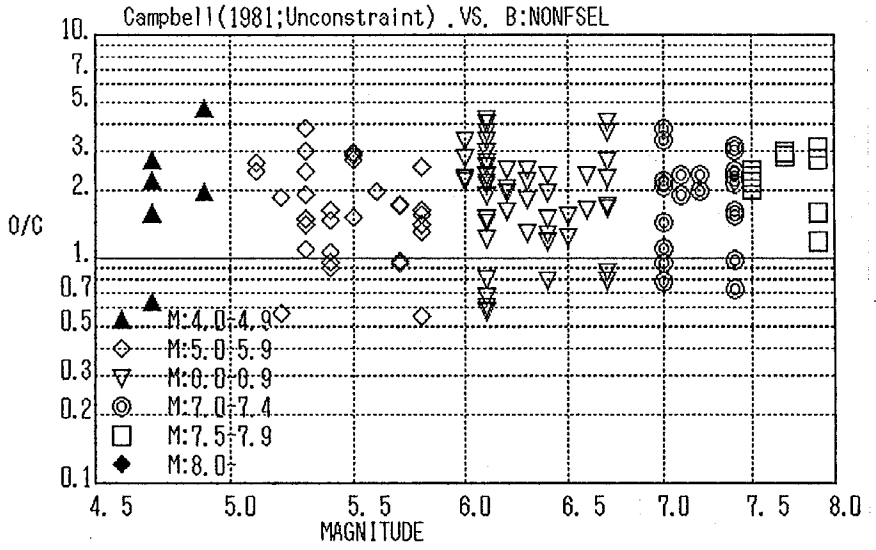

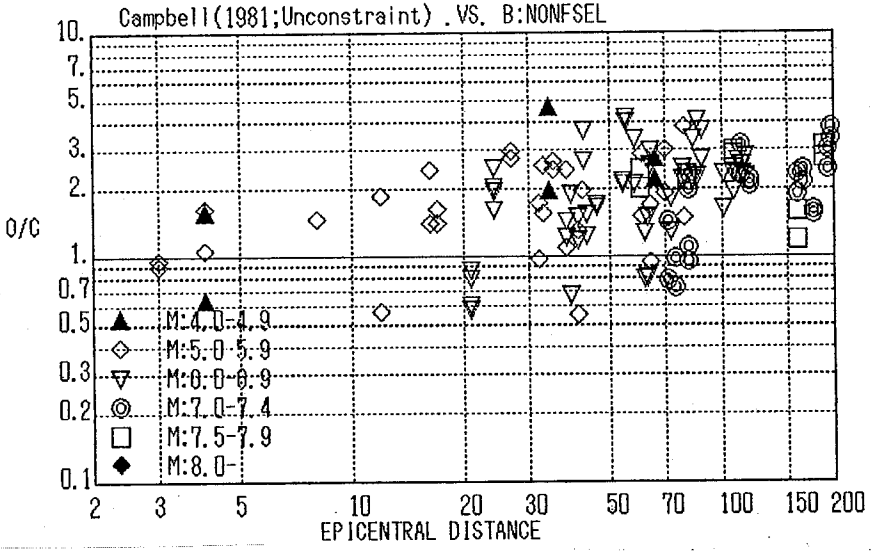

Figure 3.2.9 Fit of Campbell curve;
$A=0.0159 \cdot \exp(0.868M)[D+0.0606 \cdot \exp(0.700M)]^{-1.09}$ (G)

NUMBER OF DATA = 125
AVERAGE FITTNESS(O/C) = 1.8209
STANDARD DEVIATION = 1.61552

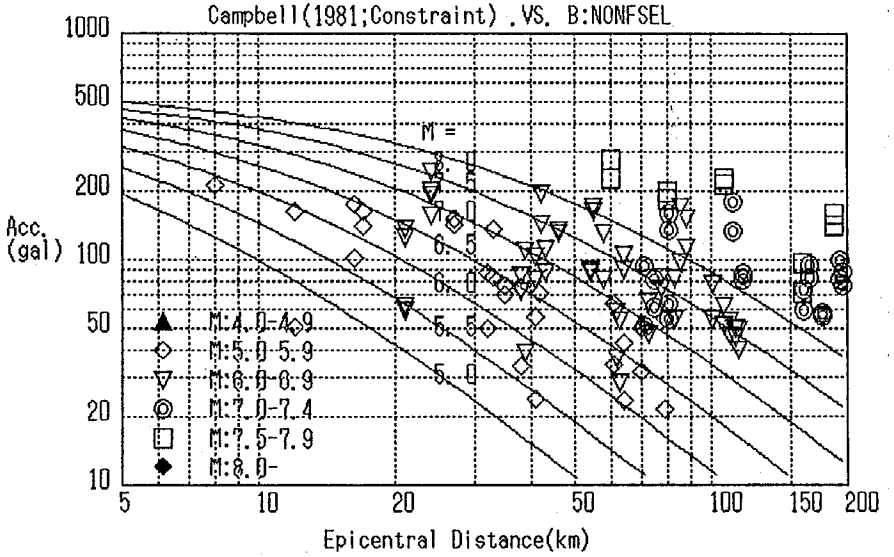

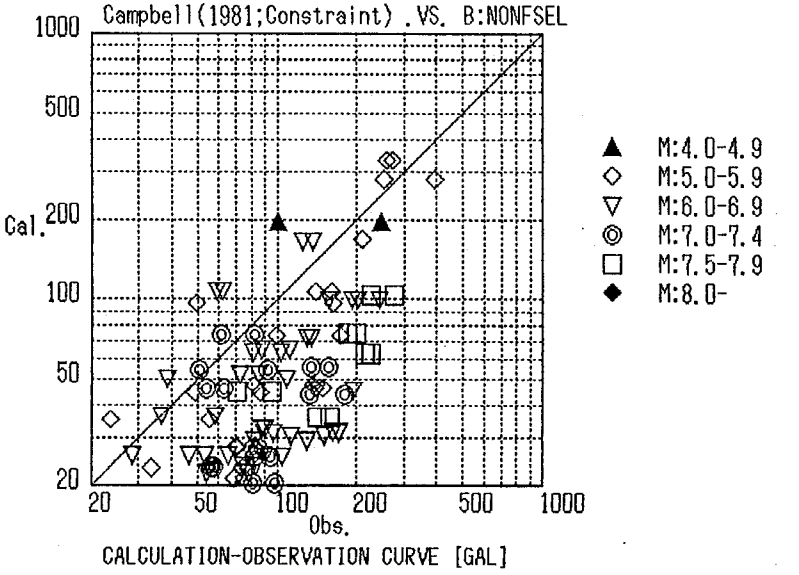

CALCULATION-OBSERVATION CURVE [GAL]

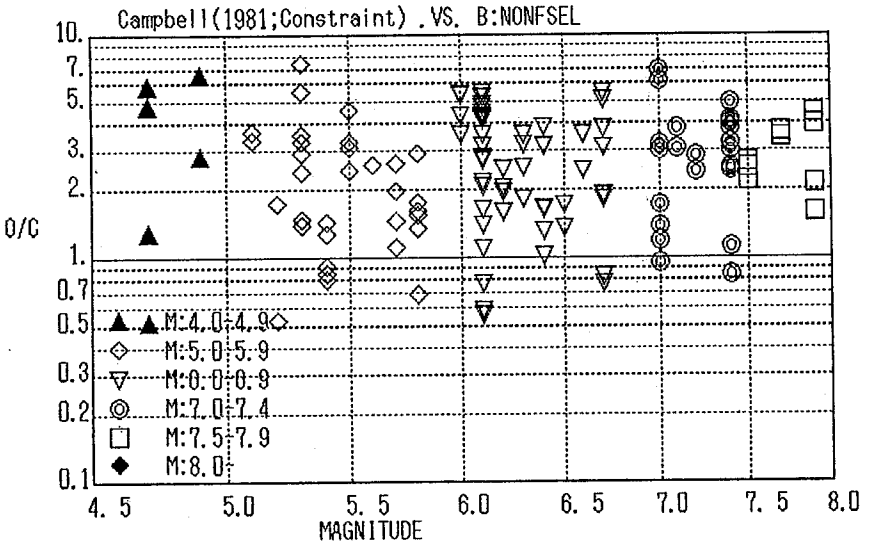

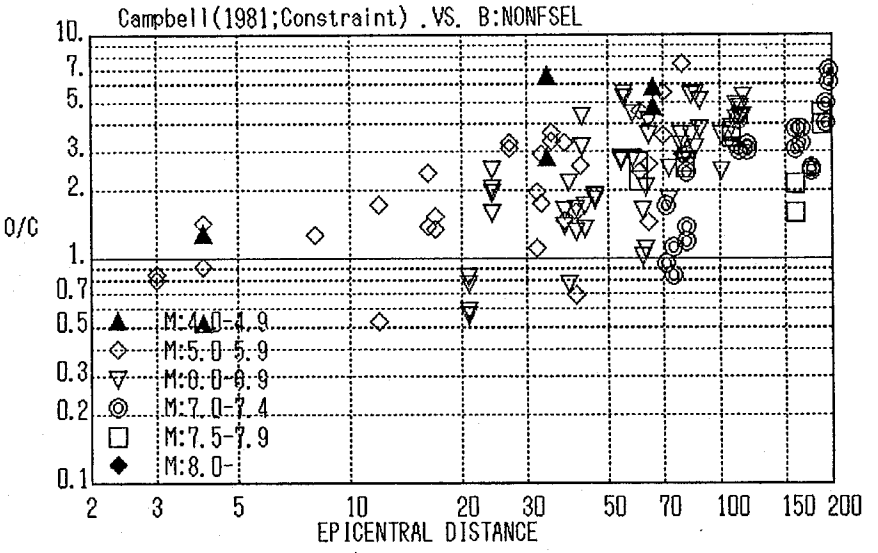

NUMBER OF DATA = 125
AVERAGE FITTNESS(O/C) = 2.34767
STANDARD DEVIATION = 1.84588

Figure 3.2.10 Fit of Campbell curve;
$A=0.0185 \cdot \exp(1.28M)[D+0.147 \cdot \exp(0.732M)]^{-1.75}$ (G)

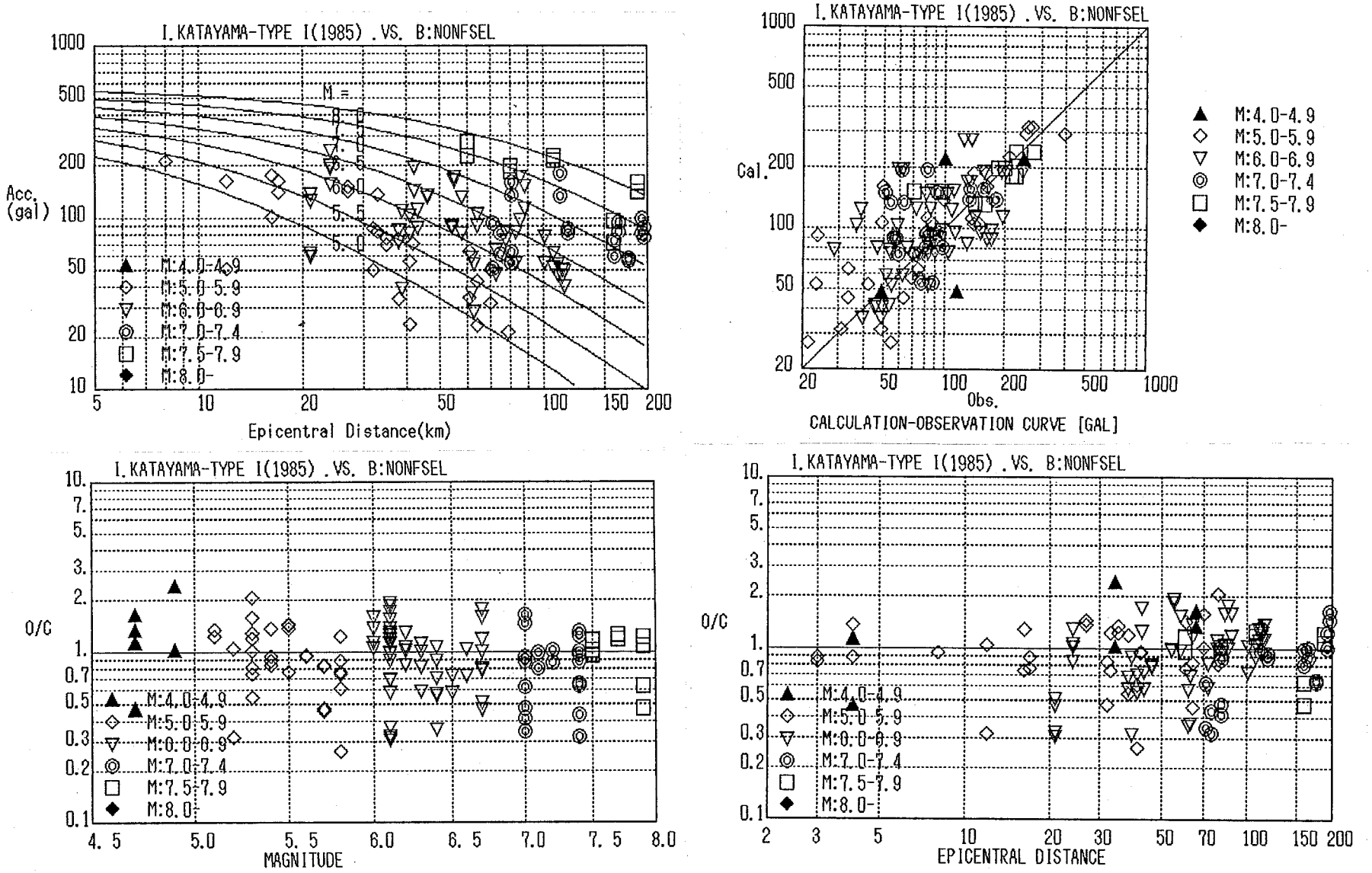

Figure 3.2.11 Fit of I.Katayama(Type I) curve;
$A=0.0302 \cdot \exp(1.281M)[D+0.300 \cdot \exp(0.752M)]^{-1.513}$ (G)

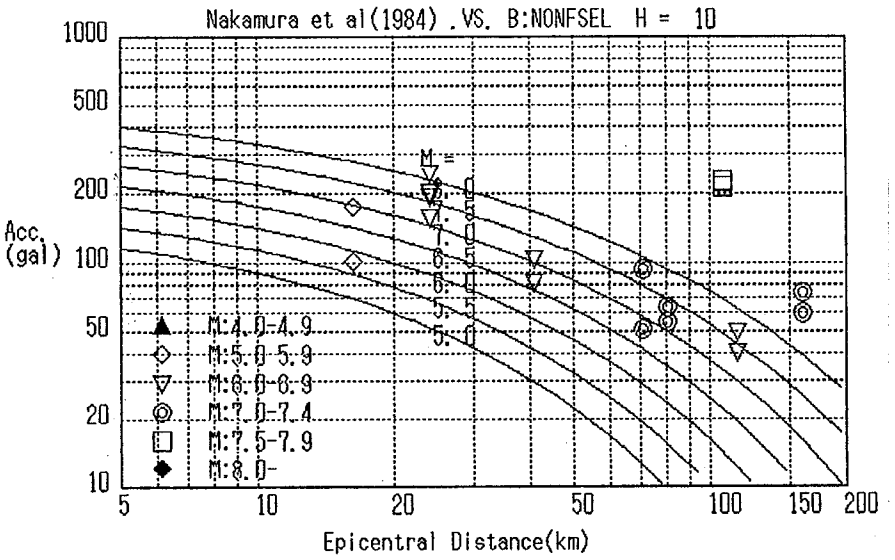

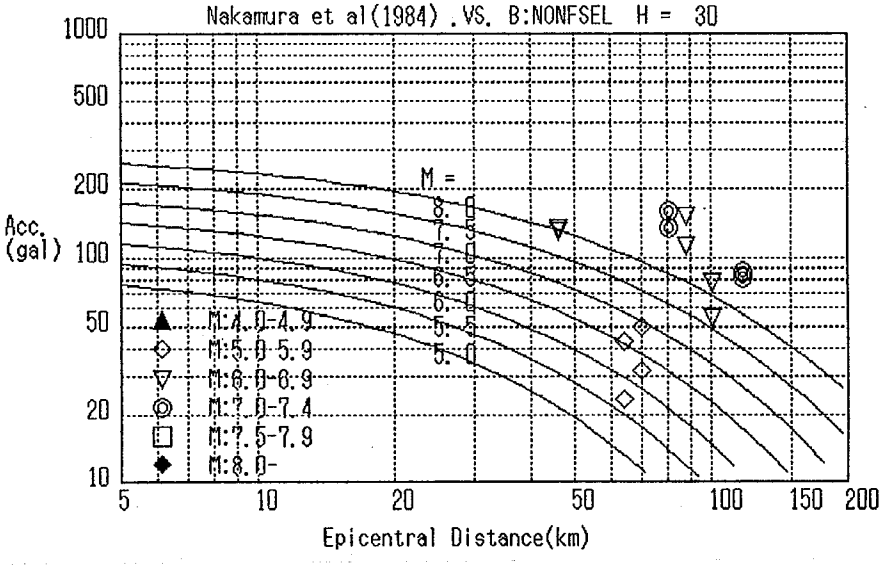

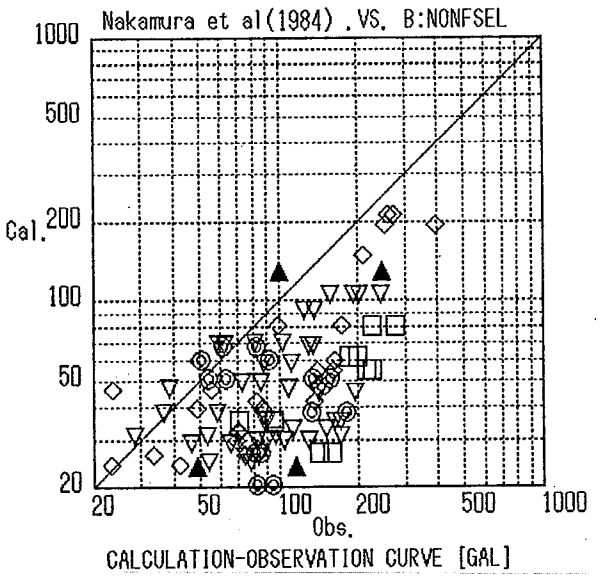

CALCULATION-OBSERVATION CURVE [GAL]

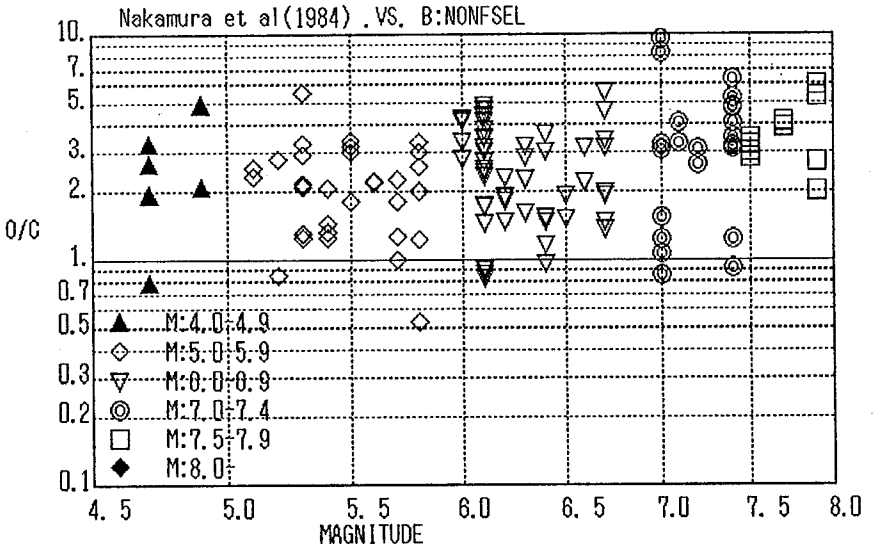

NUMBER OF DATA = 125
AVERAGE FITTNESS(O/C) = 2.36353
STANDARD DEVIATION = 1.73137

Figure 3.2.12 Fit of Nakamura et al curve;
$\log_{10}A=0.168M-0.50\cdot\log_{10}(D+H)$
$-0.0551\cdot D\cdot 10^{-0.156M}+1.86$ (gal)

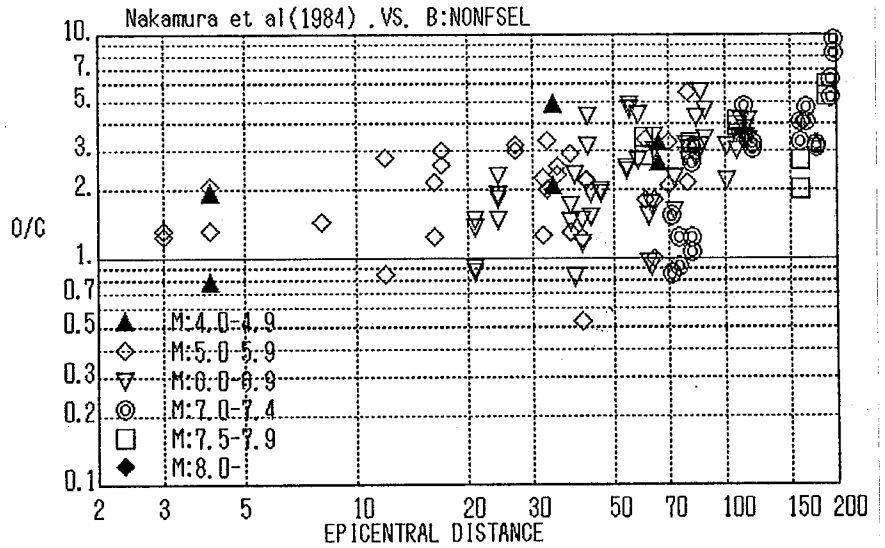
Nakamura et al(1984) .VS. B:NONFSEL
O/C
EPICENTRAL DISTANCE
M:4.0-4.9
M:5.0-5.9
M:6.0-6.9
M:7.0-7.4
M:7.5-7.9
M:8.0-

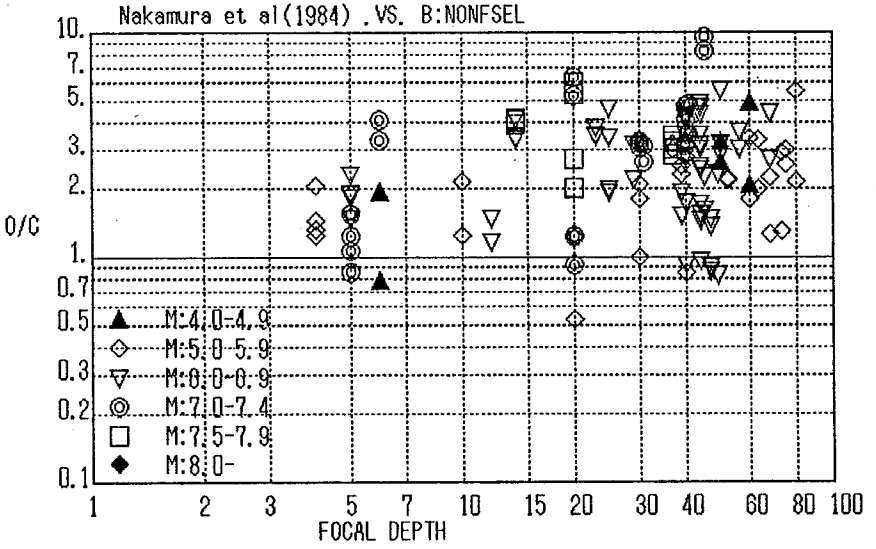
Nakamura et al(1984) .VS. B:NONFSEL
O/C
FOCAL DEPTH
M:4.0-4.9
M:5.0-5.9
M:6.0-6.9
M:7.0-7.4
M:7.5-7.9
M:8.0-

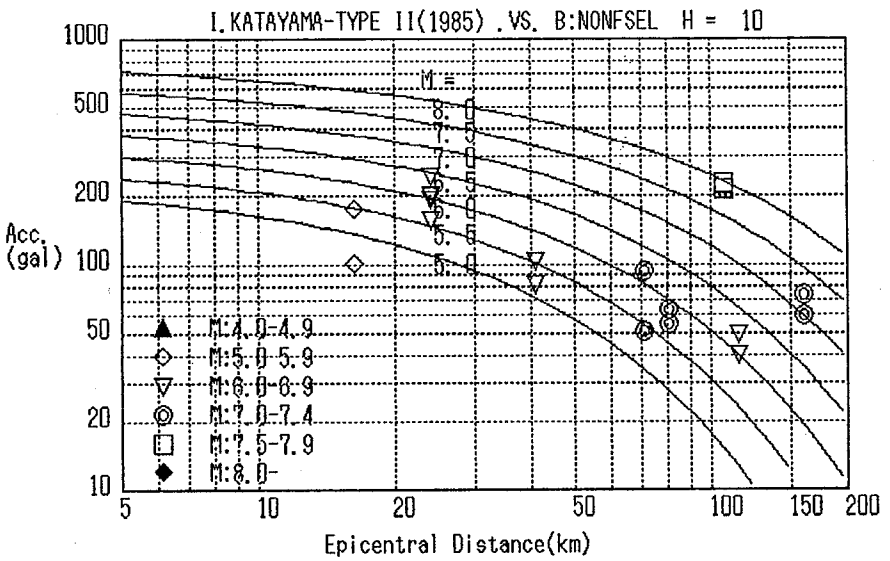

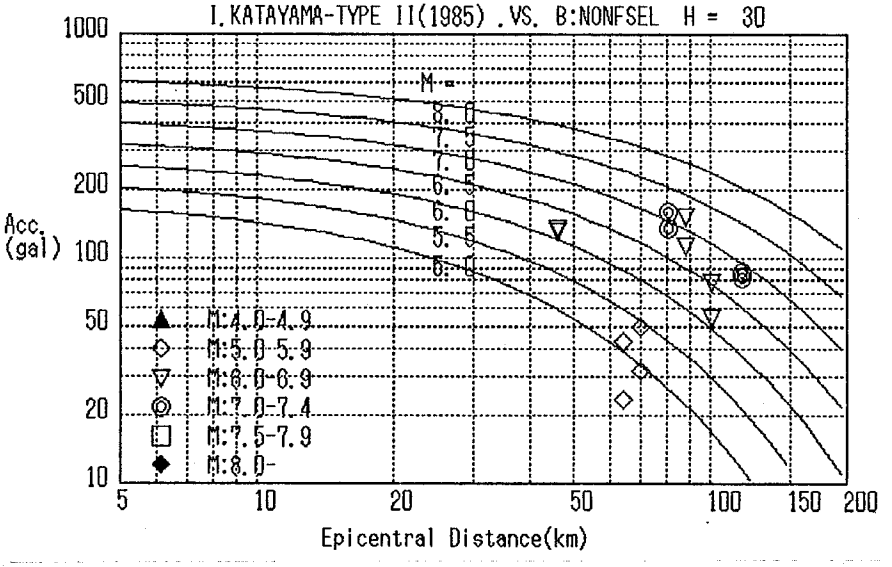

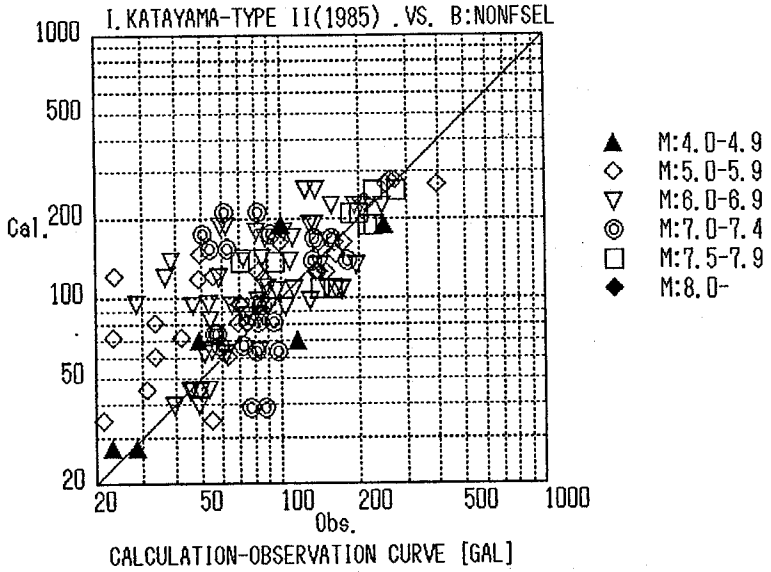

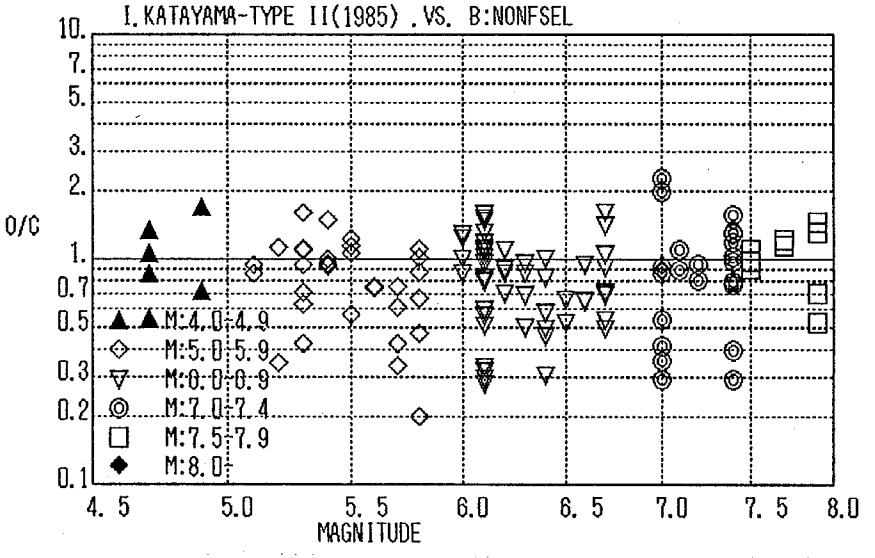

NUMBER OF DATA = 125
AVERAGE FITTNESS(O/C) = .802511
STANDARD DEVIATION = 1.59249

Figure 3.2.13 Fit of I.Katayama (Type II) curve;
$\log_{10}A=0.180M-0.193\cdot\log_{10}(D+H)$
$-0.0558\cdot D\cdot 10^{-0.157M}-1.333$ (G)

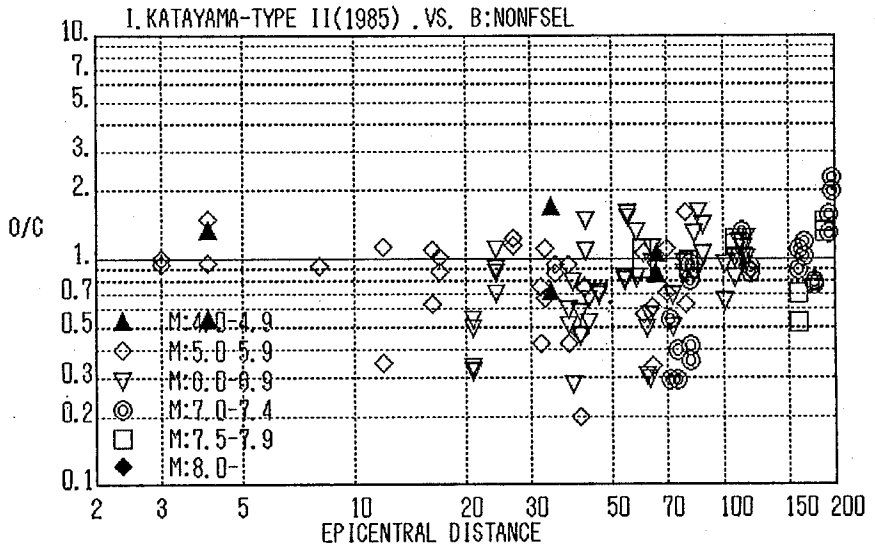
I.KATAYAMA-TYPE II(1985) .VS. B:NONFSEL
O/C
10.
7.
5.
3.
2.
1.
0.7
0.5
0.3
0.2
0.1
M:4.0-4.9
M:5.0-5.9
M:6.0-6.9
M:7.0-7.4
M:7.5-7.9
M:8.0-
2
3
5
10
20
30
50
70
100
150
200
EPICENTRAL DISTANCE

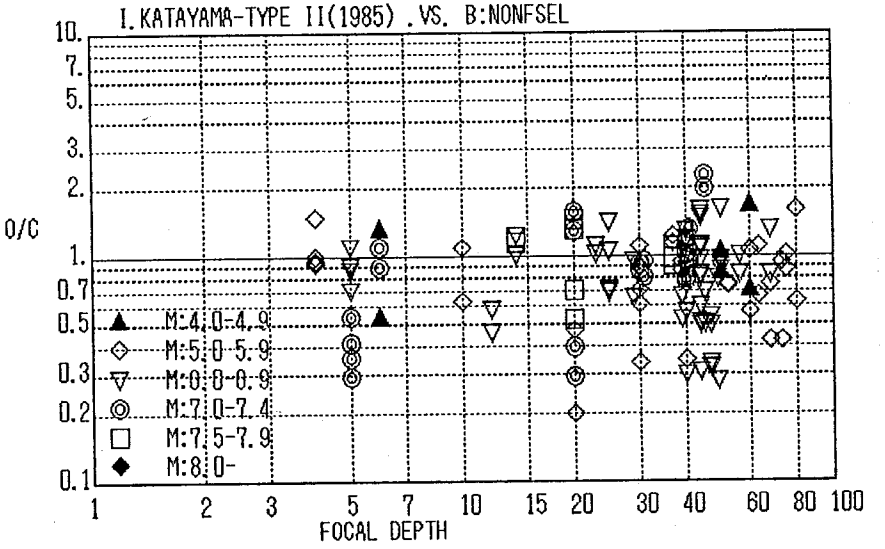
I.KATAYAMA-TYPE II(1985) .VS. B:NONFSEL
O/C
10.
7.
5.
3.
2.
1.
0.7
0.5
0.3
0.2
0.1
M:4.0-4.9
M:5.0-5.9
M:6.0-6.9
M:7.0-7.4
M:7.5-7.9
M:8.0-
1
2
3
5
7
10
15
20
30
40
60
80
100
FOCAL DEPTH

3.3 NEW EMPIRICAL FORMULA

3.3.1 NEED FOR NEW EMPIRICAL FORMULA

The two empirical formulas in eqs.(3.2.22) and (3.2.24), both of which showed almost identical fit to the present Japanese strong motion data set as was shown in Table 3.2.4 , were used to test the significance of the focal depth term in a practical application example(I.Katayama, 1985). By using the model which consists of three dimensional source model of seismically active Kanto area and each empirical formula described above, one takes and the other does not take the focal depth into account for predicting peak ground accelerations(PGA) on the practical design base layer, the seismic hazard maps of the Kanto area were calculated.

The iso-seismal maps of PGA for the period of 75 and 100 years of expectancy obtained by using each one of the above attenuation curves are shown in comparative form in Figures 3.3.1(a) through (d). From the figures, the following points are evident;

(1) In the case when the I.Katayama Type I curve is employed, the regionally high intensity zones have appeared just above the earthquake nests, Southwestern and Southern Ibaragi, and Northern and Central Chiba, where the earthquake activity of around 50 km to 90 km depth are remarkably stable and frequent(Figures 3.3.1(a) and (b)).

(2) On the other hand, when the attenuation curve I.Katayama Type II is used, the regionally high intensity zones do not appear above those regions of intermediate depth earthquakes as are evident from Figures 3.3.1(c) and (d).

(3) The past earthquakes having occurred in the above two source regions of intermediate earthquakes did not cause serious damages over these regions nor the surrounding area. The area that extends to the southwest from the Southwestern and Southern Ibaragi to the sea off Bousou Pennisula across the central Chiba prefecture is known of comparatively low rate of historical earthquake damage.

(4) Thus, the attenuation curve I.Katayama Type II is seems to give a reasonable feature of seismic intensity distribution. And the regionally high intensity in these zones is attributed simply to the attenuation curve of the I.Katayama Type I employed which neglects the appropriate contribution of focal depth to PGA. Moreover, including the above zones, the I.Katayama Type I curve gives a more

uniform intensity distribution almost over the Kanto area and this seems inconsistent with the earthquake damage history of the area; namely, giving a higher earthquake damage rate of the past in the western part of Tokyo.

Based upon the results, it can be clearly said that it is desirable to use such attenuation curve like the I.Katayama Type II in the above in combination with the three dimensional source model for the seismic hazard analysis of the Kanto area or for the similar area where the earthquake activity is remarkable from very shallow to intermediate sources. In this regard, some new empirical formula that appropriately reflects the effect of focal depth on the predicted peak ground motions is required to be developed using Japanese strong motion records.

In case of buried structures extending over distance in the longitudinal directions, the relative displacements of two points along these structures can induce the axial stress and bending moment. Assuming a horizontally traveling wave, the ground strain, e, caused by the relative displacement of the soil along the axis of a duct can be correlated with the particle velocity, v, and the phase velocity, c, as e=v/c. The axial and flexural strain are induced in the structures through the transmitting capacity between the structures and the soil.

Therefore, these new empirical formulas should also provide the information regarding those peak ground motions which are meaningful for long and extended structures, for which the surface wave components or horizontally propagating wave components rather than the vertically traveling body wave components are of primary concern.

In the estimation of the ground strain, since the phase velocity is dependent on the frequency of the surface wave as is shown in Figure 3.3.2 (Toki, 1981), the particle velocity as well as the frequency of the ground motion must be determined.

Numerous reports showing good coincidence between the ground strain and ground velocity for the periods longer than 1 sec have been available but in the frequency range higher than 1.0 Hz there are almost none. To estimate the ground strain at the latter frequency range containing mainly body waves and to apply the ground velocity directly to the relationship e=v/c seems difficult; however, owing to the results given by Fukumori and others(1984), the phase velocity decreases with frequency for the range higher than 1.0 Hz and is close to the shear wave velocity of the ground at frequencies higher than 3.3 Hz. The results seem comparable to those obtained by Sakurai and others(1970) where the

primary period and apparent velocity of the travelling wave were estimated by the primary period of the upgoing shear wave and the shear wave velocity of the ground, respectively.

Even if the theoretical rigorousness is questionable for estimating the maximum ground strain by the simple relationship using the maximum ground velocity and the apparent velocity in the frequency range higher than 1.0 Hz, considering the possibility of buried structures responding to frequency components higher than 1.0 Hz but lower than the main frequencies of the body wave higher than 2 Hz, a set of new empirical formulas are constructed for practical engineering purposes. The Japanese strong motion data set previously described as "Non-filtered data set" was filtered with the low-pass filter with a cutt-off frequency of 1.4 Hz in order to make it contain longer period components and was named as "Filtered data set (FLTDSEL)", the peak acceleration and velocity of which are shown in Table 3.3.1. The same functional form used to derive the acceleration attenuation curve was also adopted for the new attenuation curves using the above "Filtered data set".

3.3.2 PRELIMINARY REGRESSION ANALYSIS

From the preceding section, it is found that the skeleton of the Type IV curves was the most appropriate curve for the current Japanese strong motion data set; however, in order to confirm the degree of fit of the Type IV curve to the data better than those of the other type curves, a preliminary regression analysis was performed including the curves of Type I to Type III.

The regression analysis is performed selecting one representative skeleton curve from each type; Donovan's curve, Combined Kanai-Seed curve, Campbell's curve and Nakamura et al curve are selected to represent respectively the type I to IV curves. As for the Type IV curve, the functional form was converted into explicit form.

As the preliminary analysis, only the acceleration formulas are constructed by nonlinear least square regression analysis using Newton-Gauss method written by the author and the Japanese strong motion data set NONFSEL. In performing the regression analyses, no data window are used and either the hypocentral distance or the epicentral distance was used for the distance.

The results of regression analysis for each type of curve are summarized in Table 3.3.2 and the feature of the fit to the data is shown

in Figures 3.3.3 through 3.3.6, for the Type I through IV, respectively.

From Table 3.3.2, all the curves seem to have similar fit to the data both in terms of the mean O/C and the standard deviation values; however, from Figures 3.3.3 through 3.3.6, the following may be observed:

(1) The Type I and II curves show fairly large dependence of the accelerations on the magnitude at near-field and the accelerations themselves are remarkably larger than those by Type II and IV curves.

(2) The Type II curve, Combined Kanai-Seed curve, has a peculiar shape in the intermediate distance range, 30 to 60 km of the hypocentral distance.

(3) The Type III and IV curves commonly show smaller dependency of acceleration on the magnitude at near-field and the near-field accelerations tends to converge in a certain small range which is consistent with recent fault rupture theory. However, the level of the near-field accelerations seems a little smaller if compared with that of the accelerations recorded in some recent events in California. In general, the fit is good as a whole.

From the above results, it can be confirmed that the Type IV curve involving the focal depth term can be adapted for Japanese strong motion data and this will give a more desirable situation for predicting the peak ground motions of earthquakes occurring at various depths.

3.3.3 NEW EMPIRICAL FORMULAS

Based on the results obtained in the preceding sections and the current need for predicting the peak ground motions directly applicable to structures constructed underground, two sets of attenuation curves are derived, each of which can predict both the peak ground acceleration (PGA) and peak ground velocity (PGV) at the surface of ordinary soil layers. For this purpose, the foregoing two Japanese strong motion data sets, Non-filtered data set and Filtered data set, are used. The regression analysis method is the same as that used in the previous section and the skeleton curve of the Type IV curve is used.

3.3.3.1 Formulas for the structures on the ground surface

As the empirical formula to be applied for structures constructed

directly on the ground surface, the following set of formulas were derived based on the "Non-filtered data set" in which the one written in eq.(3.3.1) is the same as that already given in Table 3.3.2 and the fit of the above two formulas are illustrated in Figures 3.3.7 and 3.3.8;

$$A_{max}=0.1125\exp(0.269M)[D+H]^{-0.339}\exp[-0.480\exp(-0.694M)D](1.53)^{y} \quad (3.3.1)$$

$$V_{max}=1.5302\exp(0.514M)[D+H]^{-0.373}\exp[-0.923\exp(-0.859M)D](1.67)^{y} \quad (3.3.2)$$

3.3.3.2 Formulas for structures underground

As the empirical formula to be applied for such structures suc as long tunnels or ducts constructed underground, the following set of formulas were derived using the "Filtered data set" and the fit of the above two formulas are illustrated in Figures 3.3.9 and 3.3.10;

$$A_{max}=0.0023\exp(0.602M)[D+H]^{-0.261}\exp[-1.097\exp(-0.817M)D](2.28)^{y} \quad (3.3.3)$$

$$V_{max}=0.1615\exp(0.798M)[D+H]^{-0.393}\exp[-0.700\exp(-0.810M)D](2.23)^{y} \quad (3.3.4)$$

In the above formulas, A_{max} and V_{max} are peak ground acceleration (PGA;in G) and velocity (PGV;in kine) , and M, D, and H are the magnitude of earthquake(in JMA), epicentral distance and focal depth(in km), respectively. Also, in the above equations, y specifies the data coverage of estimation; when y=0 it gives the median value and y=1 it covers 84 percentile of the data.

3.3.3.3 On the application of formulas

These attenuation curves shown above are derived based on the strong motion data recorded on the surface of ordinary soils and it might be questioned whether these formulas can be applicable to buried ducts and underground tunnels at shallow depths. For this, because these formulas are derived using the data set "FLTDSEL" containing mostly the wave components longer than 0.75 seconds and the wave components are out of the primary period range of strong motions observed on ordinary soils(usually 0.1 sec to 0.5 sec), these formulas may give a good approximation for the peak values of actual underground motions in shallow depths.

When the peak ground motions of the practical design base layer

defined practically by SPT-value larger than 50 or by shear wave velocity higher than 300 m/sec respectively are required, the peak ground motion (PGM) values calculated by the above equations can be divided by 1.5 and 1.2 for PGA and PGV, respectively; Figure 3.3.11 illustrates the distribution of the acceleration amplification factors of the surface layers of fifty five substations located in the Kanto area, in which the mean acceleration amplification factor between the ground surface and the design base layer is about 1.5. Similarly, the mean velocity amplification factor was about 1.2.

3.3.4 REFERENCES

(1) Toki, K., Aseismic design of structures, New system of Civil Engineering(JSCE editor), Vol. 11, Gihoudou, pp.62-63, 1981(in Japanese).

(2) Fukumori, Y., M. Sako, T. Kikuta, Y. Yanabu and K. Toki, Detection of dispersion characteristics of apparent wave velocity, Research Activities from '80 to '84, Earthquake Engineering Research Group, Research Report No. 84-01, School of Civil Engineering, Kyoto Univ., 1984.

(3) Sakurai A., C. Takahashi, C. Kurihara and H. Yajima, Seismic capability of buried pipelines in view from ground strains during earthquakes, Report of the Central Research Institute for Power Industries, No. 69807, 1970.

(4) Katayama, I., Investigative Study of Ground Motions for Existing Substations, a consulting report for Tokyo Electric Power Co.(TEPCO), Inc. by Tokyo Electric Power Services Co., Ltd.(TEPSCO), pp. 114, 1981(in Japanese).

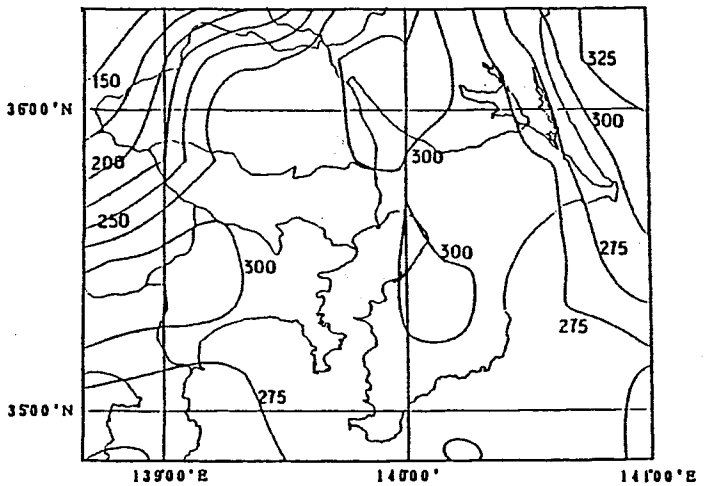

Return period 75 years

(a)

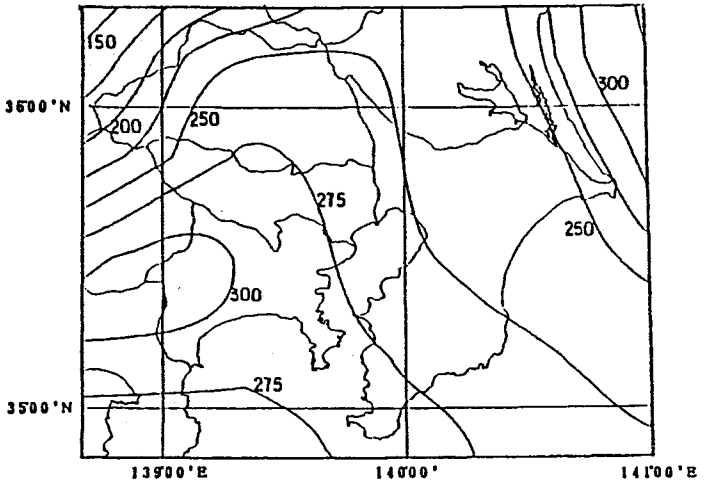

Return period 75 years

(c)

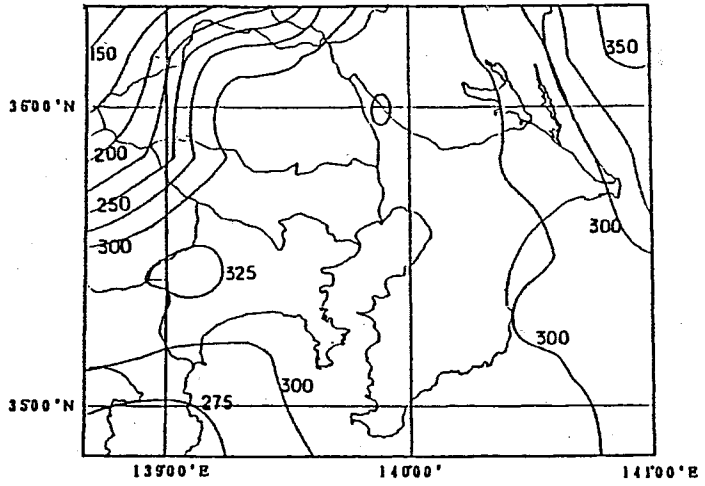

Return period 100 years

(b)

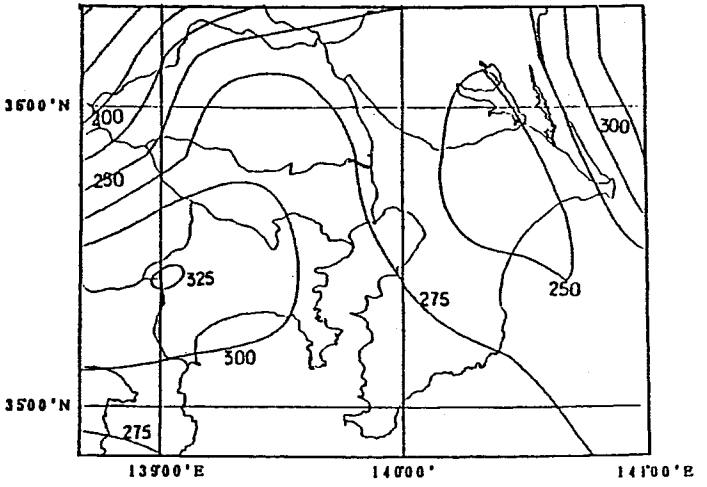

Return period 100 years

(d)

Figure 3.3.1 Iso-seismal maps for 75 and 100 years of expectancy; (a) and (b) for the case of Type I curve, and (c) and (d) for Type II curve are used, respectively

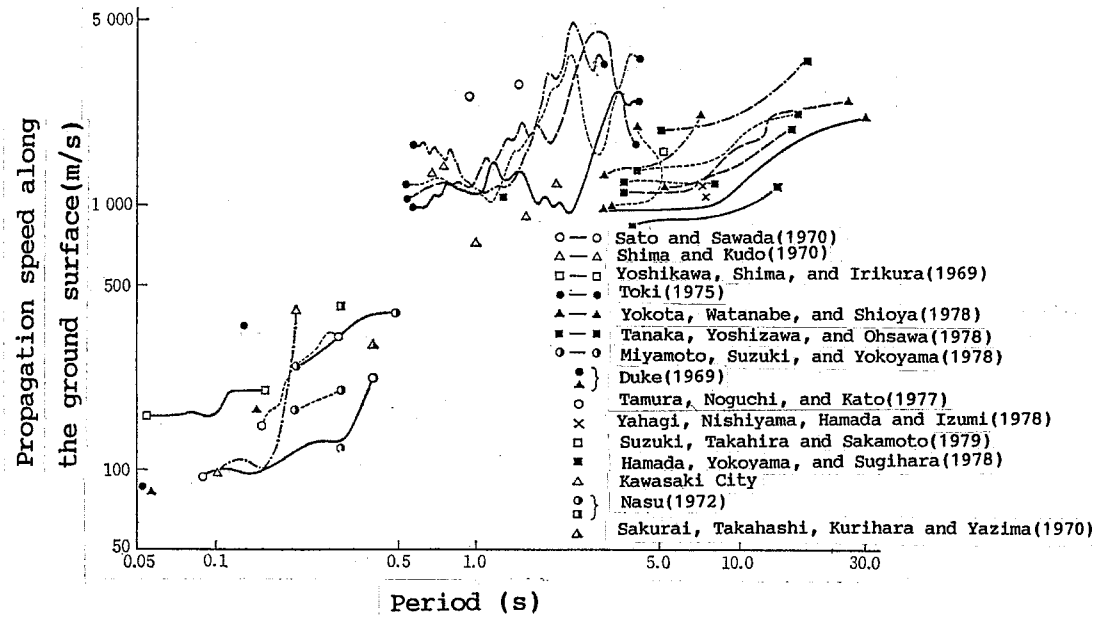

Figure 3.3.2 Examples of the observed propagation speed at the ground surface (After Toki, 1981)

Table 3.3.1 The peak acceleration and velocity data used for regression analysis (Filtered; FLTDSEL)

Date of Event	M	H	Observation Site	Epi. Dist. (km)	S C	Max. Acc. (gal)		Max. Vel. (kine)	
						Comp 1	Comp 2	Comp 1	Comp 2
1963/08/04 20:43	5.1	39	KT014	35.0	2	.0159	.0031	2.5	0.3
1966/04/05 17:51	5.4	4	CB020	8.0	3	.0344	.0000	5.6	0.0
1966/04/05 17:51	5.4	4	(2)	4.0	2	.1194	.0371	14.2	4.6
1966/04/05 17:51	5.4	4	(3)	3.0	2	.0620	.0474	8.7	7.7
1966/04/17 10:22	4.7	6	(2)	4.0	2	.0074	.0051	0.9	0.8
1968/04/01 09:42	7.5	37	KS002	60.0	3	.1526	.0970	27.7	15.3
1968/04/01 09:42	7.5	37	SK006	80.0	3	.1429	.1069	16.5	12.3
1968/05/16 09:48	7.9	20	HK013	159.0	3	.0209	.0202	4.5	4.4
1968/05/16 09:48	7.9	20	TH014	187.0	1	.0158	.0157	2.8	2.7
1968/ 5/16 19:39	7.4	20	AOMORI	193.0	3	.0556	.0414	8.7	8.1
1968/05/16 19:39	7.4	20	HK013	75.0	3	.0130	.0100	3.2	2.4
1968/05/23 04:29	6.3	50	TH014	78.0	1	.0025	.0011	0.3	0.1
1968/06/12 22:42	7.2	31	TH014	81.0	1	.0185	.0142	2.5	2.2
1968/07/01 19:45	6.1	68	TK056	58.0	3	.0457	.0402	6.9	4.9
1968/07/05 20:28	6.4	44	TH005	62.0	3	.0292	.0176	4.4	2.5
1968/08/07 17:00	5.7	68	HK004	32.0	2	.0168	.0138	2.1	1.9
1968/10/08 09:50	5.3	73	KT004	38.0	3	.0087	.0063	1.1	0.9
1968/11/14 03:42	6.0	40	TH014	83.0	1	.0022	.0009	0.3	0.1
1969/04/21 16:19	6.5	39	KS002	43.0	3	.0380	.0349	4.7	4.2
1969/09/09 14:15	6.6	29	AC017	101.0	3	.0256	.0226	3.0	2.9
1970/ 1/21 2:33	6.7	25	CHIYODA BRIDGE	87.9	3	.0425	.0300	6.5	4.9
1970/01/21 02:33	6.7	25	HK013	46.0	3	.0247	.0228	4.6	4.0
1970/04/01 23:23	5.8	75	TH014	17.0	1	.0116	.0062	1.5	1.0
1970/07/26 07:41	6.7	47	KS002	21.0	3	.0523	.0470	7.9	7.3
1970/07/26 16:10	6.1	47	KS002	21.0	3	.0119	.0114	1.5	1.4

Table 3.3.1 (Continued)

Date of Event	M	H	Observation Site	Epi. Dist. (km)	S C	Max. Acc. (gal)		Max. Vel. (kine)	
						Comp 1	Comp 2	Comp 1	Comp 2
1970/10/16 14:26	6.2	5	YUUHEI BRIDGE	24.1	3	.0420	.0387	7.6	6.9
1970/10/16 14:26	6.2	5	YUUHEI BRIDGE	24.1	3	.0500	.0410	9.2	6.7
1971/ 1/ 5 6: 9	6.1	44	KINUURA	54.2	3	.0619	.0396	7.1	4.7
1971/ 1/ 5 6: 9	6.1	44	TOYOHAMA BRIDGE	42.3	3	.0449	.0218	5.5	2.6
1971/01/05 06:09	6.1	44	KK026	64.0	3	.0430	.0294	5.0	4.4
1971/02/26 04:27	5.5	37	CB030	27.0	2	.0269	.0232	4.5	3.0
1971/ 7/23 7: 7	5.3	10	SAKAIGAWA BRIDGE	16.3	1	.0224	.0106	2.8	2.1
1971/08/02 16:25	7.0	45	HK004	196.0	2	.0371	.0307	6.6	5.0
1971/10/11 19:16	5.2	40	KT050	12.0	2	.0286	.0090	3.9	1.1
1972/05/11 09:45	5.8	63	HK004	33.0	2	.0241	.0217	3.4	3.4
1972/10/26 22: 2	4.3	10	OCHIAI BRIDGE	10.6	3	.0140	.0043	1.7	0.8
1973/ 3/27 11: 8	4.9	60	KANNONZAKI	34.0	1	.0160	.0041	2.3	1.0
1973/06/17 12:55	7.4	41	HK004	112.0	2	.1226	.0787	24.8	13.4
1973/11/19 22:02	6.4	56	TH033	107.0	3	.0266	.0194	2.8	2.2
1974/03/03 13:50	6.1	49	KT036	39.0	2	.0594	.0311	7.7	5.5
1974/07/08 14:45	6.3	45	KT036	73.0	2	.0120	.0089	2.0	1.8
1974/09/04 18:20	5.6	52	TH029	42.0	2	.0197	.0175	2.4	2.2
1974/11/16 8:32	6.1	44	P.W.R.I KASHIMA	55.0	3	.0722	.0637	9.0	9.0
1974/11/16 08:32	6.1	44	KT036	38.0	2	.0525	.0260	7.2	4.0
1975/04/21 02:35	6.4	12	KS014	41.0	2	.0087	.0077	2.3	1.7
1978/ 1/14 12:24	7.0	5	SHIMIZU-MIHO	71.4	2	.0685	.0274	12.6	6.4
1978/ 1/14 12:24	7.0	5	YAMASHITA-HEN	80.9	3	.0174	.0141	3.2	2.4
1978/ 1/15 7:31	5.8	20	SHIMIZU-MIHO	41.0	3	.0274	.0102	3.5	2.0
1978/ 2/20 13:37	6.7	50	KAIHOKU BRIDGE	85.8	1	.0153	.0139	3.7	2.2
1978/ 6/12 17:14	7.4	40	TAIRA BRIDGE	165.4	3	.0611	.0541	14.0	10.0
1978/ 6/12 17:14	7.4	40	ONAHAMA	175.8	3	.0377	.0319	6.9	5.5
1982/ 3/ 6 19:16	5.3	30	HOSOSHIMA-S	70.0	3	.0117	.0110	1.5	1.4
1982/ 3/ 7 8:14	5.5	60	KASHIMA-ZOKAN-S	61.0	3	.0089	.0080	1.1	1.1
1982/ 4/19 11:25	4.7	50	KAWASAKI-DAIGO	66.0	3	.0023	.0010	0.3	0.2
1982/ 6/ 1 5:13	6.1	40	OFUNATO-BOCHI	63.0	1	.0143	.0048	1.9	0.5
1982/ 6/ 1 5:13	6.1	40	MIYAKO-S	110.0	1	.0024	.0023	0.5	0.5
1982/ 7/23 23:23	7.0	30	KASHIMA-ZOKAN-S	118.0	3	.0229	.0215	4.0	3.7
1982/ 8/12 13:33	5.7	30	YAMASHITA-HEN	64.0	3	.0143	.0127	2.7	2.2
1982/ 8/23 14:50	5.3	80	SHIOGAMA-KOJYO	79.0	3	.0128	.0095	2.0	1.6
1983/ 5/26 12: 2	7.7	14	AKITA-S	107.0	2	.1439	.1067	28.0	23.8
1983/ 6/ 9 21:49	6.1	23	AKITA-S	113.0	2	.0218	.0179	4.8	2.9
1983/ 6/ 9 22: 4	6.0	14	AKITA-S	115.0	2	.0096	.0076	1.7	1.5
1983/ 6/21 15:26	7.1	6	AOMORI-S	160.0	3	.0565	.0266	7.8	6.1

Table 3.3.2 Results of regression analysis using the Japanese strong motion data (Non-filtered; NONFSEL)

Reference	Derived Formula	(O/C) av.	(O/C) σ
Type I curves Donovan type	$A=0.0652 \cdot \exp(0.494M)(R+0.58)^{-0.656}$ (G)	1.00	1.55
Type II curves Combined Kanai-Seed type	$A_0=(1/Tp) \cdot 10^B$ (gal) $Tp=(0.000512M-0.00143)(X+100)+0.02$ (After Seed et al, 1968) $B=0.339M-P\log_{10}X+Q$; $X=(D^2+H^2)^{1/2}$ $P=-0.217-13.08/X$; $Q=-4.37-3.4/X$	.983	1.55
Type III curves I. Katayama Type I (Campbell type)	$A=0.0284 \cdot \exp(1.285M) \cdot (D+0.300 \cdot \exp(0.752M))^{-1.54}$ (G)	1.03	1.58
Type IV curves I. Katayama Type II (Nakamura et al Type)	$A=0.1125 \cdot \exp(0.269M) \cdot (D+H)^{-0.339} \exp(-0.480 \cdot \exp(-0.694M) \cdot D)$ (G)	1.00	1.53

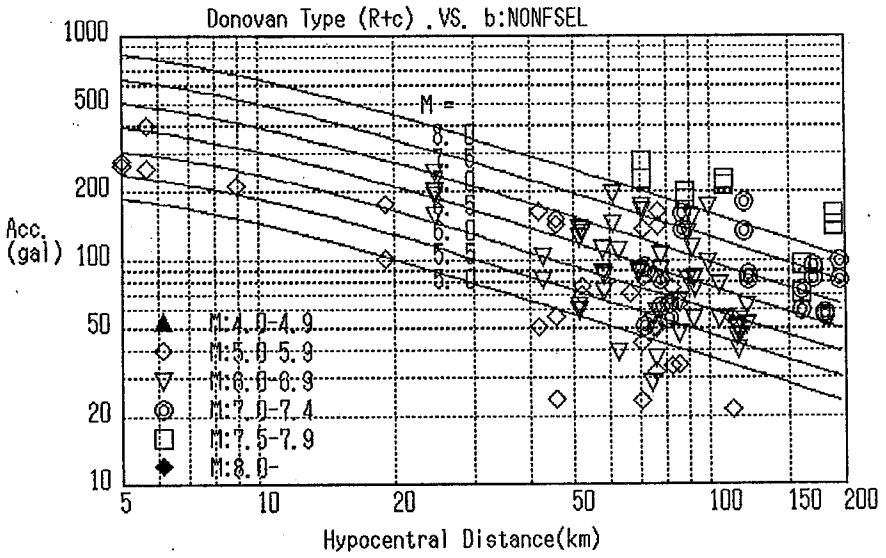

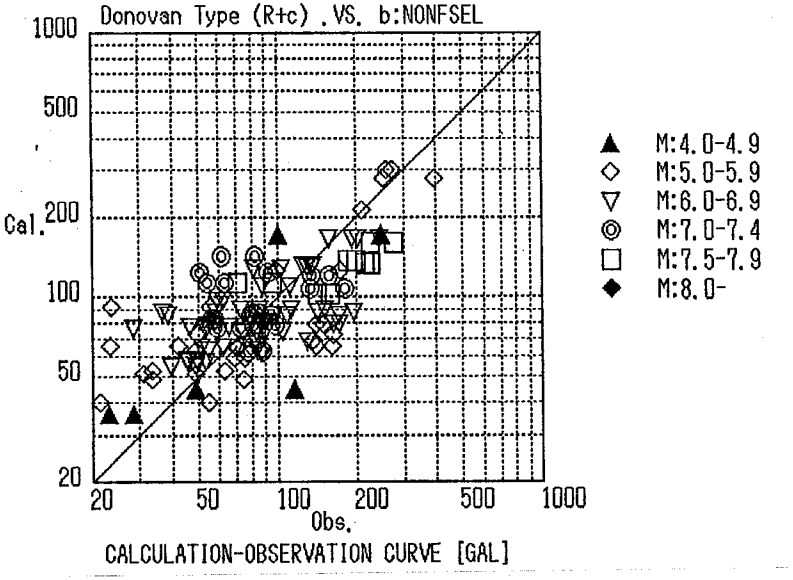

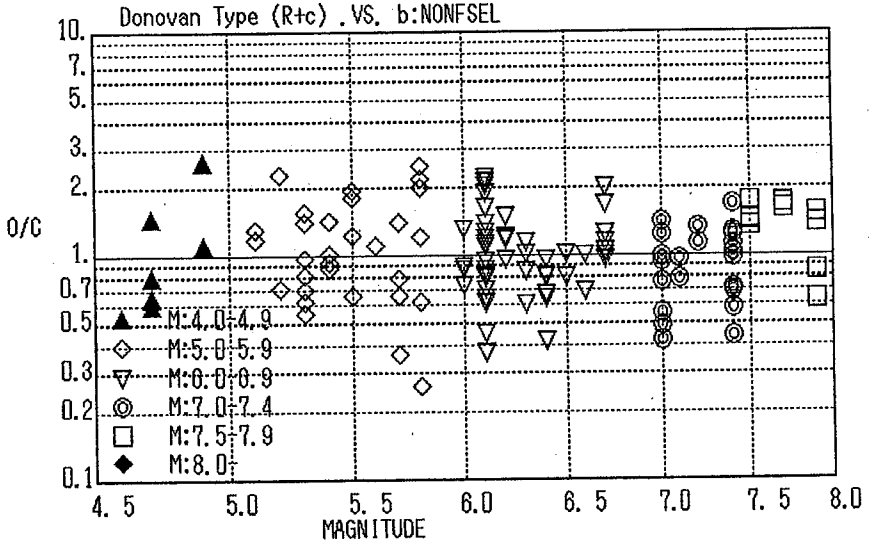

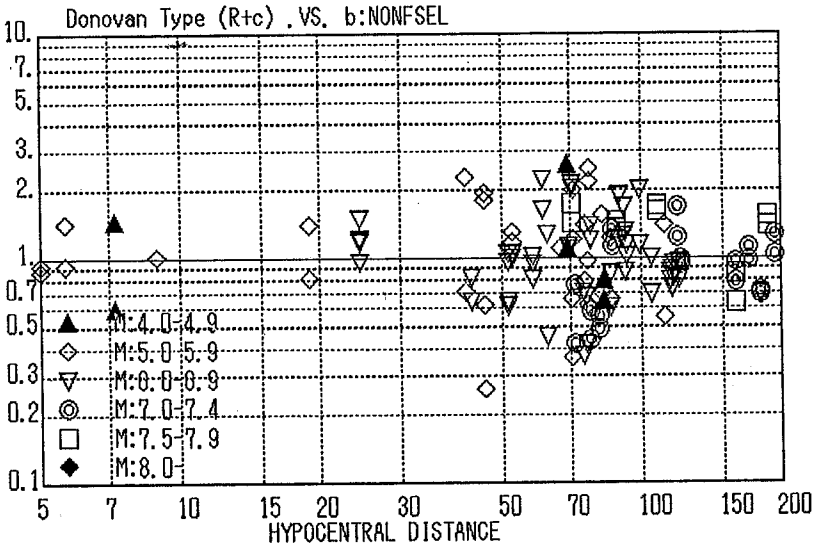

Figure 3.3.3 Result of regression analysis for Type I curve;
$A=0.0652 \cdot \exp(0.494M)(R+0.58)^{-0.656}$ (G)

NUMBER OF DATA = 125
AVERAGE FITTNESS(O/C) = 1.00139
STANDARD DEVIATION = 1.55177

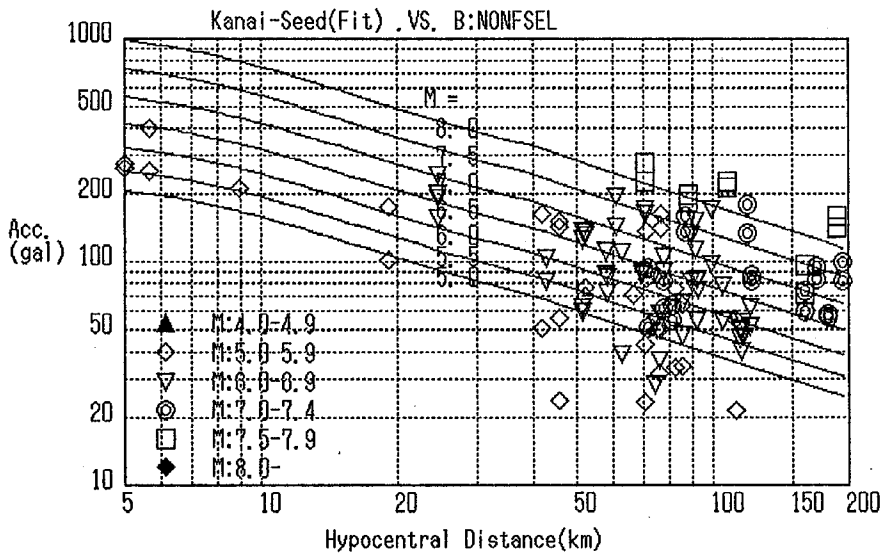

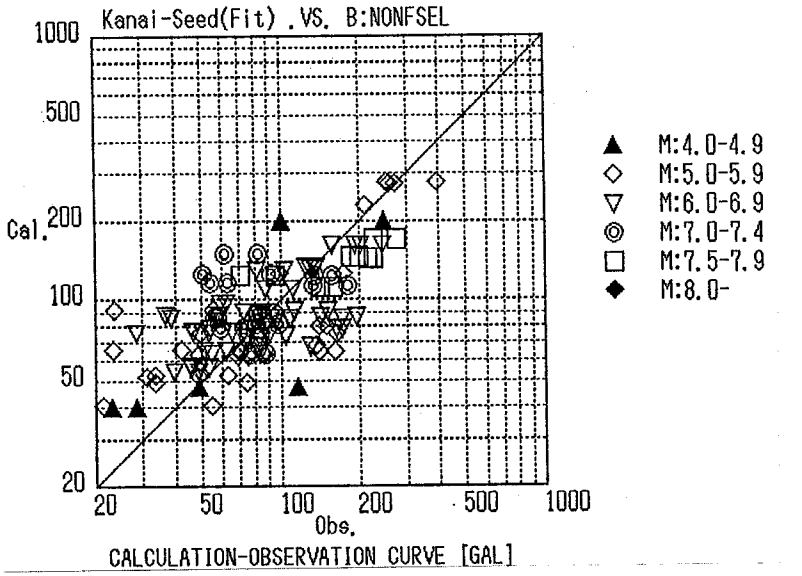

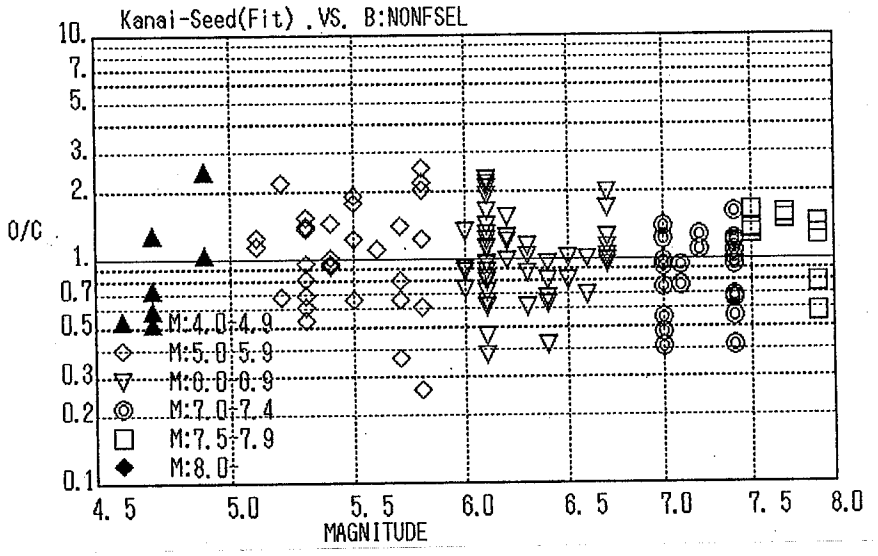

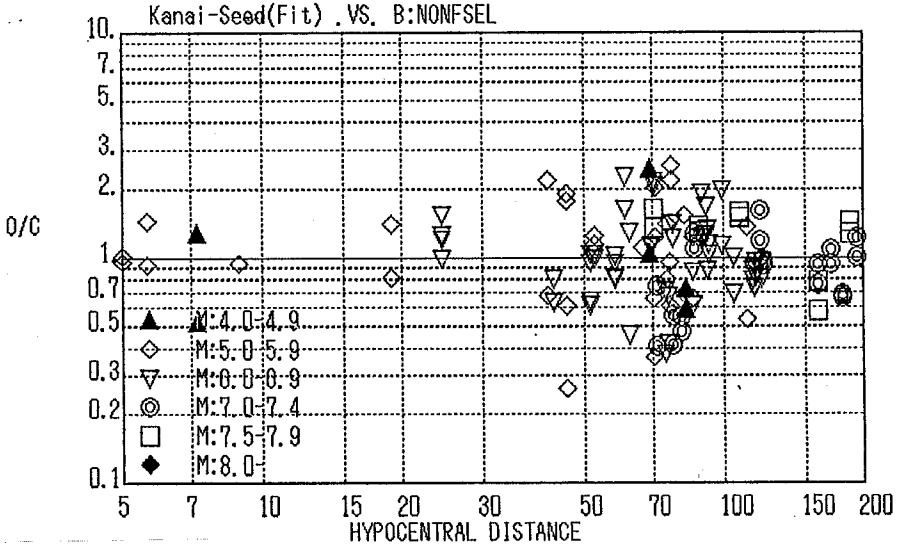

Figure 3.3.4 Result of regression analysis for Type II curve; $A_0=(1/Tp)\cdot 10^{B}$; $Tp=(0.000512M-0.00143)\cdot(X+100)+0.02$; $B=0.339M-P\log_{10}X+Q$; $X=(D^2+H^2)^{1/2}$ $P=-0.217-13.08/X$; $Q=-4.37-3.4/X$ (gal)

NUMBER OF DATA	=	125
AVERAGE FITTNESS(O/C)	=	.983144
STANDARD DEVIATION	=	1.55174

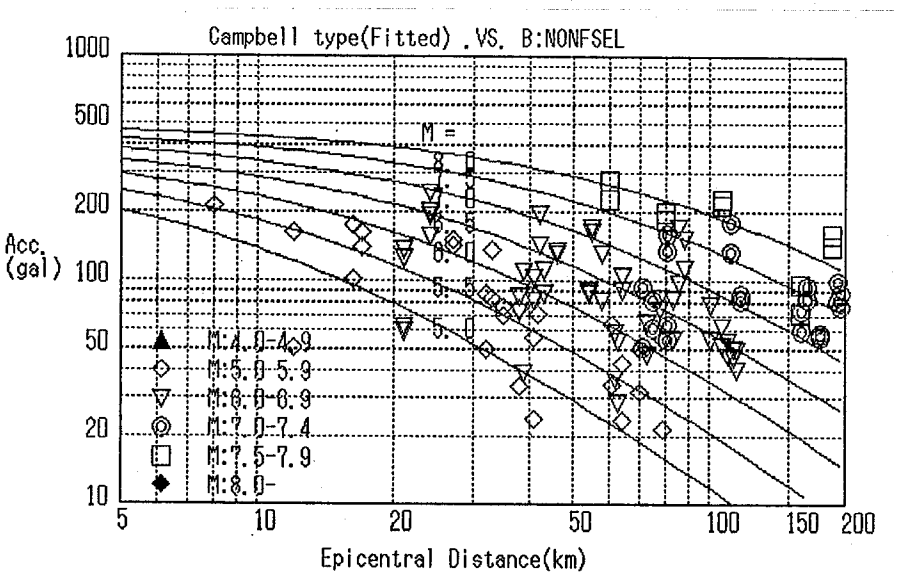

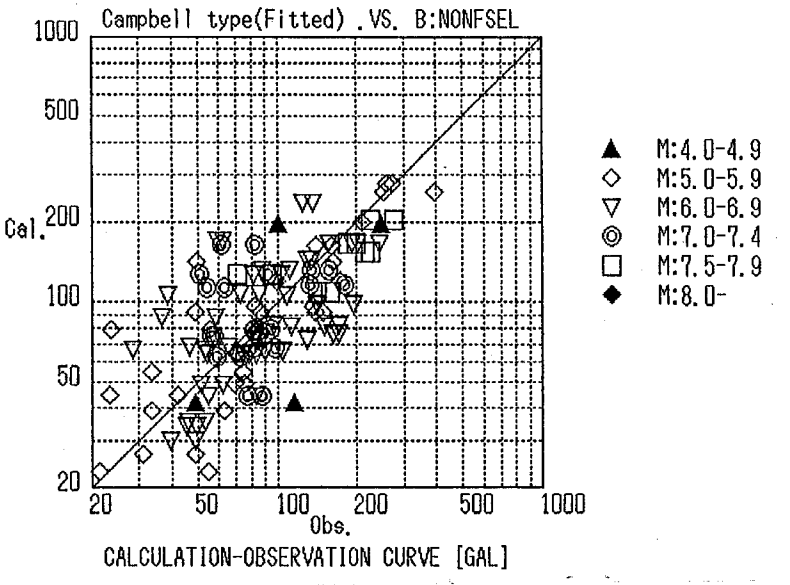

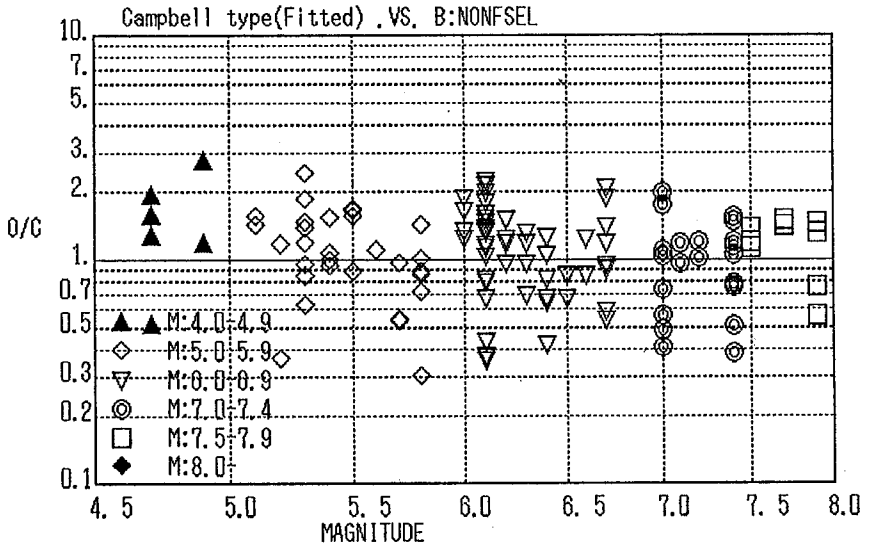

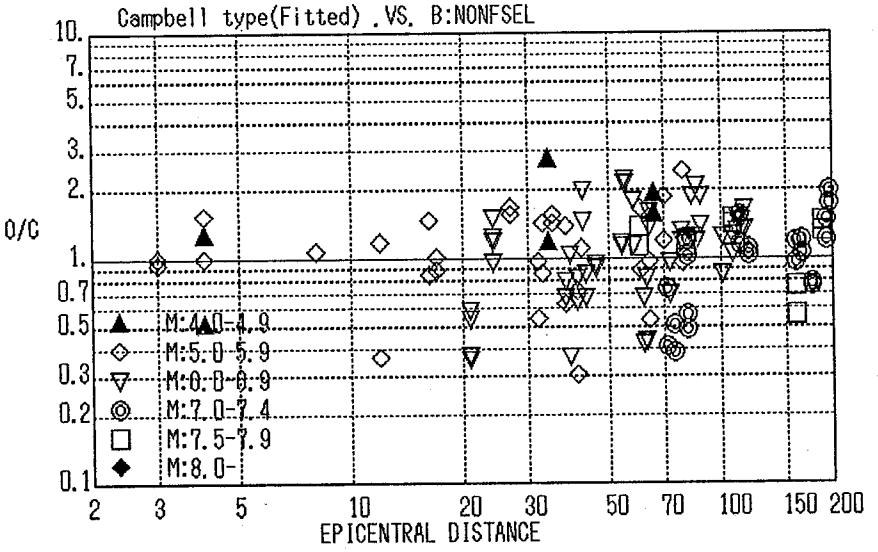

Figure 3.3.5 Result of regression analysis for Type III curve;
$A=0.0284 \cdot \exp(1.285M) \cdot [D+0.300 \cdot \exp(0.752M)]^{-1.54}$ (G)

NUMBER OF DATA	=	125
AVERAGE FITTNESS(O/C)	=	1.03319
STANDARD DEVIATION	=	1.5825

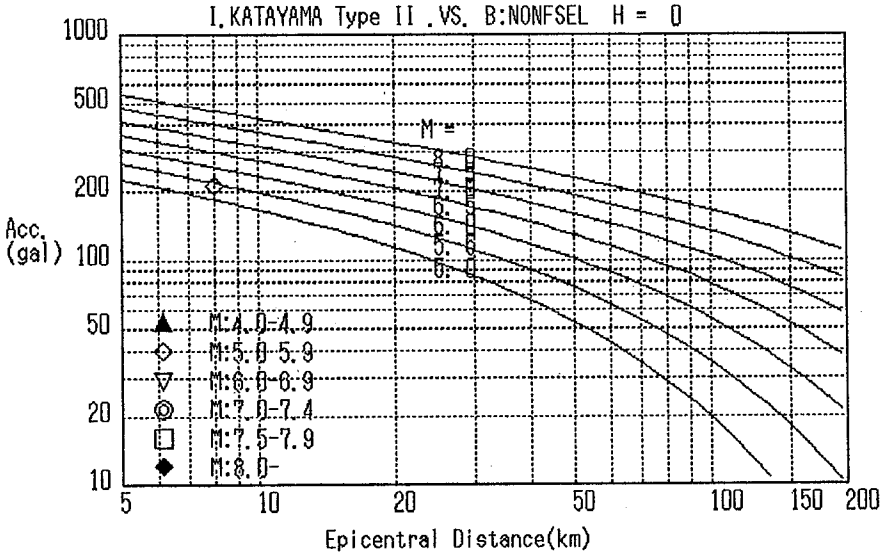

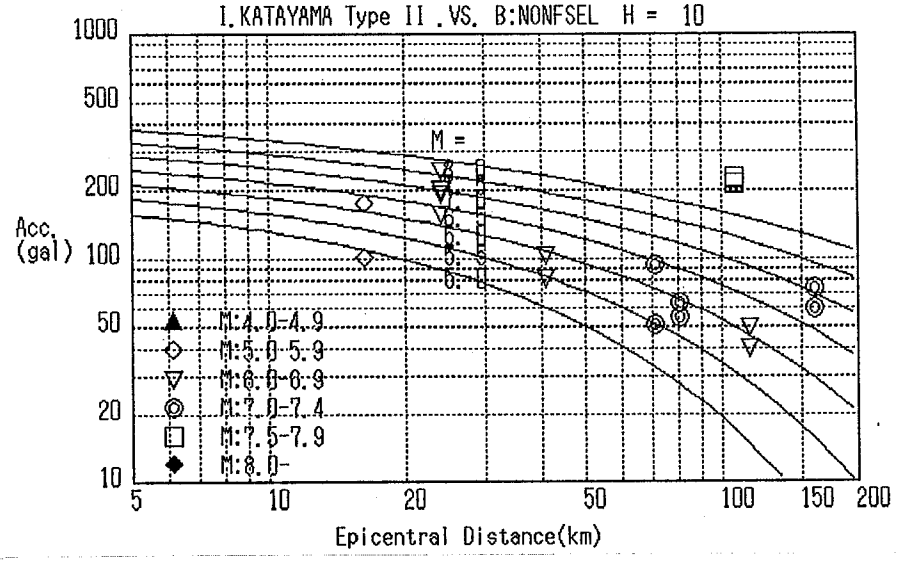

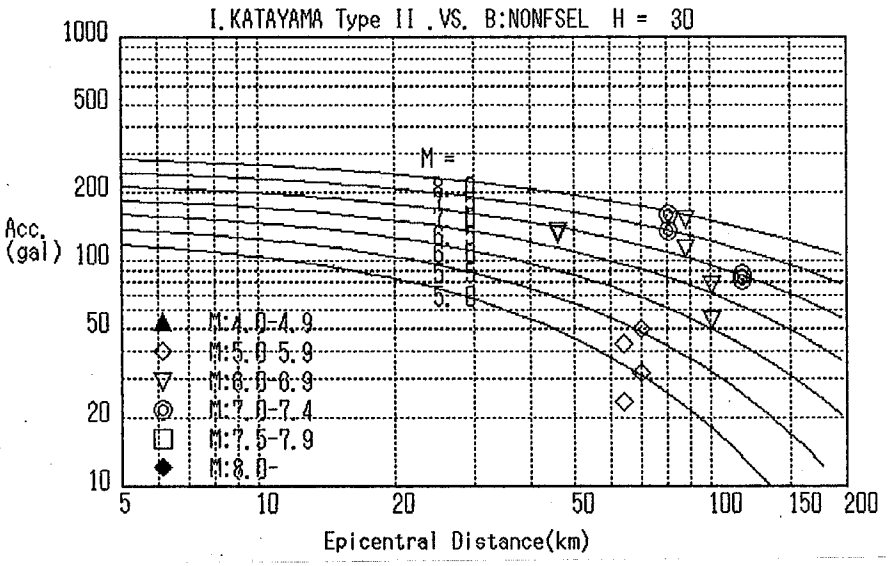

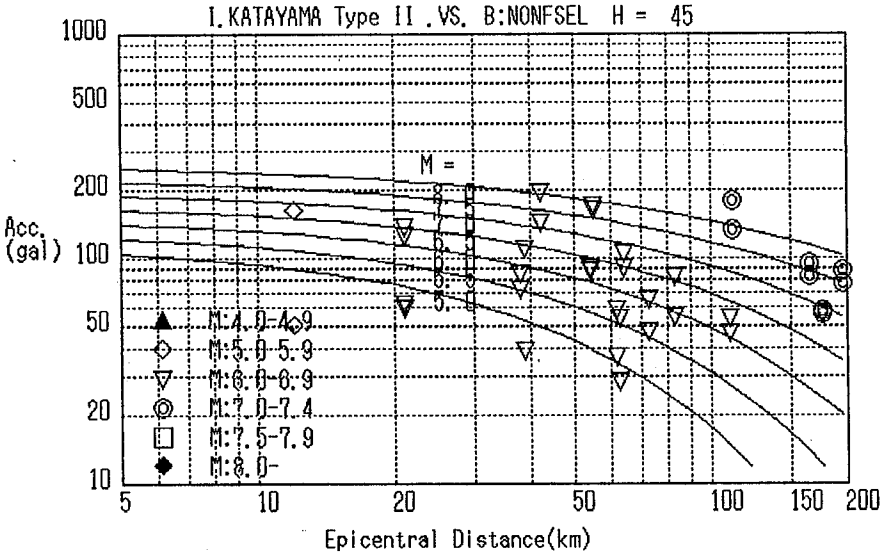

Figure 3.3.6 Result of regression analysis for Type IV curve;

$$A = 0.1125 \cdot \exp(0.269M)[D+H]^{-0.339} \cdot \exp[-0.480 \cdot \exp(-0.694M) \cdot D] \quad (G)$$

NUMBER OF DATA = 125
AVERAGE FITTNESS(O/C) = .999412
STANDARD DEVIATION = 1.52873

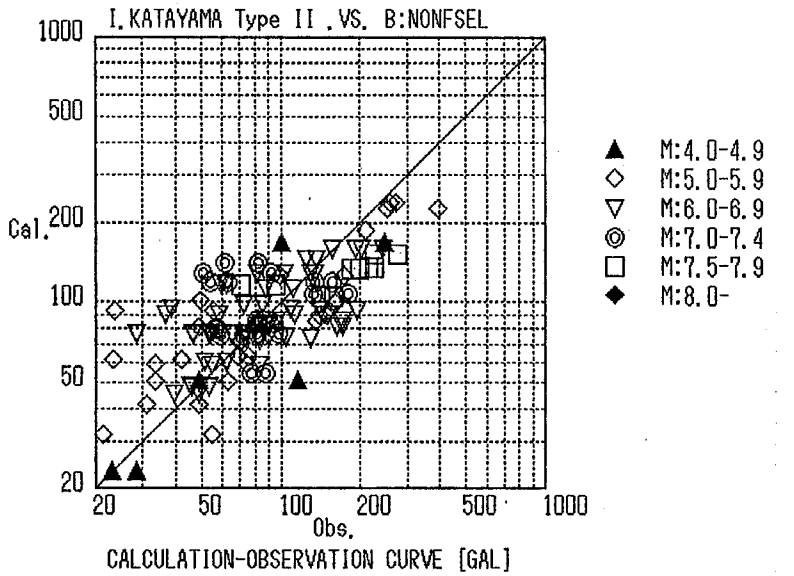

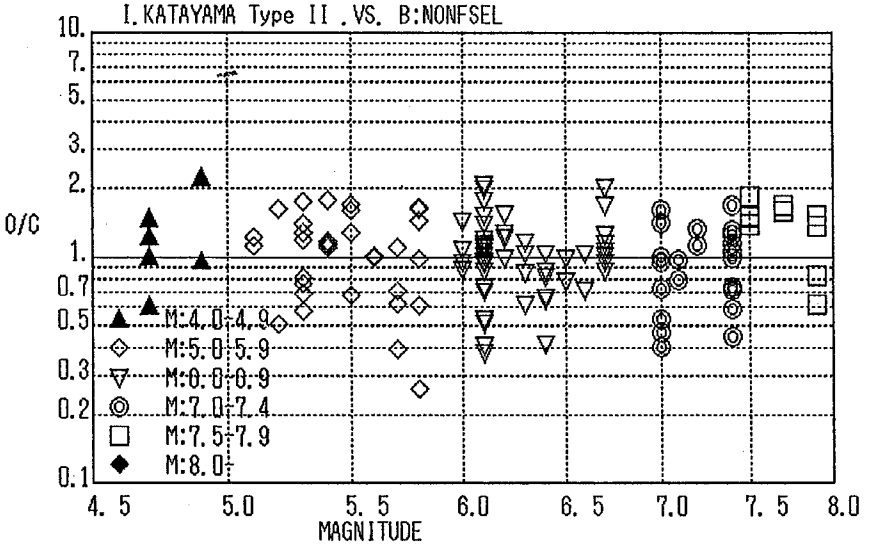

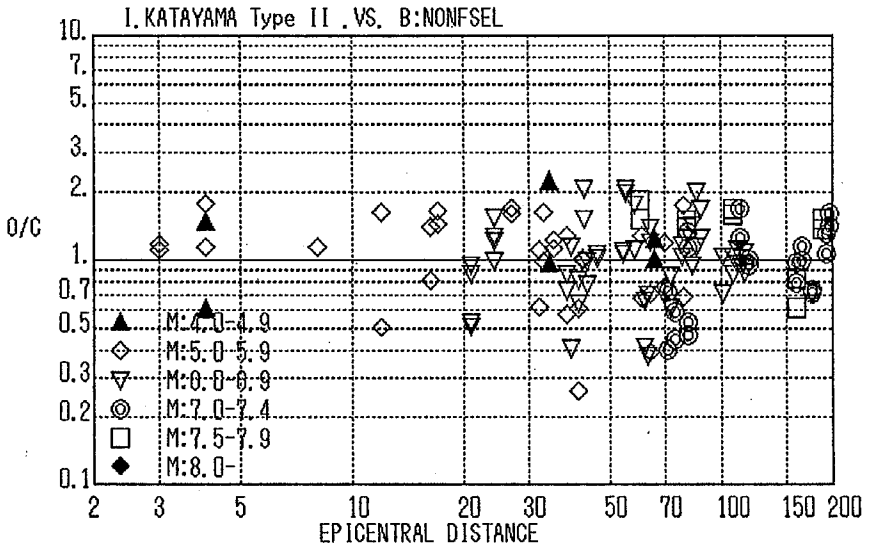

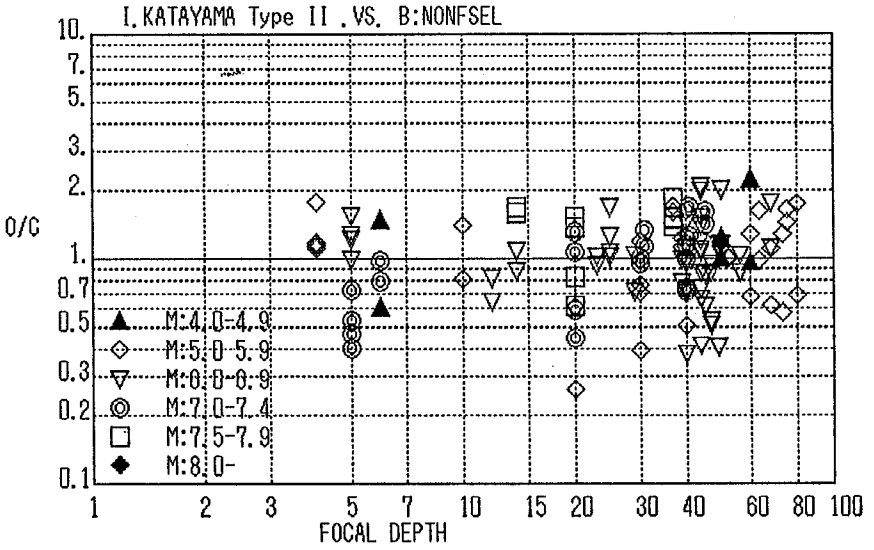

Figure 3.3.6 (Continued)

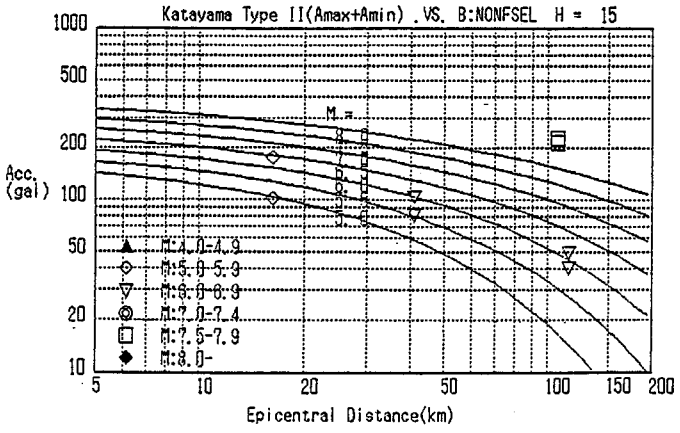

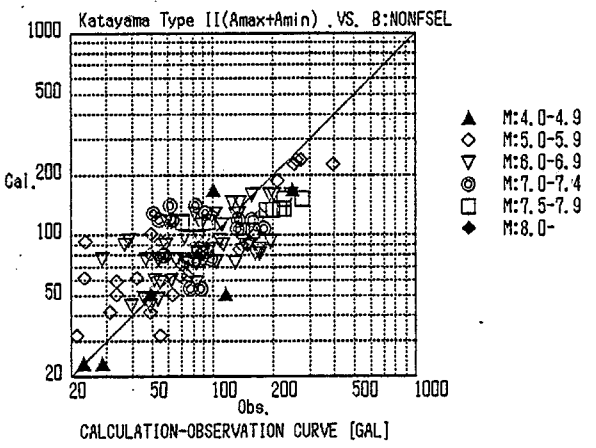

NUMBER OF DATA = 125
AVERAGE FITTNESS(O/C) = .999953
STANDARD DEVIATION = 1.52873

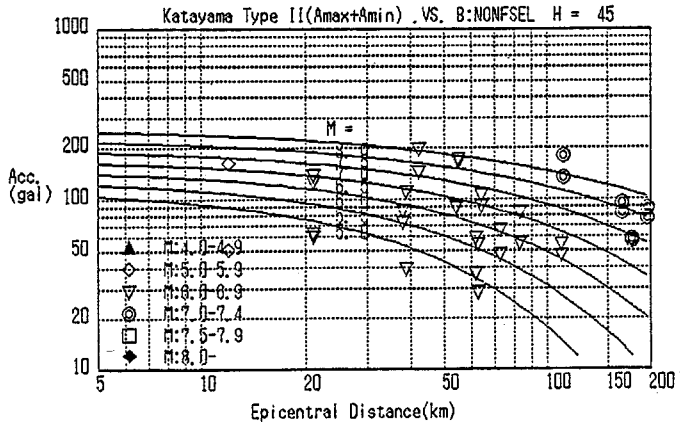

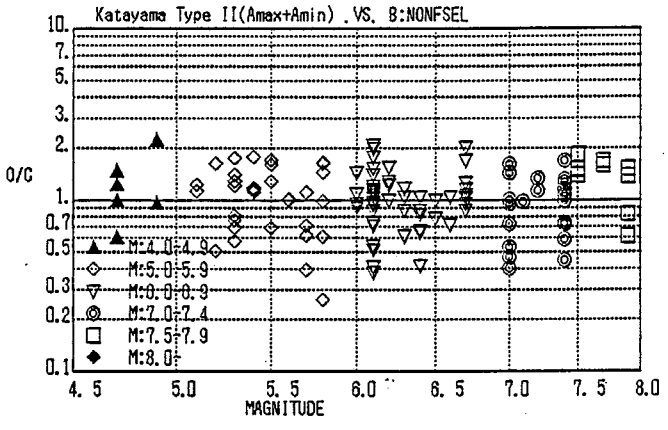

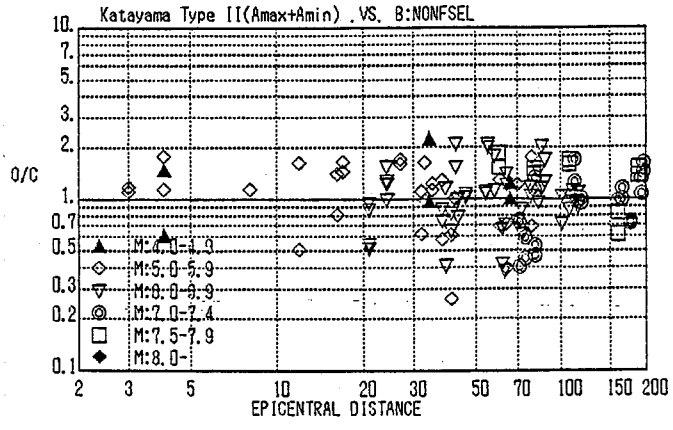

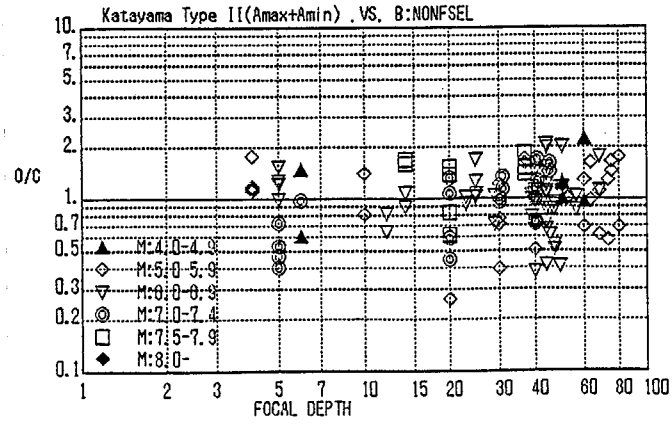

$$A_{max}=0.1125\exp(0.269M)[D+H]^{-0.339}\exp[-0.480\exp(-0.694M)D](1.53)^{Y}$$

in 980cm/sec^2

Figure 3.3.7 Proposed formula of PGA for structures on the ground surface of ordinary soil

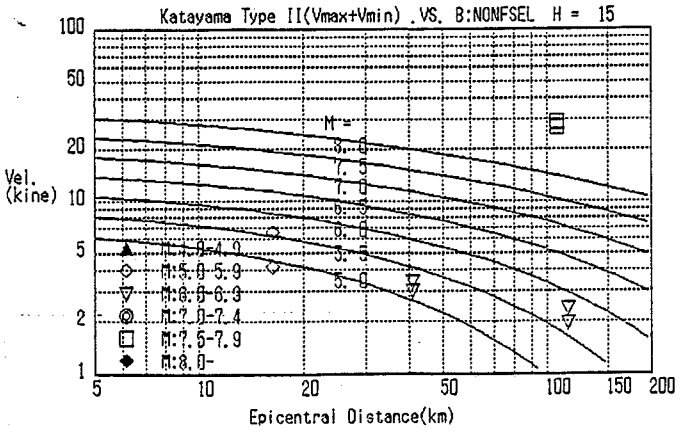

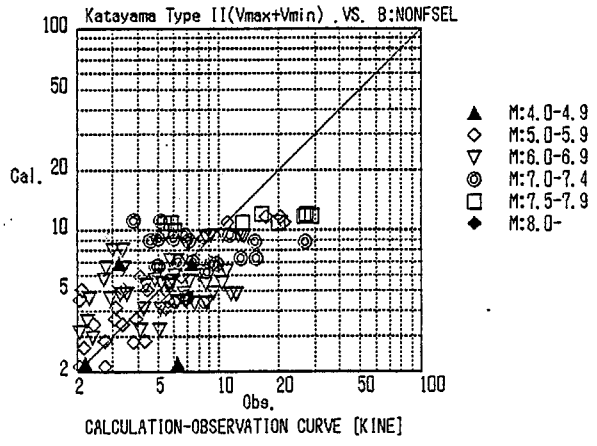

NUMBER OF DATA = 125
AVERAGE FITTNESS(O/C) = .999848
STANDARD DEVIATION = 1.67409

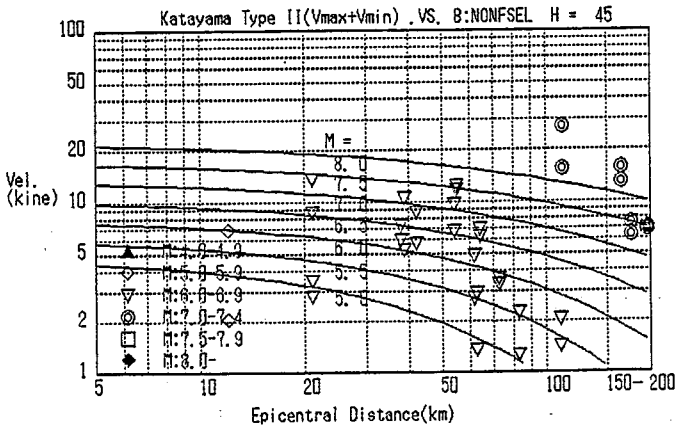

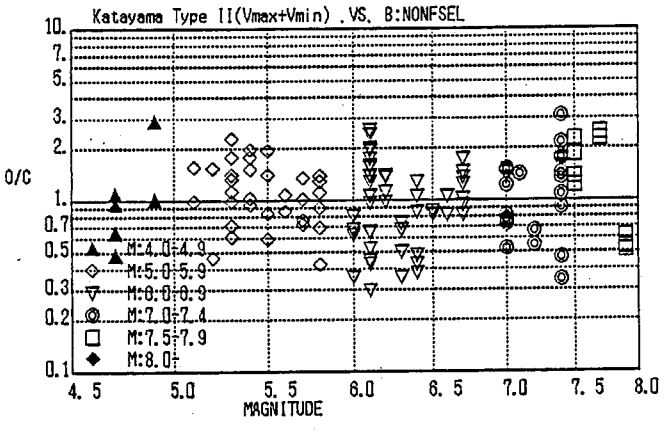

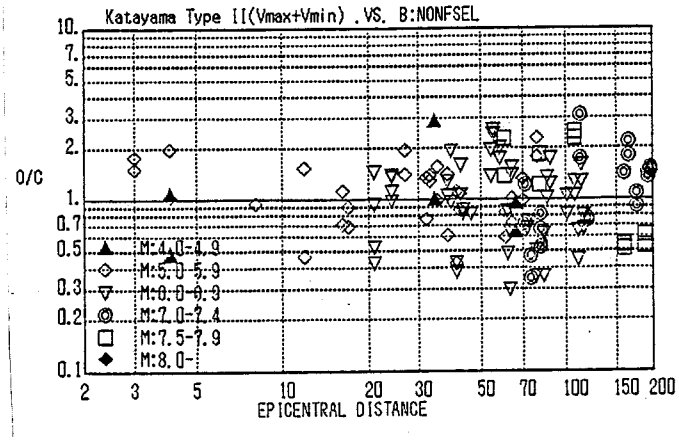

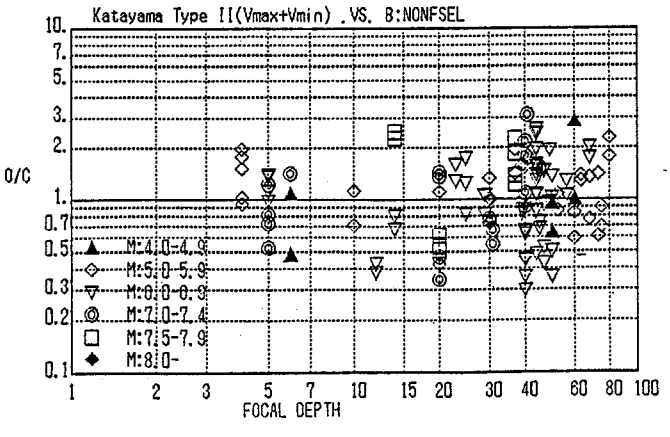

$$V_{max}=1.5302\exp(0.514M)[D+H]^{-0.373}\exp[-0.923\exp(-0.859M)D](1.67)^{Y}$$

in cm/sec

Figure 3.3.8 Proposed formula of PGV for structures on the ground surface of ordinary soil

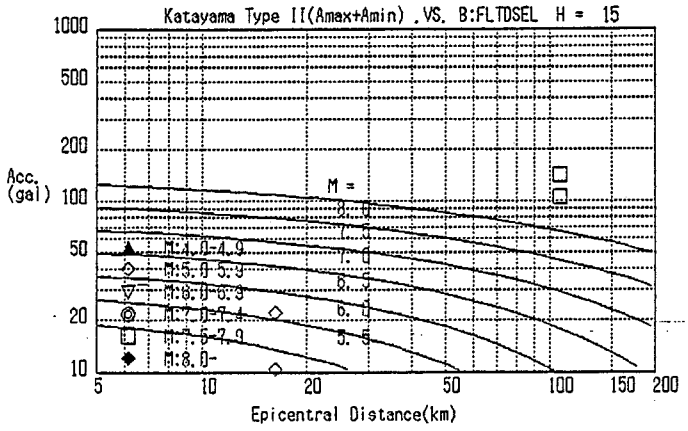

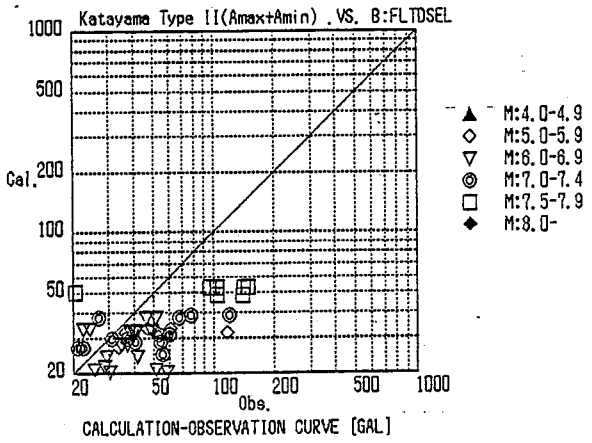

NUMBER OF DATA = 125
AVERAGE FITTNESS(O/C) = .999676
STANDARD DEVIATION = 2.27619

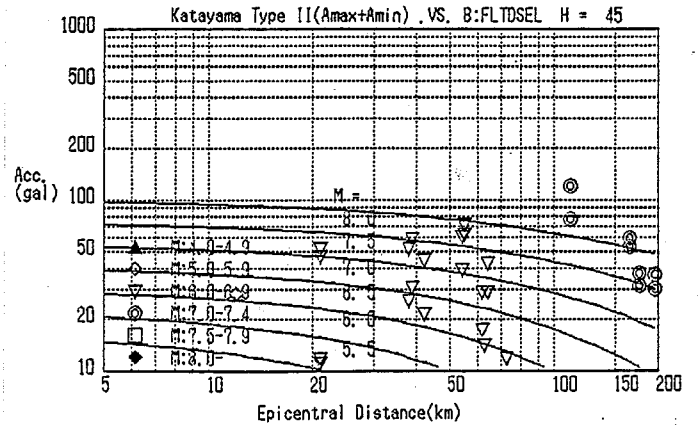

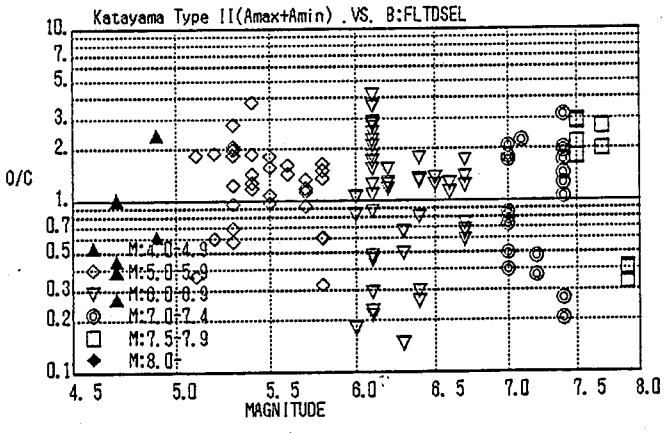

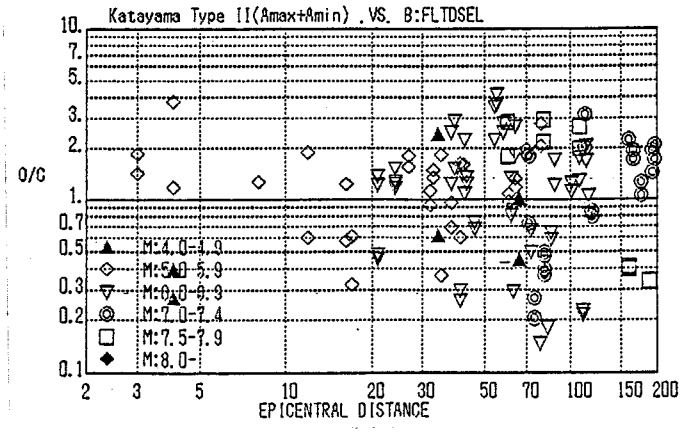

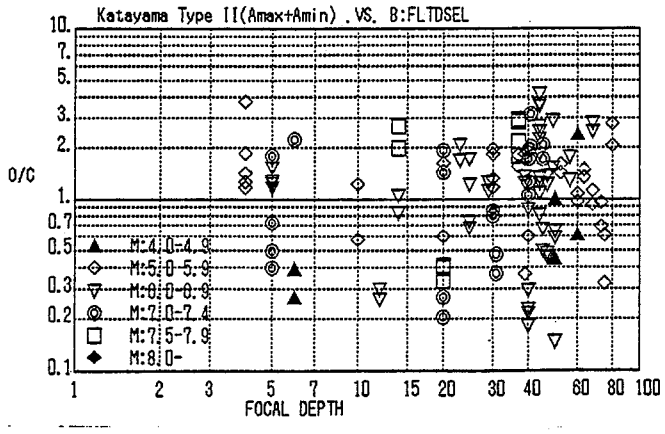

$$A_{max}=0.0023\exp(0.602M)[D+H]^{-0.261}\exp[-1.097\exp(-0.817M)D](2.28)^{Y}$$

in 980cm/sec^2

Figure 3.3.9 Proposed formula of PGA for structures buried in the ground of ordinary soil

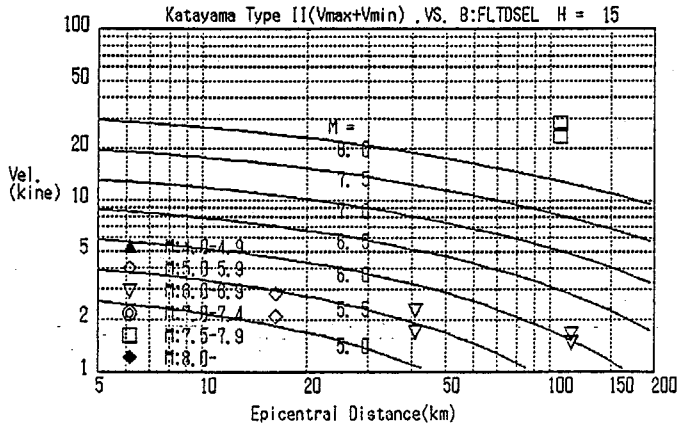

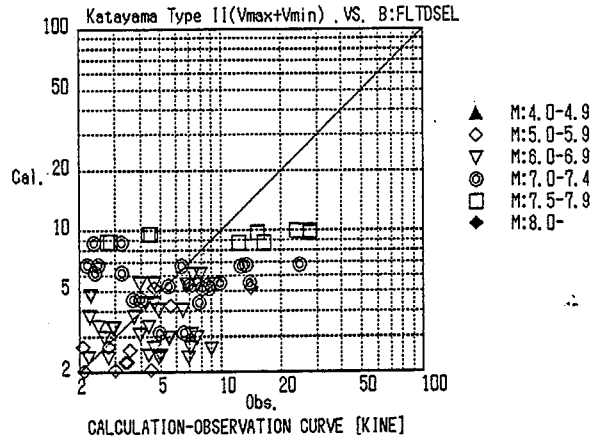

NUMBER OF DATA = 125
AVERAGE FITTNESS(O/C) = 1.00014
STANDARD DEVIATION = 2.23261

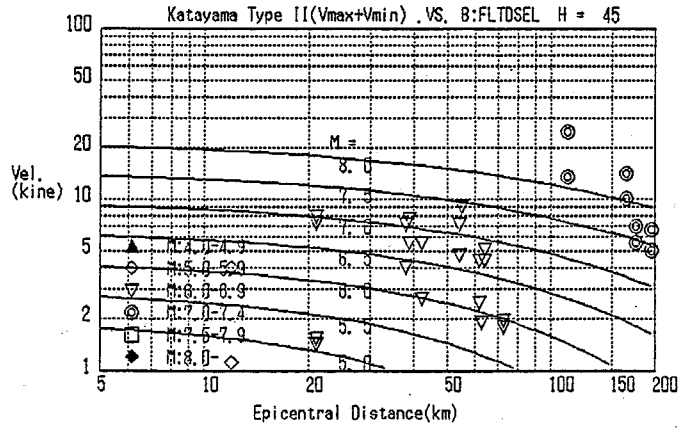

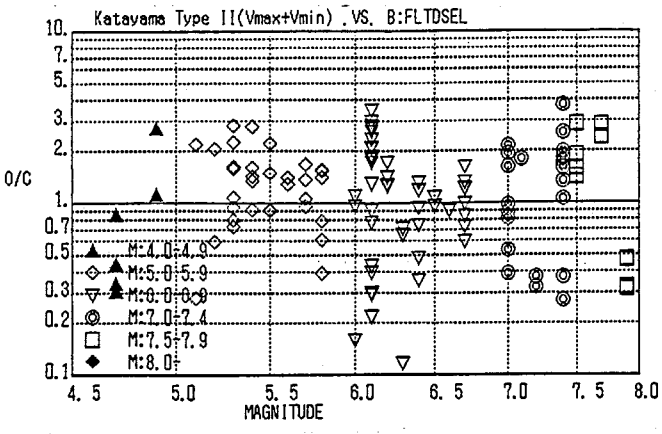

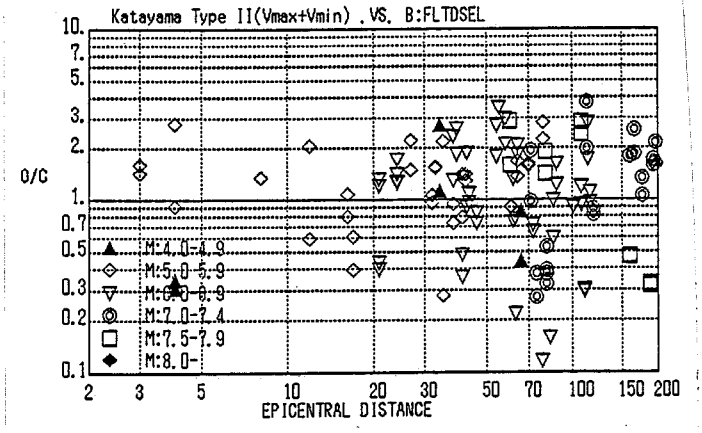

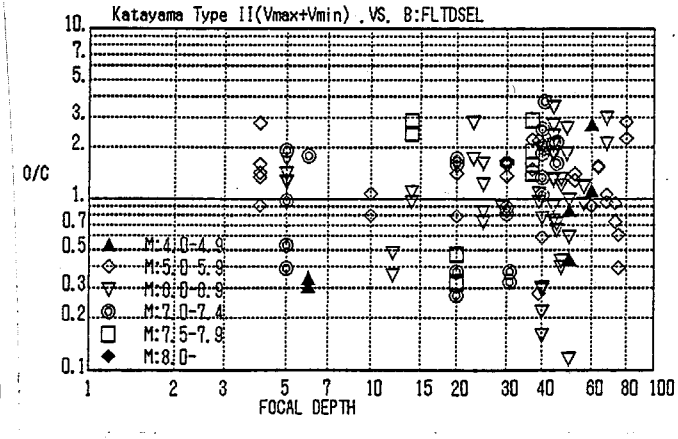

$$V_{max}=0.1615\exp(0.798M)[D+H]^{-0.393}\exp[-0.700\exp(-0.810M)D](2.23)^{Y}$$

in cm/sec

Figure 3.3.10 Proposed formula of PGV for structures buried in the ground of ordinary soil

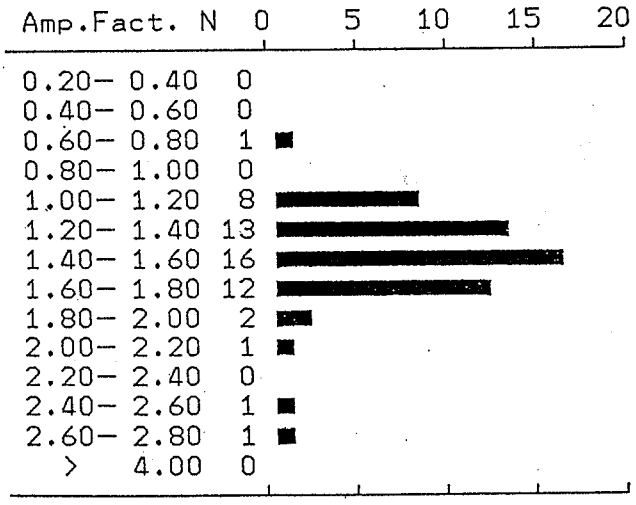

NUMBER OF UNUSED DATA = 0
NUMBER OF DATA USED = 55
AVERAGE AMPLIFICATION = 1.46

Figure 3.3.11 Distribution of maximum acceleration amplification factor of the surface layer of 55 substaions in the Kanto area.

3.4 SEISMIC RISK MAP OF KANTO AREA

3.4.1 INTRODUCTION

Recent advances of electronic technology and communication networks have given increased importance on the reliability of lifeline systems of power transmission system in Metropolitan Tokyo as an international center of economy and politics. The power transmission system in Tokyo consists of many types of structures, including overhead power transmission and transform facilities, underground substations, and power transmission tunnels and ducts.

Because the seismic activity of the Kanto area is known by the remarkable activity of earthquakes both in the crust and the upper-most mantle in some particular regions, a three-dimensional seismic source model which considers the three-dimensional distribution of seismically active regions is proposed.

With the above situation, for studying the seismic hazard of Kanto area, the seismic hazard analysis model which combines a three-dimensionally distributed seismic source regions and the attenuation curves reflecting the effect of focal depths on the peak ground accelerations was proposed(I.Katayama, 1985 and 1986).

Further, as the power transmission system includes various types of structures constructed on the surface ground as well as underground and the horizontally propagating waves rather than vertically incident waves are of primary concern for the longitudinal response of buried tunnels and ducts, two sets of new attenuation curves derived earlier are applied to the seismic hazard of the Metropolitan area.

In this study, the above new attenuation curves are combined with the same seismic source model and the results are presented by contour maps applicable to both on surface and underground structures, in terms of the expected peak ground acceleration and velocity for some representative exposure times. Some of the results of this study were already used for the seismic reliability analysis of the power transmission system of Tokyo which contains various types of structures included in the the system (I.Katayama and others, 1989).

3.4.2 CONSTRUCTION OF SOURCE MODEL FOR SEISMIC HAZARD ANALYSIS

3.4.2.1 Characteristics of seismic activity of the Kanto area

In and around the Kanto area, earthquakes both in the crust and the upper-most mantle are occurring in cluster in some particular regions. The spatial distribution and focal mechanisms of earthquakes of this area have been systematically studied using microearthquakes located by sensitive seismograph networks of the Earthquake Research Institute, University of Tokyo (ERI), and the Tokai-Kanto Observational Network of the National Research Center for Disaster Prevention (NRCDP). Observational information has been periodically reported in the circular of the Coordinating Committee for Earthquake Prediction (CCEP).

Fine spatial distribution of earthquakes in the Kanto area has been studied by Tsumura (1973), who showed a fine structure of the seismicity and the seismic zones using the earthquakes observed and located by ERI; he showed Figure 3.4.1, where the double-planed seismic zone of the Pacific plate (PAC) subducting westwards beneath the Eurasian plate (EUR) at the Japan trench and the seismic zone of the Philippine Sea plate (PHP) dipping northeastwards from the Izu Pennisula which seems to meet the PAC at depths between 60 and 80 km beneath northern and central Chiba, and southern and southwestern Ibaragi. The relationship of the subducting plates with the seismic activity around the plates are suggested also from the distribution of hypocenters as shown in Figures 3.4.2(a) to (c)(ERI, 1982), for example.

Hamada and Kasahara(1981) proposed a plate model, as shown in Figure 3.4.3, which explains the tectonics of the Kanto-Tokai area as the place of interaction of the previous three plates beneath the area.

Using the earthquake data collected by ERI from 1970 through 1974, the characteristics of some active regions of stable seismicity within the Kanto district were studied by Usami and Watanabe(1976) and they derived 21 "earthquake nests" with the range of focal depth shown in Figure 3.4.4.

Maki and others(1980) studied the focal mechanisms of 49 subcrustal earthquakes which occurred in the seismically active regions of the Kanto area by using the data collected from the observational stations of ERI, the seismological bulletins of Japan Meteorological Agency (JMA) and the International Seismological Center(ISC). They found that the spatial distribution and the focal mechanisms of shallower earthquakes located at a depth of about 45 km below the western end of Ibaragi Prefecture and

along the upper boundary of PAC are consistent with the underthrusting PAC to the northwest. Deeper earthquakes occurring in depths around 70 km within the PAC beneath the western part of Chiba Prefecture and the southwestern part of Ibaragi Prefecture are explained as those caused by the subcrustal collision of PAC with PHP. They showed the distribution of the epicenters in the Kanto area with vertical sections as are shown in Figures 3.4.5(a) to (c). These figures clearly show the three-dimensional feature of the earthquake activity in the Kanto area as the previous researchers have already emphasized with the relationship to subducting plates under the district.

Ishida(1984) examined the spatial distribution of earthquake hypocenters and the three-dimensional velocity structure of P wave for the Kanto-Tokai District by using 3,025 events among 5,000 relocated events which occurred within the area bounded by latitudes 33.7 N and 37.0 N and longitudes 136.7 E and 141.7 E during the period from January to December 1980. Figure 3.4.6(a) shows the distribution of the relocated hypocenters with different depths and magnitudes by different symbols and Figures 3.4.6(b) and (e) are the vertical sections which show the distribution of hypocenters within the area as shown in the top of these figures (Figures 2, 4, 5, 6 and 7 of Ishida(1984)).

3.4.2.2 Contour map of upper surface of seismically active zones

To perform the seismic hazard analysis of the Metropolitan Tokyo based on the characteristics described above of the seismic activity of the Kanto area, a model as shown in Figure 3.4.7 is constructed, which specifies three-dimensionally seismically active surface planes of the seismically active zones along the subducting plates. On the three-dimensional surface of the model, each seismically active region will be distributed. Those earthquakes that occur within the region and with the focal depths deeper than the depth of the region are projected onto the surface plane of the region and combined with the attenuation curves, resulting in a conservative evaluation of the peak ground motions.

For this purpose, a series of figures plotted by Ishida(1984, Figs. 2 to 14) were used to draw smooth upper surfaces of seismically active zones along PHP and PAC, some examples of which are drawn on the previous figures. Thus drawing the smooth curves designated to become the upper surfaces of seismically active zones on the vertical sections, the contour maps showing the upper surface trace of seismically active zones for both PHP and PAC were obtained as shown in Figures 3.4.8(a) and (b).

3.4.2.3 Seismically active fields

The hypocenter distribution of about 2,100 events larger than 3.0 in magnitude located by JMA during the period from January 1961 to December 1982 is plotted in Figure 3.4.9(a) with different symbols of varying size for different focal depth and magnitude, respectively. These events were replotted separately with the three depths, shallower than 20 km, 20 km to 30 km, and 30 km to 100 km, as in Figures 3.4.9(b) to (d). The earthquakes or earthquake activities which will be taken into account in subsequent part of this chapter are those that fall within the area encompassed by solid lines in these figures.

Before specifying a particular seismic source region as discussed by Usami and Watanabe(1976) of remarkably stable seismicity with seismic parameters, the author divided the seismically active regions of the Kanto area into the following three fundamental fields, based on the characteristics of the seismicity of the Kanto area as previously reviewed, the overall distribution of earthquakes, focal mechanisms and implied tectonic force field caused by subduction of PAC and PHP under EUR, and also taking the model proposed by Hamada and Kasahara(1981) into reference:

(1) Seismically active field I which basically represents the seismicity within the two subducting plates and along the intersecting zones of PHP and PAC; The earthquakes at depths shallower than 20km in and around Izu Pennisula and Southeastern Yamanashi, the earthquakes within both plates up to the depth of 100 km, and the earthquakes occurring in cluster beneath Southwestern and Southern Ibaragi and Central and Northern Chiba at depths between 40 and 80 km are the representative earthquakes of this field.

(2) Seismically active field II which represents basically the remarkable zones of seismicity in the east off the Bousou Pennisula inbetween the lower half of EUR(the zone deeper than 21 km) and the upper surface planes of seismically active zones of PAC and PHP as are shown in Figure 3.4.8.

(3) Seismically active field III which represents the widely distributed earthquake activity at depths shallower than 20 km in the EUR except the regions cited in (1), the sea of Kashima, and the sea off Bousou Pennisula.

The regions as classified in the above three fields appear separately in these figures as noted by the symbols, I, II, and III, because

these fields are attributed mainly to three kinds of three-dimensionally subducting plates or the accompanying interaction among these plates. The meaning of the suffices attached therewith are explained later.

3.4.2.4 Seismically active source regions

There are reports of several small regions in the Kanto area where current seismic activity is stable and frequent in cluster and some past disastrous-earthquakes were located inside or close to the areas as pointed out by Usami and Watanabe(1976) and Maki and others(1980).

By following these references and through preliminary study of b-value analysis using the events plotted in Figures 3.4.9(a), the earthquakes were attributed to smaller source regions as shown separately with depths in Figures 3.4.9(b) to 3.4.9(d).

As for the source regions in the seismically active field I, I_{A1} denotes the source region known as Southeastern Yamanashi. I_{A2} and I_{A3} are the very shallow source regions known as in and around Izu Pennisula. I_{B1} and I_{B2} are the Southwestern to Southern Ibaragi region and the Northern to Central Chiba region, respectively as noted by Hamada and Kasahara(1981) and Maki and others(1980). I_{C1} to I_{C3} are often referred to as the seismically active region of the Sea of Kashima and off Chosi. Other regions denoted by I_{A4}, I_B, I_{B3} and I_C in these figures are not so remarkable earthquake clustering regions but were defined somewhat arbitrarily. The seismicity of the above regions come directly from the tectonic stress within the subducting PHP and PAC or by the collision of both plates(I_{B1} and I_{B2}). Future earthquakes of each region in this field I are assumed to occur at the depth of the region located on the surface plane shown in Figure 3.4.8.

Among those regions in the seismically active fields II, only II_{C1} was meaningful to be specified as a stable source region by the F-test of b-value with 5 % significance level. Those regions, II_A, II_B, and II_C were gathered into one region and will be determined for its seismicity parameters. Thus the above regions are attributed to the seismic activity by the interaction of PHP and PAC with EUR. Future earthquakes of each region of this field II are assumed to occur at the depths of 21 km.

Earthquakes at depths shallower than 20 km in the crust are basically infrequent in the area of concern except the regions noted as III_{C1} and III_{C2}, the sea of Kashima and the sea off Bousou Pennisula, and the

active geologic features relating to the seismicity is also unknown. Therefore, those earthquakes shallower than 20 km and not classified into the above seismically active source regions were all included as III_{BC}. Future earthquakes of each region of this field III are assumed to occur at a depth of 10 km.

The subtotal number of divided seismically active regions are 12, 2 and 3 for respective seismically active fields I, II and III, and the total is 17.

As for such great earthquake as the 1923 Kanto Earthquake with estimated recurrence period more than a few times the period of the earthquake data, it is very difficult to evaluate suitably its contribution to the seismicity of the area. In this study, the type of earthquake along the Sagami trough was considered in the seismicity of the region I_B in Figure 3.4.9(a).

3.4.2.5 Seismicity parameters

With the above interpretation of the seismicity and the spatial distribution of the seismically active regions, the seismicity parameters of each source region were determined using the following earthquakes and the truncated magnitude-frequency relationship.

The parameters to define the magnitude-frequency relation of each source region were determined by assuming the truncated Gutenberg and Richter's law;

$$\log n(M)=a-bM \qquad M \leq M_{max}$$

$$n(M)=0 \qquad M>M_{max} \tag{3.4.1}$$

where $n(M)dM$ is the number of events between M and M+dM, M_{max} is the upper limit of magnitude.

Let M_{min} be the lower limit of magnitude above which the data is complete, the cumulative number N(M) of events of magnitude larger than M is given by

$$\log N(M) = \log \frac{[\exp(b\cdot\ln(10)(M_{max}-M)-1)]}{[\exp(b\cdot\ln(10)(M_{max}-M_{min})-1)]} N(M_{min}) \tag{3.4.2}$$

where M_{min} is determined by considering the minimum level of magnitude to

fit the data linearly for equation (3.4.1) and M_{max} from the past maximum event, respectively. $N(M_{min})$ is the total number of events of magnitude larger than M_{min}.

It is desirable to determine the seismicity parameters representing those events possible to cause some damages in the near-field; however, the number of such events may become insufficiently small for obtaining reliable parameters if the source regions are divided into small areas.

For this reason, first those earthquakes of magnitude larger than 3.0 occuring at depths up to 100 km from the Supplementary Volume No. 6 to the seismological bulletin of JMA for the period from 1926 through 1960, the seismological bulletins of JMA from 1961 through December 1982 and the earthquakes in the catalogues by Utsu(1979, 1982) from 1885 through 1925 were collected. Those events defined for depths of "vs", "s", and "d" in the last catalogues were assigned depths of 10 km, 60 km, and 99 km, respectively.

Next, using this data base, the M-log(N) relationship of each seismically active region was examined by plotting similar figures as shown in Figure 3.4.10.

Finally, clipping the minimum magnitude M_{min} at 5.5, the parameters of equation (3.4.2) for each region were determined by best fit analysis for the portion of the M-N curve larger than M_{min}. The selected events larger than 5.5 in magnitude and shallower than 100 km in depth are plotted within the encompassed area of Figure 3.4.11. The total number of such earthquakes was 632. The determined truncated M-log(N) relations of each seismically active field and that of the total area are shown by the solid lines in Figure 3.4.11. The parameters of the identified small source regions marked by suffices I_{A1}, I_{B1}, etc in Figures 3.4.9(b) to (d) are shown in Table 3.4.1.

As previously described, the seismicity along the Sagami trough including the 1923 Kanto great earthquake was considered in the region I_B and the maximum event of the region was assumed to be M7.9 and the return period of this maximum event is determined to be about 100 years; this seems more conservative than the assumed return period of this type of great earthquakes as obtained by Kakimi and others (1967).

3.4.3 ATTENUATION CURVES FOR ESTIMATING PGA AND PGV

Two sets of attenuation curves for estimating the peak ground

acceleration (PGA) and velocity (PGV) as already given by eqs.(3.3.1) to (3.3.4) are to be used as follows;

For structures on the ground surface;

$$A_{max}=0.1125\exp(0.269M)[D+H]^{-0.339}\exp[-0.480\exp(-0.694M)D](1.53)^{y} \quad (3.3.1)$$

$$V_{max}=1.5302\exp(0.514M)[D+H]^{-0.373}\exp[-0.923\exp(-0.859M)D](1.67)^{y} \quad (3.3.2)$$

and for underground structures;

$$A_{max}=0.0023\exp(0.602M)[D+H]^{-0.261}\exp[-1.097\exp(-0.817M)D](2.28)^{y} \quad (3.3.3)$$

$$V_{max}=0.1615\exp(0.798M)[D+H]^{-0.393}\exp[-0.700\exp(-0.810M)D](2.23)^{y} \quad (3.3.4)$$

where: A_{max} = Peak ground acceleration (PGA), in G
V_{max} = Peak ground velocity (PGV), in kine
M = Magnitude of earthquake, in JMA scale
D = Epicentral distance, in km
H = Focal depth, in km
y = 0; for median curve
y = 1; for median plus one standard deviation curve

3.4.4 SEISMIC HAZARD OF KANTO AREA

3.4.4.1 Seismic hazard maps for the Kanto area

The location of the point for estimating the peak ground motions (e.g., PGA and PGV) relative to the seismically active source regions on the seismically active planes is illustrated in the previous Figure 3.4.7 which is comparable to Figures 3.4.8(a) and (b)). Within a source which is further divided into small unit areas of 5 km square, the occurrence of events is controlled by the M-N relation already given for the region. The unit area is selected as 5 km square for accuracy of calculation and considering the relation of the lower limit of magnitude M_{min} and the size of the rectangular area which was estimated from Utsu(1966);

$$\log S=M-3.7 \quad (3.4.2)$$

where S is the area of after shocks in km^2, and this area is assumed to be equivalent to the source area of magnitude M.

Given a magnitude M_i and the rectangular area equivalent to the

magnitude, $C(M_i)$ the chance of events that may be located within a source region can be computed by moving the rectangular area within the region by every 5 km step; when either the rectangle corresponding to M_i or the center of the rectangle falls within a particular source region in each step, the chance is counted.

Let $C_e(M_i)$ be the chance of PGA (or PGV) at a point on the grid of 10 min. exceeding a given level A_j which is calculated by using an attenuation curve with both the planar distance and the depth from the point to the center of possible source plane equivalent to the event M_i within a source region on the upper surface of the seismically active planes in Figure 3.4.7, and $n(M_i)$ the average number of occurrences per year of event M_i controlled by the prescribed M-N relation, the annual rate of occurrence of PGA (or PGV) larger than A_j (or V_j) at a point from a given source region is obtained as

$$p(A_j)=n(M_i)C_e(M_i)/C(M_i) \qquad (3.4.3)$$

Assuming that the occurrence of events at all sources is not correlated, the contribution of all the source regions are summed to obtain the final annual rate of occurrence at a point. In these calculations, the deviation of a given attenuation curve from the estimated median is considered by taking y in the equations from (3.3.1) through (3.3.4) up to 2.2 and 1.8 times the standard deviations given in these equations for acceleration and velocity, respectively.

The results are usually shown by iso-seismal maps of the expectancy of PGAs and PGVs for various periods, e.g. 50 or 100 years, otherwise by the annual probability of exceedance versus PGAs and PGVs at some particular points of concern.

The calculations of expected PGA and PGV values for various exposure times were performed for each set of attenuation curves for structures on the ground and underground. Figures 3.4.12 to 3.4.15 shows the iso-seismal maps of the expectancy of PGAs and PGVs for 25, 50, 75 and 100 years, in which those shown in (a) and (b) are designated to be applied to structures on the ground and underground, respectively.

3.4.4.2 Annual probability of exceedance

The rate of occurrence of earthquake exceeding a given peak ground motion(PGM) at the point of interest is also converted into the probability of exceedance of PGM by assuming the Poisson distribution;

the probability of exceedance from all sources during a time interval of duration t is

$$P_N=1-e^{-vt} \qquad (3.4.4)$$

where v and t are the mean occurrence rate of earthquakes from all the sources and the time interval.

An example of the seismic hazard in the form of the annual probability of exceedance versus PGAs and PGVs at various points in the Kanto area are shown in Figures 3.4.16.

3.4.5 REFERENCES

(1) Tsumura, K., Microearthquake activity in the Kanto district, Publication for the 50th anniversary of the Great Earthquake, 1923, Earth. Res. Inst., pp.67-87, 1973 (in Japanese).

(2) ERI, Seismicity Maps of the Kanto District, 1971-80, Earthq. Res. Inst., Univ. of Tokyo, Rept. CCEP, Vol. 27, 1982.

(3) Hamada, K. and Kasahara, K., A Plate Model for Explanation of the Tectonics of the Kanto-Tokai Area, (NRCDP), Report of the Coordinating Committee for Earthquake Prediction (Rep. CCEP), Vol. 25, 1981.

(4) Usami, T. and Watanabe, T., Definition and Characteristic Features of a Seismically Active Region (Earthquake Nest) in the Kanto District, Bull. of ERI, Vol.52, pp.379-406, 1977(in Japanese).

(5) Maki,T., I.Kawasaki, and A. Horie, Earthquake Mechanisms Associated with the Conjunction of the Sinking Plates beneath the Kanto District, Central Japan, Bull. ERI, Vol. 55, pp. 577-600, 1980.

(6) Ishida, M., The spatial Distribution of Earthquake Hypocenters and the Three-Dimensional Velocity Structure in the Kanto-Tokai District, Japan, J. Phys. Earth, 32, pp.399-422, 1984.

(7) Utsu, T., The New Catalogue of Earthquakes of M≥6.0 felt in Japan and Smaller Earthquakes which caused Damage in Japan, Bull. Earth. Res. Inst., Vol. 54, 1979(in Japanese).

(8) Utsu, T., Catalogue Large Earthquakes in the Region of Japan from 1885 through 1980, Bull. Earth. Res. Inst., Vol.57, pp.401-463, 1982

(in Japanese).

(9) Kakimi, T., Y. Sato, K. Tsumura and M. Ishida(1976), Seismicity, Crustal Movement and Neotectonics in Kanto District, Symposium on earthquake prediction, pp. 21-45.

(10) Ishida, M., The configuration of the Philippine Sea and the Pacific Plates as estimated from the high-resolution microearthquake hypocenters in the Kanto-Tokai District, Japan, Research Report, National Research Center for Disaster Prevention, 1985 (in press; in Japanese).

(11) Katayama, I. and others, Observational study on the behavior of buried duct, a consulting report to TEPCO for the Fiscal Year 1987, 1988(in Japanese).

(12) Katayama, I. and others, Reliability of Electric Power Transmission Systems in Seismically Active Metropolitan Tokyo, Part 2: Seismic Hazard Analysis, Proc. of the 3rd International Conference on Structural Safety and Reliability, Vol.1, pp.701-708, Anaheim, Los Angeles, Aug. 7-11, 1989.

(13) Utsu, T., After shocks and earthquake statistics (I), J. Fac. Sci., Hokkaido Univ., Ser. VIII, 3, pp. 129-195,1969.

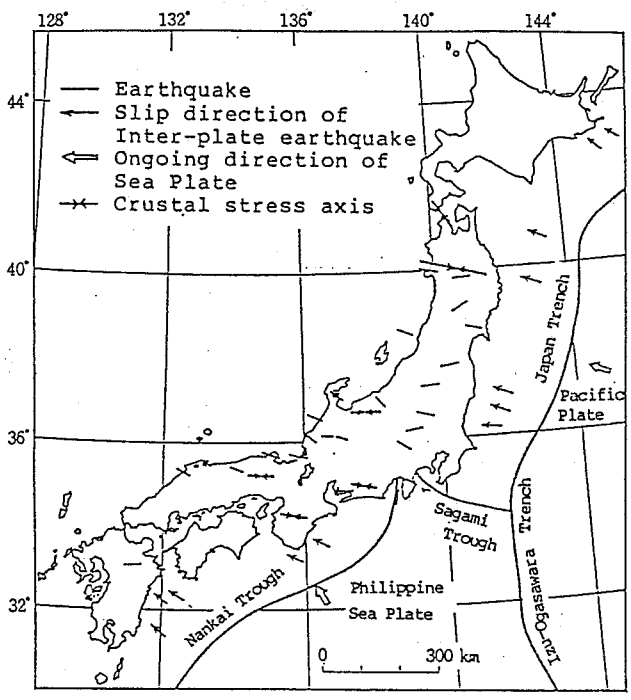

Figure 3.4.1 Inter-relationship among Tectonic Features (After Tsumura,1973)

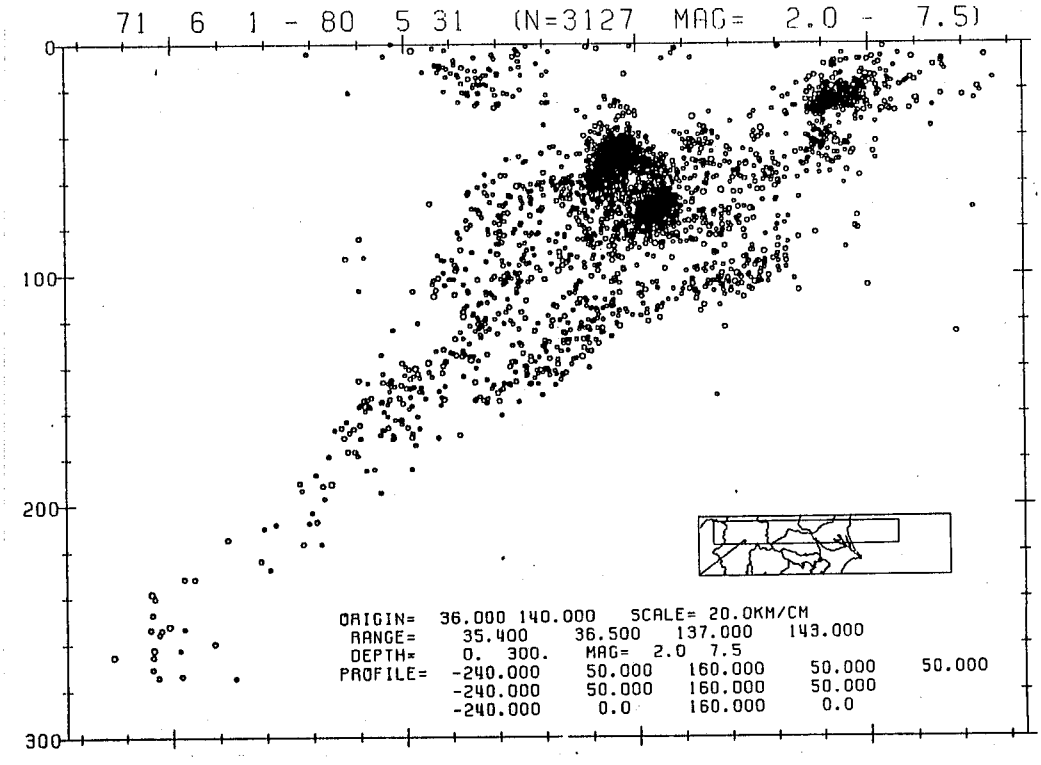

Figure 3.4.2(a) Distribution of hypocenters in the Kanto area; showing the double seismic planes(After ERI,1982)

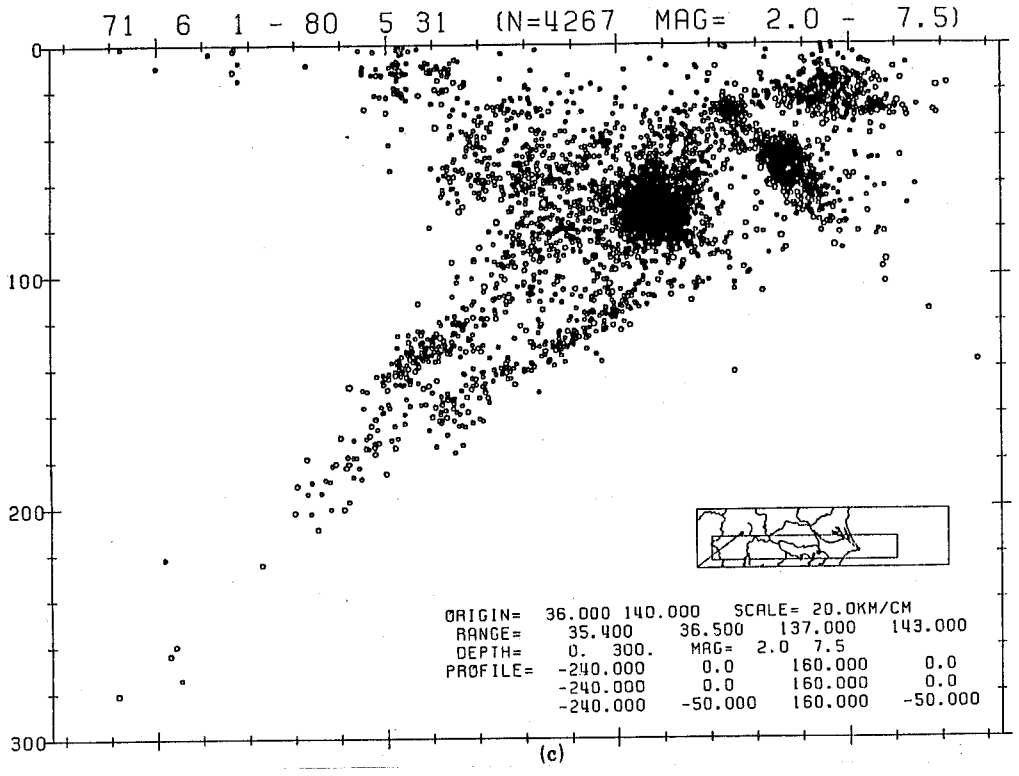

Figure 3.4.2(b) Distribution of hypocenters in the Kanto area; showing the double seismic planes(After ERI,1982)

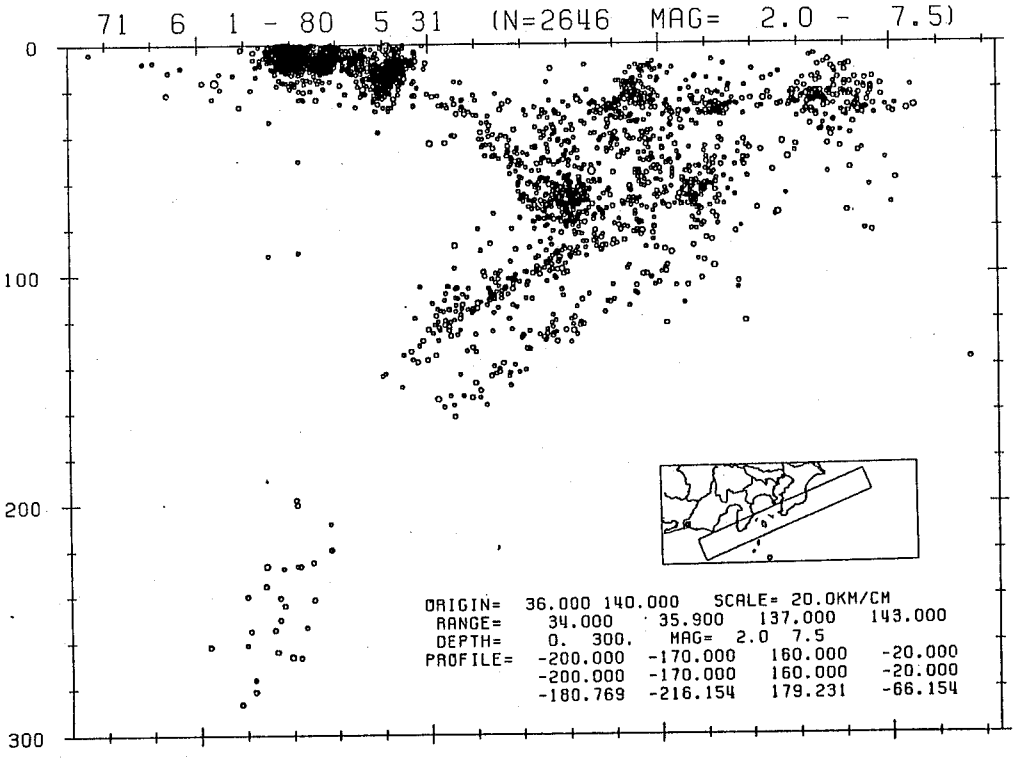

Figure 3.4.2(c) Distribution of hypocenters in the Kanto area; showing the double seismic planes(After ERI,1982)

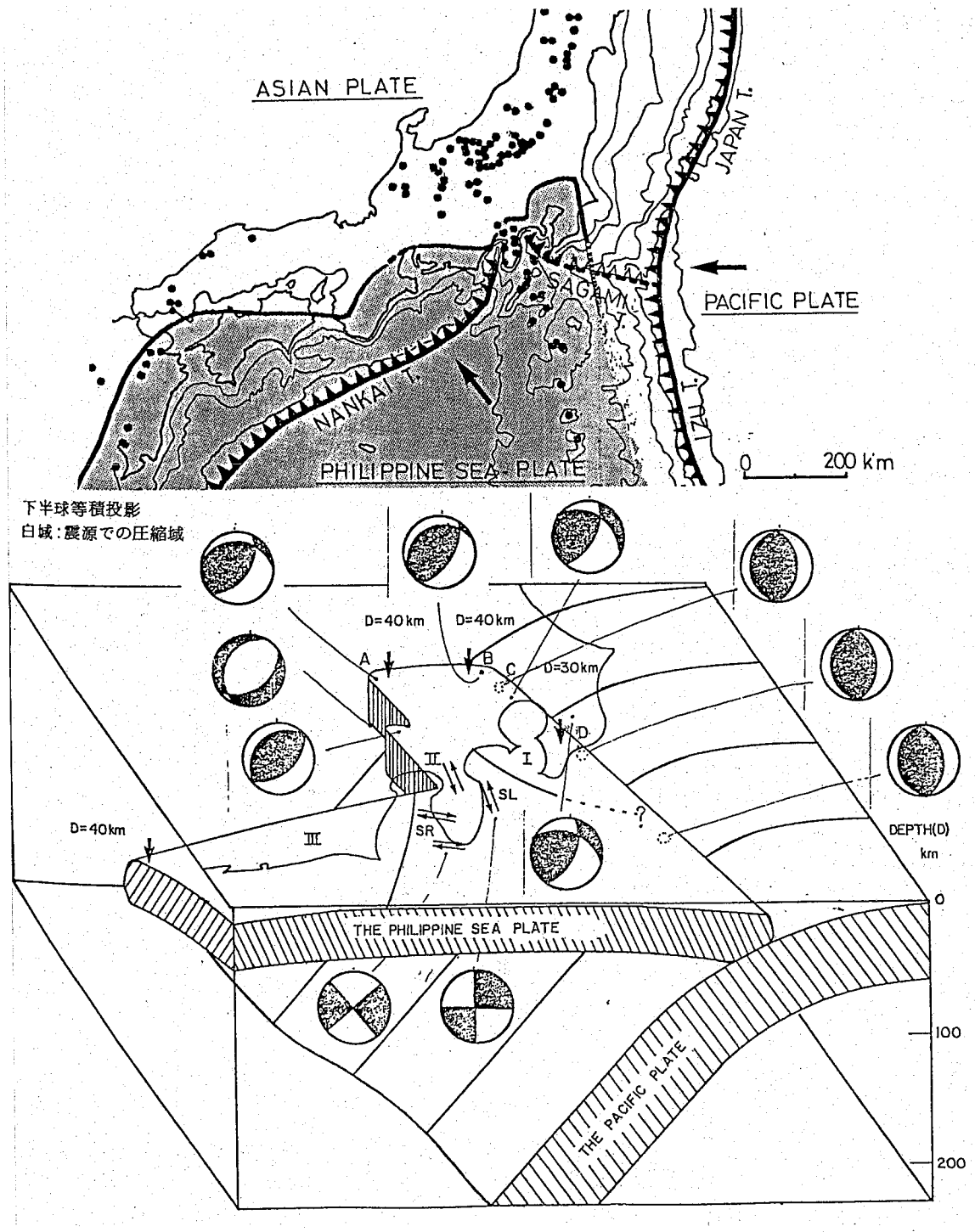

Figure 3.4.3 Illustration of the tectonic model by Hamada and Kasahara(1981)

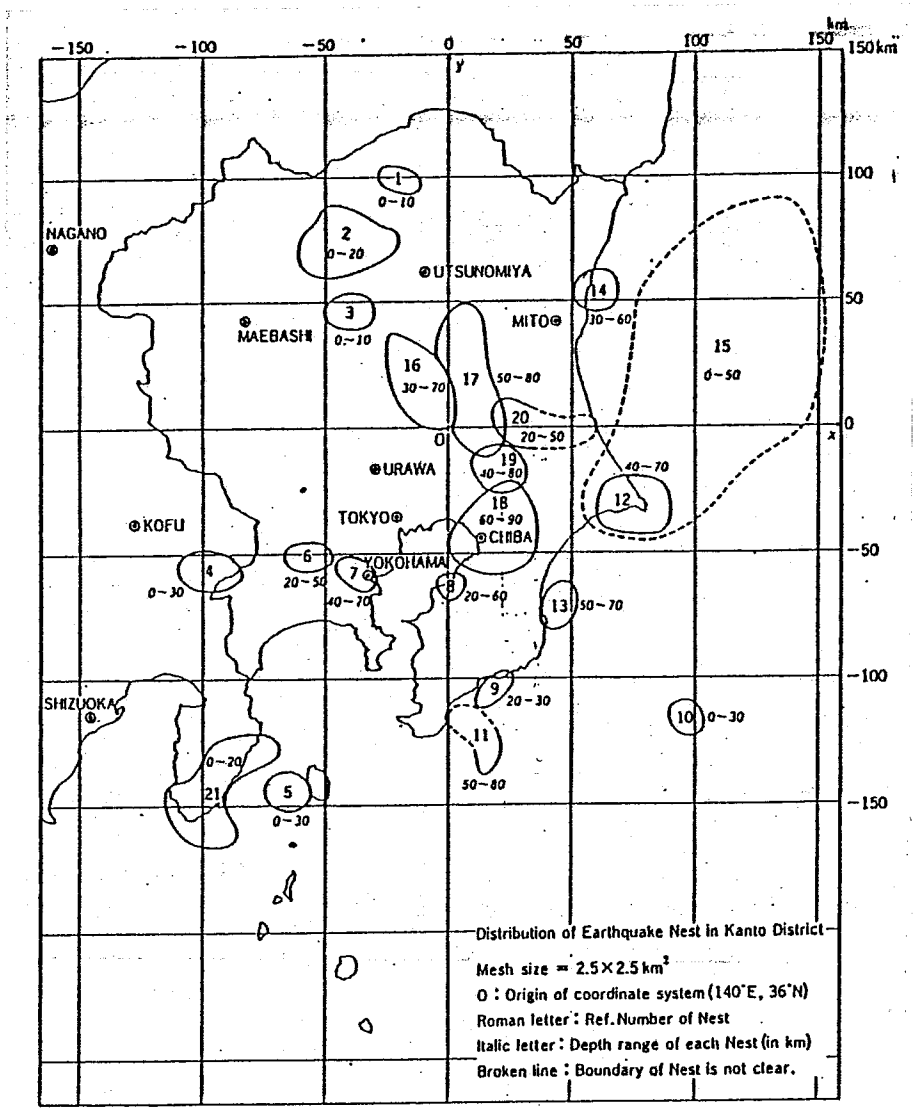

Ref. No.	Name of Location	Range of Depth
		km
1	Takahara mt.; 高原山	0 - 10
2	Ashio; 足尾	0 - 20
3	Ashikaga; 足利	0 - 10
4	E. Yamanashi Pref.; 山梨県東部	0 - 30
5	Off coast Ohshima; 大島近海	0 - 30
6	Machida City; 町田市	20 - 50
7	Yokohama; 横浜	40 - 70
8	Ichihara City; 市原市	20 - 60
9	Sea off Kominato; 小湊沖	20 - 30
10	S.E. Sea off Bousou; 房総南東沖	0 - 30
11	Off coast Bousou S. end; 房総南端沖	50 - 80
12	Around Choushi; 銚子付近	40 - 70
13	Sea off Ichinomiya; 一の宮沖	50 - 70
14	Kujigawa R. mouth; 久慈川河口	30 - 60
15	Sea of Kashima; 鹿島灘	0 - 50
16	W. Tsukuba mt. 1; 筑波山西 1	30 - 70
17	W. Tsukuba mt. 2; 筑波山西 2	50 - 80
18	Around Chiba City; 千葉市付近	60 - 90
19	Inbanuma Lake; 印旛沼	40 - 80
20	Kasumigaura-Kitaura Lake; 霞ヶ浦・北浦	20 - 50
21	S. part Izu Peninsular; 伊豆半島南部	0 - 20

Figure 3.4.4 The earthquake nests in the Kanto area by Usami and Watanabe (1976)

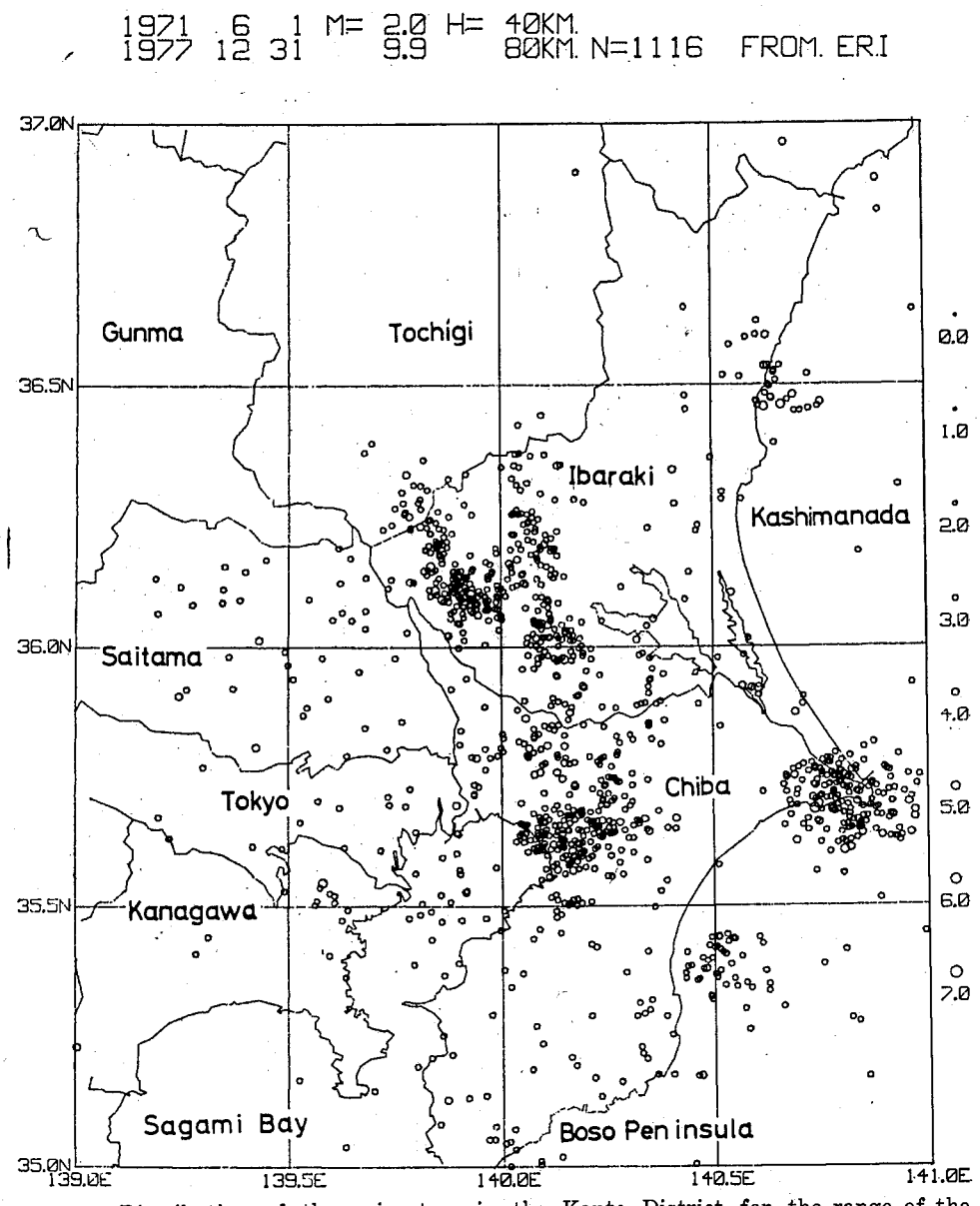

Fig. 2. Distribution of the epicenters in the Kanto District for the range of the earthquake magnitude greater than 2.0 and of focal depths from 40 to 80 km. The earthquakes plotted here have been determined by four or more stations of ERI with standard errors less than 7.5 km.

Figure 3.4.5(a) Distribution of epicenters in the Kanto area for the range of the earthquake magnitude greater than 2.0 and focal depths from 40 to 80 km. The earthquakes plotted here have been determined by four or more stations of ERI with standard erros less than 7.5 km. (After Maki and others, 1980)

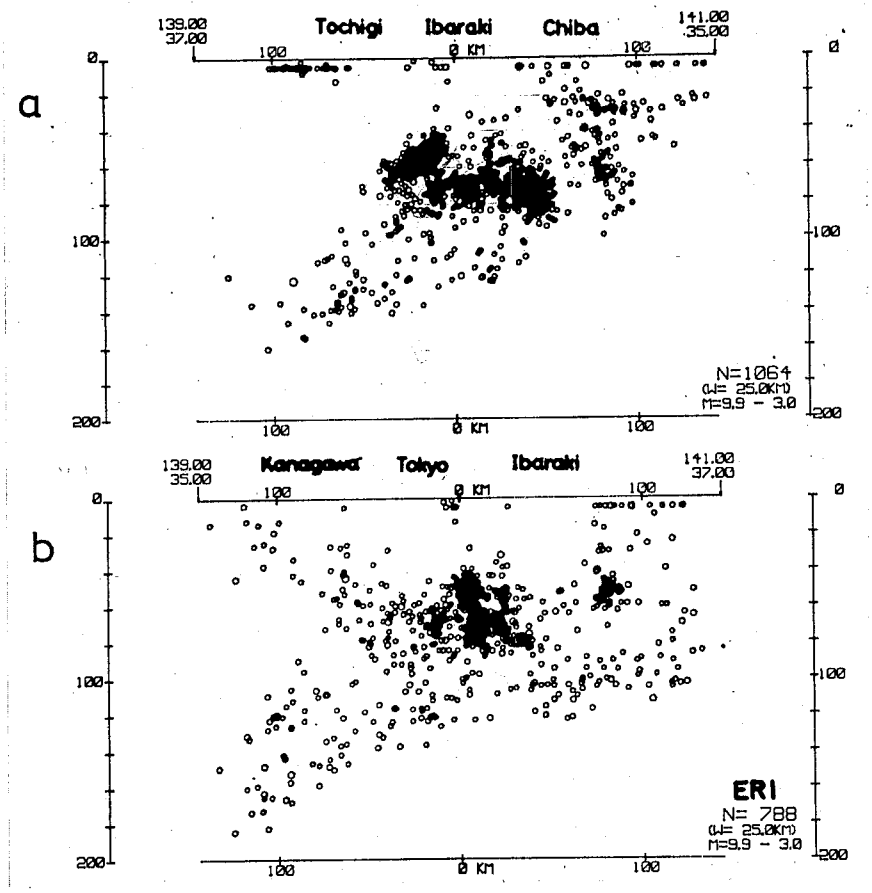

Figure 3.4.5(b) Distribution of earthquakes along the sections passing through the southwestern part of Ibaragi Prefecture (a) in the direction of northwest-southwest and (b) in the direction of southwest-northeast, within 25 km on the both sides of the lines plotted. (same)

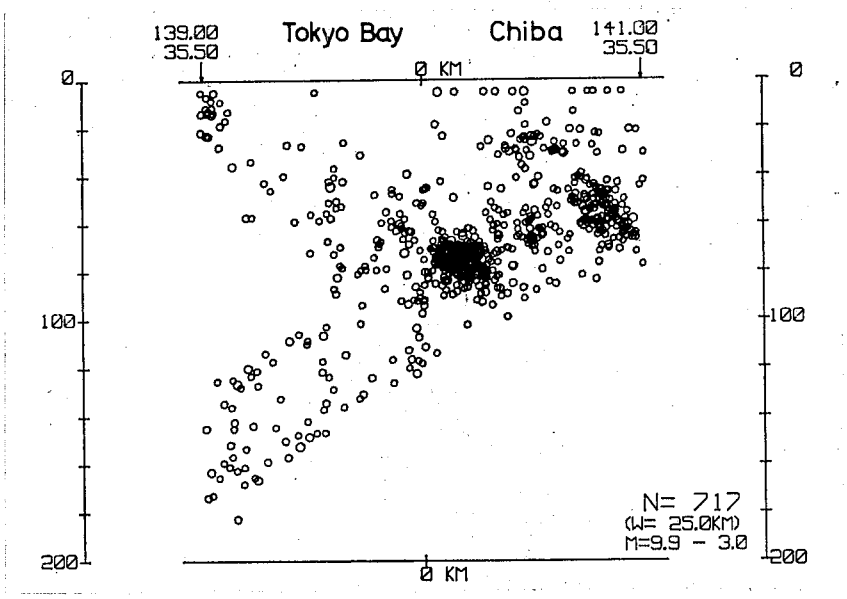

Figure 3.4.5(c) Distribution of the earthquakes along the section passing through the middle part of Chiba Prefecture in the direction of east-west. (same)

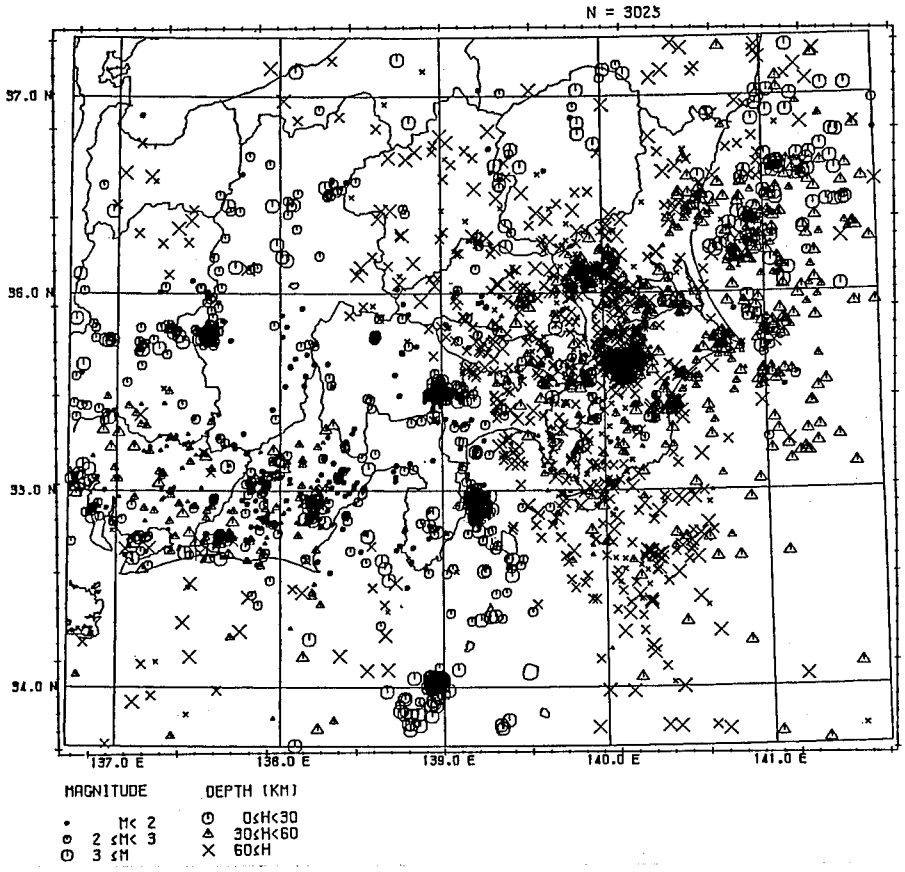

Figure 3.4.6(a) Map used for specifying the upper surface planes of seismically active regions in PHP and PAC; Epicenter distribution of microearthquakes (After Ishida, 1984)

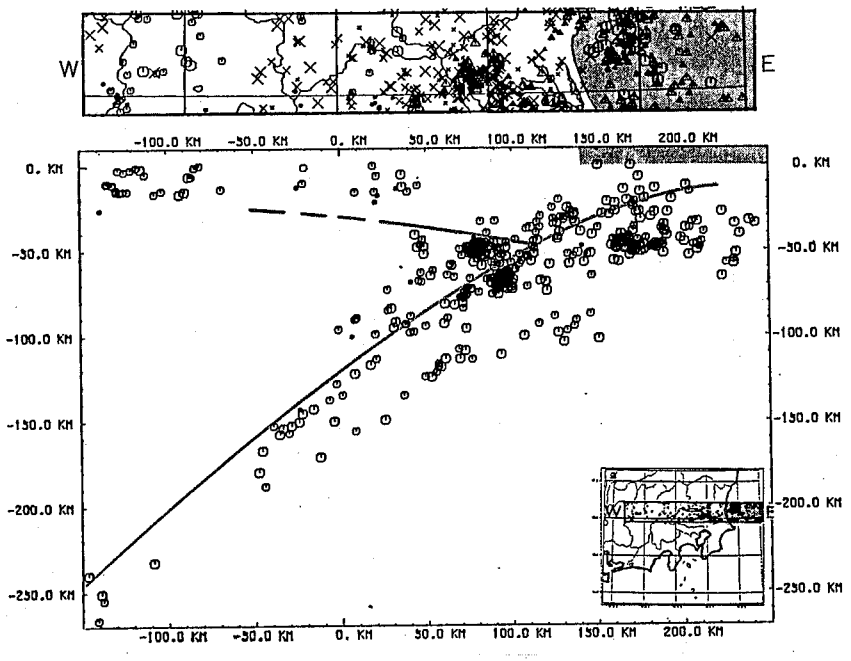

Figure 3.4.6(b) Map used for specifying the upper surface planes of seismically active regions in PHP and PAC; Plane and vertical section of the area shown in the inserted map (After Ishida, 1984)

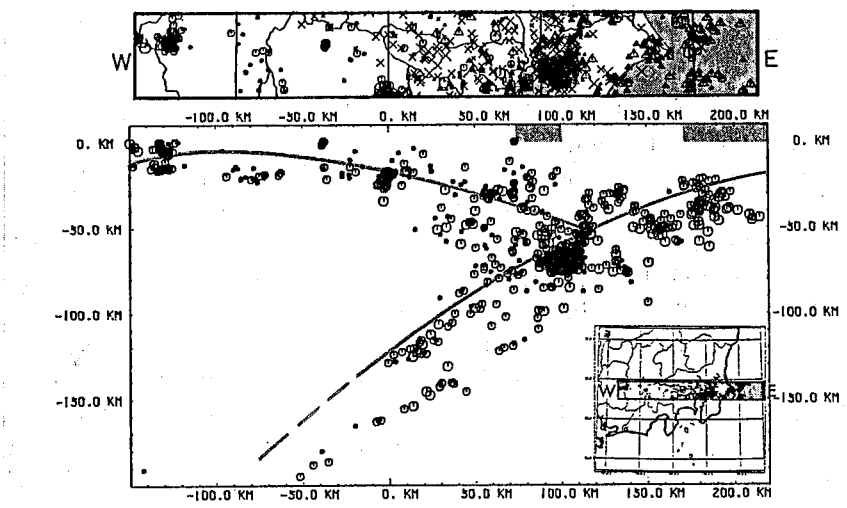

Figure 3.4.6(c) Map used for specifying the upper surface planes of seismically active regions in PHP and PAC; Plane and vertical section of the area shown in the inserted map (After Ishida, 1984)

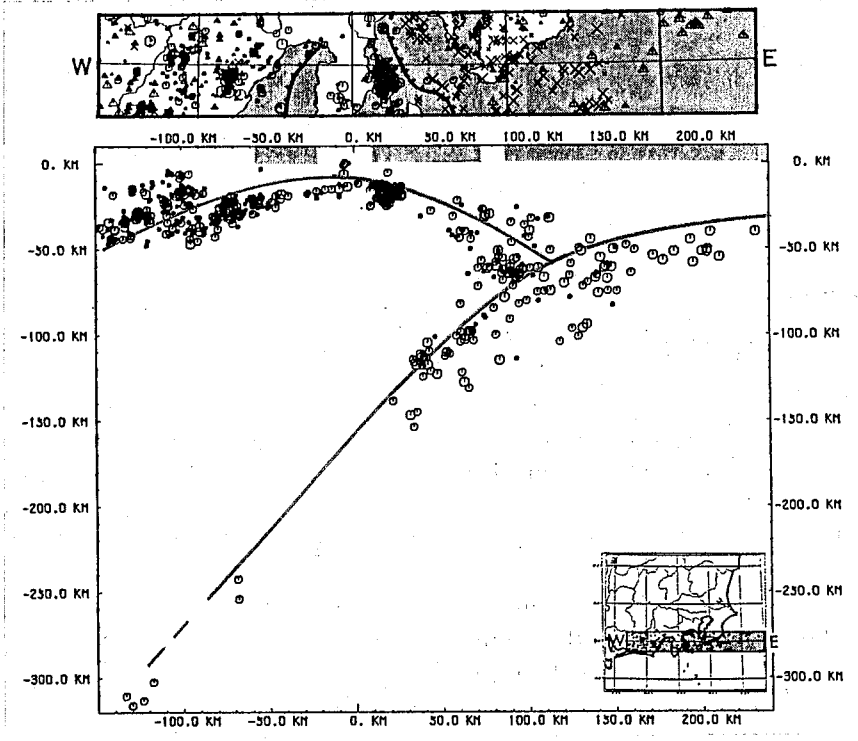

Figure 3.4.6(d) Map used for specifying the upper surface planes of seismically active regions in PHP and PAC; Plane and vertical section of the area shown in the inserted map (After Ishida, 1984)

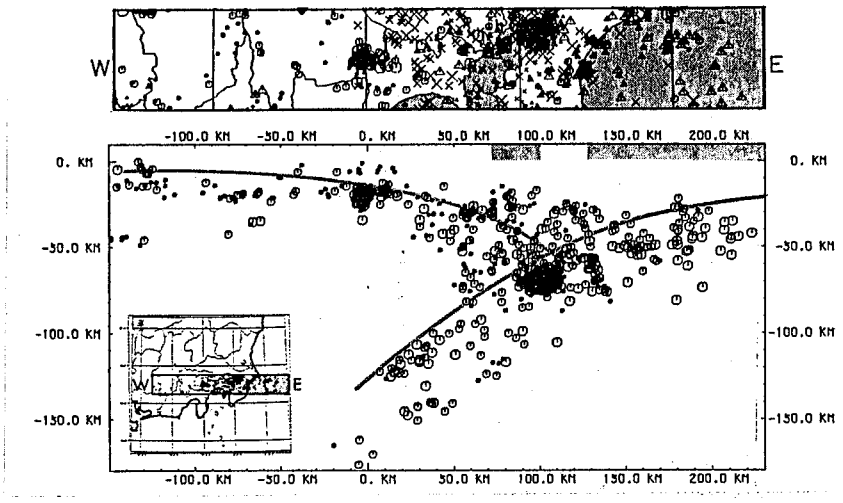

Figure 3.4.6(e) Map used for specifying the upper surface planes of seismically active regions in PHP and PAC; Plane and vertical section of the area shown in the inserted map (After Ishida, 1984)

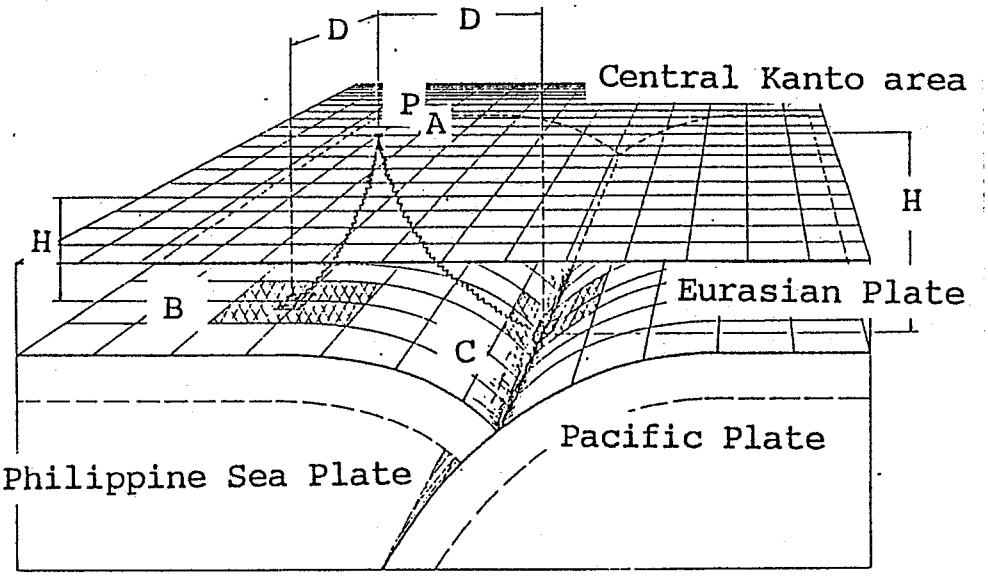

Figure 3.4.7 Illustrative evaluation of seismic hazard point P_A caused by sources B and C on three dimensional seismic surface defined in subducting plates.

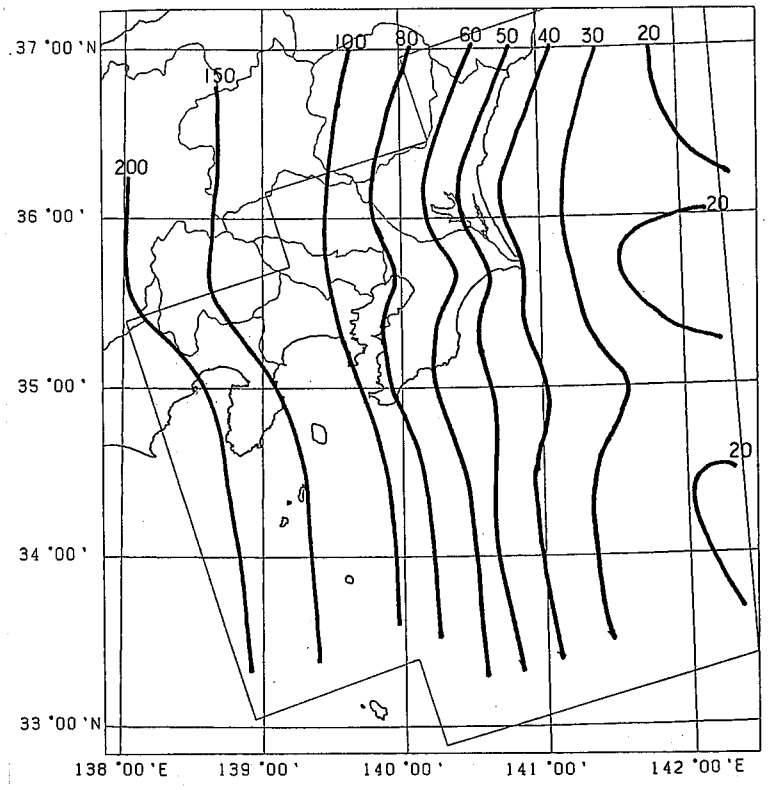

Figure 3.4.8(a) The configuration of the seismically active surface of the Pacific Plate(PAC)

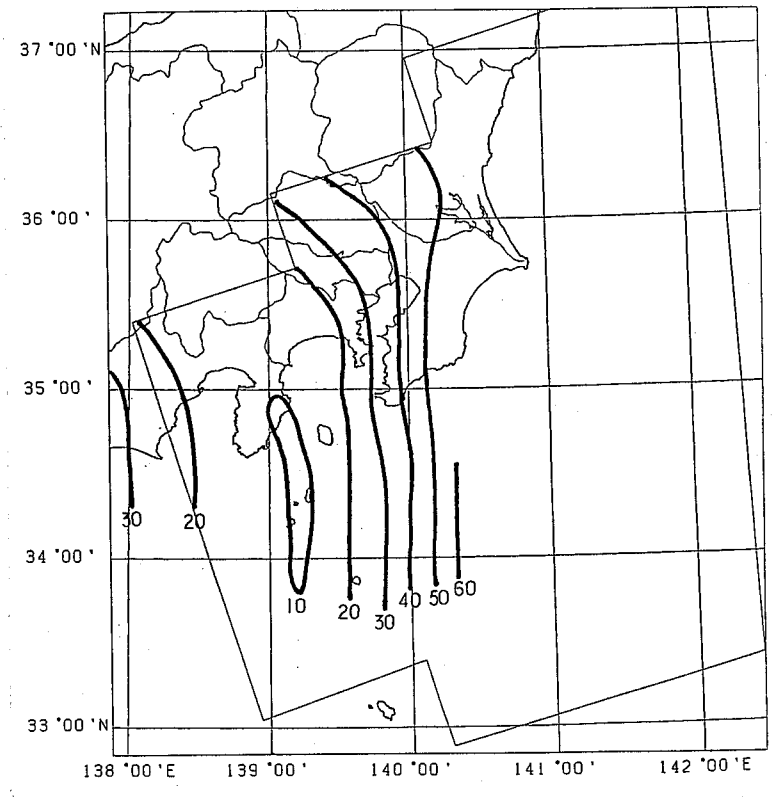

Figure 3.4.8(b) The configuration of the seismically active surface of the Philippine Sea Plate(PHP)

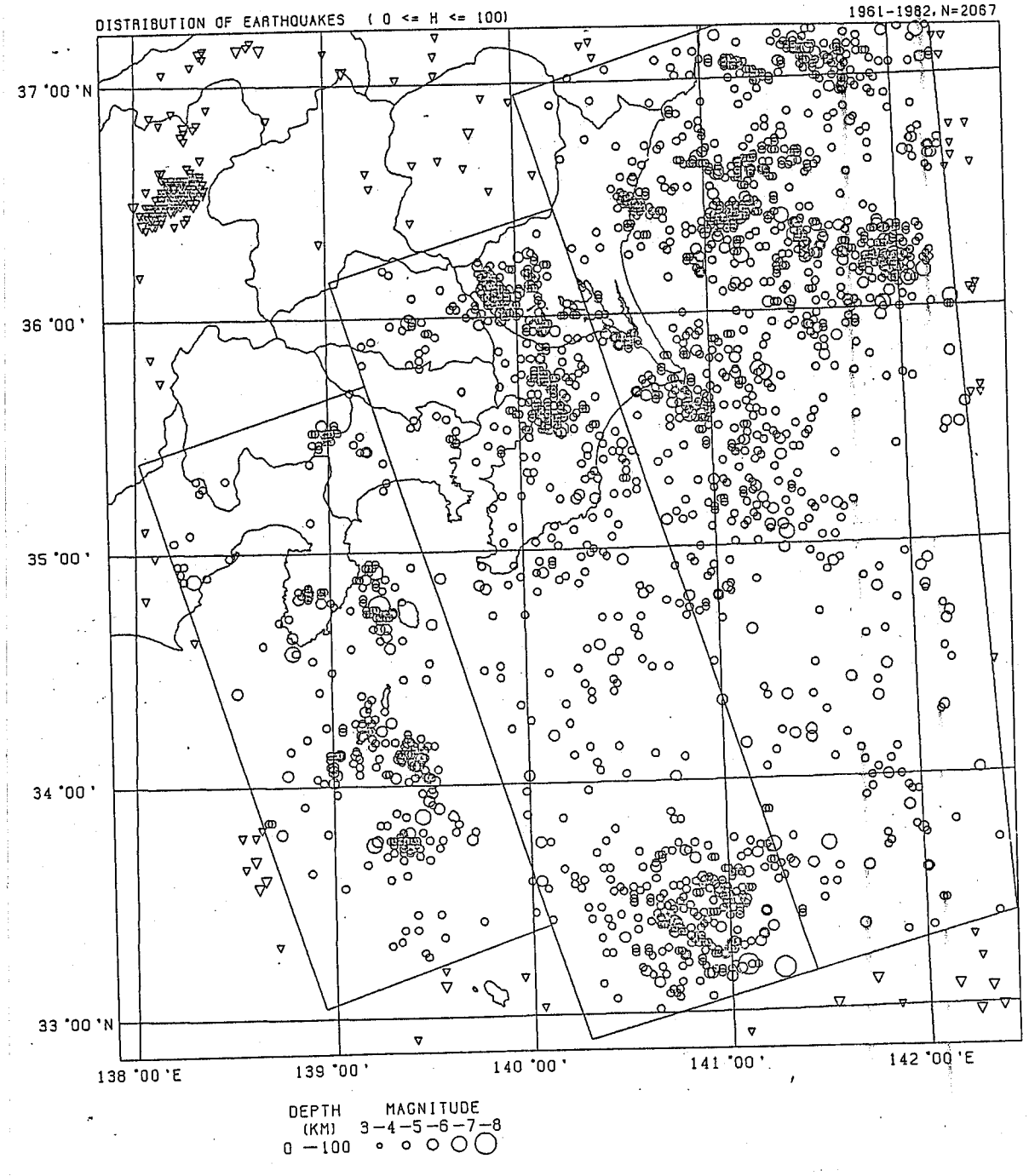

Figure 3.4.9(a) Epicenter distributions of earthquakes located at a depth of 0 to 100 km by JMA from 1961 through 1982 used for dividing seismically active regions. I,II,III denote seismically active fields and those with suffices are respective seismically active regions in each field.

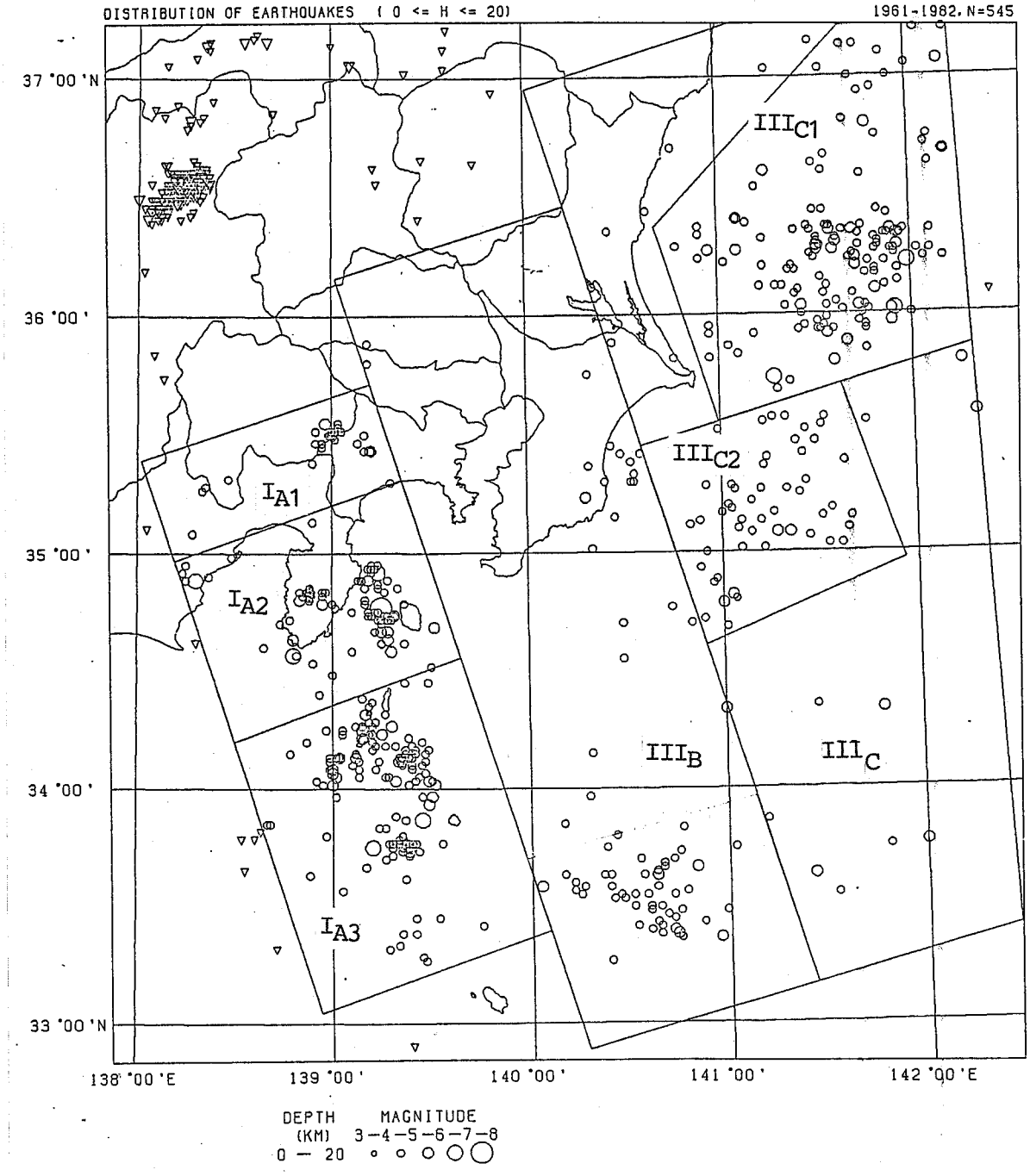

Figure 3.4.9(b) Epicenter distributions of earthquakes located at a depth of 0 to 20 km by JMA from 1961 through 1982 used for dividing seismically active regions. I,II,III denote seismically active fields and those with suffices are respective seismically active regions in each field.

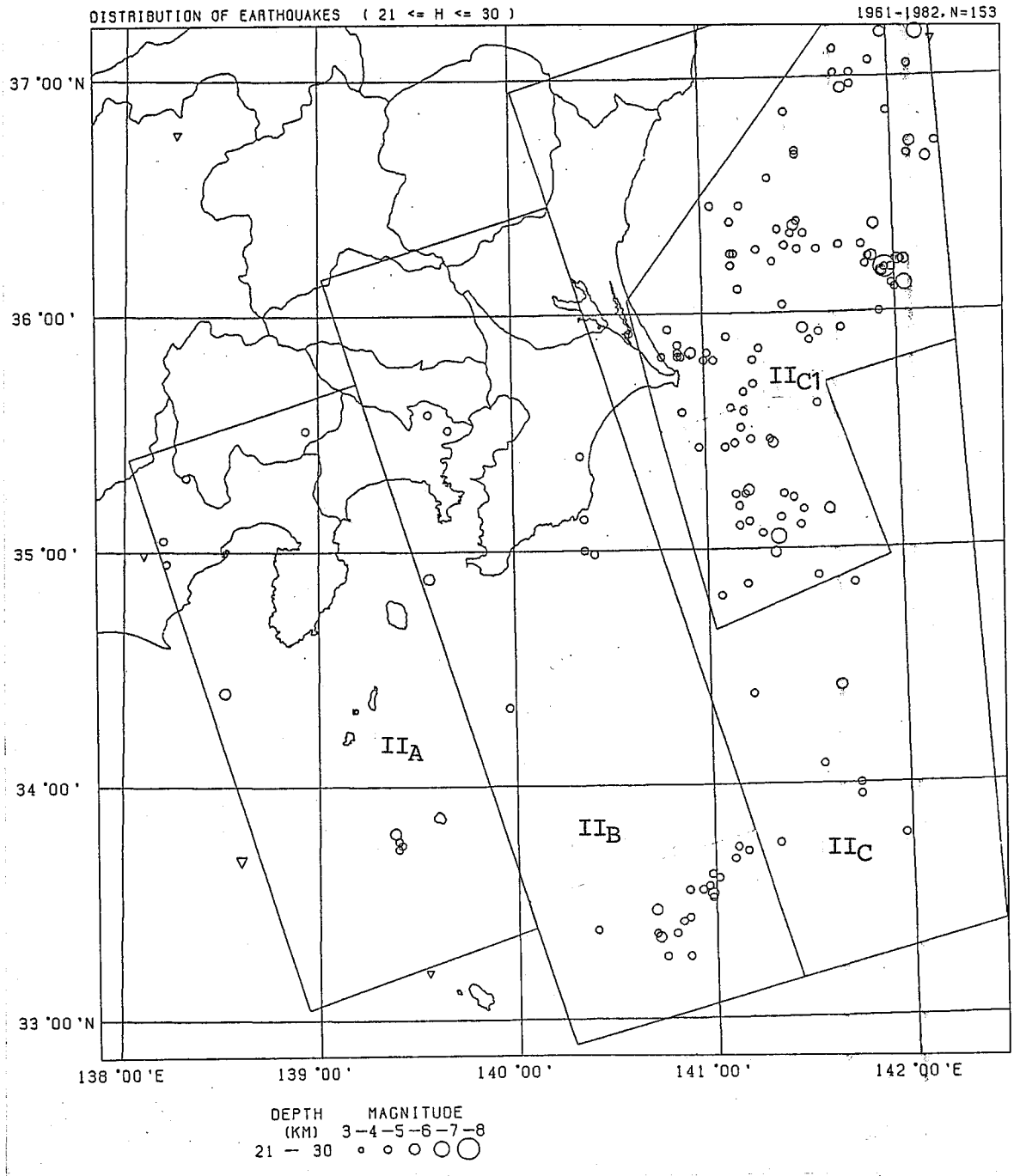

Figure 3.4.9(c) Epicenter distributions of earthquakes located at a depth of 21 to 30 km by JMA from 1961 through 1982 used for dividing seismically active regions. I,II,III denote seismically active fields and those with suffices are respective seismically active regions in each field.

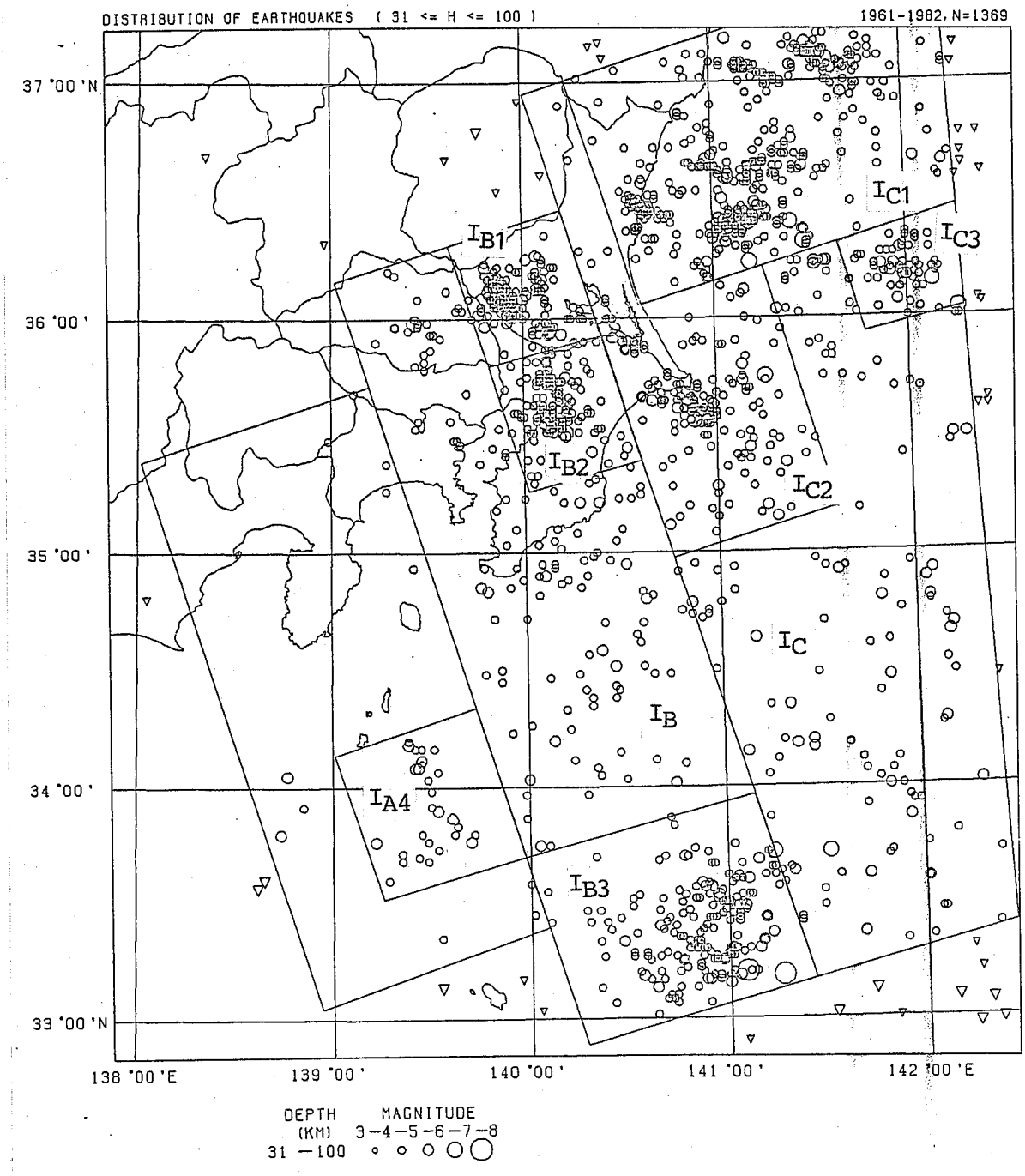

Figure 3.4.9(d) Epicenter distributions of earthquakes located at a depth of 31 to 100 km by JMA from 1961 through 1982 used for dividing seismically active regions. I,II,III denote seismically active fields and those with suffices are respective seismically active regions in each field.

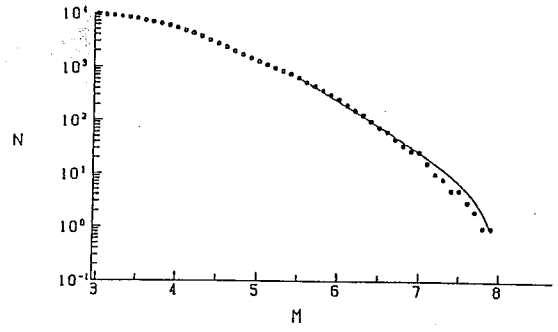

M_{min} = 5.5
M_{max} = 7.9
$N(M_{min})$ = 632
b = 0.891

(a)

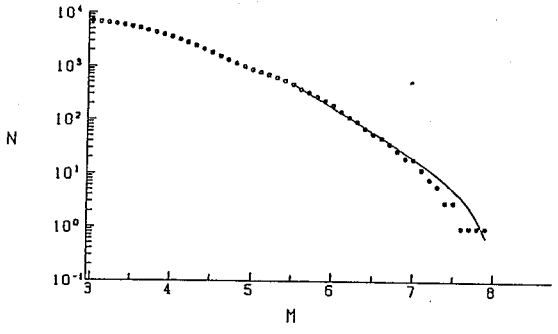

M_{min} = 5.5
M_{max} = 7.9
$N(M_{min})$ = 467
b = 0.880

(b)

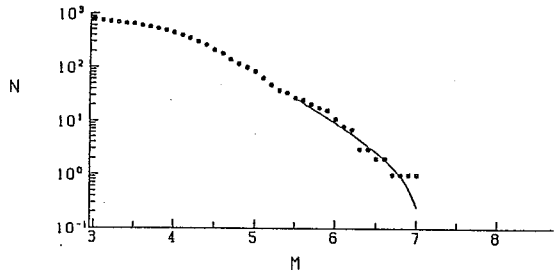

M_{min} = 5.5
M_{max} = 7.0
$N(M_{min})$ = 27
b = 0.878

(c)

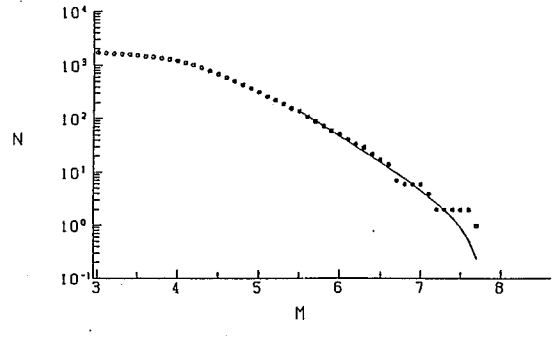

M_{min} = 5.5
M_{max} = 7.7
$N(M_{min})$ = 138
b = 0.931

(d)

Figure 3.4.10 Truncated M-log(N) relation of total area and each seismically active field; (a) stands for the fields I+II+III, (b), (c), and (d) seismically active field I, II, and III, respectively.

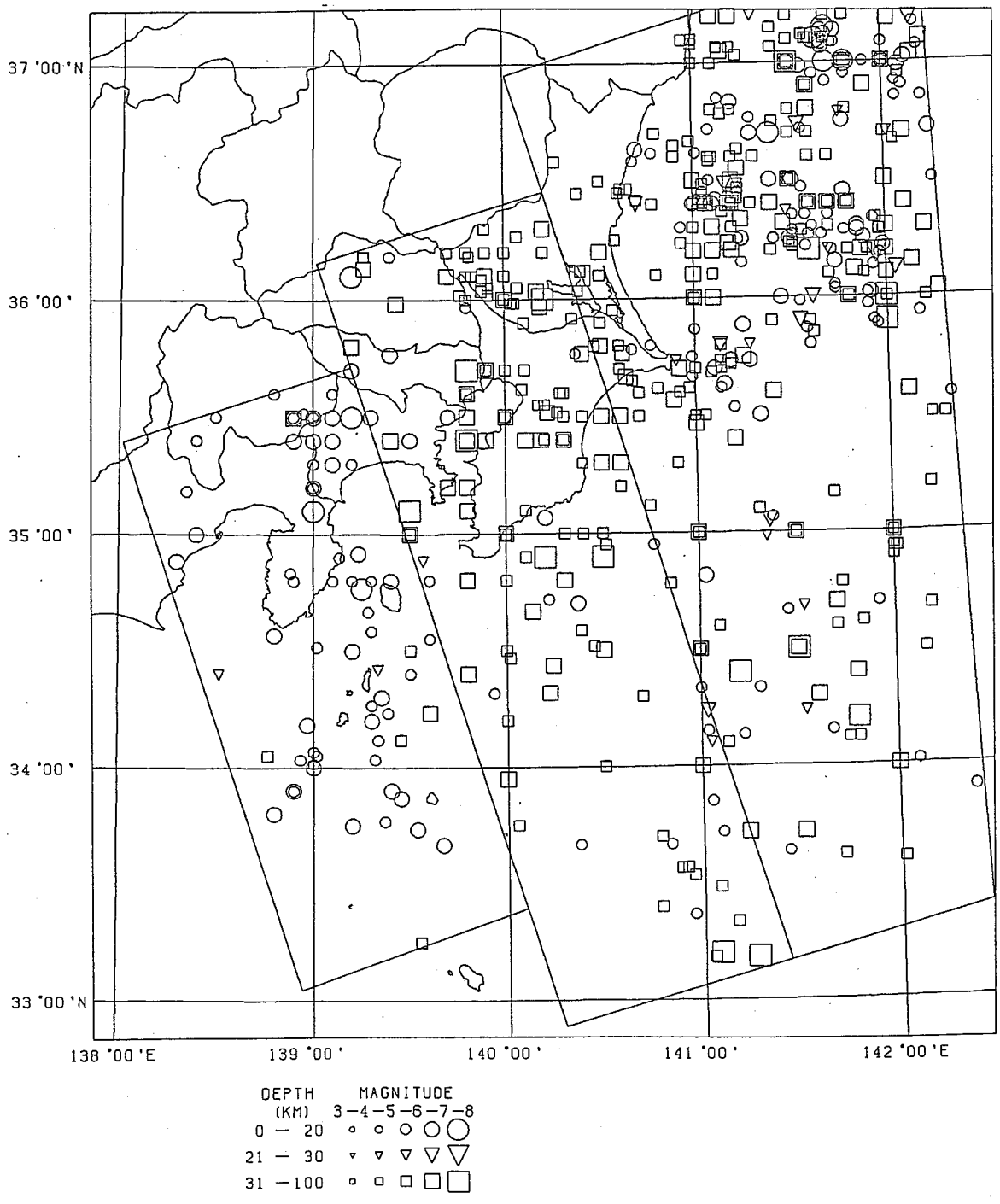

Figure 3.4.11 Hypocenter distribution of the earthquakes greater than 5.5 by magnitude during the period from 1885 through 1982 and used for determining the seismicity parameters of each seismically active region

Table 3.4.1 The seismicity parameters of each seismically active source region.

Seismically active field	Seismically Active Region	b-value	Mmax	N(Mmin)
I	IA1 (PHP) <20km	0.658	7.3	25
	IA2 (PHP) Izu Pennisula	0.663	7.0	20
	IA3 (PHP) <20km	0.748	6.8	26
	IA4 (PHP) 30 - 100km	0.668	6.3	2
	IB1 (PHP-PAC)SW Ibaragi	1.455	7.0	33
	IB2 (PHP-PAC)Centr. Chiba	1.057	6.5	28
	IB3 (PAC) 30 - 100km	0.944	7.2	10
	IB (PHP) Sagami Trough	0.677	7.9	63
	IC1 (PAC) Sea off Kashima	1.000	7.0	129
	IC2 (PAC) Sea off Kashima	1.123	6.4	41
	IC3 (PAC) Off Kashima	0.738	7.1	26
	IC (PAC) Off Bousou Penn.	0.867	7.5	64
	Subtotal of I	0.880	7.9	467
II	IIC1 (in between PAC & EUR)	0.765	7.0	17
	IIABC (same as above)	1.174	6.6	10
	Subtotal of II	0.878	7.0	27
III	IIIC1 (EUR) Off Kashima	0.834	7.7	96
	IIIC2 (EUR) Off Katsu-ura	0.827	6.6	4
	IIIBC (EUR) SE Sea off	1.342	7.0	38
	Subtotal of III	0.931	7.7	138
Grand total		0.891	7.9	632

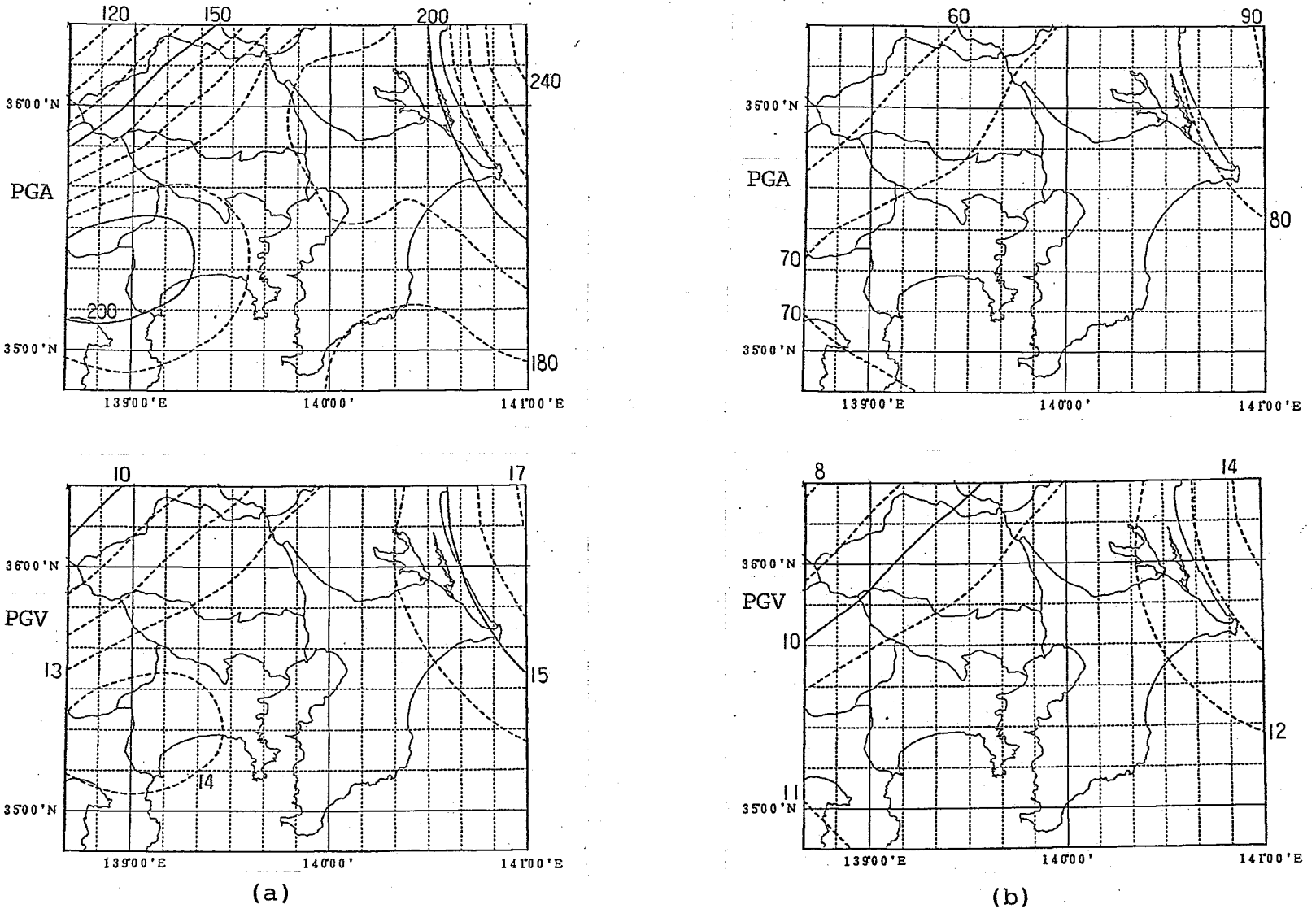

(a) (b)

Figure 3.4.12 Isoseismal map for the mean return periods of 25 years; (a) and (b) are for surface and buried structure

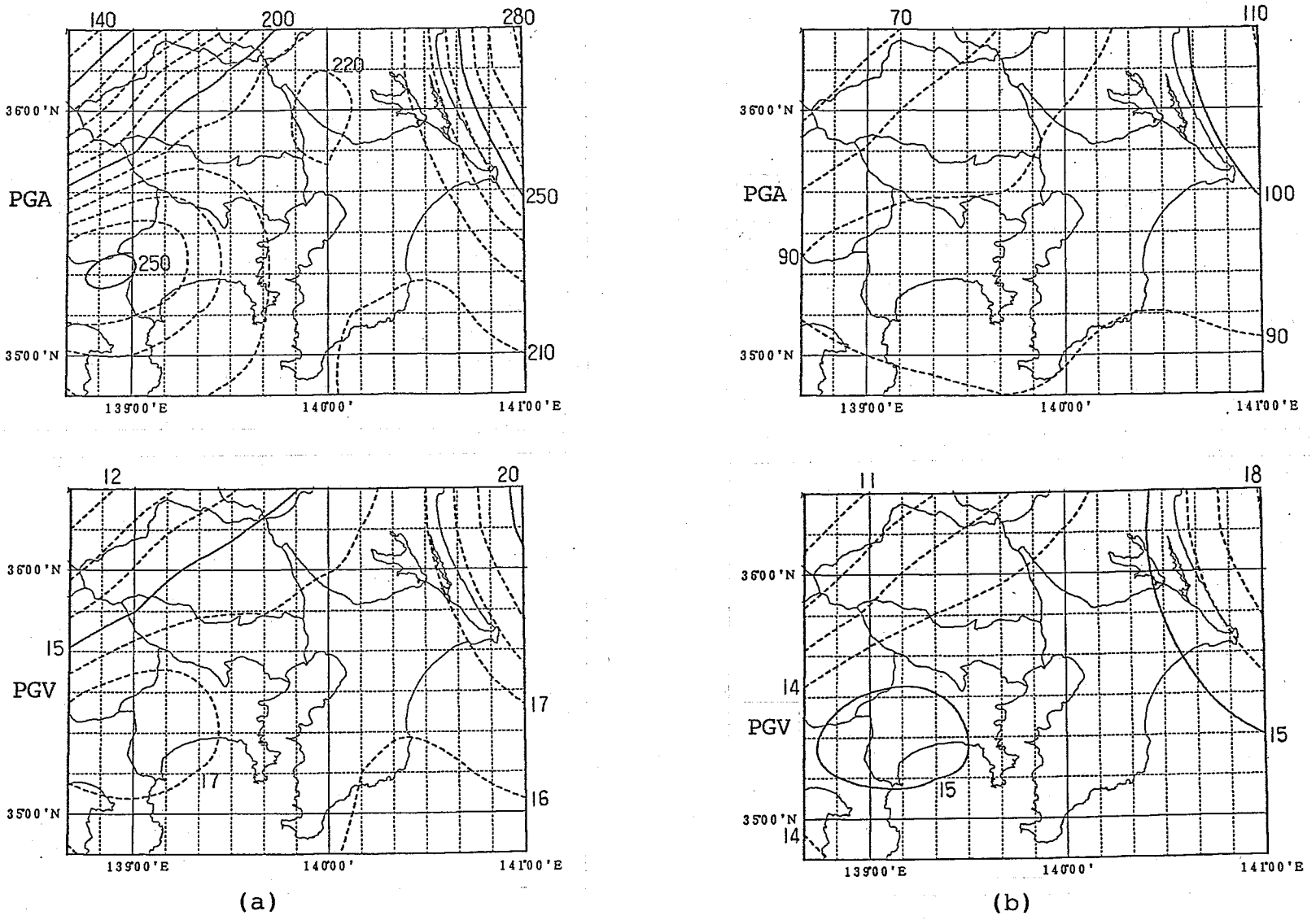

(a) (b)

Figure 3.4.13 Isoseismal map for the mean return periods of 50 years; (a) and (b) are for surface and buried structure

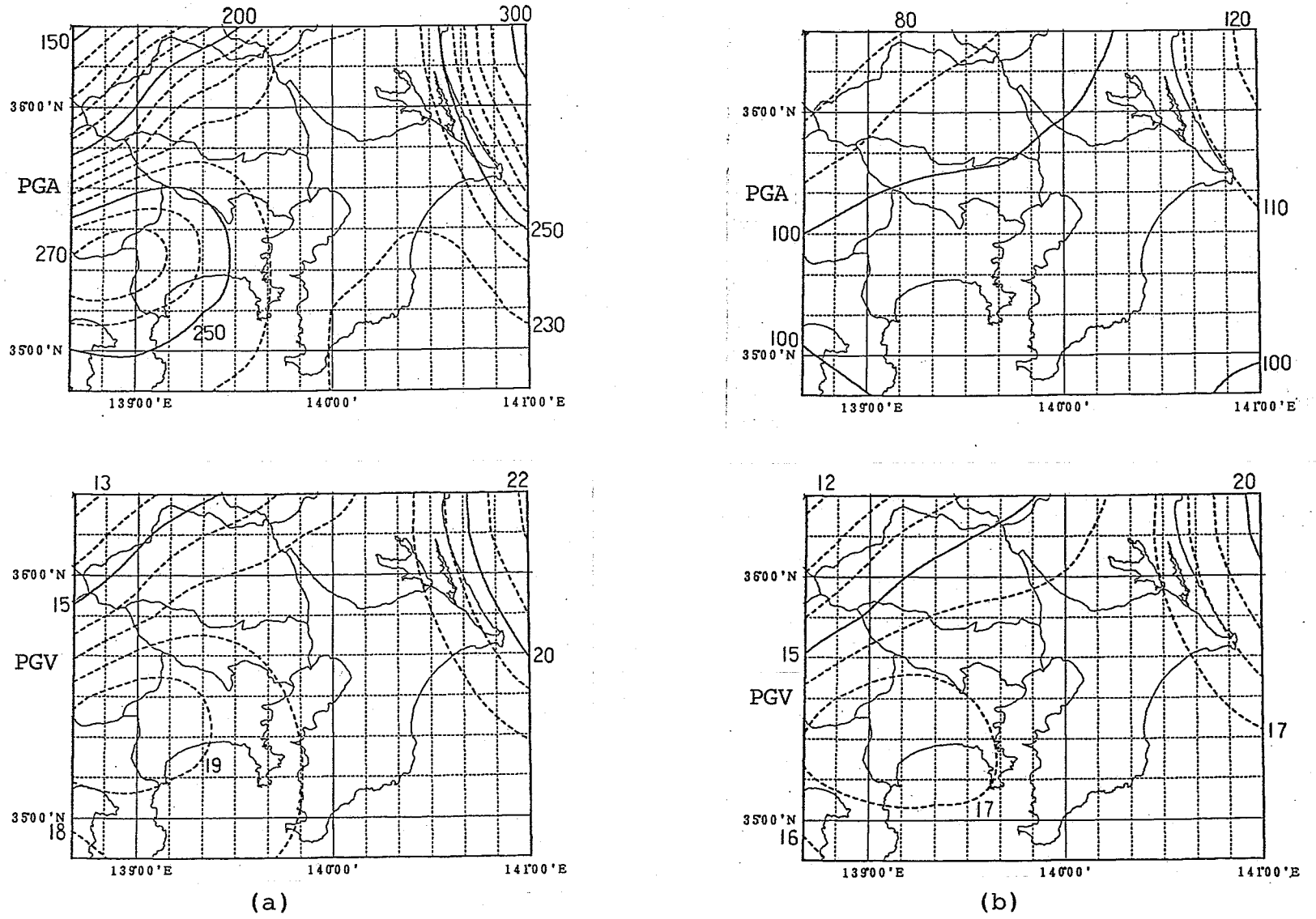

(a) (b)

Figure 3.4.14 Isoseismal map for the mean return periods of 75 years; (a) and (b) are for surface and buried structure

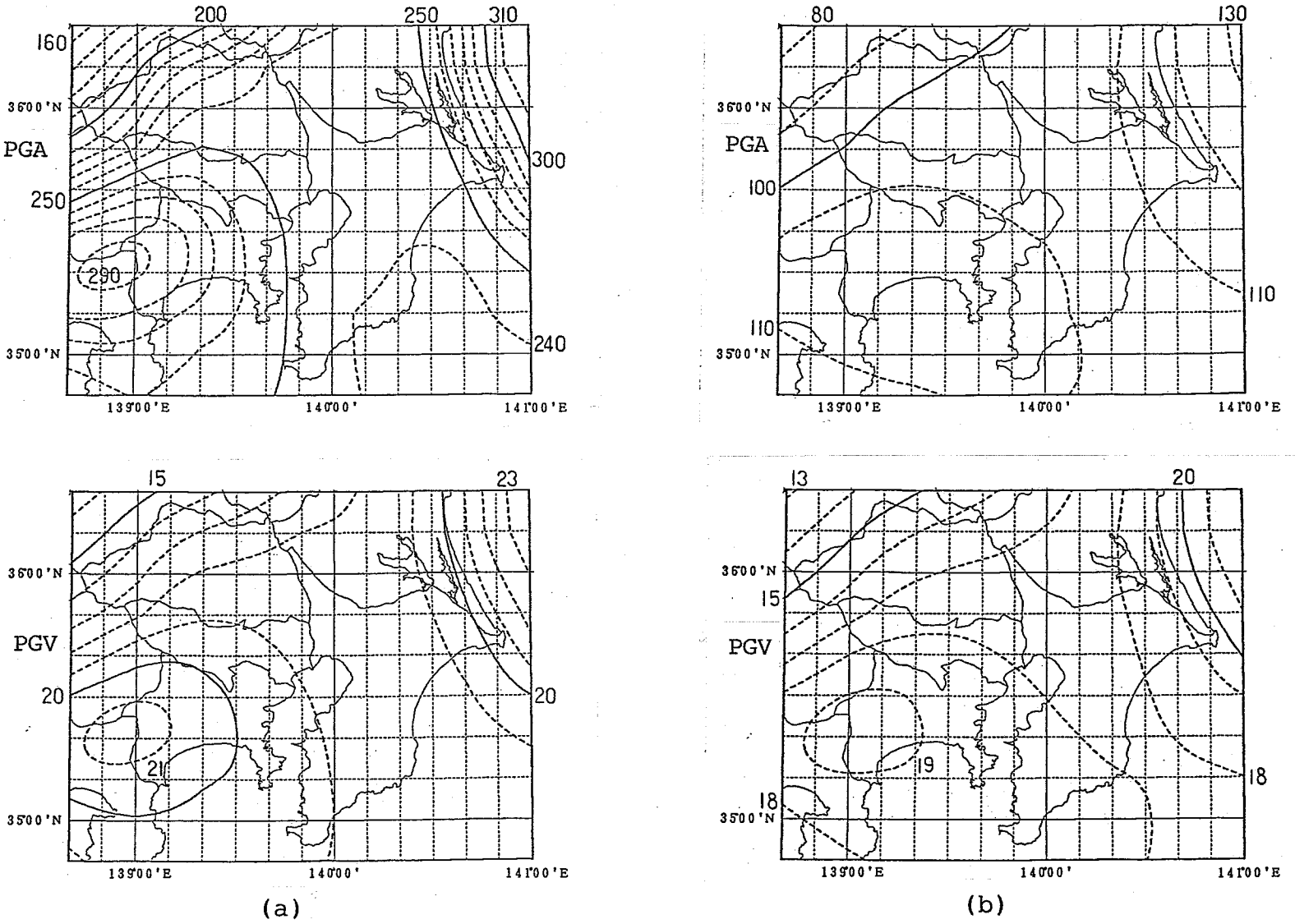

Figure 3.4.15 Isoseismal map for the mean return periods of 100 years; (a) and (b) are for surface and buried structure

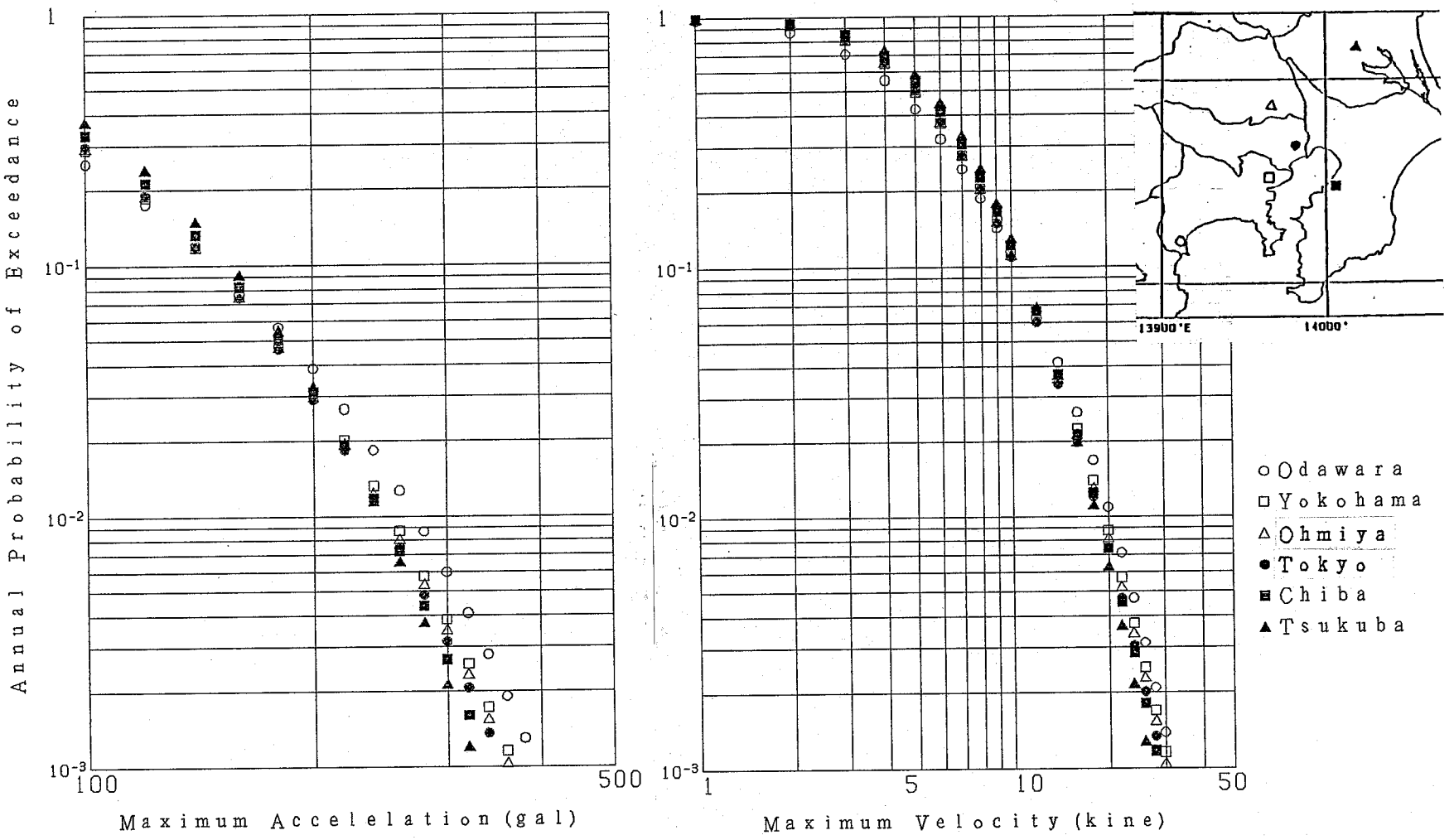

Figure 3.4.16 Annual probability of exceedance versus PGM at the sites shown here; (a) and (b) are for PGA and PGV, respectively.

3.5 CONCLUSION

For studying the seismic hazard or the peak ground motions of the Kanto area where the seismicity is attributed to the three dimensionally distributed seismic source regions, the attenuation curves appropriately reflecting the effect of focal depths on the peak ground motions were considered desirable.

Existing attenuation curves were classified into four types from the physical meaning of skeleton curves used and were tested for their fit to the Japanese strong motion records that were corrected and selected for this study (NONFSEL). Among the formulas that do not contain explicitly the focal depth, the Campbell's curve (Type III) showed the best fit, however, the Nakamura et al curve(implicit form of Type IV curve) gave almost the same degree of fit with the data.

Based on the results obtained by I.Katayama(1985, 1986), the combination of the three-dimensional earthquake source model and the attenuation curve I.Katayama Type II which belongs to the above Type IV curve gave reasonable seismic hazard maps of the Kanto area for various exposure times. Therefore the skeleton of Type IV curve was chosen to obtain new attenuation curves using the NONFSEL data.

Because the horizontally propagating waves rather than vertically incident waves are of primary concern for the longitudinal response of buried ducts or pipes, the strong motion records NONFSEL were filtered by using a high-cut filter with a cutt-off frequency of 1.4Hz and a filtered strong motion data set was prepared(FLTDSEL) for the further study of the peak ground motions meaningful for buried structures.

Using both strong motion data sets, two sets of attenuation curves were derived. The curves obtained by using the non-filtered strong motion data set NONFSEL was designated to be used in predicting the peak ground motions for structures on the ground and the other set of curves obtained by using the filtered strong motion data set FLTDSEL was prepared for underground structures.

As an application of these formulas and to provide design data for power transmission systems which includes various types of structures constructed on ground and underground, the above two sets of new attenuation curves were combined with a three-dimensional source model of the Kanto area to assess its seismic hazard.

Assuming a Poisson process of occurrence of earthquakes, the seismic

hazard of the Kanto area was presented by contour maps of the expected peak ground acceleration and velocity for representative exposure times which can be used for predicting the peak ground motions meaningful to both structures on the ground surface and buried in shallow depths.

CHAPTER 4. DEVELOPMENT OF SIMPLIFIED DYNAMIC ANALYSIS METHOD FOR BURIED STRUCTURES

4.1 OBJECTIVES AND SCOPE

Recently there are increasing the need for reasonable and practical analysis methods to predict the dynamic behavior of buried lifeline structures of large cross-sections. In some conventional design codes, we can find simplified analytical methods of buried ducts, e.g. so-called "Response Displacement Method" that has been recommended. However, the method has yet too many options in its application assumptions and often significantly over-estimates or under-estimates the response of buried ducts if compared with the results obtained by rigorous analyses (I.Katayama and others, 1984). Such irregular or unreliable results are caused by the poor mechanism for converting the shear deformation of the surrounding soil into the response of the ducts(I.Katayama and others, 1985).

For providing a practical and reliable tool for practicing design engineers and for refinement of the cross-sectional design of buried structures which is frequently controlled by highly varying properties of soil materials, the author proposes his simplified analysis method GRAMBS(Ground Response Acceleration Method for Buried Structures) for the cross-sectional design of structures such as buried ducts and tunnels in layered soils.

First it is shown that the proposed quasi-static method, GRAMBS, is theoretically an approximate method to predict the maximum response of buried structures surrounded by a uniform soil such that the maximum response may be obtained by a two-dimensional dynamic finite element analysis. The procedure to be followed in the calculation follows. Next, a one-story duct surrounded by a uniform soil is analyzed under various conditions relative to the surrounding soil by available analytical methods including GRAMBS and the results are compared with those obtained by the two-dimensional dynamic finite element code, FLUSH-VB(I.Katayama, 1984 and 1985).

With the fact that the moment distribution in a one-story duct from the experiment performed by the Central Research Institute for Electric Industries showed good coincidence with the result obtained by FLUSH (Tohma and others, 1985), the validity of the simplified method proposed here is verified for the case of one-story duct surrounded by a uniform soil.

Further, the validation of GRAMBS for a multi-story shaft in a layered soil is shown by comparing the result obtained by GRAMBS with the recorded response of the underground power transmission shaft reported by Kaizu, Annaka, and Ohki (1989(a), 1989(b)) and Kaizu, Harada, Annaka and Ohki(1989).

Finally, an application to the dynamic stress analysis of a large scale underground cavity for geologic repository of high-level nuclear wastes is shown and the input ground motion problem for underground cavity is discussed(I.Katayama, 1985).

4.2 THEORETICAL BACKGROUND OF THE PROPOSED METHOD

When a structure is buried in a soil, the structure in most cases can not behave independently from the surrounding soil. Here, the major external force to the structure is provided by the effective dynamic response of the surrounding soil. The dynamic problem of such buried structures certainly becomes the quasi-static interaction problem of the system consisting of a structure and its surrounding soil.

Consider a system in a plane strain state which consists of a concrete duct with unit length and the surrounding uniform soil layer with unit width as illustrated in Figure 4.2.1, and assume that the shear vibration will dominate this whole system.

When this two-dimensional system is excited by the horizontal input ground motion, $\ddot{\mathbf{Z}}(t)$, the equation of motion is written by

$$[\mathbf{M}]\ddot{\mathbf{X}}(t) + [\mathbf{C}]\dot{\mathbf{X}}(t) + [\mathbf{K}]\mathbf{X}(t) = -[\mathbf{M}]\ddot{\mathbf{Z}}(t) \qquad (4.2.1)$$

where [**M**], [**C**] and [**K**] are the mass matrix, the damping matrix, and the stiffness matrix, respectively. The $\mathbf{X}(t)$ means the relative displacement vector.

It is usual in a system like this one that the reduced specific weight and rigidity of the structure, which are calculated by re-distributing the weight and rigidity uniformly over the entire area covered by the structure in the soil, are almost the same as those of the surrounding soil. Therefore, first we neglect the actual duct and assume the above system to consist only of the layered soil.

The problem therefore turns out to be that of the free-field response of a uniform soil. Define [**D**] and [**B**] as the stress matrix and the strain matrix, respectively. Take the time t_m when $\mathbf{S}^j$ = the stress of a small portion of the soil from the depth j to j+1; e.g.

$$\mathbf{S}^j=[\mathbf{D}][\mathbf{B}]\mathbf{u}^j \qquad (4.2.2)$$

reaches maximum, then $\mathbf{u}^j$ = the relative displacement between the depth j and j+1 must be maximum and also satisfy eq.(4.2.1) as

$$\mathbf{X}^j(t_m)=\mathbf{X}^{j+1}(t_m) + \mathbf{u}^j \qquad (4.2.3)$$

Eq.(4.3.1) can be rewritten as

$$[\mathbf{K}]\mathbf{X}(t_m) = -[\mathbf{M}](\ddot{\mathbf{X}}(t_m)) + \ddot{\mathbf{Z}}(t_m)) - [\mathbf{C}]\dot{\mathbf{X}}(t_m) \qquad (4.2.4)$$

where the right hand side is the dynamic force applied working on the whole system at time t_m. Because the time is fixed, the solution of eq.(4.2.4) becomes a solution of the static problem.

If the damping of the soil is small, eq.(4.2.4) may be approximated as

$$[\mathbf{K}]\mathbf{X}_a(t_m) = -[\mathbf{M}](\ddot{\mathbf{X}}(t_m) + \ddot{\mathbf{Z}}(t_m)) \qquad (4.2.5)$$

and the new approximate relative displacement vector $\mathbf{X}_a(t_m)$ and corresponding stress vector $\mathbf{S}_a$ at time t_m will be obtained by solving the eq.(4.2.5). In the above, if the soil reached its non-linear strain level at time t_m, the strain-dependent soil property at the time is preserved in the subsequent procedure. To solve this equation is equivalent to solving a static stress problem under the prescribed body force and the new solution must be very close to the original solution if the damping (which is neglected) is small enough.

If the portion of the soil, that originally consisted of the duct and its cavity but was once replaced by an equivalent soil, is again replaced by the duct and its cavity, then the corresponding parts of the matrices [**M**], [**K**], [**D**] and [**B**] relating to the calculation of the maximum stress described earlier are replaced by those of the ducts, and $\mathbf{u}^j$ becomes equivalent to the maximum relative displacement between the top and bottom levels of the duct. If this new system is solved, the stress state of the system at the time when the portion replaced by the duct reaches the maximum stress state must be obtained; e.g., the maximum stress state of the duct surrounded by the soil is approximately predicted.

The model of a single story duct and uniform soil surrounding the duct was considered in the above; however the above approximation of the dynamic response problem can be expanded to a multi-story duct and multi-layered soil system as follow:

The above condition to define t_m, the time when the portion of the soil to be replaced by a buried structure shows the maximum relative displacement between the top and bottom levels of the duct, is derived as a special case of a single story duct and uniform soil of a more general multi-story and multi-layered system.

Let $\mathbf{G}^i(t)$, $\mathbf{e}^i(t)$ and $\mathbf{h}^i$ be the shear modulus, the shear strain and

the thickness of the i-th soil layer, and $U^j(t)$, the shear strain energy of the portion of the soil between the depth j and j+1, is obtained as

$$U^j(t) = \text{Sum } [(1/2)G_i(t)e_i^2(t)h_i] \quad (i=j \text{ to } j+1) \qquad (4.2.6)$$

Here we assume that the maximum energy provided by the surrounding soil will cause the maximum deformation or stress in the portion of concern.

If the duct is surrounded by a uniform soil, then because $G_i(t)=G(t)$, $e_i(t)=e(t)$ and $h_i=h$, $U^j(t)$ becomes maximum when $u^j=e(t)h$ the relative displacement between the depth j and j+1 becomes maximum. For the more general case of multi-story ducts or multi-layered soil, at the time when the shear strain energy of the portion of the soil becomes maximum, the maximum stress state will be generated in the soil portion.

Thus the case of combined duct and soil system, in which the duct is either single-storied or multi-storied and the soil is either uniform or layered, can be solved by maximizing the above shear strain energy in eq.(4.2.6) following the analytical process described for the single story duct and uniform soil case.

Summarizing the above, the analytical procedure needed for the proposed GRAMBS is stated as follows:

(1) The duct as shown in Figure 4.2.1(a) is idealized in a two-dimensional model following standard finite element technique. The maximum height of the horizontally layered mesh is determined similar to an analysis using codes like FLUSH, and the lateral and vertical size of the soil region must be determined considering the propagation of the affected force disturbance by the redistribution of stresses surrounding the duct. The side boundary condition of the soil region should be that of horizontal rollers.

(2) Neglecting the duct, the free-filed soil response analysis by the equivalent linear method as is used in SHAKE is performed for the surrounding soil with the soil column having the same layering pattern as that of the two-dimensional model shown in Figure 4.2.1(b). The time dependent displacement and acceleration response of each layer are stored with the converged soil properties.

(3) The time-dependent shear strain energy $U^j(t)$ in eq.(4.2.6) is calculated using the time-dependent displacement, the converged shear modulus and the thickness of each layer within the depth interval of

the top and bottom levels of the duct, and the time t_m when the energy becomes maximum is sought. The response acceleration profile at t_m is taken over the full depth of the soil column and converted into the seismic coefficient of each layer to be used for the input data for the body force in the static analysis.

(4) In the two-dimensional static finite element model prepared in (1) above, the converged soil moduli obtained in (2) above, the mass and the seismic coefficient derived in (3) above are used to solve the stress analysis problem under the body force by static finite element analysis. The resultant stress state of the duct at the time t_m is deemed as the approximate maximum stress state.

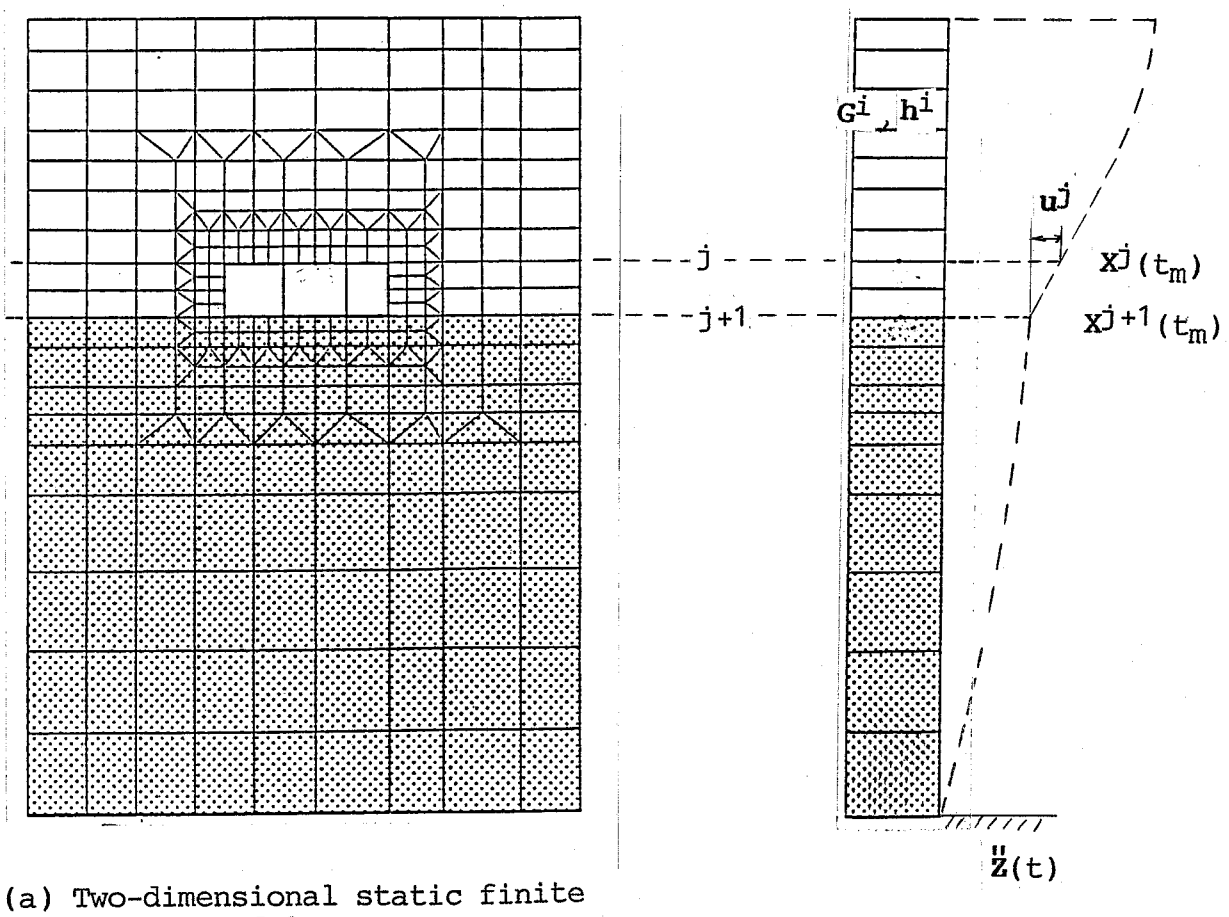

(a) Two-dimensional static finite element model

(b) Continuum free-field soil model used in one-dimensional wave propagation analysis

Figure 4.2.1 Numerical model scheme of quasi-static analysis method GRAMBS

4.3 APPLICATION TO A SIMPLE DUCT AND ITS VALIDATION

4.3.1 Introduction

A one-story multi-cell concrete duct, which is a typical multi-purpose duct, is analyzed by GRAMBS under various installation conditions relative to the surrounding soil (I.Katayama et al, 1984 and 1985). The analytical results obtained by GRAMBS are always compared with those of FLUSH. And referring to the results of a comparative study by Tohma and others(1985) showing that the dynamic behavior obtained by experiment and numerical analysis (using FLUSH) are consistent, the validity of GRAMBS is confirmed.

4.3.2 Model duct and the surrounding soil

A one-story multi-cell concrete duct shown in Figure 4.3.1 is analyzed by GRAMBS under various installation conditions considering possible situation in practical design as is shown in Table 4.3.1 for different cases analyzed. The depth burial of the duct is varied from the ground surface to the top of the soft rock. The depths of both the soil and rock are varied also as shown in the table. The case number of the analyses is denoted by the model numbers.

The dynamic material properties of the duct, the surrounding soil and the underlying soft rock are indicated in Table 4.3.2. To simulate the behavior of similar ducts during strong ground motion excitation, a typical strain dependent material properties of the soil and the rock in Figure 4.3.2 are designated for the model system.

4.3.3 Input ground motion

To examine the change of dynamic behavior of the duct against different kind of ground motions, two strong motion time histories were prepared; a strong motion from the Taft records obtained at the 1957 Kern County earthquake (deconvolved to the free-field motion at the outcrop of the underlying soft rock of the recording site) and a strong motion record obtained at the Lake Hughes array station No. 9 in the 1971 San Fernando earthquake(the site is classified as a rock site).

Both acceleration time histories are shown in Figure 4.3.3 adjusted for a peak acceleration of 300 gals. These strong ground motions are input as the incident wave applied at the lower boundary of both numeri-

cal models described below.

4.3.4 Numerical models

Two numerical models were prepared for each model as shown in Figure 4.3.4 in which the lower boundary was set at the depth of 80 m below the ground surface and the figure shows the first 40 m portion of the model. One is semi-infinite horizontally layered model for use in the one-dimensional wave propagation analysis neglecting the presence of ducts. For this model, an analytical infinite boundary is used at the lower boundary. The other is a two-dimensional finite element model with plane strain assumption used in both the dynamic analysis by FLUSH-VB already described in this paper and the quasi-static analysis by GRAMBS. When the model is used for the dynamic analysis by FLUSH-VB, the viscous dampers are attached in both the horizontal and vertical directions at the lower boundary and transmitting boundaries were adopted for the side boundaries; whereas for the quasi-static analysis by GRAMBS the lower boundary was fixed and horizontal rollers were attached to the side boundaries.

4.3.5 Analyses

First the free-field soil response analysis was performed as a representative case to obtain each response acceleration distribution over all depths of the model at the time the relative displacement of the soil between the top and bottom level of the submerged duct of each analysis model, Model-1 to Model-9, in the previous Table 4.3.1 becomes maximum.

The resultant response acceleration distributions are converted into the seismic intensity distributions to the elements in the two-dimensional quasi-static finite element models containing the ducts prescribed in Table 4.3.1. A schematic illustration of the seismic intensity distribution is shown in Figure 4.3.4. The static stress analyses were performed with the body force corresponding to the seismic intensity distribution of each case and the results were expressed in terms of the cross-sectional moment(M), axial force(N) and shear force(Q).

Next, all the models shown in Table 4.3.1 were analyzed by FLUSH-VB under the conditions as already described and the results were given also in the form of the cross-sectional forces described above.

In both the analyses by one-dimensional wave propagation analysis of the free-field soil and the two-dimensional dynamic analysis of the system with a duct, the initial damping factor of the soft rock was assumed as 2 % and the calculations were repeated until the strain dependent soil properties reach the convergence limit of 5 %.

4.3.6 Results

The results of both analyses by FLUSH-VB and GRAMBS are summarized for the maximum end-moment, axial force and shear force of each case shown in Table 4.3.3 and the details of these cross-sectional forces are shown in Figures 4.3.5 to 4.3.7. From these table and figures, the results obtained by GRAMBS are amazingly close to those obtained by FLUSH-VB.

The end-moments obtained through Model-2 and Model-9 are shown in Figures 4.3.8 and 4.3.9, respectively, in comparative manner with the additional results by other simplified analysis methods; these include the so-called Response Displacement Method (hereafter called as RDM) and the method proposed by CRIEPI (hereafter called RDM-C) in its report to the JSCE(JSCE, 1984). From these figures, it is evident that the results obtained by FLUSH-VB and GRAMBS are very close regardless of the condition of the duct relative to the surrounding soil, whereas the results obtained by RDM and RDM-C give either under-estimated or over-estimated the results with changes in the conditions.

Figure 4.3.10 shows the stress states at the outer surface of the duct obtained by FLUSH-VB and GRAMS. They are close with each other and this clearly states that both of the above simplified methods, RDM and RDM-C, should have assumed from the beginning such compatible soil springs with these models consistent with the resultant stress distribution around the duct that have been obtained by FLUSH and GRAMBS.

On the other hand, by simply prescribing the maximum lateral relative displacement of the soil between the top and bottom of the duct with the connected soil springs to the duct, this being the fundamental assumption of these analysis methods, such stress distribution as shown in this figure may not be foreseeable before doing a rigorous analysis, say by FLUSH-VB.

The other trials using the RDM methodology but introducing such stress-compatible soil springs gave better results than those given this

time; this can be realized just after knowing the stress distribution by the rigorous analysis. Such a procedure can not be followed in practice because these methods assume the independent normal springs and shear springs connected to the duct by ignoring the constitutive law governing the above two springs in a continuum element of the soil.

The results obtained by RDM-C seems a little closer than RDM to the result by FLUSH-VB; however, the method assumes to introduce additionally the time independent maximum response acceleration distribution of the soil irrespective of the mass of the duct, resulting in an inconsistent simplification caused by neglecting the basic equation of motion of the dynamic system.

In practice, the soil springs assumed in both RDM and RDM-C have been obtained by using almost the same two-dimensional static finite element model with the cavity corresponding to the embedded duct. The number of calculations as well as the computer time required for obtaining these soil springs exceeds always the single calculation of the system with the embedded duct needed for GRAMBS. Therefore, the current RDM or RDM-C or similar methods with many options of load assumption do not appear to be rational nor economical.

Table 4.3.4 compares the results only for the maximum end-moment obtained by at models other than those previously mentioned. From this table, the results obtained by GRAMBS always give very close results with those obtained by FLUSH-VB and stable for the possible change of situation of the embedment of the duct. Even if the shear wave velocity of the surface soil is varied from 200 m/s to 300 m/s and also the input ground motion was changed from the Taft record to Lake Hughes record; e.g., if the frequency characteristic of the input ground motion is changed, the results obtained by GRAMBS are consistently very close to those obtained by FLUSH as shown in Table 4.3.5.

Finally, in Figure 4.3.11, the acceleration response spectra of the free-field soil response motion of the top of the layer No. 8 and the response obtained by FLUSH-VB of the nodal point No. 193 at the center of the top slab of the duct for the Model-9 are compared, the locations of which are shown in the previous Figure 4.3.4. There are certainly some difference between the two results and this difference may show the load transmitting characteristics in the lower frequency due to a sudden change in the rigidities of the soil and the duct, and the soil-structure interaction effect at the higher frequency range, even if it seems small.

As for the time required for GRAMBS, it took only one tenth of the

computer time required for the analysis by FLUSH-VB.

From all the above analytical results, it can be said with confidence that the GRAMBS proposed by the author will be a good approximate method for predicting the maximum stress state of the type of buried ducts analyzed here or for similar single-story structures in uniform soil that would otherwise require a more rigorous two-dimensional finite element analysis like FLUSH-VB.

4.3.7 Validation of GRAMBS in comparison with experimental result

The dynamic response of a simple duct embedded in loose sand layer during strong ground motion has been studied using a shear soil column on a shaking table by Tohma and others of CRIEPI(Tohma and others, 1985).

The simple duct made of plastics of the size 45 cm by 60 cm was embedded in a naturally dried state fine sand packed in a cylindrical tank of internal diameter 300 cm and height 150 cm as shown in Figure 4.3.12. This model was designed to correspond to the prototype duct of concrete embedded in soil with a shear wave velocity of around 250 m/s which is very close to the numerical model already analyzed in this paper.

The model was forced to vibrate by the transient motion equivalent to the 1940 El Centro record, the frequency characteristics of the input motion to the shaking table and the response motion observed at the surface of the sand column are shown in Figure 4.3.13.

The results of the shaking test for the case when the duct is embedded in the sand as the bottom of the duct reaches the depth equal to its height("shallow case" in their report) are given in terms of the maximum bending moment distribution of the duct walls as shown in Figure 4.3.14.

The response of this duct during the shaking test was analyzed by the numerical model as shown in Figure 4.3.15 using the strain-dependent properties of the sand in Figure 4.3.16 which was obtained by performing the resonance column test using the same shear column without the model duct as one test of the series of experiments. The computer code FLUSH was used for the simulation analysis of the experiment and the results are similarly given by the maximum bending moment distribution of the duct walls which is also plotted in the previous Figure 4.3.14. The maximum bending moment distributions of the duct obtained by the

experiment and the numerical analysis using FLUSH coincide well with each other.

In Figure 4.3.17, which is similar to the previous Figure 4.3.11, the acceleration response spectra of the free-field surface response and the acceleration response of the top slab of the duct are shown, and from the good agreement between these results it is concluded that the acceleration response of the duct and the surrounding soil are behaving almost equally.

The above comparative study of the experimental and numerical response behavior of the model duct clearly shows that the two-dimensional dynamic analysis code which considers the non-linear effect of the soil surrounding the duct can reproduce the dynamic behavior of the buried duct adequately.

The foregoing analyses using various models under various conditions relative to the surrounding soil showed amazingly good agreement in the numerical results obtained by FLUSH-VB and GRAMBS. The fundamental situation of the model in these two studies are almost common.

Therefore, it can be finally concluded that the GRAMBS proposed by the author can be used as a practical and reliable design analysis tool for predicting the maximum stress state of the type of prototype buried ducts having the conditions assumed here or for similar single-story structures in uniform soil.

4.3.8 References

(1) Katayama, I., M. Adachi, M. Shimada and T. Tsuzuki, On the practical analysis method for design analysis of buried structures, 19th Annual Meeting of Japan Society of Soil and Foundation, Abstracts, pp. 144-145, June, 1984(in Japanese).

(2) Katayama, I., M. Adachi, M.Shimada, T.Tsuzuki and Y. Seshimo, A quasi-static analysis method for for buried structures - A proposal of "Response Acceleration Method", Abstracts, 40th Annual Meeting of Japan Society of Civil Engineers, Part 1, pp. 737-738, Sept., 1985 (in Japanese).

(3) JSCE, Study on the evaluation of foundation - The study on the standardization of evaluation methodology of foundation, 1984.

(4) Tohma, J. et al, Model experiment of sea water intake duct of nuclear power plant, Denryoku doboku, No. 197, pp. 36-44, July, 1985(in Japanese).

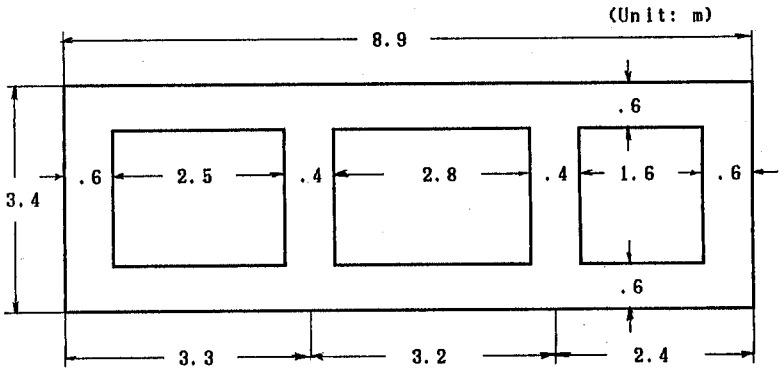

Figure 4.3.1 The model of one storied multi-cell concrete duct

Table 4.3.1 Installation conditions of the duct and the case number of the analyses

(Unit:m)

		Ld= 2.75	Ld= 15.0	Ld= 27.75	Ld= 40.0
Ls	Ls/L	Ld/L= .069	Ld/L=.375	Ld/L=.694	Ld/L=1.00
40.0	1.00	MODEL - 1	MODEL - 2	MODEL - 3	MODEL - 4
27.8	.694	MODEL - 5	MODEL - 6	MODEL - 7	Regend (Ls, L, Ld)
15.0		MODEL - 8	MODEL -9		

Notes: L ; Total depth of model
Ld; Embedment depth of duct
Ls; Depth of surface soil
denotes soft rock layer

Table 4.3.2 Dynamic material properties used for the model

	Specific weight t/qub. m	Poisson's ratio	Shear wave velocity m/s	Shear modulus t/sq. m
R. F. Concrete	2. 4	0. 1667	----	1. 16 million
Surface soil	1. 8	0. 4	200	7, 350
Soft rock	1. 9	0. 35	500	48, 470
Base rock	2. 3	0. 3	1, 000	234, 690

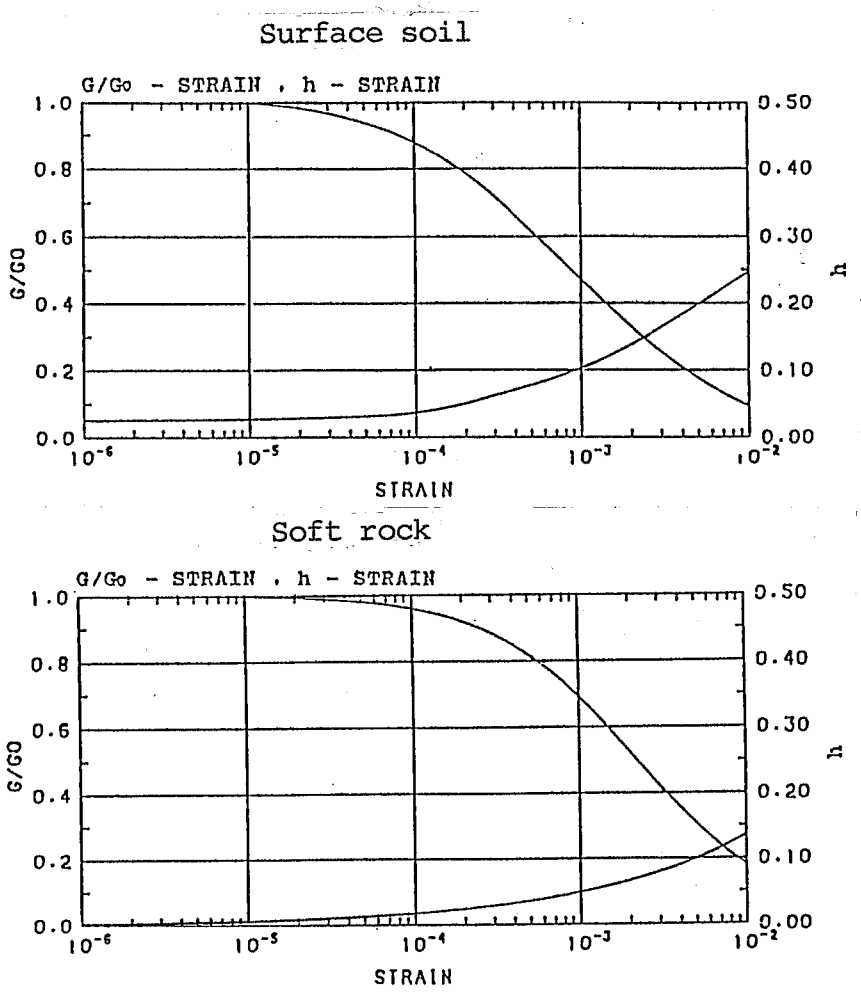

Figure 4.3.2 Strain dependent dynamic properties of the soil and the soft rock

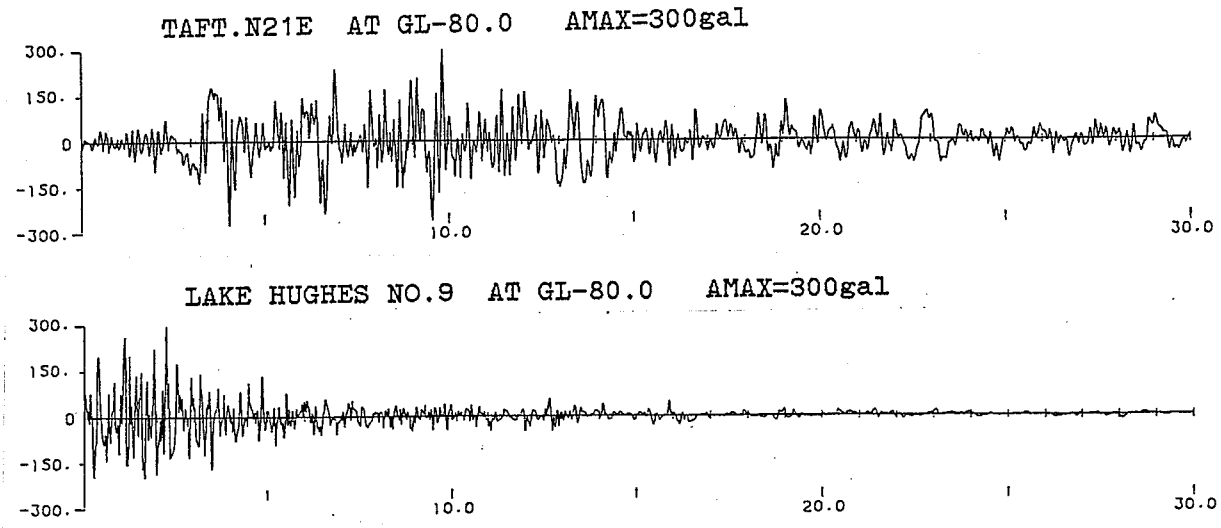

Figure 4.3.3 Input ground motions used for analyses; the upper figure shows the strong motion originated from Taft records (1957) and the lower from Lake Hughes array No. 9 (1971).

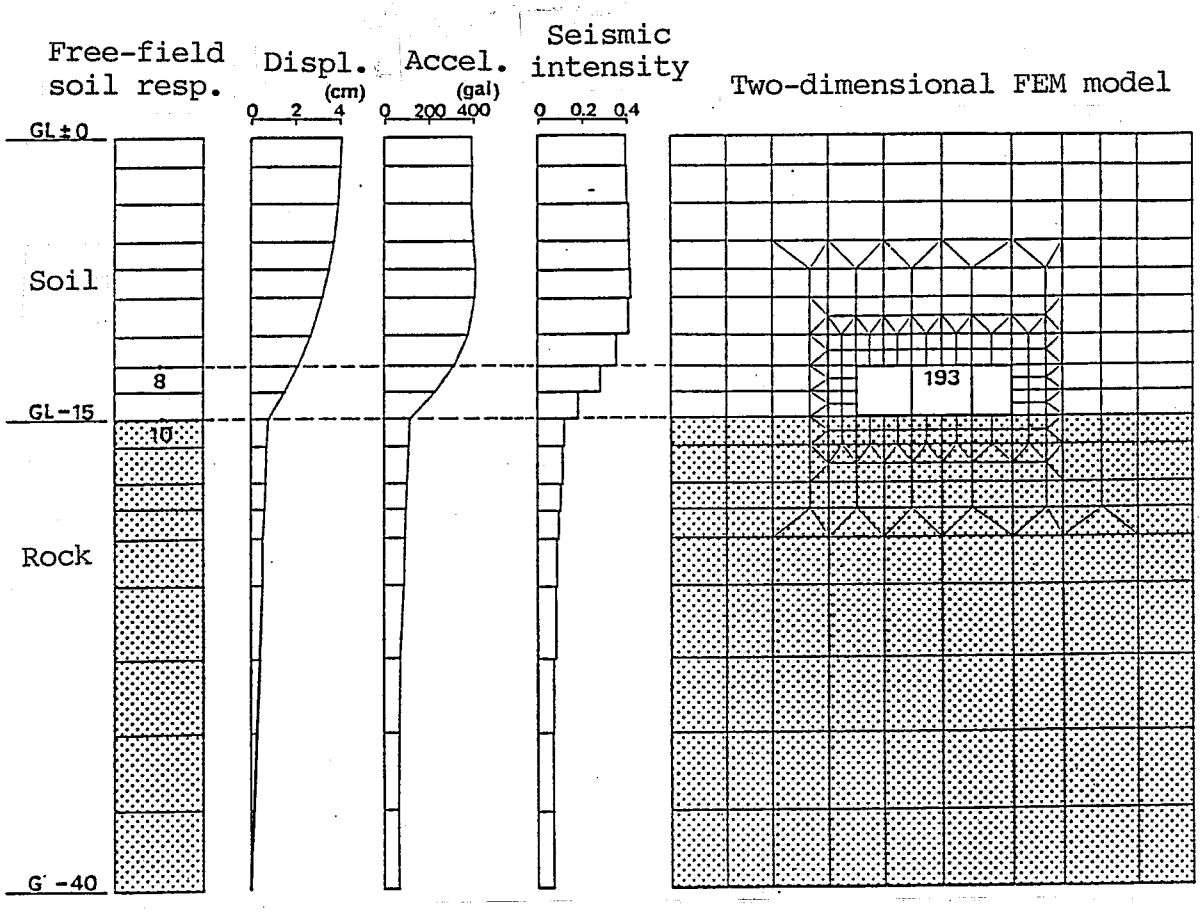

Figure 4.3.4 Numerical models for the free-field soil response analysis and the two-dimensional finite element dynamic analysis and the quasi-static analysis; the lowest boundaries are at 80 meters depth and only the first 40 meters portions are shown in this figure.

Table 4.3.3 Comparison of the maximum cross-sectional forces obtained through the analyses by FLUSH-VB and GRAMBS(Vs=200 m/s;Taft record).

	FLUSH - VB	GRAMBS
MODEL - 1	2.8 1.8 2.6 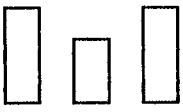 M N Q	2.8 1.8 2.6 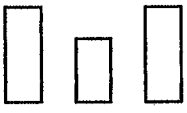 M N Q
MODEL - 2	27 11 18 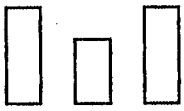 M N Q	27 11 19 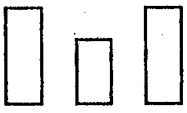 M N Q
MODEL - 9	68 33 51 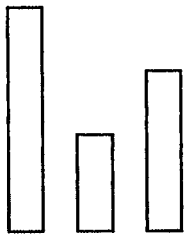 M N Q	61 34 45 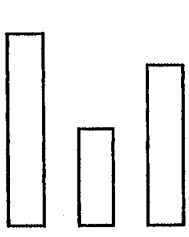 M N Q

Notes: M; Maximum end moment (ton • m)
N; Maximum axial force (ton)
Q; Maximum shear force (ton)

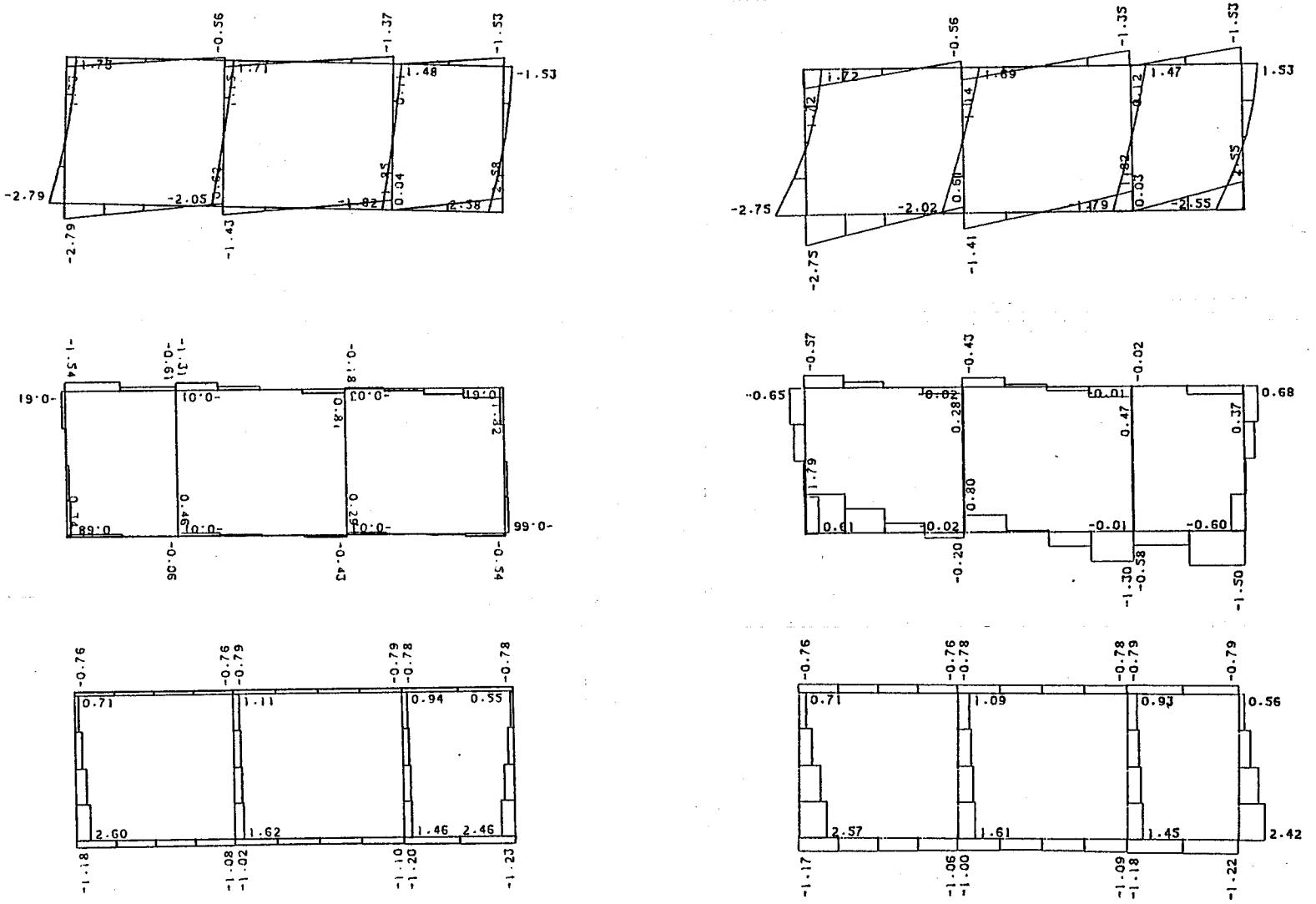

(a) by FLUSH-VB (B) by GRAMBS

Figure 4.3.5 The cross-sectional force distribution of Model-1 (T_M=4.02 sec.); (a) the results by FLUSH-VB and (b) the results by GRAMBS

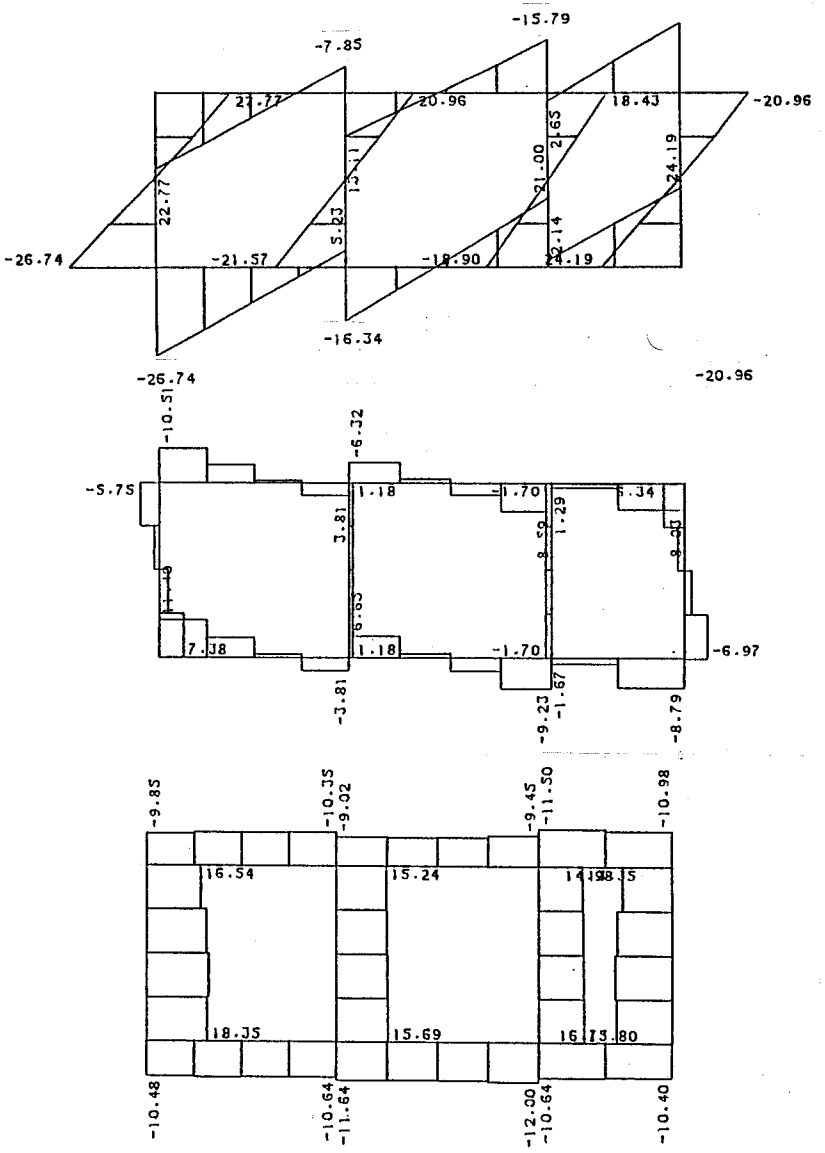

(a) by FLUSH-VB

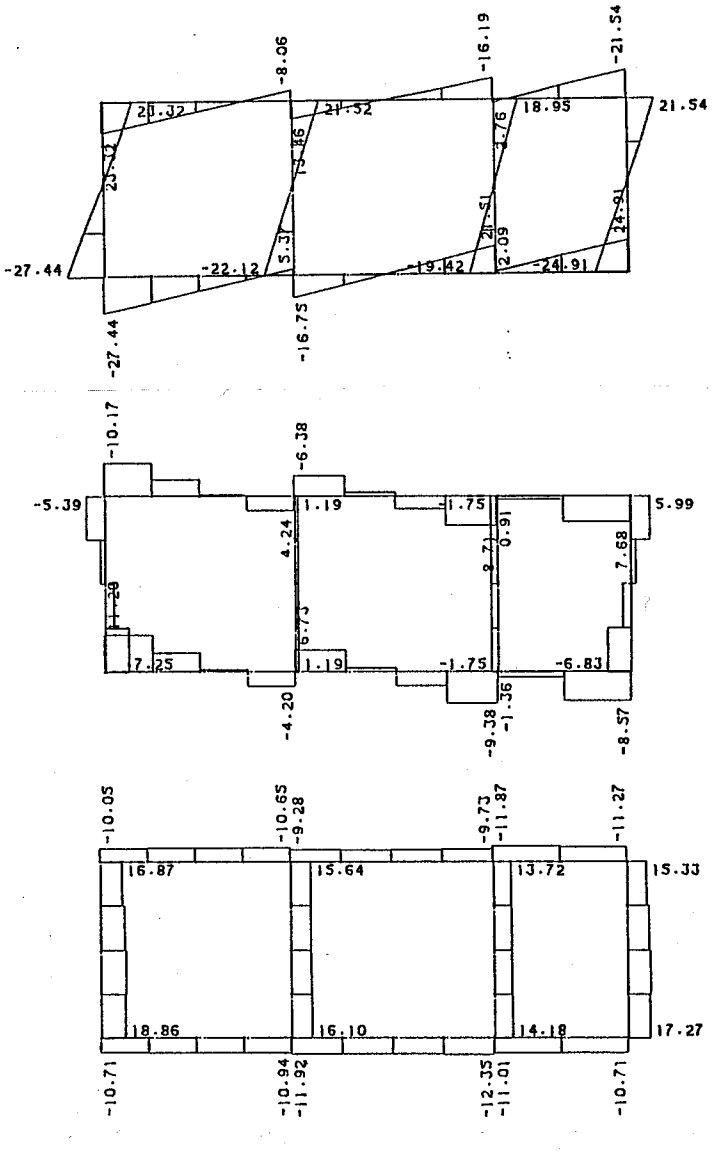

(B) by GRAMBS

Figure 4.3.6 The cross-sectional force distribution of Model-2 (T_M=4.06 sec.); (a) the results by FLUSH-VB and (b) the results by GRAMBS

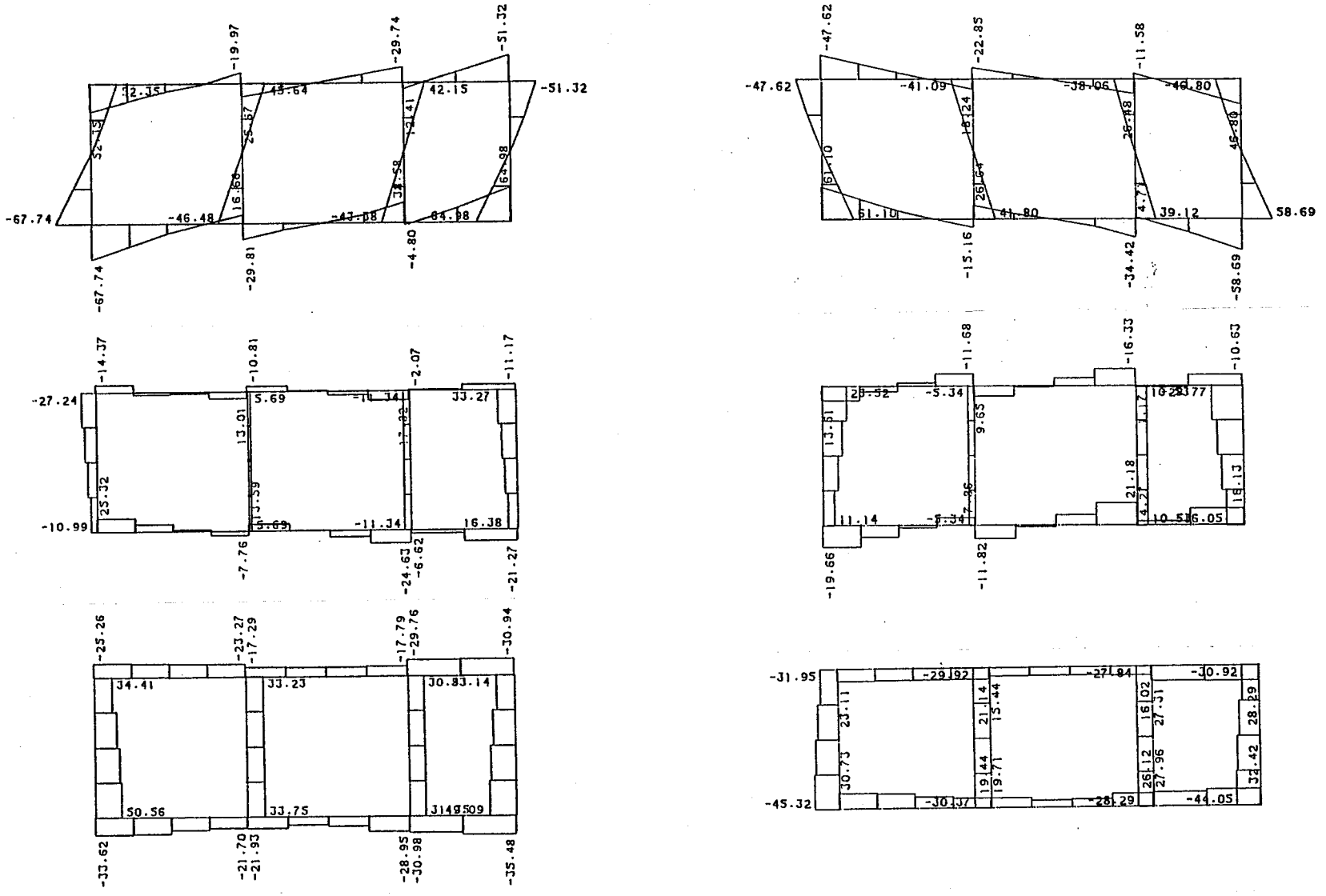

(a) by FLUSH-VB

(B) by GRAMBS

Figure 4.3.7 The cross-sectional force distribution of Model-9 (T_M=6.82 sec.); (a) the results by FLUSH-VB and (b) the results by GRAMBS

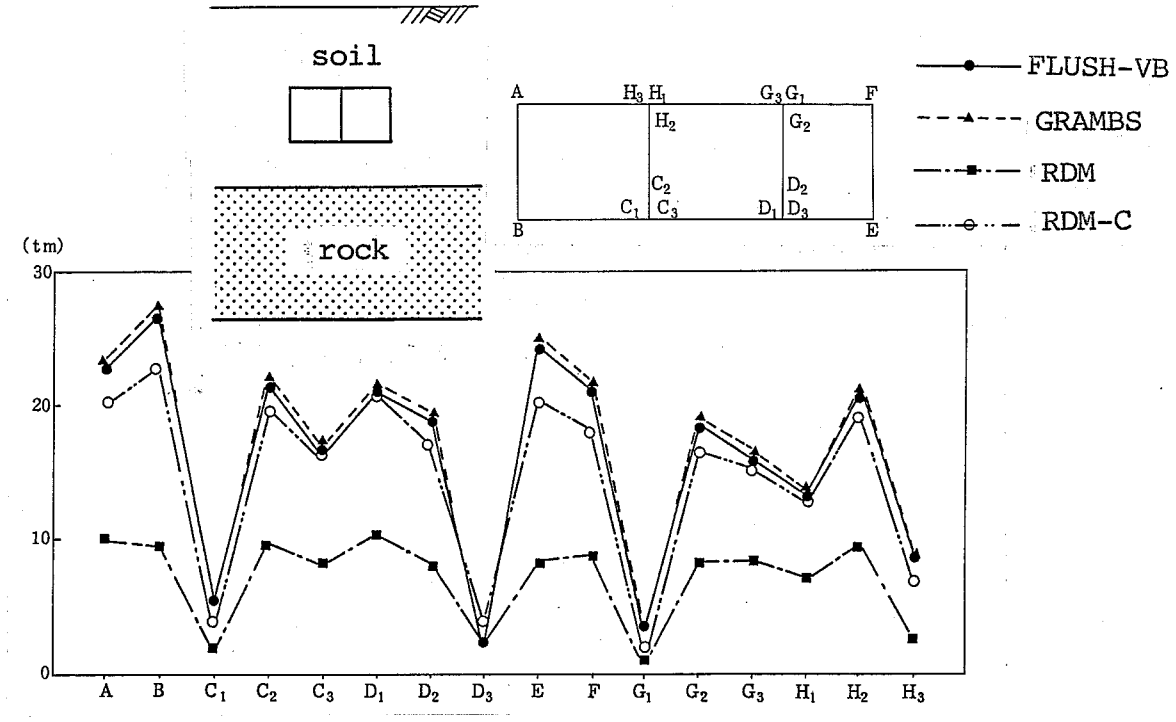

Figure 4.3.8 Comparison of the end-moment distribution of Model-2 obtained by various analysis methods; the evaluating position of the end-moments is in the figure attached.

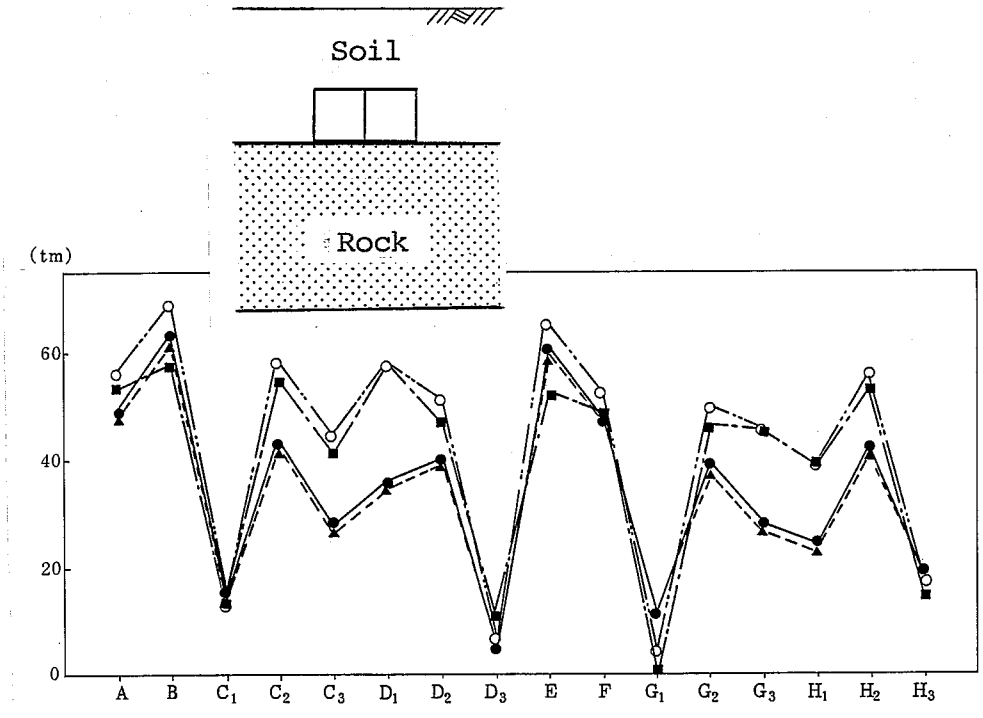

Figure 4.3.9 Comparison of the end-moment distribution of Model-9 obtained by various analysis methods; the evaluating position of the end-moments is same as is in Figure 4.3.8.

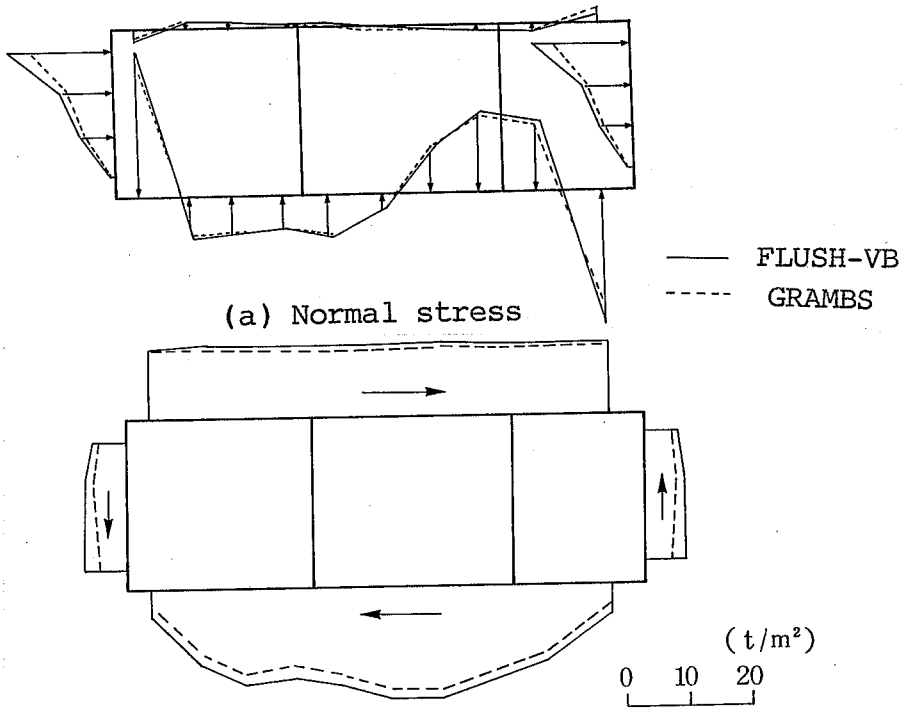

Figure 4.3.10 Comparison of the stress distribution at the outer surface of the duct by FLUSH-VB and GRAMBS in case of Model-9; (a) and (b) shows the normal stress and shear stress, respectively.

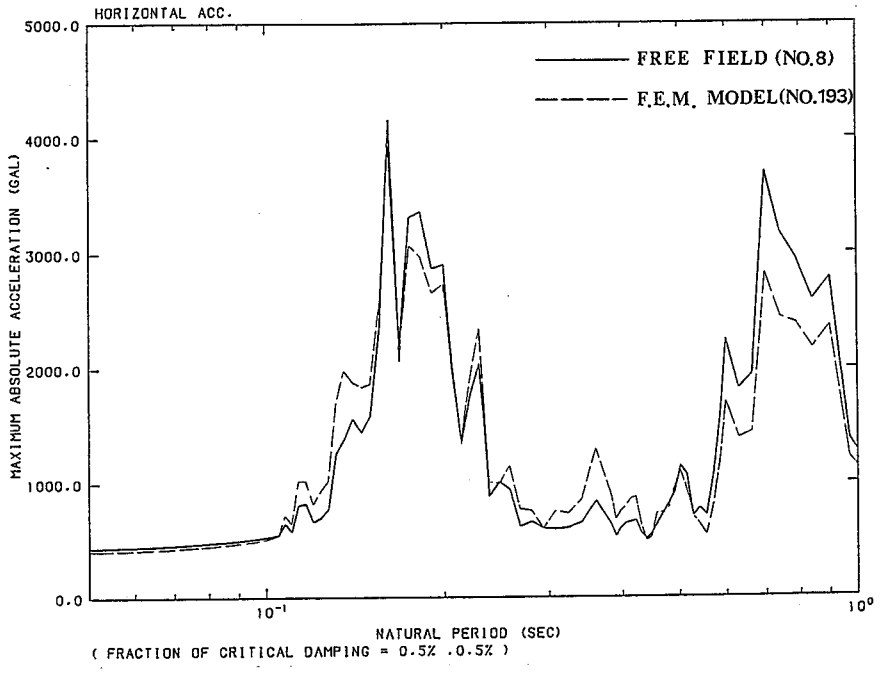

Figure 4.3.11, Comparison of the acceleration response spectra of the free-field soil response motion of the top of the layer No. 8 and the response obtained by FLUSH-VB of the nodal point No. 193 at the center of the top slab of the duct for the Model-9.

Table 4.3.4 Comparison of the maximum end-moments obtained by FLUSH-VB and GRAMBS with the models analyzed by using Vs=200 m/s and Taft record.

FLUSH-VB	GRAMBS	FLUSH-VB	GRAMBS	FLUSH-VB	GRAMBS
2.8 M	2.8 M	27 M	27 M	47 M	47 M
MODEL - 1		MODEL - 2		MODEL - 3	
3.7 M	3.7 M	35 M	37 M	80 M	80 M
MODEL - 5		MODEL - 6		MODEL - 7	
6.6 M	6.5 M	68 M	61 M		
MODEL - 8		MODEL - 9			

UNIT: M (ton • m)

Table 4.3.5 Comparison of the maximum end-moments obtained at Model-3 when the shear wave velocity of the surface soil layer and the input ground motioncompares were changed.

	Shear velocity of surface soil(Vs)			
	200 m/s		300 m/s	
TAFT RECORD	FLUSH-VB 47 M	GRAMBS 47 M	FLUSH-VB 61 M	GRAMBS 56 M
LAKE HUGHES RECORD	FLUSH-VB 21 M	GRAMBS 22 M	FLUSH-VB 29 M	GRAMBS 29 M

UNIT: M (ton • m)

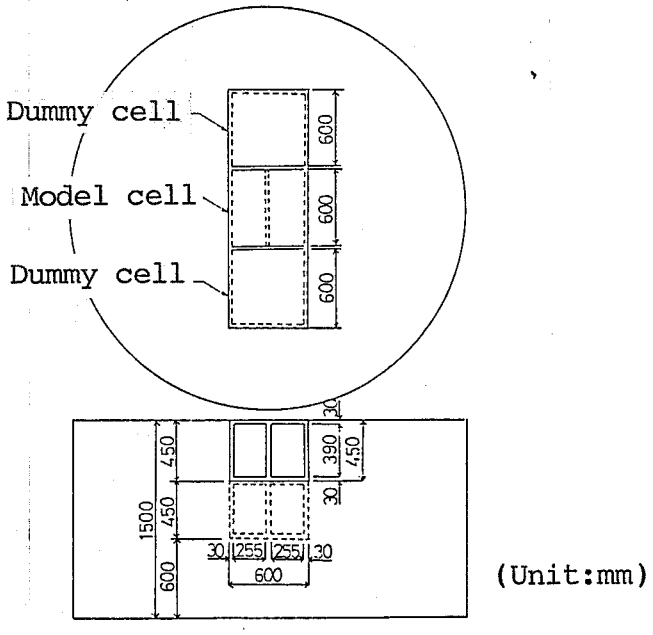

Figure 4.3.12 Plastic duct and shear soil column used in the experiment (After Tohma and others, 1985)

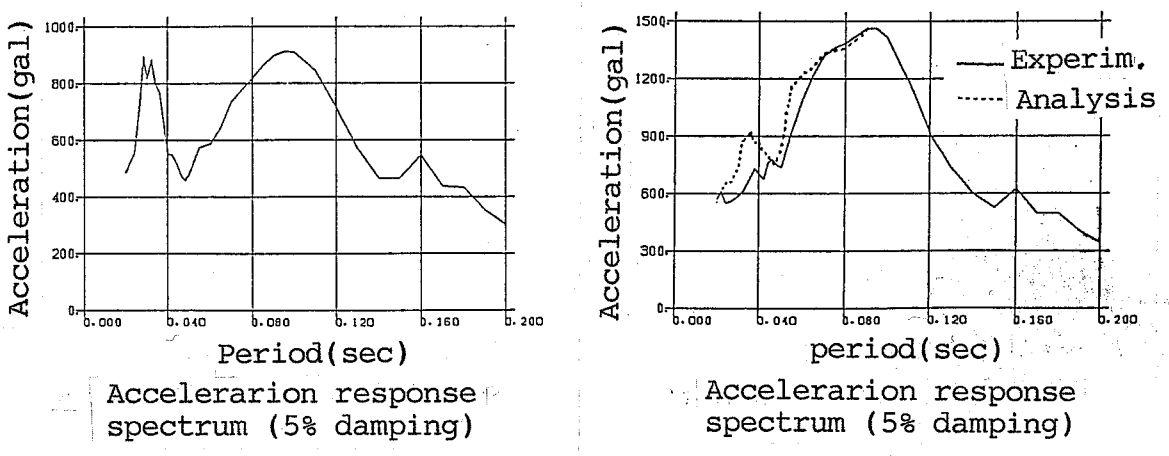

Figure 4.3.13 Frequency characteristic of the input motion and the measured response of the soil column surface motion (After Tohma and others, 1985)

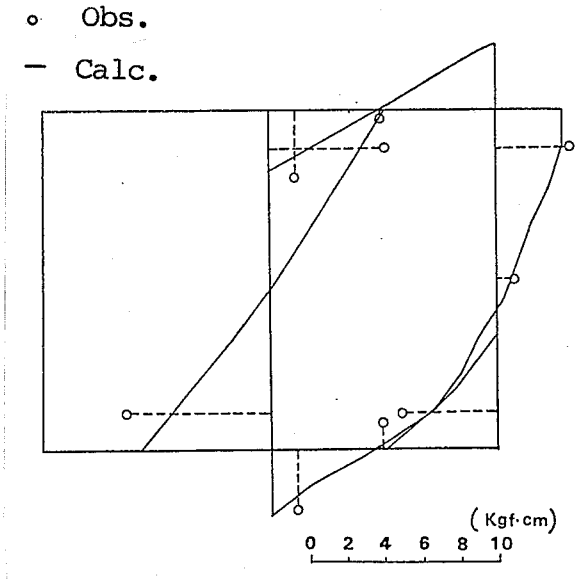

Figure 4.3.14 Maximum bending moment distribution of the duct walls obtained by the experiment ("shallow case"; After Tohma and others, 1985)

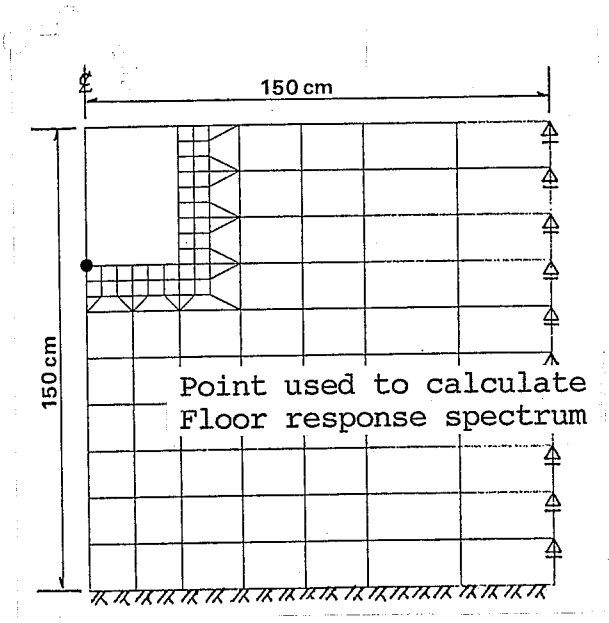

Figure 4.3.15 Numerical model used in the simulation of the experimental results by FLUSH (After Tohma and others, 1985)

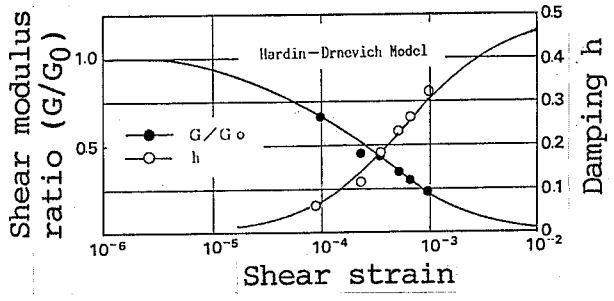

Figure 4.3.16 Strain dependent properties of the sand used in the experiment (After Tohma and others, 1985)

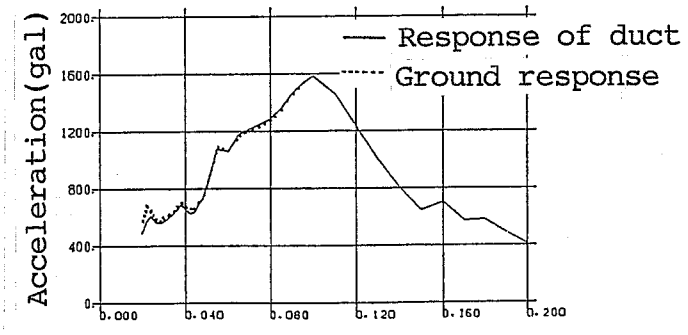

Figure 4.3.17 Acceleration response spectra of the free-field surface response and the acceleration response of the top slap of the duct (After Tohma and others, 1985)

4.4 APPLICATION TO AN UNDERGROUND POWER TRANSMISSION SHAFT IN LAYERED SOIL

Kaizu, Annaka, and Ohki(1989(a) and (b)) and Kaizu, Harada, Annaka and Ohki(1989) reported that the dynamic behavior of a shaft clearly corresponded to the shear deformation of the surrounding soil through the analysis of observed response records. As these authors were kind enough to allow the author to use their data and figures, the author analyzed by GRAMBS the shaft using the same analytical model, soil properties and input ground motion as they used.

4.4.1 Observed response and analytical results

A shaft for underground power transmission system of the Tokyo Electric Power Co., Inc. constructed at a site in Metropolitan Tokyo has been installed with sophisticated instrumentation of seismometers, soil pressure meters and re-bar extensometers and the observation of the dynamic behavior of the shaft has been extensively performed.

Kaizu, Annaka, and Ohki(1989(a) and (b)) and Kaizu, Harada, Annaka and Ohki(1989) have reported in a series of their papers the characteristics of the dynamic behavior of the shaft during earthquake and they simulated the maximum response accelerations, re-bar stresses and soil pressures by the two-dimensional finite element analysis using FLUSH-VB already mentioned in this paper.

The vertical section with the installed measuring sensors, the soil profile and soil properties explored in-situ are shown in Figure 4.4.1, in which the values of the shear wave velocity and damping ratio of each soil layer were determined as those giving a best fit to the observed free-field response of the records of the vertical array. Figure 4.4.2 shows the plan of the shaft and the location of the vertical array installed about 31 m away from the shaft to observe the free-field soil response.

The examples of the soil response motions recorded by the vertical array and the response of the shaft in the event of the Southern Ibaragi Prefecture Earthquake on October 4, 1985 are shown in Figure 4.4.3.

To simulate the response of the shaft during the earthquake, the ground response at the vertical array was first simulated and the simulated motion by one-dimensional wave propagation analysis is shown in comparison with the recorded motion at the point GL. -44.81 m and its

Fourier spectrum ratio in Figure 4.4.4. In Figure 4.4.5, the deconvolved outcrop motion at the depth of -82.55 m is shown in terms of time history and Fourier spectrum, which has been used as the input ground motion in the numerical model shown in Figure 4.4.6(a). Figure 4.4.6(b) shows the simulated and the observed maximum accelerations of the shaft, the surrounding soil and the free-field soil; the good agreement between the calculated and observed response is evident from the figure. Finally they obtained the results of the simulation as shown in Figure 4.4.7, in which the absolute maxima obtained in the re-bar extensometers and soil pressure meters by the simulation analysis and observation are clearly shown with good agreement.

4.4.2 Simulation by GRAMBS

To simulate by GRAMBS the same maximum observations shown above, first the free-field response analysis was performed using basically the same soil profile and properties already determined and the acceleration profile of the soil at the time t_m=5.75 sec when the shear strain energy between the portion of the soil from the ground surface to the bottom of the shaft became maximum was obtained as shown in Figure 4.4.8 converted into the seismic intensity profile for use in subsequent analysis. The determination of the time t_m was easy as shown in Figure 4.4.9.

By using the seismic intensity and the converged values of soil properties in the previous Figure 4.4.1 in the static finite element model of the system consisting of the shaft and the surrounding soil shown in Figure 4.4.10 for the quasi-static analysis by GRAMBS, the shear stress distribution of the soil at the contact surface of the shaft was obtained as shown in Figure 4.4.11 in comparison with the results obtained in the simulation by FLUSH-VB previously described. The difference between the two results was within a few percent. The model used this time has more wide soil regions than the model used for the simulation by FLUSH-VB, because the analysis by GRAMBS is basically a static analysis and the applied body force does not alternate its direction as in an actual seismic load. The boundary conditions of the model are basically the same as were already described in the foregoing section.

The results of the simulation by GRAMBS are shown in Figure 4.4.12 indicated for time t_m already mentioned of the records and the results obtained by FLUSH -VB. This figure indicates the alternate nature of the response of the duct which is different from the maximum absolute values given in the previous Figure 4.4.7; however, it is already evident that

the GRAMBS first developed for one-story duct with uniform soil can be applied also to structures like this shaft which consists of multi-story structures surrounded by multi-layered soil through the assumption of determining the time t_m that maximize the contribution of the shear strain energy of the soil to the embedded structure.

4.4.3 References

(1) Kaizu, N., T. Annaka, and H. Ohki, Observation of behavior of underground power transmission shaft during earthquake, 20th Oral Meeting of Earthquake Engineering Research, Japan Society of Civil Engineers, July 1989(a)(in Japanese).

(2) Kaizu, N., T. Annaka, and H. Ohki, Analysis of behavior of underground power transmission shaft during earthquake, 20th Oral Meeting of Earthquake Engineering Research, Japan Society of Civil Engineers, July, 1989(b)(in Japanese).

(3) Kaizu, N., M. Harada, T. Annaka and H. Ohki, Observation and numerical analyses of shaft for underground transmission lines, The American Society of Mechanical Engineers, PVP - Vol. 162, pp. 183-190, 1989.

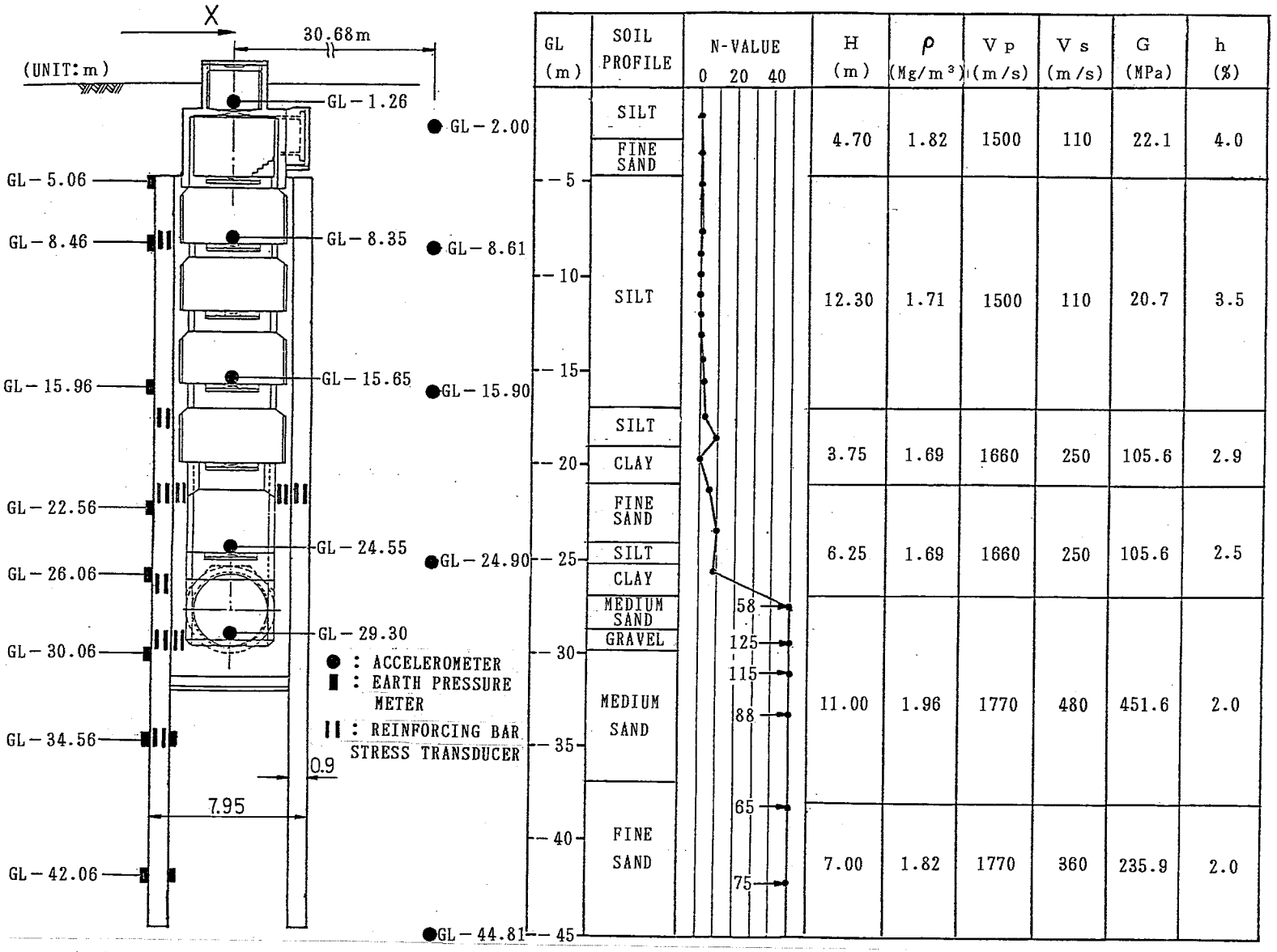

Figure 4.4.1 Vertical section of shaft, location of seismometers, re-bar extensometers, soil pressure meters of the shaft, soil profile and properties of surrounding soil.

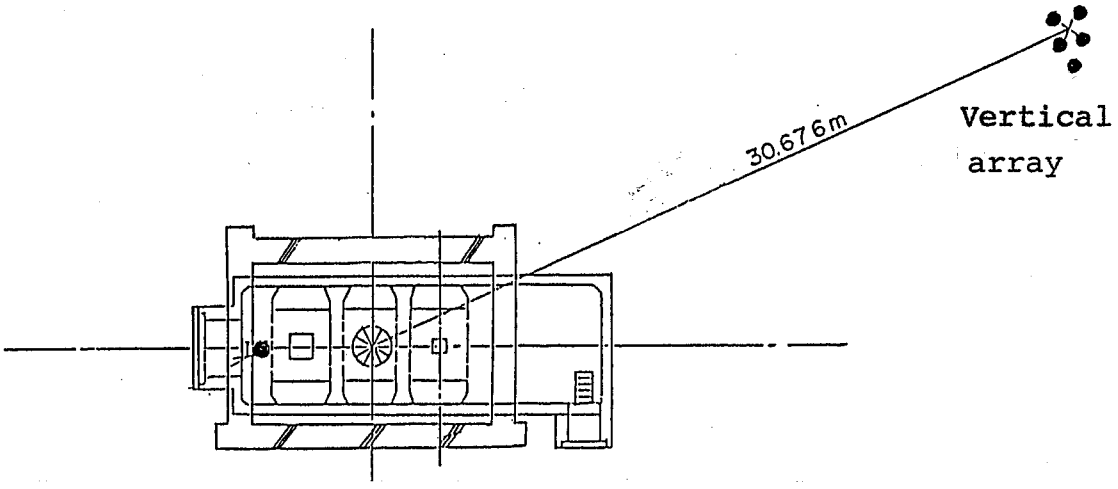

Figure 4.4.2 Plan of shaft and the location of vertical array; the location of the seismometers is in Figure 4.4.1).

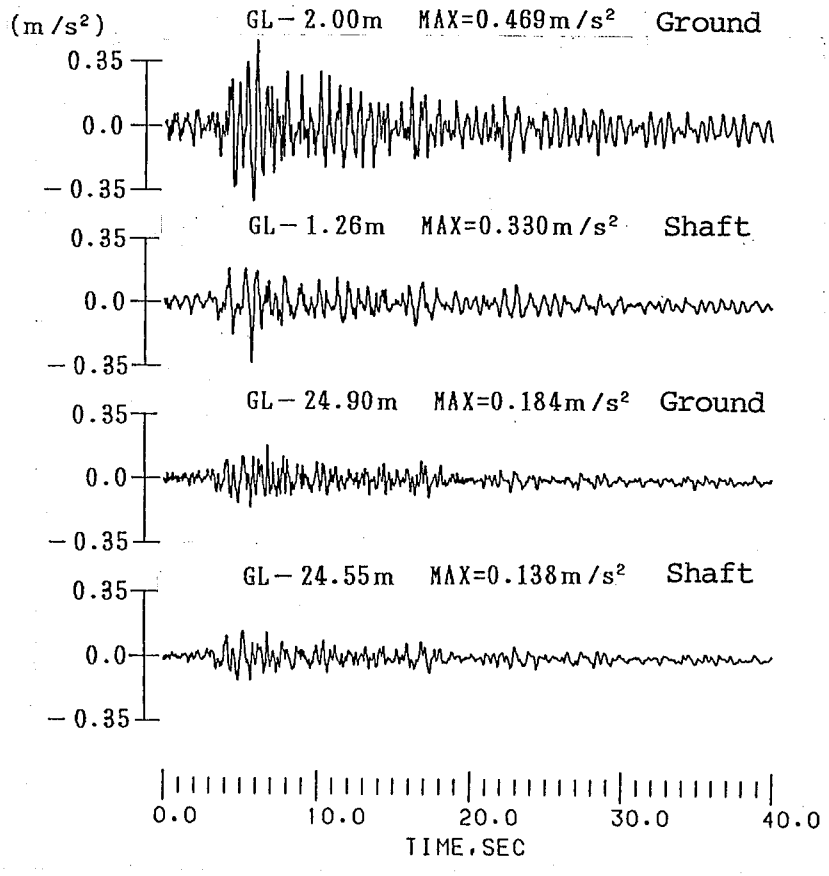

Figure 4.4.3 The examples of the soil response motions recorded at the vertical array and the response of the shaft in the event of the Southern Ibaragi Prefecture Earthquake on October 4, 1985.

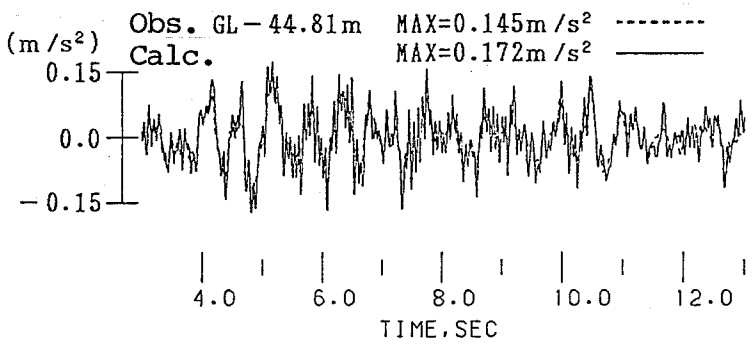

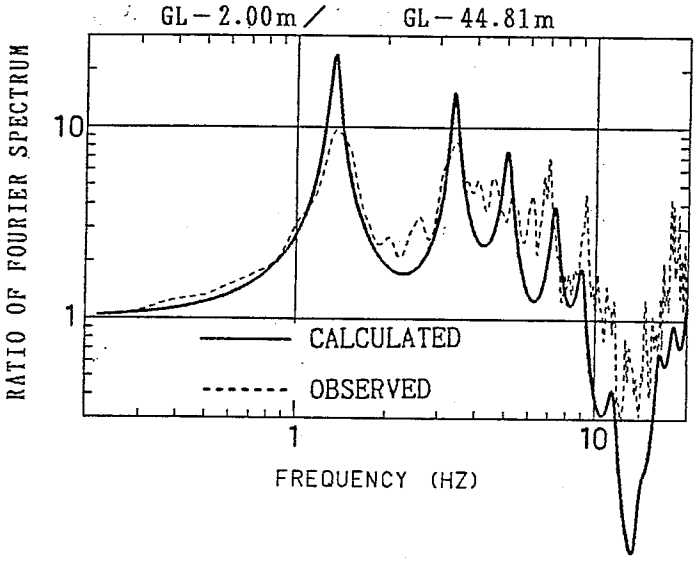

Figure 4.4.4 Simulated time history and the recorded motion of the point GL. -44.81 m and the respective Fourier spectrum ratios

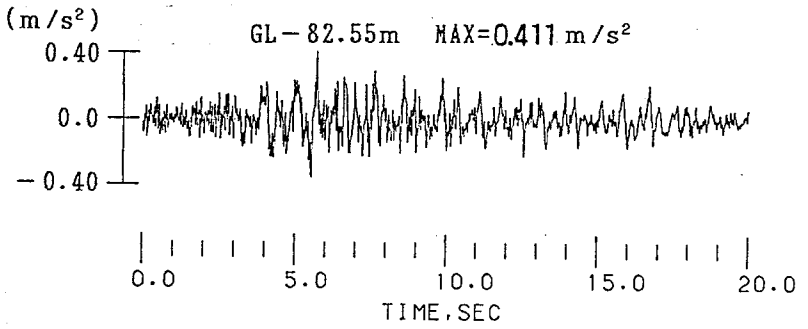

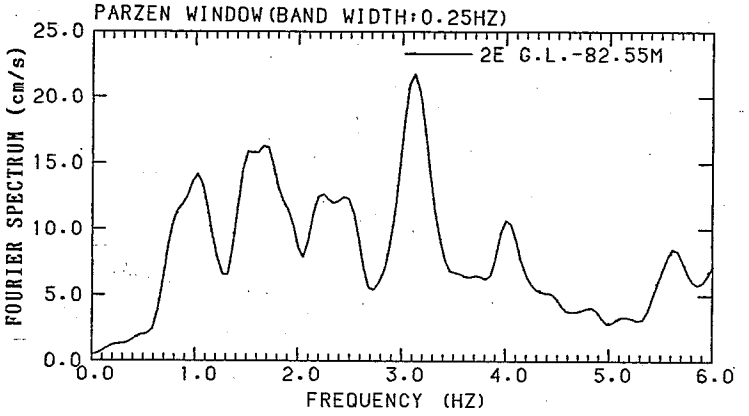

Figure 4.4.5 Deconvolved outcrop motion at the depth of -82.55 m and Fourier spectrum used as the input motion of the numerical model shown in Figure 4.4.6(a)

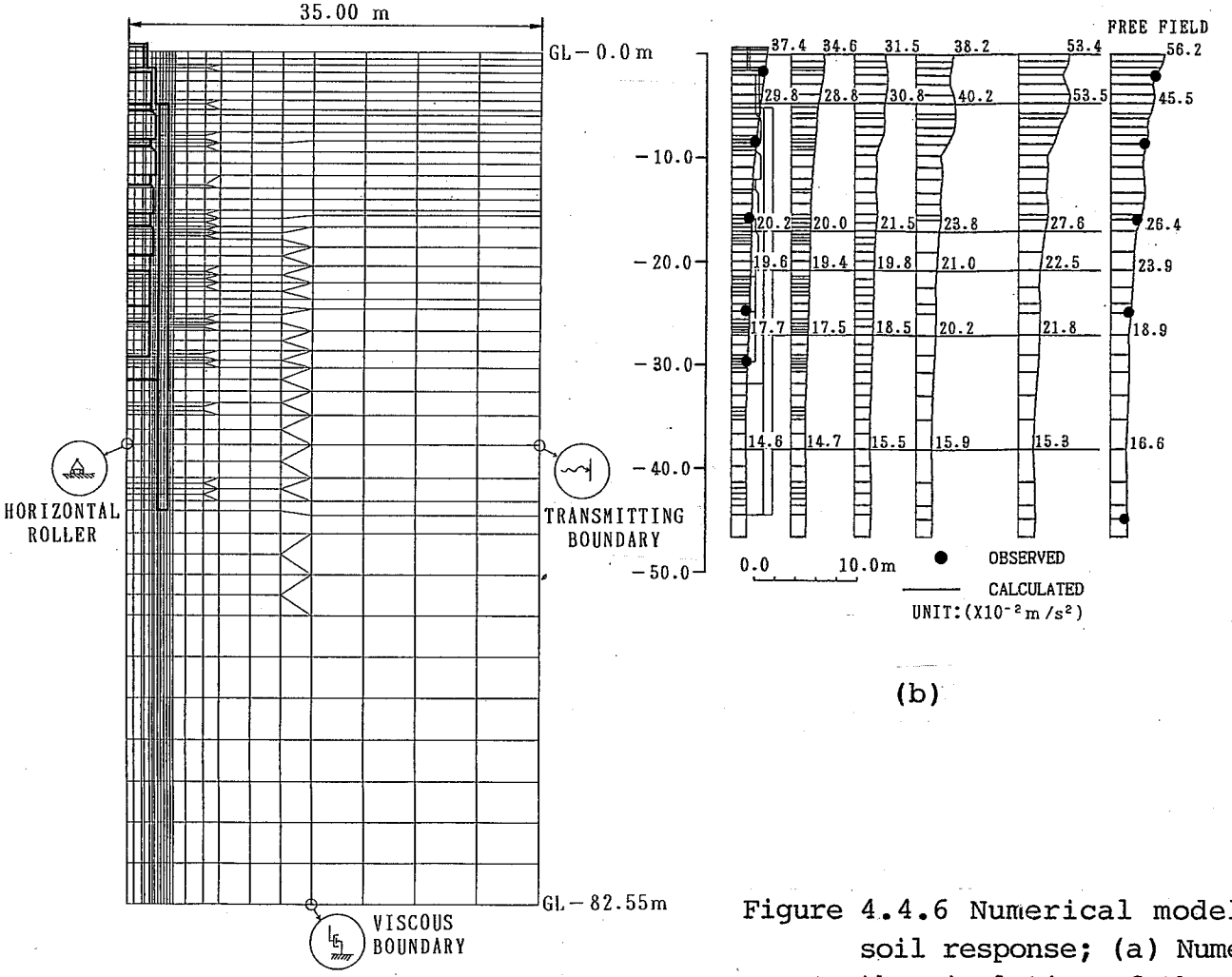

Figure 4.4.6 Numerical model and the simulated soil response; (a) Numerical model used for the simulation of the shaft by FLUSH-VB and (b) the simulated and the observed maximum accelerations of the shaft, the surrounding soil and the free-field soil

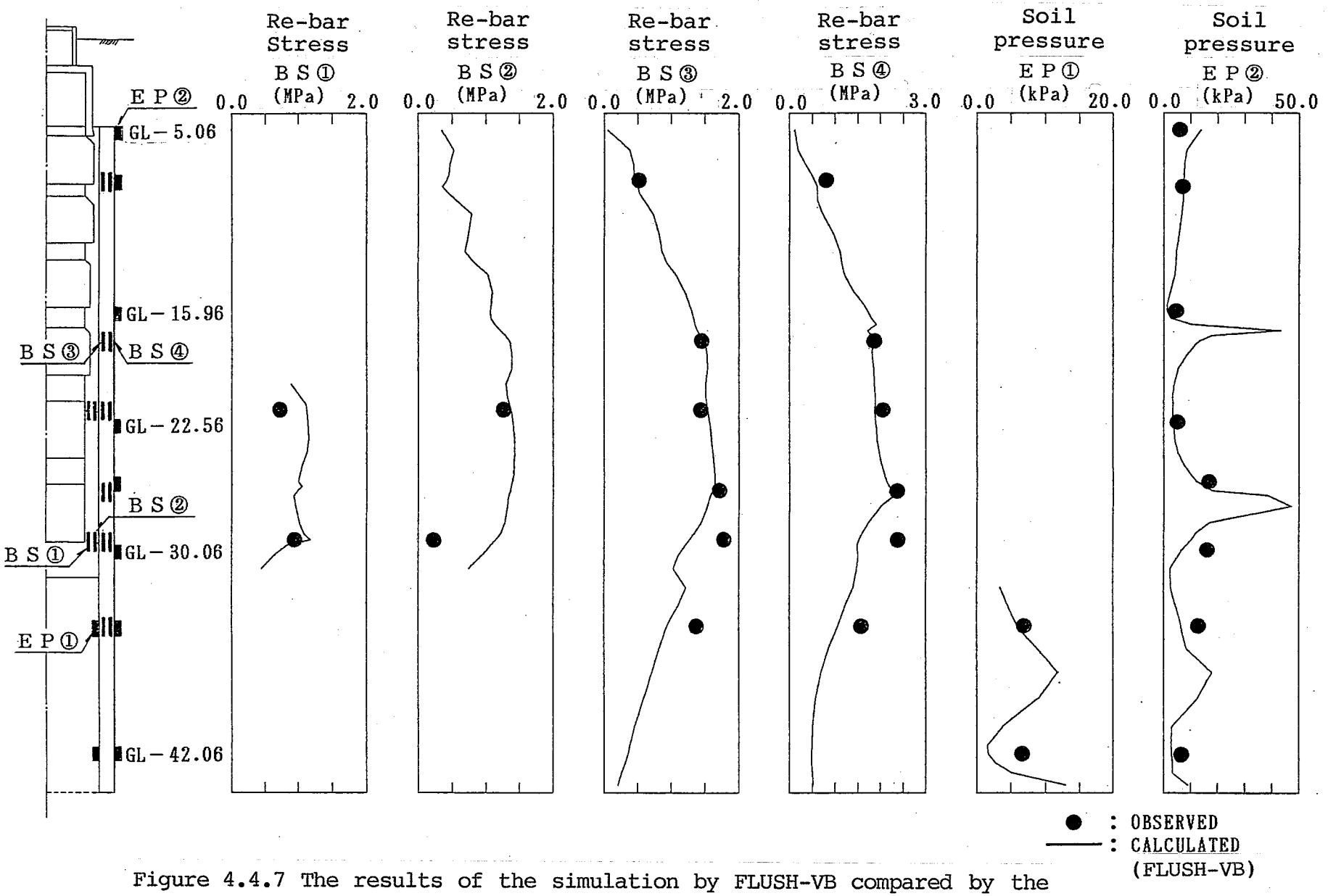

Figure 4.4.7 The results of the simulation by FLUSH-VB compared by the absolute maximum indications of re-bar extensometers and soil pressure meters observed

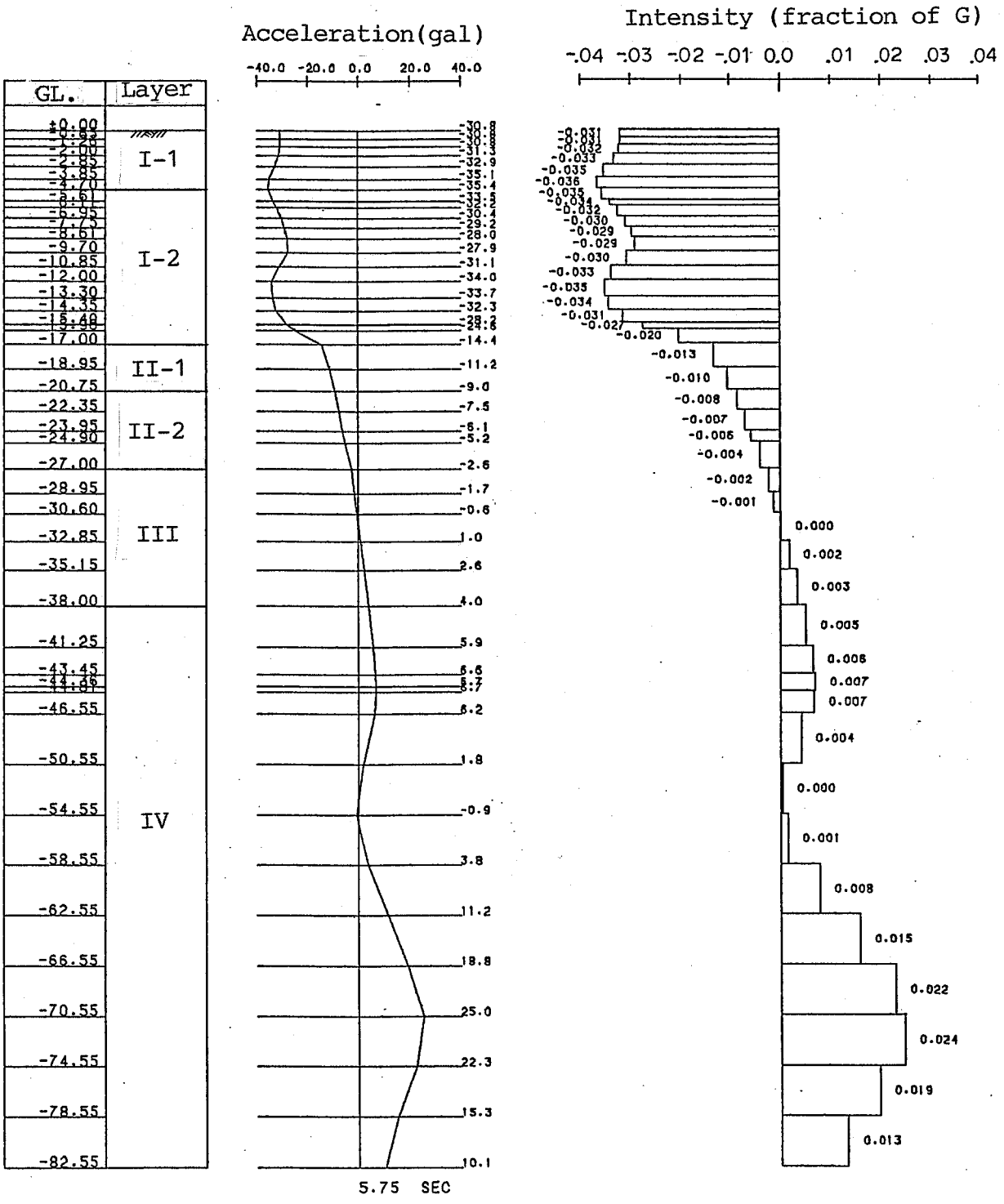

Figure 4.4.8 The details of free-field soil and the response result at t_m=5.75 sec

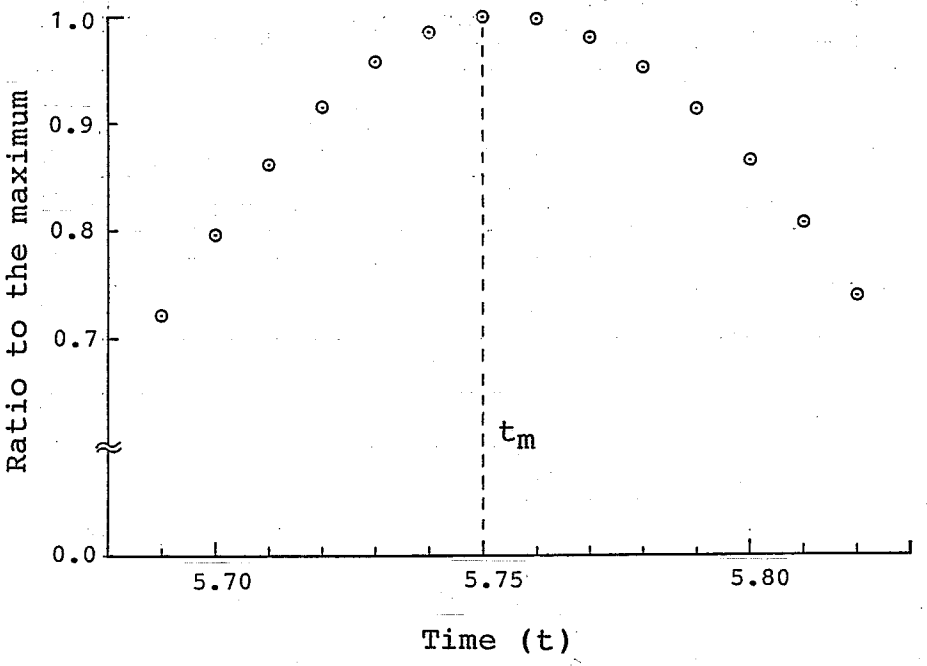

Figure 4.4.9 The determination of the time t_m

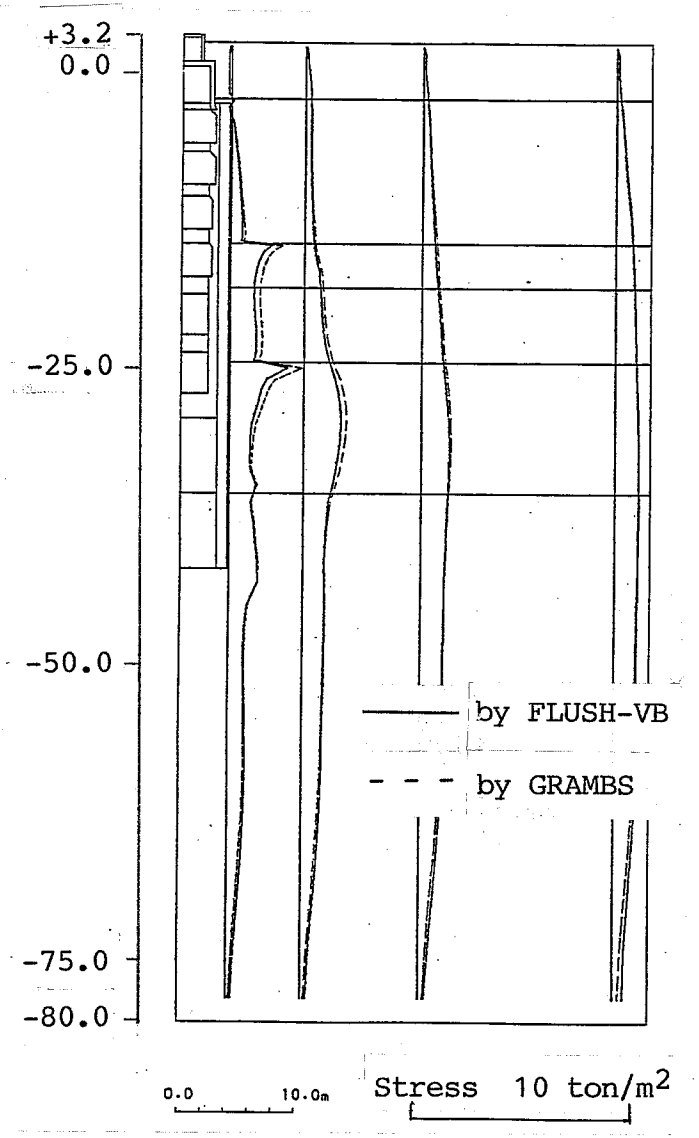

Figure 4.4.11 Comparison of the shear stress distribution by GRAMBS and FLUSH-VB(at t_m=5.75 sec)

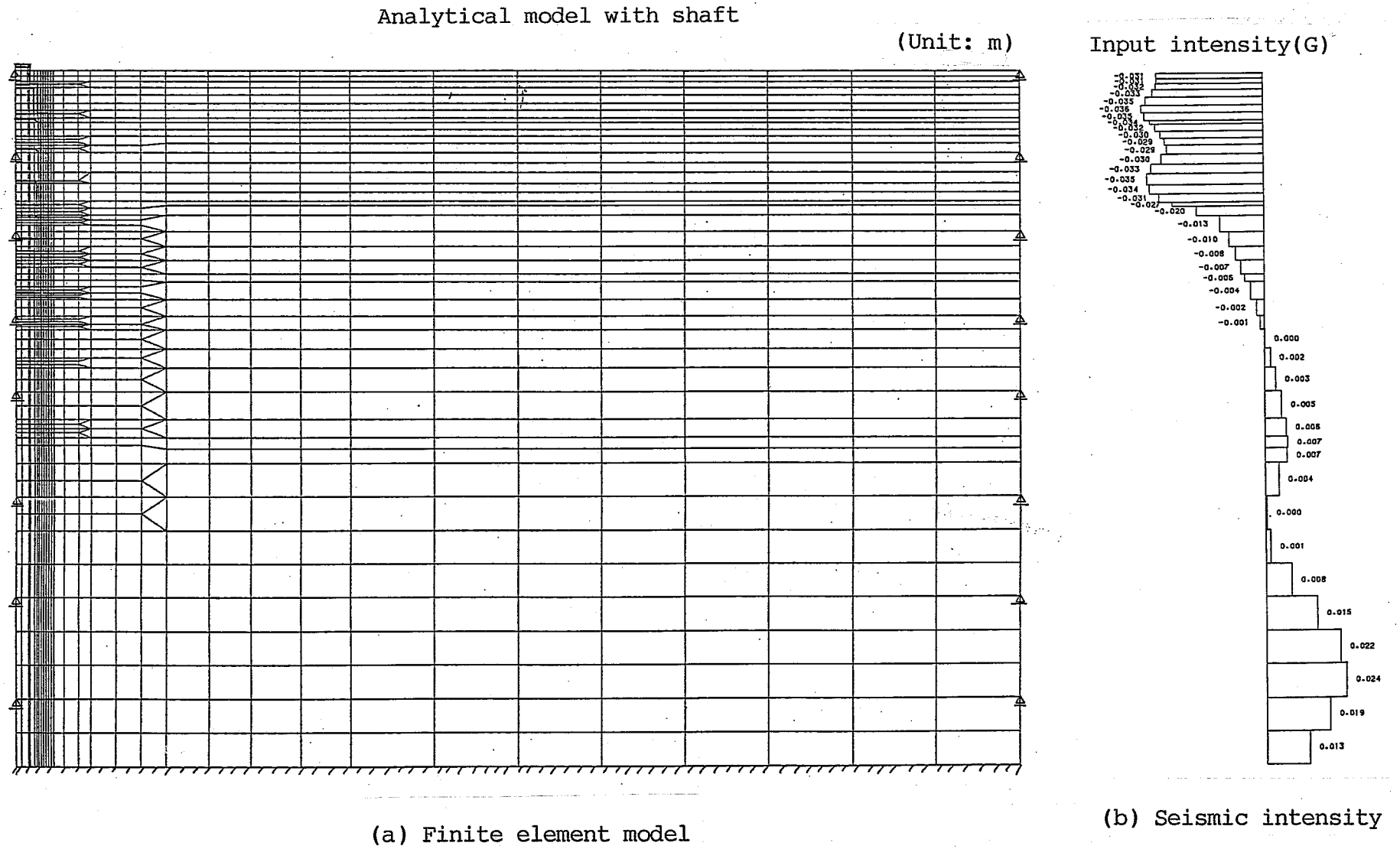

(a) Finite element model

(b) Seismic intensity

Figure 4.4.10 Finite element model and the seismic intensity input to the model in the analysis by GRAMBS

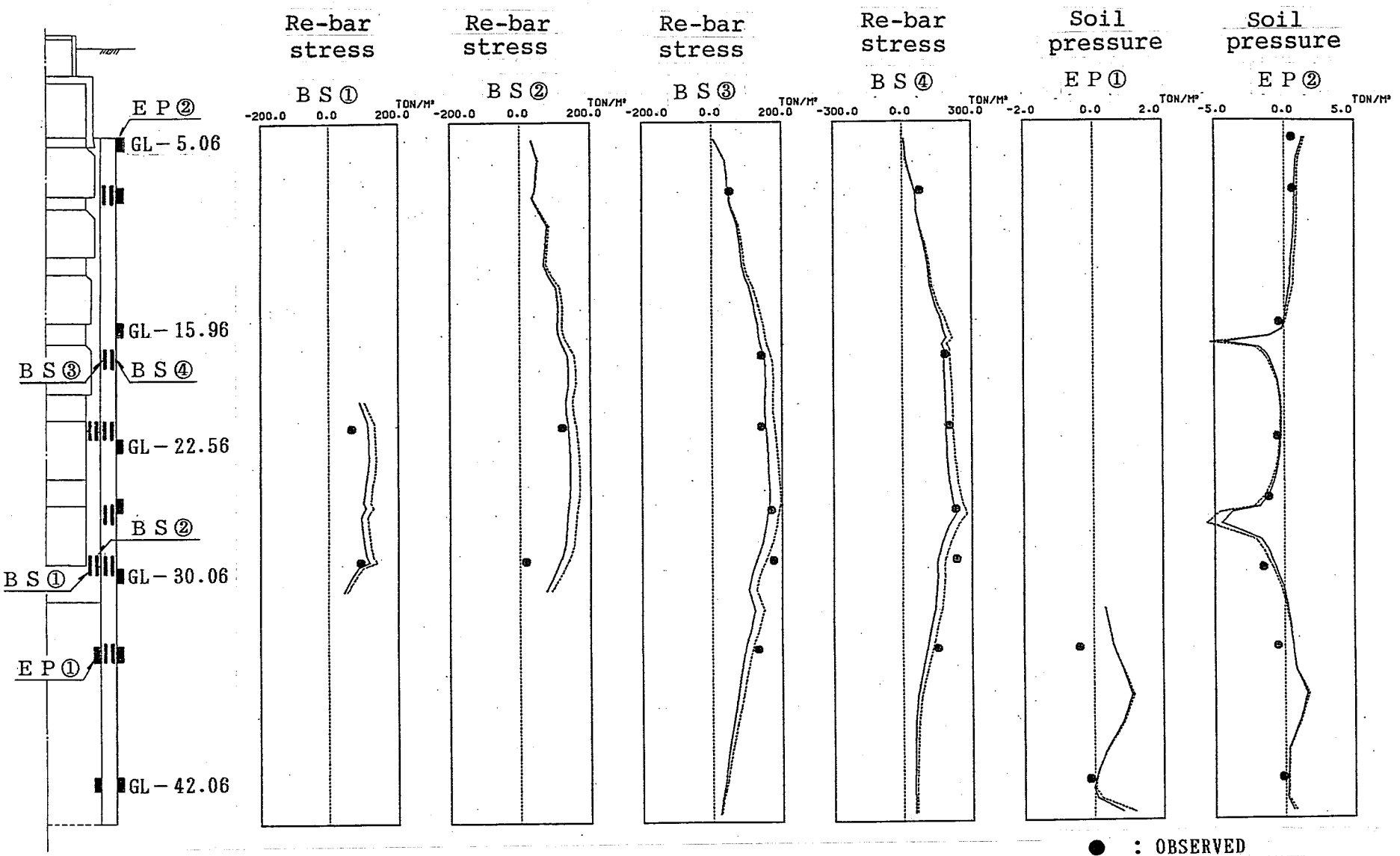

Figure 4.4.12 Comparison of the results obtained by GRAMBS with the observed and calculated by FLUSH-VB at the time t_m=5.75 sec

4.5 APPLICATION TO LARGE SCALE UNDERGROUND CAVITY

As an example of the application of GRAMBS to the design analysis of underground cavity, the cross-sectional stress analysis of a cavern assembly during a strong ground motion was performed by GRAMBS and the results were compared with those obtained by FLUSH.

4.5.1 Model cavern assembly and analytical model

The cavern assembly in Figure 4.5.1(a) whose cross-section is shown in Figure 4.5.1(b) is assumed to be subjected to a strong ground motion defined at the surface of the soft rock. The shear wave velocity of the rock formation is assumed to be 1,000 m/s at the ground surface and slowly increases with depth and the unit weight of the rock is 2.6 tons per cubic meters. Six parallel caverns were extracted from the assembly and arranged as shown in Figure 4.5.1(c) in the FEM model in order to consider the effects of the parallel arrangement of caverns on the modification of input motion and the resultant stress state if they should exist and are significant.

4.5.2 Dynamic analysis by FLUSH

The control motion of 0.5 G defined at the ground surface was first converted into the input motion at the fixed lower boundary of the two-dimensional FEM model by deconvolution analysis using one dimensional wave propagation analysis code, SHAKE, and the deconvolved motion was then applied to the two dimensional dynamic analysis code, FLUSH, as the input motion. Both time histories are shown Figure 4.5.2. The analysis was performed assuming linear state because the soft rock was considered sound enough for the response of around 0.3 G and 0.5 G at the lower boundary and at the surface, respectively.

The resultant response motions at the invert of these caverns are almost similar with each other as shown in Fig. 4.5.3 and also very close to that obtained at the same level by a one dimensional wave propagation analysis. This suggests that the ground motions at the invert of these caverns are not significantly affected by the existing caverns. It is widely believed that the input ground motions of underground facilities or caverns are less severe than those of surface structures; however, as evident from the above result, the wave form and the intensity of the input motion for the cavern can be unchanged and the severity can remain almost the same at its original level. Such phenomenon may be possible

and usual in most of the caverns excavated in sound rock, provided the size of these structures or cavernsis is smaller than the wave length of the significant frequency components of the input ground motion.

The results of the stress state of the concrete lining wall are shown in the left half of Fig. 4.5.4 for the maximum fiber stress and shear stress. These stress values are shown in the tables attached.

4.5.3 Quasi-static analysis by GRAMBS

The one dimensional wave propagation analysis of the rock region without any cavity or structure was performed and the response acceleration distribution at the time when the shear strain energy of the rock between the top and bottom of the cavity became maximum was taken out, and the compatible seismic intensity as is shown in Figure 4.5.5 was transferred to the finite element model with the cavities in the same figure.

The results of the stress state of the concrete lining wall are shown in the right half of the previous Figure 4.5.4 by the maximum fiber stress and shear stress. These stress values are shown in the tables attached.

4.5.4 Comparison of the results by FLUSH and GRAMBS

The stress distribution, the maximum fiber stress and shear stress of the concrete lining wall of the cavern A obtained by GRAMBS showed good agreement with those obtained by FLUSH within an error of less than 1 %. Thus, the GRAMBS can also be adopted for calculating the maximum stress state of structures like tunnels or caverns, in case the cross-sectional stress state is of concern and the plane strain assumption is valid. The computer time used for the analysis by GRAMBS was one fifteenth of the time required for the analysis by FLUSH.

The analysis with GRAMBS has further advantage in this example and also in usual cases of analyses; the finite element model that includes the cavities is common in both analyses for obtaining the maximum stress state by earthquake load and for the initial stress state under the overburden load. In this example, the dynamic stresses of the lining wall and the rock surrounding the caverns are superposed with the resultant stresses caused by an overburden load obtaind by changing the load pattern and the Poisson's ratio in the analysis. The principal

stresses in the rock surrounding the caverns due to the above two kinds of loads are separately shown in Figure 4.5.6. The final stress state of the rock surrounding the caverns and the lining wall under the combined loads are shown in Figure 4.5.7.

4.5.5 Reference

(1) Katayama, I., An approach to evaluate ultra-long term stability of high-level radioactive waste storage caverns for the development of geological repository and current status of the site selection in Japan, an invited paper at the 8th International Conference on Structural Mechanics in Reactor Technology, Session C6., The Transportation and Disposal of Spent Nuclear Fuel and High-Level Radioactive Wastes, The Technical Criteria and Institutional Constitution, Brussels, Belgium, August 19-23, 1985.

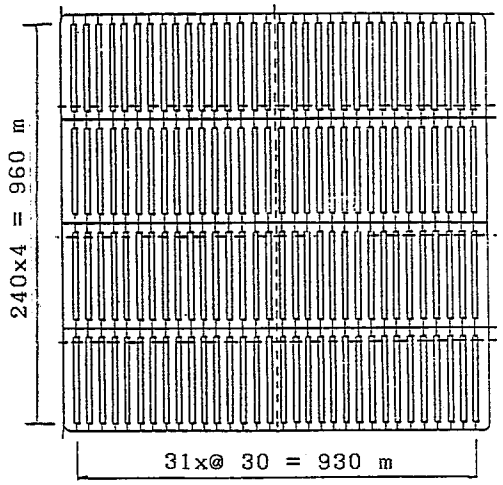

(a) Plan of cavern assembly assumed

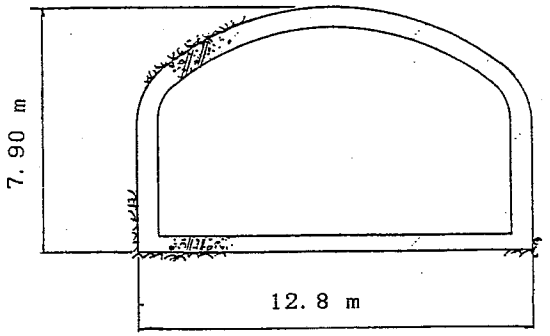

(b) Cross-section of cavern with concrete lining wall of 50 to 70 cm thickness

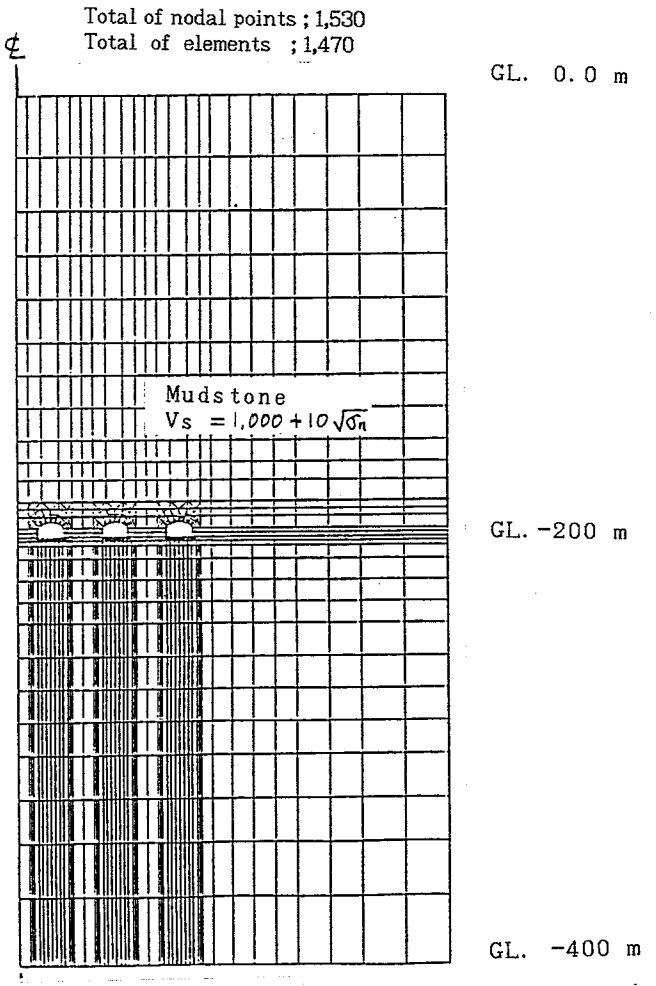

(c) Plane strain finite modeling of representative caverns for the analysis by FLUSH and GRAMBS

Figure 4.5.1 Cavern assembly and the modeling concept

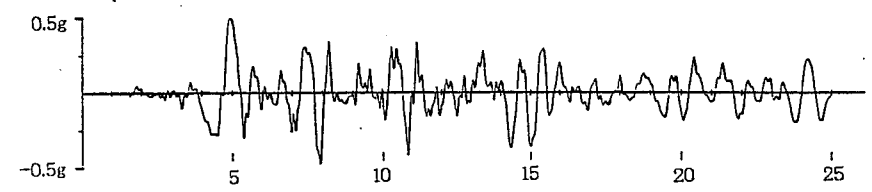

(a) Control motion defined at the surface

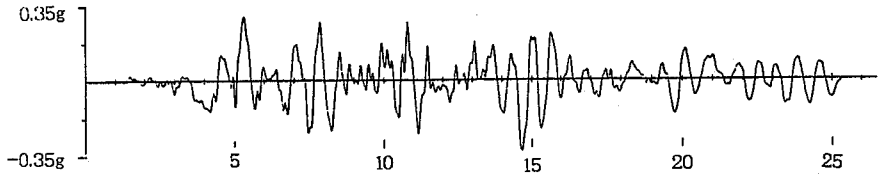

(c) Input motion at the fixed lower boundary deconvolved by one dimensional wave propagation analysis.

Figure 4.5.2 Control motion and input motion for dynamic analyses

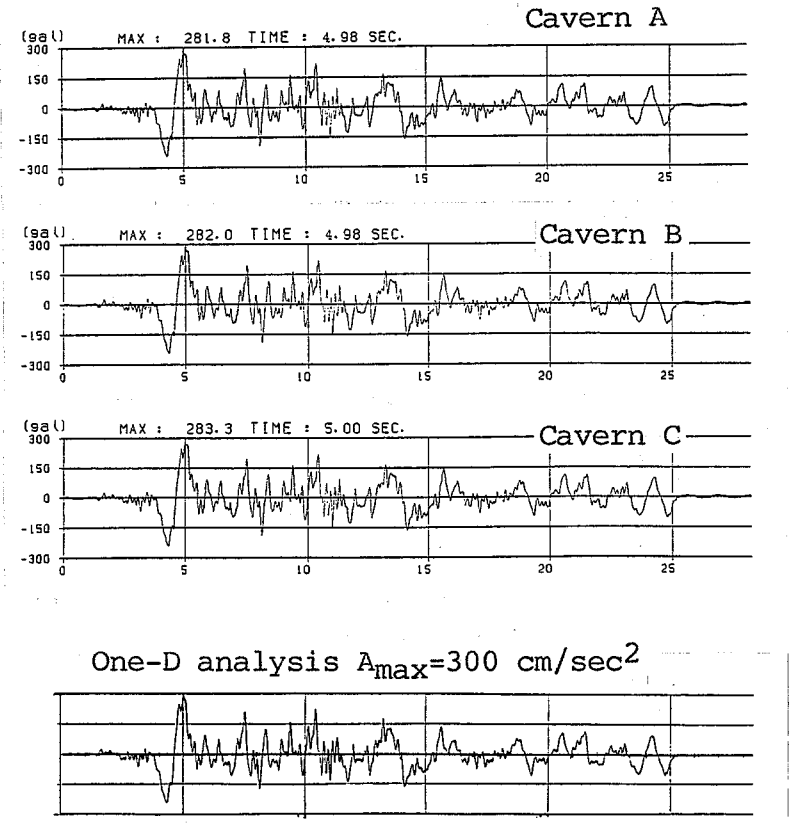

Figure 4.5.3 The comparison of the response acceleration time histories at the invert of caverns and the time history at the same level by one dimensional wave propagation analysis

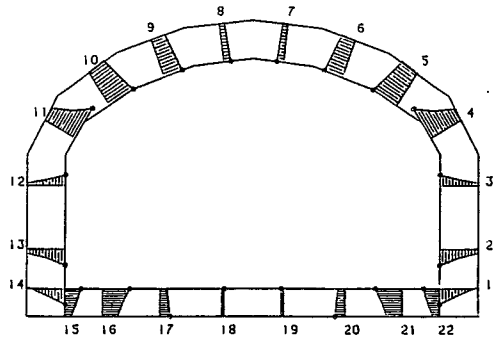

fiber stress

NO.	max.value	NO.	max.value
1	846.15	12	587.08
2	862.73	13	-862.52
3	-584.26	14	-846.71
4	-1868.13	15	-895.45
5	-1551.82	16	-1487.54
6	-1052.95	17	-552.65
7	-375.40	18	-141.65
8	371.16	19	143.57
9	1050.97	20	554.43
10	1553.56	21	1488.54
**11	1873.67	22	895.42

** : the max. of max.values

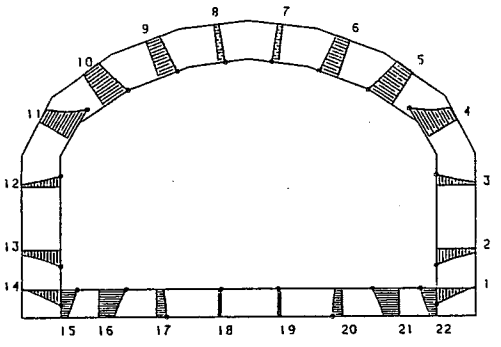

fiber stress

NO.	max.value	NO.	max.value
1	851.55	12	593.84
2	868.07	13	-868.26
3	-588.48	14	-852.26
4	-1880.61	15	-901.32
5	-1561.91	16	-1497.22
6	-1059.58	17	-556.18
7	-377.58	18	-142.48
8	373.77	19	144.61
9	1057.86	20	558.13
10	1563.57	21	1498.42
**11	1885.61	22	901.36

** : the max. of max.values

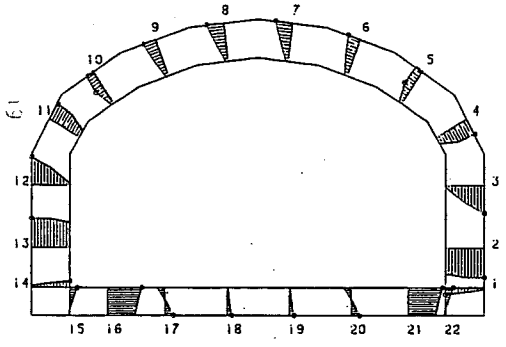

shear stress

NO.	max.value	NO.	max.value
1	89.01	12	367.58
2	391.40	13	391.90
3	366.60	14	88.54
4	223.85	15	-101.91
5	-119.26	**16	-460.11
6	-175.88	17	-109.98
7	-234.02	18	-60.07
8	-234.54	19	-60.05
9	-176.83	20	-109.88
10	-120.20	21	-460.02
11	223.62	22	-102.33

** : the max. of max.values

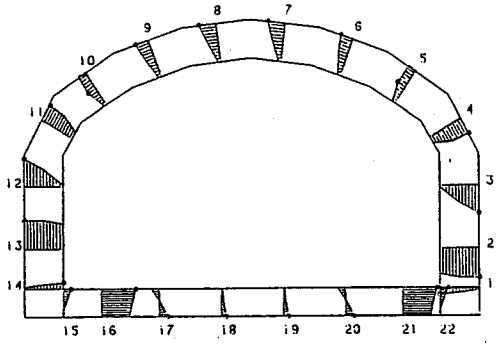

shear stress

NO.	max.value	NO.	max.value
1	89.67	12	369.97
2	394.02	13	394.49
3	369.03	14	89.19
4	225.25	15	-102.64
5	-120.11	**16	-463.12
6	-177.07	17	-110.73
7	-235.54	18	-60.48
8	-236.05	19	-60.46
9	-177.95	20	-110.64
10	-120.95	21	-463.03
11	225.11	22	-103.37

** : the max. of max.values

(a) Calculated by FLUSH

(b) Calculated by GRAMBS

Figure 4.5.4 Comparison of dynamic stresses of the inner concrete lining wall obtained by FLUSH and GRAMBS

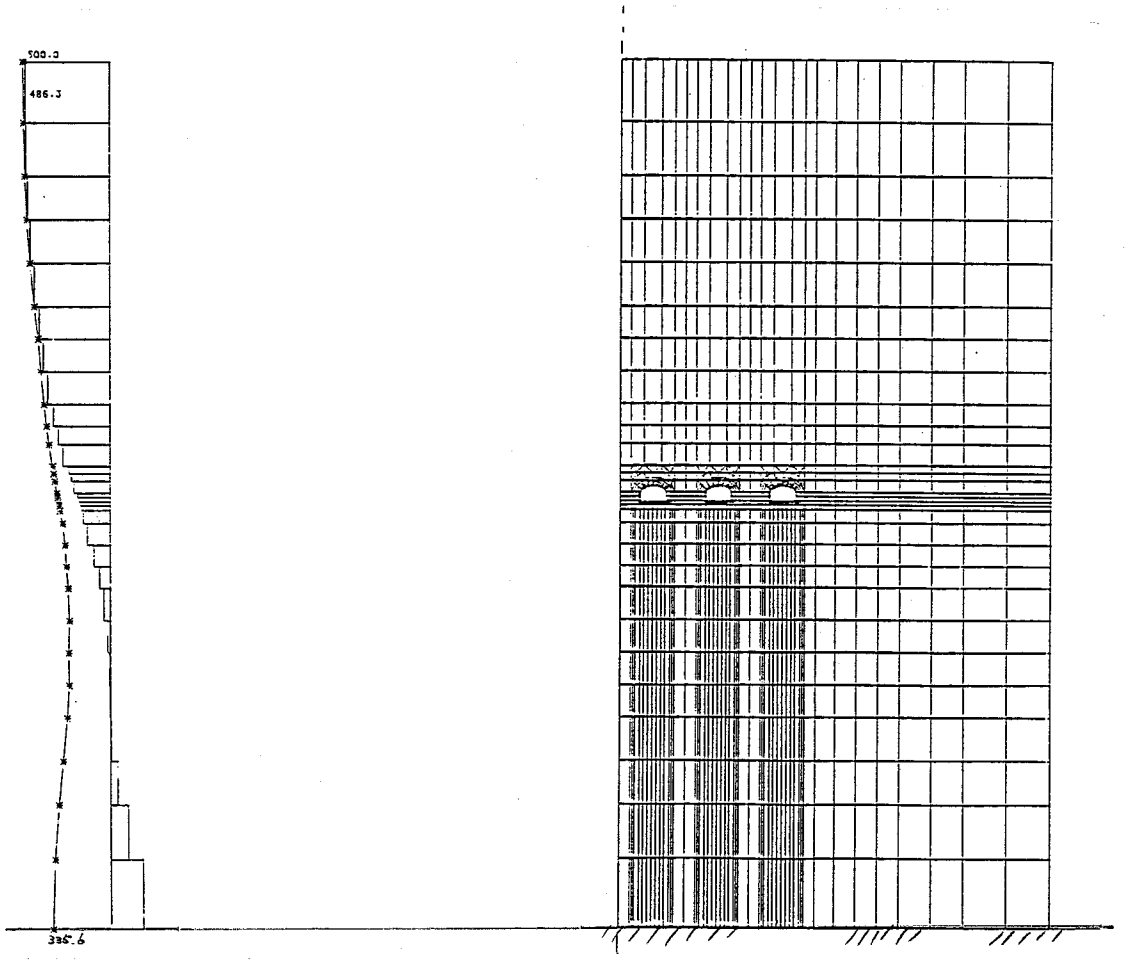

(a) Sismic intensity
at t_m=4.98 sec

- the maximum accelerations

(b) Model for quasi-static analysis
by GRAMBS

Figure 4.5.5 Input seismic intensity distribution and quasi-static analysis model

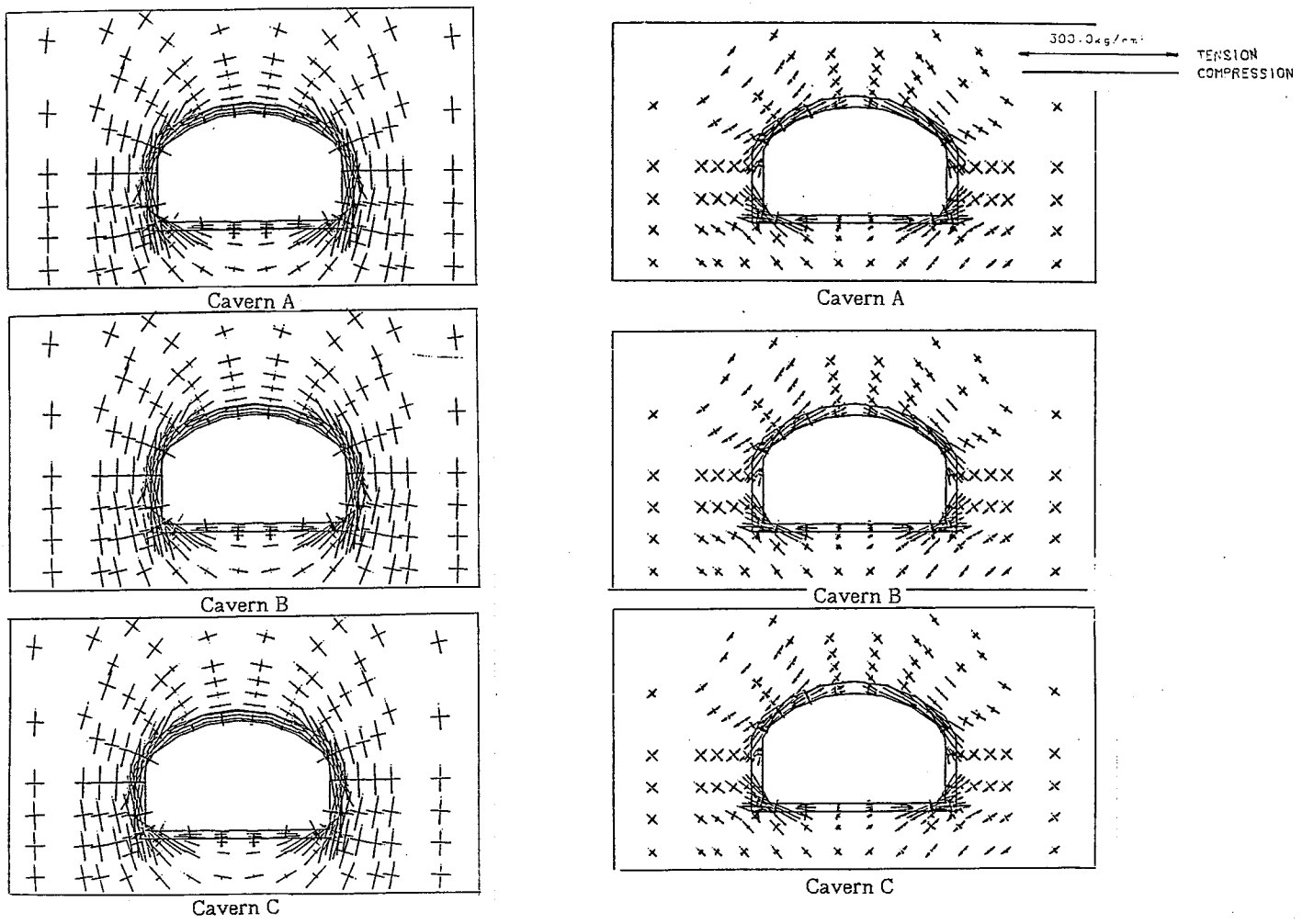

Figure 4.5.6 Principal stress states surrounding the parallel caverns by overburden pressure and seismic force (by GRAMBS)

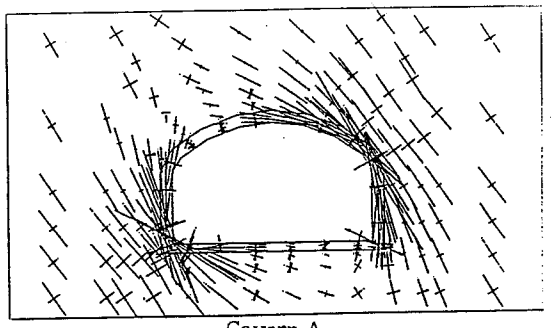

Cavern A

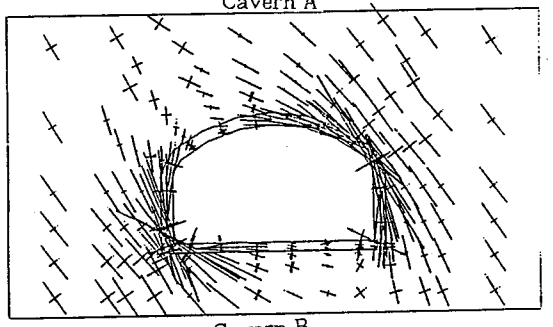

Cavern B

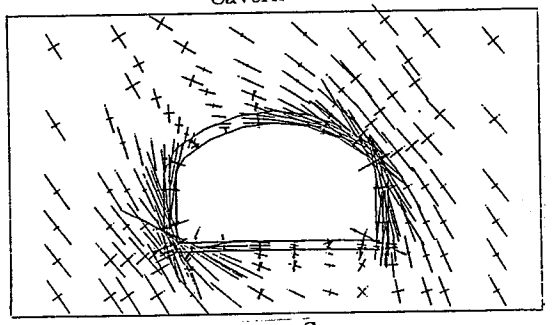

Cavern C

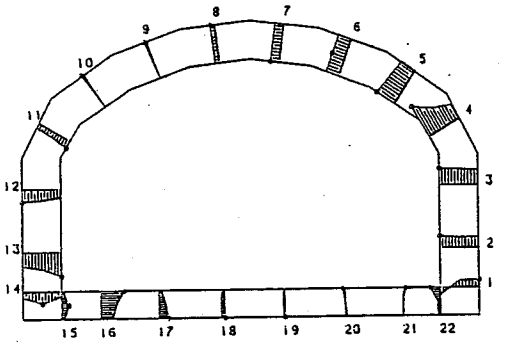

Fiber stress of Cavern A

NO.	max.value	NO.	max.value
1	-1064.74	12	-1800.38
2	-1664.38	13	-3402.91
3	-2315.91	14	-1722.11
•• 4	-4927.96	15	-956.40
5	-3038.54	16	-3278.20
6	-1992.55	17	-1389.66
7	-1338.52	18	-536.70
8	-707.85	19	-254.16
9	-345.92	20	417.92
10	-300.23	21	-280.47
11	-1161.31	22	1548.84

•• : the max. of max.values

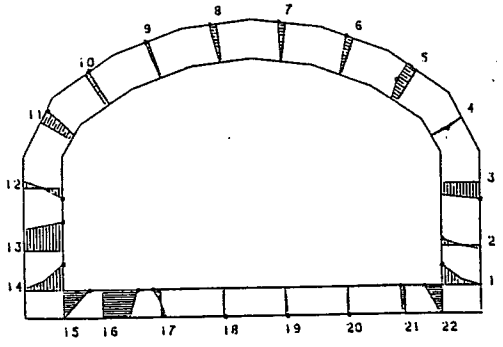

Shear stress of Cavern A

NO.	max.value	NO.	max.value
1	-637.43	12	-328.25
2	-220.53	13	901.17
3	523.27	14	817.04
4	77.45	15	-779.93
5	-372.56	••16	-1083.52
6	-258.19	17	249.35
7	-239.76	18	-56.34
8	-231.44	19	-64.63
9	-96.93	20	-52.93
10	143.74	21	156.70
11	424.44	22	573.46

•• : the max. of max.values

Figure 4.5.7 Principal stress states around the parallel caverns and the fiber and shear stress of the inner concrete lining wall of the cavern A for combined loads (by GRAMBS)

4.6 CONCLUSIONS

For providing a practical yet reliable tool for practicing design engineers and for refinement of the cross-sectional design of buried structures, the author proposed his simplified analysis method GRAMBS(Ground Response Acceleration Method for Buried Structures) for the cross-sectional design of structures such as buried ducts and tunnels in layered soil.

When a structure is buried under a soil, the major external force to the structure is provided by the effective dynamic response of the surrounding soil. Assuming a plane strain dynamic system consisting of buried structures surrounded by layered soil, it was shown theoretically that the proposed GRAMBS is a quasi-static method which approximately predicts the maximum response of the buried structures surrounded by soil which can be obtained by a two-dimensional dynamic finite element analysis.

By introducing the acceleration distribution at the time when the portion of the soil in contact with the structure reaches the maximum strain energy state as the conserved body force acting on the system and by using the converged strain-dependent soil properties, both given by the response analysis of the free-field soil surrounding the structure, the GRAMBS solves the system idealized by a two-dimensional finite element model as a static problem.

The procedure to be followed in the calculation was explained through the analyses of a single story duct surrounded by a uniform soil with varying embedment depth, soil properties and thickness of the soil layer. The results of the analyses were shown by the cross-sectional forces and compared with the results of the analyses by a representative dynamic analysis code FLUSH-VB.

The agreement between the above results was amazingly good. And based on the fact that the FLUSH could successfully reproduce the cross-sectional bending moment of a single story duct model embedded in a dry sand layer obtained by an experiment performed and reported by Tohma and others(1985) of CRIEPI, the validity GRAMBS was confirmed for application to the single story duct surrounded by uniform soil.

Further, Kaizu, Annaka, and Ohki (1989(a), 1989(b)) and Kaizu, Harada, Annaka and Ohki(1989) reported that the observed response of re-bar stress and contact soil pressure of a multi-story shaft in a multi-layered soil being used as an underground power transmission system shaft

could be well reproduced by the FLUSH-VB. Utilizing the data included in their study with additional data supplied by Mr. Kaizu, the numerical analysis was performed by GRAMBS. The above observational results were again well reproduced by GRAMBS.

With the results obtained in the above, the validity of GRAMBS is completely confirmed and its application to a large scale cavern assembly was shown as an additional promising area for its application.

CHAPTER 5. SUMMARY AND CONCLUSIONS

As the first item of the objectives of his study, and recognizing the significance of the radiation damping effect as one of the important fundamental components in SSI analysis, the author tested a practical modeling concept to reasonably simulate the actual dam response recorded at an arch dam. The modeling concept consists of the three-dimensional finite dam elements with far-field impedances of infinite strips along the abutment which are constant for a significant frequency range of the dam and foundation modes, with the reservoir water elements upstream and transmitting boundaries defined by impedance ratios at the water-water boundary and the water-gorge and bottom boundary, and frequency domain analysis scheme. Through the analysis, the author found the following significant conditions to be selected for successfully explaining the recorded response of the dam.

(1) The analytical model which is capable to reflect the far-field boundary effect by an approximate impedance function along the dam abutment will give reasonable prediction of the dam response.

(2) When the dam was modeled with limited volume of foundation rock with fixed boundary, the dam response became unreasonably large when a reasonable value of material damping is used for the dam and the foundation rock.

(3) The reservoir water was found to suppress the upstream-downstream response of the dam, however, it does not contribute to its antisymmetric mode of vibration.

(4) To obtain a good fit to the recorded motions of the dam, it was required to take the spatial variation of the input ground motions into account. This fact suggests the need for observing reliable spatially varied input ground motions preferably in the form of free-field motions.

Also under the same objective in the study of SSI analysis, the linear and non-linear three-dimensional soil-structure interaction analysis codes, HASSI-4 and HASSI-7, were tested for their validity by correlation studies using the forced vibration data and earthquake response records at a small scale reactor building model. The soil properties obtained by in-situ and laboratory test were used. Some ambiguous nature inherent with these soil properties affected the results; however, the properties used in reproducing the records remained

within a reasonable range of the variation of soil properties actually observed.

From the predicted results of the 1987 January 17th earthquake by the three-dimensional analysis code, two-dimensional analyses, and the stick model with soil springs, the following SSI features were found;

(1) The transfer functions of the surface motions at a series of the points located in the near-field soil region showed a very rapid and sharp decay with distance from the side wall of the structure foundation in the case of the three-dimensional code, HASSI-4, whereas the transfer functions of the two-dimensional code, FLUSH-VB, showed slower and is of a dispersive nature.

(2) In the two-dimensional analyses, the frequency shift was not so significant but the over damping is very serious resulting in an excessive underestimation of the response of the structure. The effective dampings in HASSI-2D and FLUSH-VB were estimated to be 8.4 and 4.9 times that in HASSI-4, respectively.

(3) The total damping applied in the simulation by the three-dimensional code, HASSI-4, was estimated as about 2 %, whereas in the simulation by the two-dimensional codes, HASSI-2D and FLUSH-VB, corresponding damping was estimated as 9.8 % and 16.8 %, respectively.

(4) In the case of HASSI-2D, the over-damping can be explained by the inadequacy of converting the truly infinite half-space problem into the infinite strip problem. As for the case of FLUSH-VB, the interpretation comparable to the above may not be appropriate, because we can neither distinguish between the material damping and the radiation damping nor give clear explanation of the mechanism of damping in this system. However, it may be pointed out that FLUSH-VB will give us significant underestimate of the three-dimensional response of a truly three-dimensional structure.

Next, taking far stronger earthquake response records which were obtained at the 1987 December 17th earthquake with recorded maximum acceleration of 301.2 gals at the roof top and 73.5 gals at the ground surface, the non-linear version, HASSI-7 was tested for its validity.

The agreement between the calculated and observed response of the model structure was fair as a whole. However, the predicted maximum accelerations became smaller than the observed; this may be attributed to the applied damping being defined as proportional with frequency in

a complex modulus method.

However, through the simulation, it was clearly shown that the strain levels of the free-field soil and the soil near the foundation structure are remarkably different and that the soil strongly affected by the soil-structure interaction was limited to a fairly small region, the radius of which was less than two times the radius of the structure. This also indicates that only a three-dimensional analysis can reproduce the rapidly decaying nature of the wave generated at the soil-structure interface of a truly three-dimensional structure.

As already pointed out by Luco and Hadjian(1974) and Wolf(1985), it is almost impossible to model a three-dimensional structure with a two-dimensional modeling, and a two-dimensional model will significantly underestimate the true three-dimensional response by a small shift in frequency and significant over-damping of the vibration system.

From the above results, it can be clearly stated that we should avoid to treat soil-structure interaction phenomena of truly three-dimensional structures with two-dimensional modeling, in order not to underestimate the true response of the three-dimensional structures, that the radiation damping must be reasonably reflected in any analysis code and that in case of large structures like the dam considered here, the effect of spatially varied input ground motions to the structure should be extensively studied further with on-site observations.

The second item of the objectives of his study is to recognize the characteristics of the seismicity of the Kanto area where the seismicity is mostly attributed to three-dimensionally distributed seismic source regions, and to derive the attenuation curves appropriately reflecting the effect of focal depths on the peak ground motions. Combining the above three-dimensional seismic source regions and the attenuation curves, it was aimed to provide a series of seismic hazard maps of the area or a data base for predicting the peak accelerations and velocities applicable to the practical design of lifeline structures on the ground and underground.

Existing attenuation curves were classified into four types from the physical meaning of skeleton curves used and tested for their fit to the Japanese strong motion records that were corrected and selected for this study (NONFSEL). Among the formulas which do not contain explicitly the focal depth, the Campbell's curve(Type III) showed the best fit. However, the Nakamura et al curve(implicit form of Type IV curve) gave

almost the same degree of fit with the data.

Based on the results obtained by I.Katayama(1985, 1986), the combination of the three-dimensional earthquake source model and the attenuation curve I.Katayama Type II which belongs to the above Type IV curve gave a reasonable seismic hazard map of the Kanto area for various exposure times. The skeleton of the Type IV curve was chosen to obtain new attenuation curves using the NONFSEL.

Considering that the horizontally propagating waves rather than vertically incident waves are of primary concern for the longitudinal response of buried ducts or pipes and the possibility of their response for the horizontally travelling waves up to the frequency range just lower than the usual frequency range of body waves, the strong motion records NONFSEL were filtered using a high-cut filter with a cut-off frequency of 1.4Hz and a filtered strong motion data set was prepared (FLTDSEL) for the further study of the peak ground motions meaningful for buried structures.

Using both strong motion data sets, two sets of attenuation curves were derived. The curves based on the non-filtered strong motion data set NONFSEL were designated to be used in predicting the peak ground motions for structures on the ground, and the other set of curves based on the filtered strong motion data set FLTDSEL were prepared for underground structures.

As an application of these formulas and to provide a design data for power transmission systems which includes various types of structures constructed on ground and underground, the above two sets of new attenuation curves were combined with a three-dimensional source model of the Kanto area to assess its seismic hazard.

Assuming a Poisson process of occurrence of earthquakes, the seismic hazard of the Kanto area was presented in terms of contour maps of the expected peak ground acceleration and velocity and for representative exposure times which can be used for predicting the peak ground motions meaningful for both structures on the ground surface and buried in shallow depths.

The third item of the objectives of his study is to provide a practical and reliable tool for practicing design engineers and for refinement of the cross-sectional design of buried structures. For this purpose, the author proposed his simplified analysis method GRAMBS(Ground

Response Acceleration Method for Buried Structures) for the cross-sectional design of structures such as buried ducts and tunnels in layered soils.

When a structure is buried under the soil, the major external force to the structure is provided by the dynamic response of the surrounding soil. Assuming a plane strain dynamic system consisting of buried structures surrounded by a layered soil, it was shown theoretically that the proposed GRAMBS is a quasi-static method that approximately predicts the maximum response of the buried structures surrounded by soil which would otherwise be obtained by a two-dimensional dynamic finite element analysis.

By introducing the acceleration distribution at the time when the portion of the soil in contact with the structure reaches the maximum strain energy state as the conserved body force acting on the system and using the converged strain-dependent soil properties, both given by the response analysis of the free-field soil surrounding the structure, the GRAMBS solves the system idealized by a two-dimensional finite element model as a static problem.

The procedure to be followed in the calculation was explained through the analyses of a single story duct surrounded by a uniform soil with varying embedment depths, soil properties and thickness of the soil layer. The results of the analyses were shown by the cross-sectional forces and compared with the results of the analyses by a representative dynamic analysis code FLUSH-VB.

The agreement between the above results was amazingly good. And based on the fact that the FLUSH could successfully reproduce the cross-sectional bending moment of a single story duct model embedded in a dry sand layer obtained from the experiment performed and reported by Tohma and others(1985) of CRIEPI, the validity of GRAMBS was confirmed for application to the single story duct surrounded by a uniform soil.

Kaizu, Annaka, and Ohki (1989(a), 1989(b)) and Kaizu, Harada, Annaka and Ohki(1989) reported that the observed response of the re-bar stress and contact soil pressure of a multi-story shaft in multi-layered soil used as an underground power transmission system shaft could be well reproduced by the FLUSH-VB. Utilizing the data included in their study reports with additional data supplied by Mr. Kaizu, a numerical analysis was performed by GRAMBS. The above observational results were again well reproduced by GRAMBS.

With the results obtained above, the validity of GRAMBS is completely confirmed and its application to a large scale cavern assembly was shown as an additional promising area for its application.